Transition Metal-Based Complexes and Organic Small Molecules for the Electrochemical Reduction of Carbon Dioxide and Dioxygen

Lauren Elizabeth Lieske
Fredericksburg, Virginia

B.S., Chemistry, Virginia Commonwealth University, 2017

A Thesis presented to the Graduate Faculty of the University of Virginia in Candidacy for the Degree of Master of Science

Department of Chemistry

University of Virginia
February 2020

Transition Metal-Based Complexes and Organic Small Molecules for the Electrochemical Reduction of Carbon Dioxide and Dioxygen

Lauren E. Lieske

Machan Laboratory

Abstract

The current primary source of energy for mankind, fossil fuels, is non-renewable and is the major source of anthropogenic carbon dioxide (CO_2) emissions that are negatively impacting the environment. There remains a need to develop alternative energy sources that are not harmful towards the environment while meeting the increasing global energy demands. One approach is to utilize electrochemical methods, using electricity generated from renewable energy sources like solar or wind, to drive forward key energy reactions such as the reduction of CO_2 and dioxygen (O_2). Imperative to this process is developing electrocatalysts capable of lowering energy barriers associated with these reactions. The major advantage molecular systems offer in contrast to heterogenous systems is that key intermediates can be observed, and therefore crucial mechanistic steps can be identified. Furthermore, molecular catalysts can be easily modified to obtain better results by simply switching out different metal centers or altering the ligand backbone. We have investigated inorganic (nickel polypyridyl complex) and organic (Cyclic (Alkyl)(Amino) Carbenes) species competent in mediating the electrochemical conversion of CO_2. Additionally, we characterized a known water-soluble catalyst, Mn(III) meso-tetra(N-methylpyridinium-4-yl)porphyrin, through the entire pH domain and found it capable of reducing O_2 to water under buffered acidic conditions.

Copyright Information

Acknowledgements

The work described in this thesis would not have been possible without the guidance of my research advisor, Dr. Charles W. Machan. I am extremely grateful for the opportunities he presented to me and the guidance he gave me with my research. During my time at UVA, I expressed an interest in teaching and he always went the extra mile to ensure that I was getting the experience I wanted in that realm and for that I will always be appreciative. The attention to detail and work ethic he demands from his students (as well as himself) has certainly made me a better researcher and I know this will help me be successful in my future pursuits. Thank you for the guidance and making the last three years a rewarding experience.

I have had the privilege of working with several remarkable scientists throughout my research. I would like to first express my deepest appreciation to my committee members – Dr. Robert Gilliard, Dr. Ian Harrison, and Dr. Sen Zhang – and their belief in my abilities. Especially to Robert, the opportunity to collaborate with him was truly an enriching experience that opened my eyes to an exciting area of chemistry that his group conducts. To each member of the Machan lab, thanks for the support! I cannot begin to express my thanks to Shelby Hooe who collaborated with me on work presented in this thesis. Her dedication to science and intense work ethic is truly inspirational. Her support, knowledge and friendship truly enriched my graduate school experience. I must also thank Asa Nichols who assisted in work presented in this thesis. I also had a great pleasure of working with Lucas Freeman whom I collaborated with on a publication presented in this thesis. I truly enjoyed working with him, his genuine excitement for chemistry is truly contagious. I'd like to recognize the help I received from the following faculty and staff

during my time with the chemistry department Dr. Diane Dickie, Dr. Jeff Ellena, and Mr. Michael Birckhead.

To my parents and brother Dustin - they have shown me so much support during my time in graduate school. Words cannot express my love and gratitude for them. Thank you for constantly believing in me and for challenging me to chase after what I want in life. Lastly, to Noah and Rebby whom were my pillars during this experience. They picked me up every time I fell and cheered me on all the way to the finish line and I will forever be grateful for our friendship.

Table of Contents

Abstract ii
Copyright Information iii
Acknowledgements iv
List of Abbreviations viii
List of Figures xii
List of Tables xxv
1.1 Introduction 2
1.1.1 Current Energy Issues 2
1.1.2 Molecular Electrocatalysis as a Solution to Energy Crisis 3
1.2 Electrochemical Techniques Brief Overview 5
1.3 Intrinsic Parameters used to Define Catalytic Efficiency 8
1.3.1 Additives to Optimize Catalysis 10
1.4 Challenges of Electrochemical Activation of CO_2 11
1.4.1 Catalytic Design Based on Nature 12
1.4.2 Examples of Inorganic Electrocatalysts for CO_2 Reduction 12
1.4.3 Pre-activation of CO_2 by Organic Molecules 14
1.5 The Oxygen Reduction Reaction (ORR) 14
1.5.1 Mechanistic Considerations 16
1.5.2 ORR Molecular Catalyst Design 17
1.6 Thesis Overview 18
1.7 References 18
2.1 Abstract 27
2.2 Introduction 27
2.3 Results and Discussion 28
2.3.1 Characterization of $[Ni(TPEN)][PF_6]_2$ 28
2.3.2 Electrochemical Characterization 30
2.3.3 Foot-of-the-Wave Analysis (FOWA) 32
2.3.4 Product and Mechanistic Characterization by Controlled Potential Experiments (CPE) 33
2.3.5 Addition of CO Scavenger 36
2.3.6 DFT Calculations and the Proposed Mechanism 37

2.4 Conclusions 39
2.5 Experimental Section 40
2.5.1 Evans Method 40
2.5.2 Determination of $^{13}CO_2$ Shift 40
2.5.3 Materials and Methods 41
2.5.4 Synthetic Procedures 42
2.5.5 Electrochemistry 51
2.5.6 IR Spectroelectrochemistry 52
2.5.7 Product Analysis 53
2.5.8 Foot-of-the-Wave Analysis (FOWA) Calculations 67
2.6. References 76
3.1 Abstract 81
3.2 Introduction 81
3.3 Results and Discussion 82
3.4 Conclusion 90
3.5 Experimental 90
3.5.1 Supporting Information 90
3.5.2 DFT Coordinates 112
3.5 Author Contributions 136
3.6 References 136
4.1 Abstract 141
4.2 Introduction 141
4.3 Results and Discussion 142
4.3.1 Electrochemical Characterization 142
4.3.2 Description of Speciation in Solution 145
4.3.3 Catalytic Activity 150
4.4 Conclusion 155
4.5 Experimental Methods 155
4.5.1 Materials and Methods 155
4.5.2 Aqueous Buffer Solutions 156
4.5.3 Electrochemistry 156
4.5.4 RRDE Experiments 157

4.5.5 Description of Number of Electrons Transferred (n_{cat}) and Overpotential (η) Calculations 159

4.5.6 TOF_{max} Calculation from CV data 160

4.5.7 UV-vis Spectroelectrochemistry 161

4.5.8 Rinse Test Procedure 162

4.6 Supporting Information 163

4.7 Author Contributions 208

4.8 References 208

5.1 Introduction 213

5.2 Conclusions 213

5.3 Outlook for Future Applications of Molecular Catalysts 215

5.3.1 Electron-Proton-Transfer Mediators (EPTM) 215

5.3.2 Flow Cell Technology for CO_2RR 216

5.4 References 217

List of Abbreviations

bpy	Bipyridine
C_2	Multi-carbon products
CAACs	cyclic(alkyl)(amino) carbenes
C*c*O	Cytochrome *c* oxidase
CO	Carbon monoxide
CO_2	Carbon dioxide
CO_2RR	Carbon dioxide reduction reaction
CO_3^{2-}	Carbonate
CODHs	Carbon monoxide dehydrogenases
CPE	Controlled potential electrolysis
CPET	Concerted proton-electron transfer
CV	Cyclic voltammetry
DFT	Density functional theory
DMF	Dimethylformamide
DPEN	dipyridylethane naphthyridine
EPTM	Electron-proton-transfer mediator
Eqn	Equation
ESI-MS	Electrospray ionization-mass spectrometry
ET	Electron transfer
Fc	Ferrocene
Fc^+	Ferrocenium
FE	Faradaic efficiencies
FOWA	Foot-of-the-Wave Analysis
GDEs	gas diffusion electrodes
H_2	Dihydrogen
H_2O_2	Hydrogen peroxide
HCO_3	Bicarbonate

HOMO	Highest occupied molecular orbital
IPCC	Intergovernmental Panel on Climate Change
IR	Infrared
IR-SEC	Infrared-spectroelectrochemistry
LUMO	Lowest unoccupied molecular orbital
MEA	Membrane electrode assembly
MeCN	Acetonitrile
MeOH	Methanol
MOFs	Molecular organic frameworks
NBO	Natural bond order
NHC	N-heterocyclic carbenes
NHE	Normal hydrogen electrode
NMR	Nuclear magnetic resonance spectroscopy
NOAA	National Oceanic and Atmospheric Administration
NRT	Natural resonance theory
O_2	Dioxygen
ORR	Oxygen reduction reaction
Ox	Oxalate
PCET	Proton-coupled electron transfer
PEM	Polymer electrolyte membrane
PhOH	Phenol
ppm	Parts per million
RRDE	Rotating-ring disc electrode
SHE	Standard hydrogen electrode
SOMO	Singly occupied molecular orbital
TBA	Tetrabutylammonium
$TBAPF_6$	Tetrabutylammonium hexafluorophosphate
TEMPO	2,2,6,6-tetramethyl-1-piperdine N-oxyl

THF	Tetrahydrofuran
TMC	1,4,8,11-tetramethyl-1,4,8,11-tetraazacyclotetradecane
TMPyP	*meso*-tetra(N-methylpyridinium-4-yl)porphyrin
TOF	Turn over frequency
TOF_{max}	Maximum turnover frequency
TON	Turn over number
TPEN	*N*,*N*,*N*′,*N*′-tetrakis(2-pyridylmethyl)ethylenediamine
UV-Vis SEC	Ultraviolet-visible spectroelectrochemistry

List of Figures

Figure 1.1. Generic CV plot demonstrating the behavior of a reversible one-electron transfer as the potential is swept from negative to positive potentials. 6

Figure 2.1. Structures of the molecular Ni species relevant to this report. Two hexafluorophosphate (PF_6^-) counter anions (not pictured) are present for both species $[Ni(TPEN)][PF_6]_2$ (**1**) and $[Ni(TMC)][PF_6]_2$ (**2**). 28

Figure 2.2. Crystal structure of (**1**). Hydrogen atoms omitted for clarity; thermal ellipsoids at 50%. C = dark grey, purple = nitrogen, orange = phosphorus, yellow = fluorine and green = Ni. CCDC 1816890. 28

Figure 2.3. CVs of (**1**), obtained under Ar saturation conditions. Conditions: 1 mM analyte, 0.1 M $TBAPF_6$/MeCN, glassy carbon working electrode, Pt wire counter electrode, Ag/AgCl pseudoreference electrode; varied scan rate; referenced to internal ferrocene standard. 30

Figure 2.4. CVs of (**1**), obtained under Ar saturation conditions (black) and CO_2 saturation conditions (red). Conditions: 1 mM analyte, 0.1 M $TBAPF_6$/MeCN glassy carbon working electrode, glassy carbon counter electrode, Ag/AgCl pseudoreference electrode; scan rate 100 mVs^{-1}; referenced to internal ferrocene standard. 31

Figure 2.5. CV's of (**1**) under CO_2 saturation conditions with variable PhOH concentration. Conditions: 1 mM analyte 0.1 M $TBAPF_6$/MeCN, glassy carbon working electrode, glassy carbon counter electrode, Ag/AgCl pseudoreference electrode; scan rate 100 mVs^{-1}, referenced to internal ferrocene standard. 31

Figure 2.6. IR-SEC spectra of a 3 mM solution of (**1**) in the presence of CO_2 **(A)** Ni–CO stretch grows in at 1986 cm^{-1} and a CO adduct attributed to a minor species grows in at 1888 cm^{-1} from the applied potentials of −1.6 V to −2.1 V **(B)** the formation of CO_3^{2-} observed at 1671 cm^{-1} and 1638 cm^{-1}. Conditions: 0.1 M $TBAPF_6$/MeCN and CO_2 sparged into solution for ~ 30 s; the cell was referenced to an internal ferrocene standard. 34

Figure 2.7. IR-SEC spectra of a 3 mM solution of **(1)** with the addition of 0.3 M PhOH and CO_2 sparged into solution for ~30 s. Conditions: 0.1 M $TBAPF_6$/MeCN; the cell was referenced to an internal ferrocene standard. 34

Figure 2.8. IR-SEC spectra of a 3 mM solution of **(1)** and 20 mM solution of $[Ni(TMC)]^{2+}$ with 0.1 M PhOH and CO_2 sparged into solution for ~ 30 s. Conditions: 0.1 M $TBAPF_6$/MeCN; the cell was referenced to an internal ferrocene standard. 36

Figure 2.9. Kohn–Sham orbital representations of $[Ni(\kappa^5\text{-TPEN})(\eta^1\text{-}CO_2)]^+$ **3** (A); SOMO (B); LUMO (C); spin density (D). ORCA 4.0; B3LYP/G; ZORA; def2-TZVP; CPCM(Acetonitrile), 2S + 1 = 2. 38

Figure 3.1. Complexes observed and the proposed electrochemical reaction pathway. 82

Figure 3.2. (A) Molecular structure of compound **1** (thermal ellipsoids at 40% probability; only one of the two chemically equivalent but crystallographically distinct molecules is shown). H atoms and co-crystallized THF solvent molecules omitted for clarity. Selected bond distances (Å) bond angles (°) and torsion angles (°): C1–C24: 1.526(4); C1–N1: 1.297(4); O1–C24 1.236(4); O2–C24: 1.234(4); N1–C1–C24: 123.9(3); O2–C24–O1: 131.5(3); O1–C24–C1: 113.7(3); N1–C1–C24–O2: 101.2(4). **(B)** Stick representations of the DFT optimized structures of **1** (black) and $\mathbf{[1]}^-$ (gray, blue and red). ORCA 4.0.1 B3LYP/G, def2-TZVP, CPCM (THF). 83

Figure 3.3. CV response of **1** at reducing potentials under an inert atmosphere (black) and CO_2 saturation (red) in THF. Conditions: 5 mM **1**, 0.1 M $TBAPF_6$/THF glassy carbon working electrode, glassy carbon counter electrode, Ag/AgCl pseudoreference electrode, referenced to internal ferrocene standard 84

Figure 3.4. (A) Disappearance of the CO_2 adduct at 1670 cm^{-1} as the reduced species $\mathbf{[1]}^-$ grows in and disappears at 1531 cm^{-1} at reducing conditions under Ar saturation monitored by IR-SEC. Presumptive ketene **2** degradation products appear at 1660 and 1603 cm^{-1}. **(B)** Comparable experiments under CO_2 saturation conditions show the loss of the CO_2 adduct upon the formation of CO_3^{2-} (1690 and 1635 cm^{-1}). 86

Figure 4.1. (A) Structure of the solid state water-soluble manganese (III) meso-tetra(N-methylpyridinium-4-yl) porphyrin pentachloride ($[Mn(TMPyP)Cl]^{4+}$) **(B)** Diaquo species expected to predominate in aqueous solution (pH 3-8), $[Mn(TMPyP)(OH_2)_2]^{5+}$. 143

Figure 4.2. Potential-pH plot constructed from CV data obtained on the Mn(III)/(II) (black and blue) and Mn(IV)/(III) (green) reduction features of $[Mn(TMPyP)Cl]^{4+}$ in Britton-Robinson buffer conditions under Ar saturation. 144

Figure 4.3. UV-vis SEC of 0.1 mM $[Mn(III)(TMPyP)Cl]^{4+}$ in a pH 10 Britton-Robinson Buffer solution **(A)** under reducing conditions and **(B)** under oxidizing conditions. Conditions: Honeycomb platinum electrode and a Ag/AgCl sat'd KCl aqueous reference electrode corrected to NHE. 147

Figure 4.4. Linear-sweep voltammetry of $[Mn(TMPyP)Cl]^{4+}$ (partial plots of CV data), demonstrating reactivity under O_2 saturation conditions with corresponding shifts **(A)** from pH 3-10 and **(B)** from pH 11-14. Conditions: Glassy carbon working electrode, glassy carbon counter electrode, 3.0 M NaCl Ag/AgCl reference electrode; Scan rate 100 mV/s. 150

Figure 4.5. CVs of $[Mn(TMPyP)Cl]^{4+}$ under Ar and O_2 saturation conditions in **(A)** pH 6 buffer **(B)** pH 12 buffer solution. Conditions: glassy carbon working electrode, glassy carbon counter electrode, 3.0 M NaCl Ag/AgCl reference electrode; scan rate 100 mV/s. 152

Figure SI 2.1. ^{1}H NMR of the TPEN ligand; CD_3CN; 600 MHz Varian. 43

Figure SI 2.2. $^{13}C\{^1H\}$ NMR of the TPEN ligand; CD_2Cl_2; 600 MHz Varian. 44

Figure SI 2.3. ESI-MS of TPEN. 45

Figure SI 2.4. ^{1}H NMR of (**1**); CD_3CN; 600 MHz Varian. Residual ethanol peaks at 3.54 and 1.11 ppm. Insert: zoom in of the ^{1}H NMR. 46

Figure SI 2.5. ESI-MS of $[Ni(TPEN)][PF_6]_2$ (**1**). 47

Figure SI 2.6. ^{1}H NMR of the TMC ligand; CD_2Cl_2; 600 MHz Varian. 48

Figure SI 2.7. ESI-MS of TMC. 49

Figure SI 2.8. ^{1}H NMR of $[Ni(TMC)][PF_6]_2$; CD_3CN 600 MHz Varian. 50

Figure SI 2.9. ESI-MS of $[Ni(TMC)]^{2+}$. 51

Figure SI 2.10. Linear Fit of variable scan rate data from **Figure 2.3** demonstrating that (**1**) shows a diffusion-limited current response. Conditions: 1 mM analyte; 0.1 M $TBAPF_6$/MeCN, glassy carbon working electrode, Pt wire counter electrode, Ag/AgCl pseudoreference electrode; varied scan rate; referenced to internal ferrocene standard. 54

Figure SI 2.11. Plot displaying the Nernstian voltage dependence of (**1**) on the concentration of PhOH in MeCN under CO_2 saturation. Conditions: 0.1 M $TBAPF_6$/MeCN, glassy carbon working electrode, glassy carbon counter electrode, Ag/AgCl pseudoreference electrode; scan rate 100 mV/s; referenced to internal ferrocene standard. Uses data from **Figure 2.5** in main text. 54

Figure SI 2.12. Log-log plot from data obtained from CVs **(Figure 2.5)** of complex (**1**), (1 mM) with variable PhOH concentrations and CO_2 saturation at −1.93 V vs Fc^+/Fc. Adapted from Sathrum and Kubiak J. Phys. Chem. Lett. **2011**, 2, 2372.[33] F is Faraday's constant, A is the electrode area, $[Q]$ is the substrate concentration, k_{cat} is the catalytic rate, D is the diffusion constant of the catalyst, [cat] is the concentration of the catalyst, and n_{cat} is the number of electrons involved in the catalytic process. Uses data from **Figure 2.5** in main text. 55

Figure SI 2.13. CVs of **(1)**, obtained under variable CO_2 concentrations with 0.5 M PhOH. Conditions: 1 mM analyte; 0.1 M $TBAPF_6$/MeCN, glassy carbon working electrode, glassy carbon counter electrode, Ag/AgCl pseudoreference electrode; scan rate 100 mV/s; referenced to internal ferrocene standard. 55

Figure SI 2.14. Log-log plot from data obtained from CVs of complex **(1)** (1 mM) under variable CO_2 concentration conditions with 0.5 M PhOH at −2.0 V vs Fc^+/Fc. 56

Figure SI 2.15. CVs of complex (**1**) at variable concentrations, obtained under CO_2 saturation and 0.5 M PhOH. Conditions: 0.1 M $TBAPF_6$/MeCN, glassy carbon working electrode, glassy carbon counter electrode, Ag/AgCl pseudoreference electrode; scan rate 100 mV/s; referenced to internal ferrocene standard.....56

Figure SI 2.16. Log-log plot from data obtained from CVs of complex (**1**) under variable concentration conditions in mM with 0.5 M PhOH and CO_2 saturation at −1.93 V vs Fc^+/Fc.....57

Figure SI 2.17. CVs showing CO_2 and PhOH control responses. Conditions: 0.1 M $TBAPF_6$/MeCN, glassy carbon working electrode, glassy carbon counter electrode, Ag/AgCl pseudoreference electrode; scan rate 100 mV/s; referenced to internal ferrocene standard.....57

Figure SI 2.18. CVs of **(1)** (1 mM) under CO_2 saturation and 0.5 M PhOH. Conditions: 0.1 M $TBAPF_6$/MeCN; glassy carbon working electrode, glassy carbon counter electrode; Ag/AgCl pseudoreference electrode; varied scan rate; referenced to internal ferrocene standard.....58

Figure SI 2.19. Linear fit between peak catalytic current over non-catalytic vs the inverse square root of the scan rate from the variable scan rate data in **Figure SI 2.18**. This establishes the validity of using the eqn for the FOWA. 58

Figure SI 2.20. Linear fit plot of TOF (s^{-1}) vs scan rate of the variable scan rate data from **Figure SI 2.18** demonstrating that (**1**) can be analyzed by FOWA using these data. 59

Figure SI 2.21. A) CV overlay between catalytic current of (**1**) under CO_2 and 0.5 M phenol (red trace) and (**1**) under Ar (black trace). **B)** Linear region from the FOWA. **C)** Entire region of i_c/i_p vs $1/(1+\exp(f\,(E-E^o))$. Conditions: 1 mM analyte; 0.1 M $TBAPF_6$/MeCN, glassy carbon working electrode, glassy carbon counter electrode, Ag/AgCl pseudoreference electrode; scan rate 100 mV/s; referenced to internal ferrocene standard. 60

Figure SI 2.22. IR controls for the following with their corresponding υ_{max}/cm^{-1} taken in MeCN: [TBA(HCO_2^-)] 1333 cm^{-1} and 1608 cm^{-1}, [TBA(HCO_3^-)] (1676 cm^{-1}), PhO^- (1589 cm^{-1}) and PhOH (3408 cm^{-1}) in MeCN. 60

Figure SI 2.23. A comparison of the $[Ni(TPEN)(CO)]^+$ stretch with labeled CO_2 without **(A)** and with 0.3 M solution of PhOH **(B)**. Conditions: 3 mM solution of (**1**); $^{13}CO_2$ and CO_2 sparged for ~ 30 s; 0.1 M $TBAPF_6$/MeCN; referenced to internal ferrocene standard.....61

Figure SI 2.24. A) IR-SEC analysis of a 3 mM solution of (**1**) with CO sparged into solution for ~30 s. **B)** Different conditions with catalyst under CO. Ni–CO stretch from $[Ni(TMC)(CO)]^+$ grows in at 1967 cm^{-1} with a shoulder associated with Ni–CO stretch from $Ni(\kappa^4\text{-TPEN})(CO)]^+$ at 1984 cm^{-1}. Conditions: 0.1 M $TBAPF_6$/MeCN; referenced to internal ferrocene standard.....61

Figure SI 2.25. A) UV-Vis of the bulk solution before and after electrolysis. B) Current vs time plot of electrolysis experiment held at −2.05 V vs Fc^+/Fc. C) Charge passed during electrolysis experiment. Conditions: 1 mM of (1); 0.5 M PhOH; 0.1 M $TBAPF_6$/MeCN, graphite working electrode, graphite carbon counter electrode, Ag/AgCl pseudoreference electrode, and 0.5 M Fc was used as a sacrificial oxidant. 62

Figure SI 2.26. IR comparison between the post bulk electrolysis experiments of (**1**) with and without $[Ni(TMC)]^{2+}$. $Ni(CO)_4$ appears at 2042 cm^{-1} while the Ni-CO stretch is observed at 1981 cm^{-1} in both solutions. 62

Figure SI 2.27. CVs of (**1**) at 1 mM, obtained under CO_2 saturation with 0.5 M PhOH and with $[Ni(TMC)]^{2+}$ titrations. Conditions: 1 mM analyte; 0.1 M $TBAPF_6$/MeCN glassy carbon working electrode, glassy carbon counter electrode, Ag/AgCl pseudoreference electrode; scan rate 100 mV/s; referenced to internal ferrocene standard. 63

Figure SI 2.28. A.) CV overlay between catalytic current of (**1**) with 2 mM $[Ni(TMC)]^{2+}$ present under CO_2 with phenol (red trace) and under Ar (black trace) **B.)** Linear region from the FOWA. **C.)** Entire region of i_c/i_p vs $1/(1+\exp(f\,(E-E^o))$. Conditions: 1 mM (**1**), 2 mM $[Ni(TMC)]^{2+}$, 0.1 M $TBAPF_6$/MeCN, glassy carbon

working electrode, glassy carbon counter electrode, Ag/AgCl pseudoreference electrode; scan rate 100 mV/s; referenced to internal ferrocene standard. 63

Figure SI 2.29. IR-SEC analysis of a 3 mM solution of (**1**) with CO_2 in a solution containing 20 mM of $[Ni(TMC)]^{2+}$. Ni-CO stretch from $[Ni(TMC)(CO)]^{+}$ grows in at 1967 cm^{-1} with a shoulder associated with Ni–CO stretch from $Ni(TPEN)(CO)]^{+}$ at 1982 cm^{-1}. Conditions: 0.1 M $TBAPF_6$/MeCN; referenced to internal ferrocene standard. 64

Figure SI 2.30. A) UV-Vis of the bulk solution before and after electrolysis. **B)** Current vs time plot of control electrolysis experiment held at −2.05 V vs Fc^{+}/Fc. **C)** Charge passed during control electrolysis experiment. Conditions: 1 mM of (**1**); 3 mM $[Ni(TMC)]^{2+}$; under Ar saturation conditions; 0.5 M PhOH; 0.1 M $TBAPF_6$/MeCN, graphite working electrode, graphite carbon counter electrode, Ag/AgCl pseudoreference electrode, and 0.5 M Fc was used as a sacrificial oxidant. 64

Figure SI 2.31. CVs of (**1**) obtained under Ar and then Ar and CO_2 upon the addition of 1 mM of $[Ni(TMC)]^{2+}$. Conditions: 0.1 M $TBAPF_6$/MeCN, glassy carbon working electrode, glassy carbon counter electrode, Ag/AgCl pseudoreference electrode; scan rate 100 mV/s; referenced to internal ferrocene standard. 65

Figure SI 2.32. IR-SEC analysis of a 20 mM solution of $[Ni(TMC)]^{2+}$ with CO_2, without the addition of **(1)**. No carbonyl-containing species are observed. Conditions: 0.1 M $TBAPF_6$/MeCN; referenced to internal ferrocene standard. 65

Figure SI 2.33. A) IR-SEC analysis of $[Ni(TMC)]^{2+}$ with CO sparged into solution for ~30 s to show the $[Ni(TMC)(CO)]^{+}$ stretch at 1967 cm^{-1}. Conditions: 0.1 M $TBAPF_6$/MeCN; referenced to internal ferrocene standard. **B)** Linear fit of $[Ni(TMC)(CO)]^{+}$ absorbance. 66

Figure SI 2.34 A comparison of the 3 mM solution of (1) with a 3 mM solution of $[Ni(TMC)]^{2+}$ to show the catalytic activity of $[Ni(TPEN)]^{2+}$. 66

Figure SI 2.35. IR-SEC spectra overlaying of 3 mM **(1)** with the addition of 20 mM $[Ni(TMC)]^{2+}$ to show the loss of $Ni(CO)_4$ formation upon the addition of the CO scavenger. Timepoints: blue 60 s; red 30 s; green 60 s. 67

Figure SI 2.36. Kohn-Sham orbital representations of $[Ni(TPEN)]^{2+}$ (**1**) (A); SOMO-I (B); and SOMO-II (C). ORCA 4.0; B3LYP/G; ZORA; def2-TZVP; CPCM(Acetonitrile), 2S+1 = 3. 69

Figure SI 2.37. Calculated spin density localization of $[Ni(TPEN)]^{2+}$ (**1**). ORCA 4.0; B3LYP/G; def2-TZVP; CPCM(Acetonitrile), 2S+1 = 3. 69

Figure SI 2.38. Kohn-Sham orbital representations of the SOMO (B) and LUMO (C) of $[Ni(TPEN)(CO)]^{+}$ 5 (A); spin density (D). ORCA 4.0; B3LYP/G; def2-TZVP; CPCM(Acetonitrile), 2S+1 = 2. 70

Figure SI 3.1. (**A**) Solution of **2** in THF under a CO atmosphere at t = 0 min after preparation. (**B**) The same solution of **2** in THF at t = 4 min after preparation. (**C**) Same solution of **2** in THF at t = 10 min after preparation. 95

Figure SI 3.2. ^{1}H NMR of compound **1** in CD_2Cl_2 taken at 298.15 K. 96

Figure SI 3.3. ^{13}C NMR of compound **1** in CD_2Cl_2 taken at 298.15 K. 97

Figure SI 3.4. Variable scan rate CVs of **[1]** in MeCN under Ar. Conditions: 5 mM analyte; 0.1 M $TBAPF_6$/MeCN, glassy carbon working electrode, glassy carbon counter electrode, Ag/AgCl pseudoreference electrode; varied scan rate; referenced to internal ferrocene standard. 100

Figure SI 3.5. The linear fit of the variable scan data from **Figure SI 3.4** demonstrating the diffusion-limited current response. Conditions: 5 mM analyte; 0.1 M $TBAPF_6$/MeCN, glassy carbon working electrode, glassy carbon counter electrode, Ag/AgCl pseudoreference electrode; varied scan rate; referenced to internal ferrocene standard. 100

Figure SI 3.6. CV response of **1** at reducing potentials under and inert atmosphere (black) and CO_2 saturation (red) in MeCN. Conditions: 5 mM 1, 0.1 M $TBAPF_6$/MeCN glassy carbon working electrode, glassy carbon counter electrode, Ag/AgCl pseudoreference electrode, referenced to internal ferrocene standard. 101

Figure SI 3.7. (A) Variable scan rate CVs of **[1]** in THF **(B)** the linear fit of the scans demonstrates the diffusion-limited current response. Conditions: 5 mM analyte; 0.1 M $TBAPF_6$/THF, glassy carbon working electrode, glassy carbon counter electrode, Ag/AgCl pseudoreference electrode; standard. 101

Figure SI 3.8. Control CVs of 5 mM CyCAAC-CO_2 in **(A)** THF and **(B)** MeCN. Conditions: 5 mM analyte; in 0.1 M $TBAPF_6$/THF or in 0.1 M $TBAPF_6$/MeCN, glassy carbon working electrode, glassy carbon counter electrode, Ag/AgCl pseudoreference electrode; varied scan rate; referenced to internal ferrocene standard. 102

Figure SI 3.9. IR-SEC analysis of a 5 mM solution of **[1]** with a ~ 30 s Ar sparge in THF. Disappearance of the CO_2 adduct occurs at 1670 cm^{-1} with the growth of the transient radical species at 1531 cm^{-1} occurs from −1.7 to −1.8 V vs Fc^+/Fc. 102

Figure SI 3.10. (A) Current vs time plot of electrolysis experiment of **[1]** under inert conditions. **(B)** Charge passed during electrolysis experiment. **(C)** IR of the bulk solution post electrolysis. Conditions: 5 mM of ^{Cy}CAAC-CO_2; 0.1 M $TBAPF_6$/THF; Ar sparge; graphite working electrode, graphite carbon counter electrode, Ag/AgCl pseudoreference electrode, and 0.5 M Fc was used as a sacrificial oxidant. 103

Figure SI 3.11. (A) IR absorbance from the ketene (2065 cm^{-1}) in THF at −70 C°. **(B)** The decay of the ketene overtime as the solution is warmed to room temperature showing a zero-order dependence. This species is highly unstable at room temperature and not observable in IR-SEC analysis. 104

Figure SI 3.12. IR-SEC analysis of a 5 mM solution of **[1]** with an Ar sparge in MeCN. **(A)** Disappearance of the CO_2 adduct occurs at 1670 cm^{-1} with the growth of a feature at 1603 cm^{-1} associated with an unknown species. **(B)** A transient radical not observed with the initial CO_2 adduct disappears while **(C)** a feature grows in at 2118 cm^{-1} believed to be the ketene in MeCN supported by computational and literature results. Applied potential is given versus Fc^+/Fc for these IR-SEC experiments. 104

Figure SI 3.13. (A) Current vs time plot of electrolysis experiment of [1] under inert conditions (B) Charge passed during electrolysis experiment. (C) IR of the bulk solution post electrolysis. Conditions: 5 mM of ^{Cy}CAAC-CO_2; 0.1 M $TBAPF_6$/THF; CO_2 sparge; graphite working electrode, graphite carbon counter electrode, Ag/AgCl pseudoreference electrode, and 0.5 M Fc was used as a sacrificial oxidant. 105

Figure SI 3.14. IR analysis of TBA(HCO_3) and [$(TBA)_2$(ox)] in THF with two absorbances from $C_2O_2^{2-}$ at 1550 and 1288 cm^{-1} (black trace) and two bands from HCO_3^- at 1675 and 1636 cm^{-1} (red trace). 106

Figure SI 3.15. IR-SEC analysis of a 5 mM solution of **[1]** with a CO_2 sparge in MeCN. Disappearance of the CO_2 adduct occurs at 1670 cm^{-1} with the growth of carbonate from the appearance of stretches at 1686 and 1647 cm^{-1} as well as, an unknown species at 1733 cm^{-1}. 106

Figure SI 3.16. IR-SEC analysis of a 5 mM solution of **[1]** with a CO_2 sparge in THF. Disappearance of the CO_2 adduct occurs at 1670 cm^{-1} with the growth of carbonate from the appearance of stretches at 1693 and 1635 cm^{-1}. Difference spectra were used to high light the band at 1693 cm^{-1}. 107

Figure SI 3.17. IR analysis of TBA(HCO_3) and [$(TBA)_2$(ox)] in MeCN with two bands from $C_2O_2^{2-}$ at 1550 and 1288 cm^{-1} (black trace) and two bands at 1674 and 1633 $cm^{-1}$from HCO_3^-. 107

Figure SI 3.18. (A) Current vs time plot of electrolysis experiment. **(B)** Charge passed during electrolysis experiment. **(C)** IR of the bulk solution post electrolysis. Conditions: 5 mM of ^{Cy}CAAC-CO_2; 0.1 M $TBAPF_6$/MeCN; CO_2 sparge; graphite working electrode, graphite carbon counter electrode, Ag/AgCl pseudoreference electrode, and 0.5 M Fc was used as a sacrificial oxidant. 108

Figure SI 3.19. (A) Current vs time plot of electrolysis experiment of **[1]** under inert conditions **(B)** Charge passed during electrolysis experiment. **(C)** IR of the bulk solution post electrolysis. Conditions: 5 mM of

^{Cy}CAAC-CO_2; 0.1 M $TBAPF_6$/MeCN; Ar sparge; graphite working electrode, graphite carbon counter electrode, Ag/AgCl pseudoreference electrode, and 0.5 M Fc was used as a sacrificial oxidant. 109

Figure SI 3.20. (A) IR-SEC comparison of a 5 mM solution of **[1]** with a CO_2 sparge (black trace) in THF versus a sparge in $^{13}CO_2$ (red trace). This shows the rapid (~less than 1 minute) between the $^{12}CO_2$ adduct with the $^{13}CO_2$ atmosphere**. (B)** IR-SEC analysis of a 5 mM solution of **[1]** in THF under a $^{13}CO_2$ atmosphere showing the reaction does not go to completion. Potentials measured against an internal Fc^+/Fc reference. 109

Figure SI 3.21. Spin density map showing the localization of the added electron density for **[1]**$^-$. ORCA 4.0.1 B3LYP/G def2-TZVP/J CPCM (THF). 111

Figure SI 3.22. HOMO **(B)**-LUMO **(C)** orbitals of Natural Transition Orbital for the predicted electronic absorbance of **2** at 622 nm by TD-DFT methods. ORCA 4.0.1 B3LYP/G def2-TZVP/J CPCM (THF). ... 111

Figure SI 3.23. Difference density plot for the predicted electronic absorbance of **2** at 622 nm by TD-DFT methods; red = ground state, blue = excited state. ORCA 4.0.1 B3LYP/G def2-TZVP/J CPCM (THF). .. 112

Figure SI 4.1. (A) Variable scan rate CVs **(B)** Linear fit demonstrating a homogenous response of the $[Mn(TMPyP)Cl]^{4+}$. Conditions: 1 mM $[Mn(TMPyP)Cl]^{4+}$ in a pH 1 (1 M HCl /0.1 M NaCl) solution under Ar saturation conditions, glassy carbon working electrode, glassy carbon counter electrode, 3.0 M NaCl Ag/AgCl reference electrode; varied scan rate. 168

Figure SI 4.2. (A) Variable scan rate CVs **(B)** Linear fit demonstrating a homogenous response of the $[Mn(TMPyP)Cl]^{4+}$. Conditions: 1 mM $[Mn(TMPyP)Cl]^{4+}$ in a pH 3 Britton-Robinson Buffer solution under Ar saturation conditions, glassy carbon working electrode, glassy carbon counter electrode, 3.0 M NaCl Ag/AgCl reference electrode; varied scan rate. 168

Figure SI 4.3. (A) Variable scan rate CVs **(B)** Linear fit demonstrating a homogenous response of the $[Mn(TMPyP)Cl]^{4+}$. Conditions: 1 mM $[Mn(TMPyP)Cl]^{4+}$ in a pH 4 Britton-Robinson Buffer solution under Ar saturation conditions, glassy carbon working electrode, glassy carbon counter electrode, 3.0 M NaCl Ag/AgCl; varied scan rate. 169

Figure SI 4.4. (A) Variable scan rate CVs **(B)** Linear fit demonstrating a homogenous response of the $[Mn(TMPyP)Cl]^{4+}$. Conditions: 1 mM $[Mn(TMPyP)Cl]^{4+}$in a pH 5 Britton-Robinson Buffer solution under Ar saturation conditions, glassy carbon working electrode, glassy carbon counter electrode, 3.0 M NaCl Ag/AgCl reference electrode; varied scan rate. 169

Figure SI 4.5. (A) Variable scan rate CVs **(B)** Linear fit demonstrating a homogenous response of the $[Mn(TMPyP)Cl]^{4+}$. Conditions: 1 mM $[Mn(TMPyP)Cl]^{4+}$ in a pH 6 Britton-Robinson Buffer solution under Ar saturation conditions, glassy carbon working electrode, glassy carbon counter electrode, 3.0 M NaCl Ag/AgCl reference electrode; varied scan rate. 170

Figure SI 4.6. (A) Variable scan rate CVs **(B)** Linear fit demonstrating a homogenous response of the $[Mn(TMPyP)Cl]^{+}$. Conditions: 1 mM $[Mn(TMPyP)Cl]^{4+}$ in a pH 7 Britton-Robinson Buffer solution under Ar saturation conditions, glassy carbon working electrode, glassy carbon counter electrode, 3.0 M NaCl Ag/Ag4Cl reference electrode; varied scan rate. 170

Figure SI 4.7. (A) Variable scan rate CVs **(B)** Linear fit demonstrating a homogenous response of the $[Mn(TMPyP)Cl]^{4+}$. Conditions: 1 mM $[Mn(TMPyP)Cl]^{4+}$ in a pH 8 Britton-Robinson Buffer solution under Ar saturation conditions, glassy carbon working electrode, glassy carbon counter electrode, 3.0 M NaCl Ag/AgCl reference electrode; varied scan rate. 171

Figure SI 4.8. (A) Variable scan rate CVs **(B)** Linear fit demonstrating a homogenous response of the $[Mn(TMPyP)Cl]^{4+}$. Conditions: 1 mM $[Mn(TMPyP)Cl]^{4+}$ in a pH 9 Britton-Robinson Buffer solution under Ar saturation conditions, glassy carbon working electrode, glassy carbon counter electrode, 3.0 M NaCl Ag/AgCl reference electrode; varied scan rate. 171

Figure SI 4.9. (A) Variable scan rate CVs **(B)** Linear fit demonstrating a homogenous response of the $[Mn(TMPyP)Cl]^{4+}$. Conditions: 1 mM $[Mn(TMPyP)Cl]^{4+}$ in a pH 10 Britton-Robinson Buffer solution under Ar saturation conditions, glassy carbon working electrode, glassy carbon counter electrode, 3.0 M NaCl Ag/AgCl reference electrode; varied scan rate. 172

Figure SI 4.10. (A) Variable scan rate CVs **(B)** Linear fit demonstrating a homogenous response of the $[Mn(TMPyP)Cl]^{4+}$. Conditions: 1 mM $[Mn(TMPyP)Cl]^{4+}$ in a pH 11 Britton-Robinson Buffer solution under Ar saturation conditions, glassy carbon working electrode, glassy carbon counter electrode, 3.0 M NaCl Ag/AgCl reference electrode; varied scan rate. 172

Figure SI 4.11. (A) Variable scan rate CVs **(B)** Linear fit demonstrating a homogenous response of the $[Mn(TMPyP)Cl]^{4+}$. Conditions: 1 mM $[Mn(TMPyP)Cl]^{4+}$ in a pH 12 Britton-Robinson Buffer solution under Ar saturation conditions, glassy carbon working electrode, glassy carbon counter electrode, 3.0 M NaCl Ag/AgCl reference electrode; varied scan rate. 173

Figure SI 4.12. (A) Variable scan rate CVs **(B)** Linear fit demonstrating a homogenous response of the $[Mn(TMPyP)Cl]^{4+}$. Conditions: 1 mM $[Mn(TMPyP)Cl]^{4+}$ in a pH 13 Britton-Robinson Buffer solution under Ar saturation conditions, glassy carbon working electrode, glassy carbon counter electrode, 3.0 M NaCl Ag/AgCl reference electrode; varied scan rate. 173

Figure SI 4.13. **(A)** Variable scan rate CVs **(B)** Linear fit demonstrating a homogenous response of the $[Mn(TMPyP)Cl]^{4+}$. Conditions: 1 mM $[Mn(TMPyP)Cl]^{+}$ in a pH 14 Britton-Robinson Buffer solution under Ar saturation conditions, glassy carbon working electrode, glassy carbon counter electrode, 3.0 M NaCl Ag/AgCl reference electrode; varied scan rate. 174

Figure SI 4.14. CVs of 1 mM $[Mn(TMPyP)Cl]^{4+}$ demonstrating the shift in $E_{1/2}$ throughout the entire pH domain studied. Ar saturation conditions, glassy carbon working electrode, glassy carbon counter electrode, 3.0 M NaCl Ag/AgCl reference electrode; Scan rate 100 mV/s. 174

Figure SI 4.15. CV of 1 mM $[Mn(TMPyP)Cl]^{4+}$ establishing the appearance of a second feature and the pH dependence of the $E_{1/2}$'s under basic conditions in a Britton-Robinson buffer. Ar saturation conditions, glassy carbon working electrode, glassy carbon counter electrode, 3.0 M NaCl Ag/AgCl reference electrode; Scan rate 100 mV/s. 175

Figure SI 4.16. (A) UV-Vis spectrum of $[Mn(TMPyP)Cl]^{4+}$ and free base TMPyP showing that de-metalation does not occur in solution by monitoring the Soret band **(B)** and Q band shifts under pH 1 or 14 conditions. 175

Figure SI 4.17. (A) UV-Vis spectrum of 3.33 x 10^{-6} M $[Mn(TMPyP)Cl]^{4+}$ throughout the pH domain with a decrease in absorbance at the characteristic Soret band occurring at 462 nm and the growth of a new band at 453 nm at higher pH **(B)** The characteristic Q band shifting from 560 to 572 towards high pH. 176

Figure SI 4.18. UV-Vis spectrum of 3.33 x 10^{-6} M $[Mn(TMPyP)Cl]^{4+}$ **(A)** Moving to higher pH demonstrates a decrease in absorbance at the Soret band (462 nm) with the appearance of a new band at 453 nm **(B)** While the Q band shifts from 560 to 572 nm. 176

Figure SI 4.19. UV-Vis SEC spectrum of 0.1 mM $[Mn(TMPyP)Cl]^{4+}$ in pH 1 showing a decrease in the Soret band at 462 nm with the appearance of a new band at 440 nm as the potential is decreased from 0.40 V to 0.10 V vs NHE. The Q band is blue shifted from 560 to 502 nm upon reduction. Conditions: Honeycomb platinum electrode and a Ag/AgCl sat'd KCl aqueous reference electrode. 177

Figure SI 4.20. UV-Vis SEC spectra of 0.1 mM $[Mn(TMPyP)Cl]^{4+}$ in **(A)** pH 3 Britton-Robinson buffer solution showing a decrease in the Soret band at 463 nm with the appearance of a new band at 450 nm as the potential is decreased from +0.20 V to –0.10 V vs NHE. The Q band is red shifted from 558 to 574 nm upon reduction. **(B)** pH 7 Britton-Robinson buffer solution showing a decrease in the Soret band at 462 nm with the appearance of a new band at 449 nm as the potential is decreased from +0.20 V to –0.10 V vs NHE. The

Q band is red shifted from 561 to 575 nm upon reduction. Conditions: Honeycomb platinum electrode and Ag/AgCl sat'd KCl aqueous reference electrode. 177

Figure SI 4.21. UV-Vis SEC spectrum of 0.1 mM $[Mn(TMPyP)Cl]^{4+}$ in pH 14 Britton-Robinson buffer **(A)** as the potential is decreased from 0.10 V to −0.20 V vs NHE a decrease in the Soret band at 457 nm occurs with the appearance of a new band at 416 nm **(B)** as the potential is increased from 0.15 to 0.50 V vs. NHE the formation of $[Mn(IV)(O)(TMPyP)(OH)]^{3+}$ occurs as apparent from the new band at 425 nm with the loss of the Soret band observed. Conditions: Honeycomb platinum electrode and a Ag/AgCl sat'd KCl aqueous reference electrode. 178

Figure SI 4.22. CV of 1 mM $[Mn(TMPyP)Cl]^{4+}$ with O_2 titration showing low activity at pH 1. Conditions: 1 mM $[Mn(TMPyP)Cl]^{4+}$ in a pH 1 (1 M HCl /0.1 M NaCl) solution; glassy carbon working electrode, glassy carbon counter electrode, 3.0 M NaCl Ag/AgCl; Scan rate 100 mV/s. 178

Figure SI 4.23. CVs under variable $[O_2]$ showing an irreversible feature under pH 2 Britton-Robinson buffer conditions. Conditions: 1 mM $[Mn(TMPyP)Cl]^{4+}$ in a pH 2 Britton-Robinson buffer conditions under Ar saturation conditions, glassy carbon working electrode, glassy carbon counter electrode, 3.0 M NaCl Ag/AgCl reference electrode; Scan rate 100 mV/s. 179

Figure SI 4.24. CVs of 1 mM $[Mn(TMPyP)Cl]^{4+}$ with O_2 titration demonstrating catalytic activity. Conditions: 1 mM $[Mn(TMPyP)Cl]^{4+}$ in a pH 3 Britton-Robinson Buffer solution; glassy carbon working electrode, glassy carbon counter electrode, 3.0 M NaCl Ag/AgCl reference electrode; Scan rate 100 mV/s. 179

Figure SI 4.25. CVs of 1 mM $[Mn(TMPyP)Cl]^{4+}$ with O_2 titration demonstrating catalytic activity. Conditions: 1 mM $[Mn(TMPyP)Cl]^{4+}$ in a pH 4 Britton-Robinson Buffer solution; glassy carbon working electrode, glassy carbon counter electrode, 3.0 M NaCl Ag/AgCl reference; Scan rate 100 mV/s. 180

Figure SI 4.26. CVs of 1 mM $[Mn(TMPyP)Cl]^{4+}$ with O_2 titration demonstrating catalytic activity. Conditions: 1 mM $[Mn(TMPyP)Cl]^{4+}$ in a pH 5 Britton-Robinson Buffer solution; glassy carbon working electrode, glassy carbon counter electrode, 3.0 M NaCl Ag/AgCl reference; Scan rate 100 mV/s. 180

Figure SI 4.27. CVs of 1 mM $[Mn(TMPyP)Cl]^{4+}$ with O_2 titration demonstrating catalytic activity. Conditions: 1 mM $[Mn(TMPyP)Cl]^{4+}$ in a pH 6 Britton-Robinson Buffer solution; glassy carbon working electrode, glassy carbon counter electrode, 3.0 M NaCl Ag/AgCl reference; Scan rate 100 mV/s. 181

Figure SI 4.28. CVs of 1 mM $[Mn(TMPyP)Cl]^{4+}$ with O_2 titration. Conditions: 1 mM $[Mn(TMPyP)Cl]^{4+}$ in a pH 7 Britton-Robinson Buffer solution; glassy carbon working electrode, glassy carbon counter electrode, 3.0 M NaCl Ag/AgCl reference; Scan rate 100 mV/s. 181

Figure SI 4.29. CVs of 1 mM $[Mn(TMPyP)Cl]^{4+}$ with O_2 titration. Conditions: 1 mM $[Mn(TMPyP)Cl]^{4+}$ in a pH 8 Britton-Robinson Buffer solution; glassy carbon working electrode, glassy carbon counter electrode, 3.0 M NaCl Ag/AgCl; Scan rate 100 mV/s. 182

Figure SI 4.30. CVs of 1 mM $[Mn(TMPyP)Cl]^{4+}$ with O_2 titration. Conditions: 1 mM $[Mn(TMPyP)Cl]^{4+}$ in a pH 9 Britton-Robinson Buffer solution; glassy carbon working electrode, glassy carbon counter electrode, 3.0 M NaCl Ag/AgCl reference; Scan rate 100 mV/s. 182

Figure SI 4.31. CVs of 1 mM $[Mn(TMPyP)Cl]^{4+}$ with O_2 titration. Conditions: 1 mM $[Mn(TMPyP)Cl]^{4+}$ in a pH 10 Britton-Robinson Buffer solution; glassy carbon working electrode, glassy carbon counter electrode, 3.0 M NaCl Ag/AgCl reference; Scan rate 100 mV/s. 183

Figure SI 4.32. CVs of 1 mM $[Mn(TMPyP)Cl]^{4+}$ with O_2 titration. Conditions: 1 mM $[Mn(TMPyP)Cl]^{4+}$ in a pH 11 Britton-Robinson Buffer solution; glassy carbon working electrode, glassy carbon counter electrode, 3.0 M NaCl Ag/AgCl reference; Scan rate 100 mV/s. 183

Figure SI 4.33. CVs of 1 mM $[Mn(TMPyP)Cl]^{4+}$ with O_2 titration. Conditions: 1 mM $[Mn(TMPyP)Cl]^{4+}$ in a pH 12 Britton-Robinson Buffer solution; glassy carbon working electrode, glassy carbon counter electrode, 3.0 M NaCl Ag/AgCl reference; Scan rate 100 mV/s. 184

Figure SI 4.34. CVs of 1 mM $[Mn(TMPyP)Cl]^{4+}$ with O_2 titration. Conditions: 1 mM $[Mn(TMPyP)Cl]^{4+}$ in a pH 13 Britton-Robinson Buffer solution; glassy carbon working electrode, glassy carbon counter electrode, 3.0 M NaCl Ag/AgCl reference; Scan rate 100 mV/s. 184

Figure SI 4.35. CVs of 1 mM $[Mn(TMPyP)Cl]^{4+}$ with O_2 titration. Conditions: 1 mM $[Mn(TMPyP)Cl]^{4+}$ in a pH 14 Britton-Robinson Buffer solution; glassy carbon working electrode, glassy carbon counter electrode, 3.0 M NaCl Ag/AgCl reference; Scan rate 100 mV/s. 185

Figure SI 4.36. Control CV of a blank pH 1 (1 M HCl / 0.1 M NaCl) solution under O_2 saturation conditions in comparison to a 1 mM $[Mn(TMPyP)Cl]^{4+}$ solution under O_2 showing the molecular regime for the catalyst. Conditions: Glassy carbon working electrode, glassy carbon counter electrode, 3.0 M NaCl Ag/AgCl reference electrode; Scan rate 100 mV/s. 186

Figure SI 4.37. Control CV of a blank pH 2 Britton-Robinson Buffer solution under O_2 saturation conditions in comparison to a 1 mM $[Mn(TMPyP)Cl]^{4+}$ solution under O_2 showing the molecular regime for the catalyst. Conditions: Glassy carbon working electrode, glassy carbon counter electrode, 3.0 M NaCl Ag/AgCl reference electrode; Scan rate 100 mV/s. 186

Figure SI 4.38. Control CV of a blank pH 3 Britton-Robinson Buffer solution under O_2 saturation conditions in comparison to a 1 mM $[Mn(TMPyP)Cl]^{4+}$ solution under O_2 showing the molecular regime for the catalyst. Conditions: Glassy carbon working electrode, glassy carbon counter electrode, 3.0 M NaCl Ag/AgCl reference electrode; Scan rate 100 mV/s. 187

Figure SI 4.39. Control CV of a blank pH 4 Britton-Robinson Buffer solution under O_2 saturation conditions in comparison to a 1 mM $[Mn(TMPyP)Cl]^{4+}$ solution under O_2 showing the molecular regime for the catalyst. Conditions: Glassy carbon working electrode, glassy carbon counter electrode, 3.0 M NaCl Ag/AgCl reference electrode; Scan rate 100 mV/s. 187

Figure SI 4.40. Control CV of a blank pH 5 Britton-Robinson Buffer solution under O_2 saturation conditions in comparison to a 1 mM $[Mn(TMPyP)Cl]^{4+}$ solution under O_2 showing the molecular regime for the catalyst. Conditions: Glassy carbon working electrode, glassy carbon counter electrode, 3.0 M NaCl Ag/AgCl reference electrode; Scan rate 100 mV/s. 188

Figure SI 4.41. Control CV of a blank pH 6 Britton-Robinson Buffer solution under O_2 saturation conditions in comparison to a 1 mM $[Mn(TMPyPCl)]^{4+}$ solution under O_2 showing the molecular regime for the catalyst. Conditions: Glassy carbon working electrode, glassy carbon counter electrode, 3.0 M NaCl Ag/AgCl reference electrode; Scan rate 100 mV/s. 188

Figure SI 4.42. Control CV of a blank pH 7 Britton-Robinson Buffer solution under O_2 saturation conditions in comparison to a 1 mM $[Mn(TMPyP)Cl]^{4+}$ solution under O_2 showing the molecular regime for the catalyst. Conditions: Glassy carbon working electrode, glassy carbon counter electrode, 3.0 M NaCl Ag/AgCl reference electrode; Scan rate 100 mV/s. 189

Figure SI 4.43. Control CV of a blank pH 8 Britton-Robinson Buffer solution under O_2 saturation conditions in comparison to a 1 mM $[Mn(TMPyP)Cl]^{4+}$ solution under O_2 showing the molecular regime for the catalyst. Conditions: Glassy carbon working electrode, glassy carbon counter electrode, 3.0 M NaCl Ag/AgCl reference; Scan rate 100 mV/s. 189

Figure SI 4.44. Control CV of a blank pH 9 Britton-Robinson Buffer solution under O_2 saturation conditions in comparison to a 1 mM $[Mn(TMPyP)Cl]^{4+}$ solution under O_2 showing the molecular regime for the catalyst. Conditions: Glassy carbon working electrode, glassy carbon counter electrode, 3.0 M NaCl Ag/AgCl reference electrode; Scan rate 100 mV/s. 190

Figure SI 4.45. Control CV of a blank pH 10 Britton-Robinson Buffer solution under O_2 saturation conditions in comparison to a 1 mM $[Mn(TMPyP)Cl]^{4+}$ solution under O_2 showing the molecular regime for the catalyst. Conditions: Glassy carbon working electrode, glassy carbon counter electrode, 3.0 M NaCl Ag/AgCl reference electrode; Scan rate 100 mV/s. 190

Figure SI 4.46. Control CV of a blank pH 11 Britton-Robinson Buffer solution under O_2 saturation conditions in comparison to a 1 mM $[Mn(TMPyP)Cl]^{4+}$ solution under O_2 showing the molecular regime for the catalyst. Conditions: Glassy carbon working electrode, glassy carbon counter electrode, 3.0 M NaCl Ag/AgCl reference electrode; Scan rate 100 mV/s. 191

Figure SI 4.47. Control CV of a blank pH 12 Britton-Robinson Buffer solution under O_2 saturation conditions in comparison to a 1 mM $[Mn(TMPyP)Cl]^{4+}$ solution under O_2 showing the molecular regime for the catalyst. Conditions: Glassy carbon working electrode, glassy carbon counter electrode, 3.0 M NaCl Ag/AgCl reference electrode; Scan rate 100 mV/s. 191

Figure SI 4.48. Control CV of a blank pH 13 Britton-Robinson Buffer solution under O_2 saturation conditions in comparison to a 1 mM $[Mn(TMPyP)Cl]^{4+}$ solution under O_2 showing the molecular regime for the catalyst. Conditions: Glassy carbon working electrode, glassy carbon counter electrode, 3.0 M NaCl Ag/AgCl reference electrode; Scan rate 100 mV/s. 192

Figure SI 4.49. Control CV of a blank pH 14 (1 M KOH / 0.1 M NaCl) solution under O_2 saturation conditions in comparison to a 1 mM $[Mn(TMPyP)Cl]^{4+}$ solution under O_2 showing the molecular regime for the catalyst. Conditions: Glassy carbon working electrode, glassy carbon counter electrode, 3.0 M NaCl Ag/AgCl reference electrode; Scan rate 100 mV/s. 192

Figure SI 4.50. Adsorption test at pH 1 (1 M HCl / 0.1 M NaCl) solution under Ar. Conditions: Glassy carbon working electrode, glassy carbon counter electrode, 3.0 M NaCl Ag/AgCl reference electrode; Scan rate 100 mV/s. 193

Figure SI 4.51. Adsorption test at pH 3 Britton-Robinson Buffer solution under Ar. Conditions: Glassy carbon working electrode, glassy carbon counter electrode, 3.0 M NaCl Ag/AgCl reference electrode; Scan rate 100 mV/s. 193

Figure SI 4.52. Adsorption test at pH 6 Britton-Robinson Buffer solution under Ar. Conditions: Glassy carbon working electrode, glassy carbon counter electrode, 3.0 M NaCl Ag/AgCl reference electrode; Scan rate 100 mV/s. 194

Figure SI 4.53. Adsorption test at pH 7 Britton-Robinson Buffer solution under Ar. Conditions: Glassy carbon working electrode, glassy carbon counter electrode, 3.0 M NaCl Ag/AgCl reference electrode; Scan rate 100 mV/s. 194

Figure SI 4.54. Adsorption test at pH 12 Britton-Robinson Buffer solution under Ar. Conditions: Glassy carbon working electrode, glassy carbon counter electrode, 3.0 M NaCl Ag/AgCl reference electrode; Scan rate 100 mV/s. 195

Figure SI 4.55. Linear Sweep Voltammograms of RRDE experiments with $[Mn(TMPyP)Cl]^{4+}$ (0.25 mM) at various rotation rates under argon **(A)** and O_2 **(B)** saturation conditions in a pH 5 buffer solution; ring potential = 1.2 V vs Ag/AgCl. Conditions: 0.25 mM analyte; glassy carbon working electrode/Pt ring working electrode, glassy carbon counter electrode, Ag/AgCl/3 M KCI reference electrode; scan rate 0.02 V/s. ... 195

Figure SI 4.56. Levich **(A)** and Koutecky-Levich **(B)** plots from data obtained from Linear Sweep Voltammograms of $[Mn(TMPyP)Cl]^{4+}$ (0.25 mM) by RRDE under argon saturation conditions at various rotation rates in a pH 5 buffer solution. 196

Figure SI 4.57. Levich **(A)** and Koutecky-Levich **(B)** plots from data obtained from Linear Sweep Voltammograms of $[Mn(TMPyP)Cl]^{4+}$ (0.25 mM) by RRDE under O_2 saturation conditions at various rotation rates in a pH 5 buffer solution. 196

Figure SI 4.58. Linear Sweep Voltammograms of the generated ring current during RRDE experiments with $[Mn(TMPyP)Cl]^{4+}$ (0.25 mM) at various rotation rates with the argon ring current subtracted from the ring current produced under O_2 saturation conditions in a pH 5 buffer solution; ring potential = 1.2 V vs Ag/AgCl. Conditions: 0.25 mM analyte; glassy carbon working electrode/Pt ring working electrode, glassy carbon counter electrode, Ag/AgCl/3 M KCI reference electrode; scan rate 0.02 V/s. 197

Figure SI 4.59. Linear Sweep Voltammograms of RRDE experiments with $[Mn(TMPyP)Cl]^{4+}$ (0.25 mM) at various rotation rates under argon **(A)** and O_2 **(B)** saturation conditions in a pH 6 buffer solution; ring potential = 1.2 V vs Ag/AgCl. Conditions: 0.25 mM analyte; glassy carbon working electrode/Pt ring working electrode, glassy carbon counter electrode, Ag/AgCl/3 M KCI reference electrode; scan rate 0.02 V/s. ...197

Figure SI 4.60. Levich **(A)** and Koutecky-Levich **(B)** plots from data obtained from Linear Sweep Voltammograms of $[Mn(TMPyP)Cl]^{4+}$ (0.25 mM) by RRDE under argon saturation conditions at various rotation rates in a pH 6 buffer solution. 198

Figure SI 4.61. Levich **(A)** and Koutecky-Levich **(B)** plots from data obtained from Linear Sweep Voltammograms of $[Mn(TMPyP)Cl]^{4+}$ (0.25 mM) by RRDE under O_2 saturation conditions at various rotation rates in a pH 6 buffer solution. 198

Figure SI 4.62. Linear Sweep Voltammograms of the generated ring current during RRDE experiments with $[Mn(TMPyP)Cl]^{4+}$ (0.25 mM) at various rotation rates with the argon ring current subtracted from the ring current produced under O_2 saturation conditions in a pH 6 buffer solution; ring potential = 1.2 V vs Ag/AgCl. Conditions: 0.25 mM analyte; glassy carbon working electrode/Pt ring working electrode, glassy carbon counter electrode, Ag/AgCl/3 M KCI reference electrode; scan rate 0.02 V/s. 199

Figure SI 4.63. Linear Sweep Voltammograms of RRDE experiments with $[Mn(TMPyP)Cl]^{4+}$ (0.25 mM) at various rotation rates under argon **(A)** and O_2 **(B)** saturation conditions in a pH 4 buffer solution; ring potential = 1.2 V vs Ag/AgCl. Conditions: 0.25 mM analyte; glassy carbon working electrode/Pt ring working electrode, glassy carbon counter electrode, Ag/AgCl/3 M KCI reference electrode; scan rate 0.02 V/s. ...199

Figure SI 4.64. Levich **(A)** and Koutecky-Levich **(B)** plots from data obtained from Linear Sweep Voltammograms of $[Mn(TMPyP)Cl]^{4+}$ (0.25 mM) by RRDE under argon saturation conditions at various rotation rates in a pH 4 buffer solution. 200

Figure SI 4.65. Levich **(A)** and Koutecky-Levich **(B)** plots from data obtained from Linear Sweep Voltammograms of $[Mn(TMPyP)Cl]^{4+}$ (0.25 mM) by RRDE under O_2 saturation conditions at various rotation rates in a pH 4 buffer solution. 200

Figure SI 4.66. Linear Sweep Voltammograms of the generated ring current during RRDE experiments with $[Mn(TMPyP)Cl]^{4+}$ (0.25 mM) at various rotation rates with the argon ring current subtracted from the ring current produced under O_2 saturation conditions in a pH 4 buffer solution; ring potential = 1.2 V vs Ag/AgCl. Conditions: 0.25 mM analyte; glassy carbon working electrode/Pt ring working electrode, glassy carbon counter electrode, Ag/AgCl/3 M KCI reference electrode; scan rate 0.02 V/s. 201

Figure SI 4.67. Linear Sweep Voltammograms of RRDE experiments with $[Mn(TMPyP)Cl]^{4+}$ (0.25 mM) at various rotation rates under argon **(A)** and O_2 **(B)** saturation conditions in a pH 3 buffer solution; ring potential = 1.2 V vs Ag/AgCl. Conditions: 0.25 mM analyte; glassy carbon working electrode/Pt ring working electrode, glassy carbon counter electrode, Ag/AgCl/3 M KCI reference electrode; scan rate 0.02 V/s. ...201

Figure SI 4.68. Levich **(A)** and Koutecky-Levich **(B)** plots from data obtained from Linear Sweep Voltammograms of $[Mn(TMPyP)Cl]^{4+}$ (0.25 mM) by RRDE under argon saturation conditions at various rotation rates in a pH 3 buffer solution. 202

Figure SI 4.69. Levich **(A)** and K4outecky-Levich **(B)** plots from data obtained from Linear Sweep Voltammograms of $[Mn(TMPyP)Cl]^{4+}$ (0.25 mM) by RRDE under O_2 saturation conditions at various rotation rates in a pH 3 buffer solution. 202

Figure SI 4.70. Linear Sweep Voltammograms of the generated ring current during RRDE experiments with $[Mn(TMPyP)Cl]^{4+}$ (0.25 mM) at various rotation rates with the argon ring current subtracted from the ring current produced under O_2 saturation conditions in a pH 3 buffer solution; ring potential = 1.2 V vs Ag/AgCl. Conditions: 0.25 mM analyte; glassy carbon working electrode/Pt ring working electrode, glassy carbon counter electrode, Ag/AgCl/3 M KCI reference electrode; scan rate 0.02 V/s. 203

Figure SI 4.71. Linear Sweep Voltammograms of RRDE experiments with $[Mn(TMPyP)Cl]^{4+}$ (0.25 mM) at 1000 rpm under O_2 saturation conditions in a pH 7 buffer solution illustrating the inability to perform RRDE analysis above pH 6 due to the greater background disk and ring current observed at pH 7; ring potential = 1.2 V vs Ag/AgCl. Conditions: 0.25 mM analyte; glassy carbon working electrode/Pt ring working electrode, glassy carbon counter electrode, Ag/AgCl/3 M KCI reference electrode; scan rate 0.02 V/s. ...204

Figure SI 4.72. Control CV of 1 mM $[Mn(TMPyP)Cl]^{4+}$ with 1 mM H_2O_2 (red trace) and 4 mM H_2O_2 (blue trace) to show catalytic response for the dismutase of H_2O_2 in a pH 3 Britton-Robinson Buffer. Conditions: Glassy carbon working electrode, glassy carbon counter electrode, 3.0 M NaCl Ag/AgCl reference electrode; scan rate 100 mV/s. 206

Figure SI 4.73. Control CV of 1 mM $[Mn(TMPyP)Cl]^{4+}$ with 1 mM H_2O_2 (red trace) and 4 mM H_2O_2 (blue trace) to show catalytic response for the dismutase of H_2O_2 in a pH 6 Britton-Robinson Buffer. Conditions: Glassy carbon working electrode, glassy carbon counter electrode, 3.0 M NaCl Ag/AgCl reference electrode; scan rate 100 mV/s. 206

Figure SI 4.74. Control UV-Vis of 1.5 x 10^{-5} M $[Mn(TMPyP)Cl]^{4+}$ and 5.0 x 10^{-5} M H_2O_2 in pH 3 Britton-Robinson buffer. 207

Figure SI 4.75. Control UV-Vis of 1.5 x 10^{-5} M $[Mn(TMPyP)Cl]^{4+}$ and 5.0 x 10^{-5} M H_2O_2 in pH 6 Britton-Robinson buffer. 207

List of Schemes

Scheme 1.1. Simple schematic comparing the fundamental differences between a homogenous molecular (homogenous) catalyst and a heterogenous catalyst. 4

Scheme 1.2. Simple square-scheme showing the different mechanisms for proton coupled electron transfers. 11

Scheme 1.3. Selected reduction potentials of (pH 7 aqueous media vs NHE under 1 atm and 25 °C) common products generated from the electrocatalytic reduction of CO_2 in the presence of a proton donor. 12

Scheme 1.4. Possible reduction pathways for the reduction O_2. 15

Scheme 1.5. Common coordination modes for O_2 with a monomeric metal center. 17

Scheme 2.1. Proposed mechanism for the electrochemical reduction of CO_2 to CO as well as the formation of $Ni(CO)_4$. 37

List of Tables

Table 4.1. Catalytic efficiencies, overpotentials and TOF_{max} determined for $[Mn(TMPyP)Cl]^{4+}$ from pH 3 to 6.....153

Table SI 2.1. The peak to peak separation as well as the peak current ratio for both **(1)** and the internal Fc^{+}/Fc reference at 100 mV/s.....67

Table SI 2.2. FOWA analysis of **(1)** with PhOH titrations.....68

Table SI 2.3. FOWA analysis of **(1)** with $[Ni(TMC)]^{2+}$ titrations at 0.5 M PhOH. 68

Table SI 3.1. Crystallographic Information.....98

Table SI 3.2 Summarized results of the electrolysis experiments under different conditions.[a] 110

Table SI 4.1. Solutions utilized in this study.....163

Table SI 4.2. Electrochemical characterization of the Mn(III)/(II) reduction in a pH 1 solution (1 M HCl /0.1 M NaCl) under Ar saturation conditions as the scan rate is increased. 163

Table SI 4.3. Electrochemical characterization of the Mn(III)/(II) reduction in pH 3 Britton-Robinson Buffer solution under Ar saturation conditions as the scan rate is increased.....163

Table SI 4.4. Electrochemical characterization of the Mn(III)/(II) reduction in pH 4 Britton-Robinson Buffer solution under Ar saturation conditions as the scan rate is increased.....164

Table SI 4.5. Electrochemical characterization of the Mn(III)/(II) reduction in pH 5 Britton-Robinson Buffer solution under Ar saturation conditions as the scan rate is increased.....164

Table SI 4.6. Electrochemical characterization of the Mn(III)/(II) reduction in pH 6 Britton-Robinson Buffer solution under Ar saturation conditions as the scan rate is increased.....164

Table SI 4.7. Electrochemical characterization of the Mn(III)/(II) reduction in pH 7 Britton-Robinson Buffer solution under Ar saturation conditions as the scan rate is increased.....165

Table SI 4.8. Electrochemical characterization of the Mn(III)/(II) reduction in pH 8 Britton-Robinson Buffer solution under Ar saturation conditions as the scan rate is increased.....165

Table SI 4.9. Electrochemical characterization of the Mn(III)/(II) reduction in pH 9 Britton-Robinson Buffer solution under Ar saturation conditions as the scan rate is increased.....165

Table SI 4.10. Electrochemical characterization of the Mn(III)/(II) reduction in pH 10 Britton-Robinson Buffer solution under Ar saturation conditions as the scan rate is increased. 166

Table SI 4.11. Electrochemical characterization of the Mn(III)/(II) reduction in pH 11 Britton-Robinson Buffer solution under Ar saturation conditions as the scan rate is increased. 166

Table SI 4.12. Electrochemical characterization of the Mn(III)/(II) reduction in pH 12 Britton-Robinson Buffer solution under Ar saturation conditions as the scan rate is increased. 166

Table SI 4.13. Electrochemical characterization of the Mn(III)/(II) reduction in pH 13 Britton-Robinson Buffer solution under Ar saturation conditions as the scan rate is increased. 167

Table SI 4.14. Electrochemical characterization of the Mn(III)/(II) reduction in pH 14 Britton-Robinson Buffer solution under Ar saturation conditions as the scan rate is increased. 167

Table SI 4.15. Electrochemical characterization of Mn(IV)/(III) feature from pH 10-14, CVs taken at a scan rate of 100 mV/s under Ar saturation conditions.....167

Table SI 4.16. $\%H_2O_2$ calculated from RRDE experiments at various pH values.....205

CHAPTER ONE

Development of Molecular Electrocatalysts for the Reduction of Carbon Dioxide and Dioxygen

1.1 Introduction

1.1.1 Current Energy Issues

The current primary source of energy for mankind, fossil fuels, is non-renewable and is a significant source of anthropogenic carbon dioxide (CO_2) emissions, resulting in rising atmospheric CO_2 concentrations that are negatively impacting the climate.[1] For millions of years the natural carbon cycle has successfully maintained the continuous flow of CO_2 between natural sources (vegetation and animals) and natural sinks (layers of the ocean) preventing excess amounts of CO_2, a greenhouse gas, from accumulating in the atmosphere and causing devastation to the Earth's ecosystem. However, the advent of the Industrial Revolution in the 18th century resulted in increased use of fossil fuels.[2] This disruption in the carbon cycle from human activity caused a continuing increase of CO_2 levels in the atmosphere that is partly responsible for global-wide climate change. This past year, global atmospheric CO_2 concentrations were reported by the National Oceanic and Atmospheric Administration (NOAA) as 407.65 ppm[3] – the highest level observed for the past 40 years and well above the predicted pre-industrial values for CO_2 (maintained between 180 and 300 ppm).[2] Consequently, Earth's primary natural CO_2 sink, the ocean, is becoming saturated with CO_2. This has led to a build-up of carbonic acid in the ocean, resulting in acidification of the ocean and negatively impacting the marine ecosystem.[2, 4] Further deleterious environmental impacts witnessed from high concentrations of atmospheric $CO_{2(g)}$ buildup include changing rainfall patterns, rising temperatures and an increase in natural disasters (heat waves, flooding, etc.).[5] These adverse environmental effects generate or exacerbate existing socioeconomic issues.[5] The severe threat posed by increasing anthropogenic CO_2 concentrations has resulted in an ambitious motive initiated

by the Intergovernmental Panel on Climate Change (IPCC) to prevent global warming from exceeding 1.5 °C above pre-industrial levels and to understand the corresponding effects this will have on the world.[5] In order to meet this goal initiated by the IPCC, net zero CO_2 emissions needs to be met globally by 2050.[6] Recently, scientific efforts have focused towards the development of CO_2 removal technologies. While CO_2 capture technology is important in eliminating CO_2 from the atmosphere, the major challenge consists in developing energy technologies that are not reliant on fossil fuels, so that increasing global energy needs are met.[6-8]

1.1.2 Molecular Electrocatalysis as a Solution to Energy Crisis

A potential solution to the above crisis is the possibility of using CO_2 as a carbon feedstock for fuels and fuel precursors.[8-9] If this process reaches suitable efficiencies, it could be the basis of a carbon-neutral energy cycle.[10] A complementary approach to a carbon-neutral energy cycle is the reduction of dioxygen (O_2) to water. When these conversions are driven using electrochemical methods, renewable energy sources can be used as the source of electricity.[8, 11-13] The direct electrochemical reduction of substrates to products on an electrode surface often requires large potential (voltage) energy, making electrocatalysts desirable for their ability to lower these energy demands while selectively driving reactions of interest forward.[8, 14]

Scheme 1.1. Simple schematic comparing the fundamental differences between a molecular (homogenous) catalyst and a heterogenous catalyst.

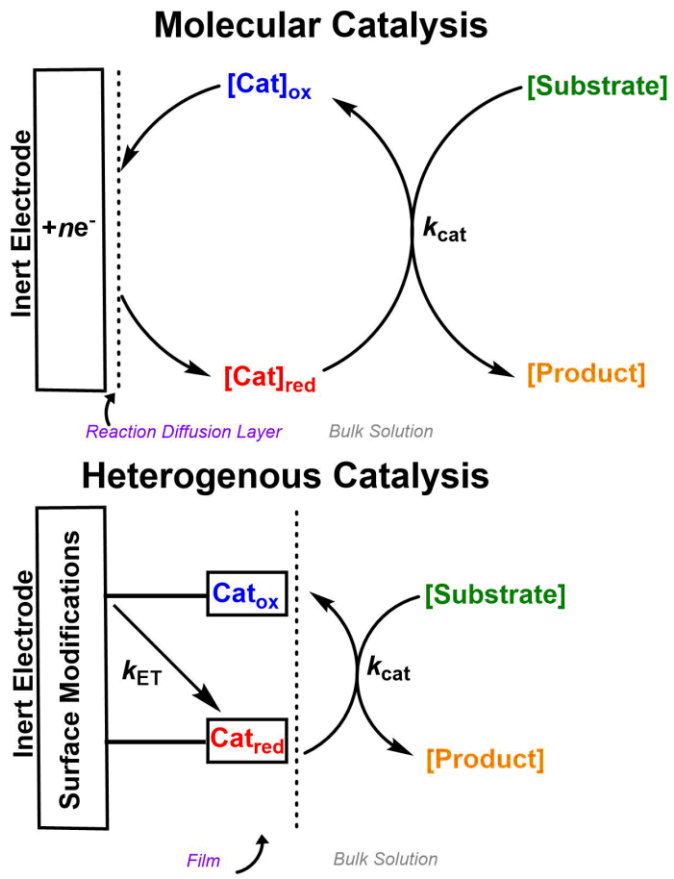

An electrocatalyst must be able to facilitate an electron transfer event while speeding up a chemical reaction. Molecular electrocatalysts are dissolved and upon their electrochemical transformation to their active form can interact with substrates of interest to yield the desired products **(Scheme 1.1, top)**. In this case, an inert electrode (such as glassy carbon) supplies electrons to the catalyst, generating an active form capable of converting a substrate to a product of interest. Typical catalyst design involves a redox active metal center supported by an organic ligand platform that can be fine-tuned to enhance its catalytic ability. A homogenous process relies on the diffusion rate of the active catalyst and the substrate towards the electrode for the reaction to occur successfully.

Limitations of this system include: solubility of the active catalyst, product isolation, incompatible diffusion rates between the substrate and catalyst, and degradation of the catalyst at the electrode.[8-9, 15] Despite these limitations, molecular electrocatalysts offer several advantages over heterogeneous alternatives, primarily in the ability to decipher discrete structural properties and mechanisms, enabling iterative catalyst optimization.[9]

Heterogenous catalysts on the other hand, lower the activation energy of the direct thermodynamic potential of the substrate by forming bonds via chemisorption before the electrochemical reaction occurs (**Scheme 1.1, bottom**).[9] Four major categories in this field include metals, metal alloys, transition metal oxides and metal organic framework's (MOFs).[9, 16-17] Once immobilized onto the electrode, a direct electron transfer occurs from the electrode to the surface-attached catalyst (**Scheme 1.1, bottom**), transforming it to the active catalyst competent to interact with the substrate of interest. Heterogenous catalysts offer a few advantages over molecular catalysts; in the case of CO_2 reduction, their ability to generate multi-carbon products (> C_2), more reduced carbon species (methanol, methane, etc.), and their ability to be scaled up.[18-21]

1.2 Electrochemical Techniques Brief Overview

Electrochemical techniques are a non-destructive method ideal for determining both qualitative and quantitative information about electrocatalytic mechanisms. Electrochemical techniques monitor the change in a redox reaction as a function of voltage and current. These methods are simpler to control reaction conditions since the electrode's energy can easily be manipulated to meets the energetic demands required to drive a specific reaction forward in comparison to using chemical oxidants and reductants.[22-23]

A popular electrochemical technique frequently used for mechanistic studies of molecular catalysis is cyclic voltammetry (CV). This technique scans across a potential range with respect to time and monitors the change in current as the electrode material exchanges an electron with the electrocatalyst in solution. Valuable information about a molecular system can be obtained from the current and potential which correspond to this exchange.

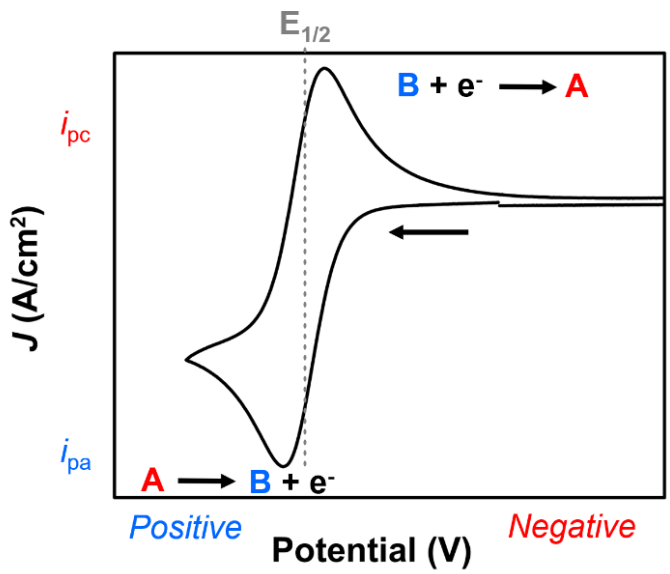

Figure 1.1. Generic CV plot demonstrating the behavior of a reversible one-electron transfer as the potential is swept from negative to positive potentials.

Quantitatively, looking at a simple electron transfer from A (reduced) to B (oxidized) as expressed in **Figure 1.1,** CVs show the equilibrium reaction between the two species (the oxidized and reduced). The Nernst equation can define the standard reduction potential of this process as shown in eq 1.

$$E = E^0 + \frac{RT}{nF} ln \frac{(B)}{(A)} \qquad (1)$$

where E is the potential of the electrochemical cell, E^0 is the standard reduction potential of the analyte, R is the universal gas constant, n is the number of electrons, and T is the

temperature.[23-24] The $E_{1/2}$ as shown in **Figure 1.1** is the average between the positive and negative peak potential and is described as the experimental value of E^0.[23] Qualitatively, looking at the current profile can show if a system is reversible, quasi-reversible or irreversible.[24] Additionally, it can characterize a system as either a homogeneous or heterogenous catalyst by measuring the current response with respect to scan rate as proven by application of the Randles-Sevick equation:

$$i_p = 0.446nFAC\left(\frac{nFvD}{RT}\right)^{1/2} \qquad (2)$$

where i_p relates to the peak current density (J (A/cm^2)), v is the scan rate (V·s^{-1}), n is the number of electrons, A is the surface area of the electrode (cm^2), D is the diffusion coefficient of the analyte (cm^2·s^{-1}) and C^0 (mol·cm^{-3}) is the bulk concentration of the analyte. [23]

In addition to CV, electrolysis experiments are used for further mechanistic studies as well as product analysis. Controlled potential electrolysis (CPE) experiments are used to determine the stability of a catalyst and the products generated during a reaction with the use of product quantification techniques (gas chromatography).[25] This is performed by holding the electrochemical cell at the potential where catalysis is observed and observing the current generated overtime, giving access to key intrinsic parameters discussed below. Furthermore, electrolysis experiments can be coupled to spectroscopic techniques. This is key in deciphering reaction intermediates generated during catalysis.[26] Common techniques include UV-Vis spectroelectrochemistry (UV-Vis SEC) or infrared spectroelectrochemistry (IR-SEC).[27] These techniques enable mechanistic analysis of key target reactions.

The shape of a CV can be informative towards evaluating a catalytic mechanism. For example, if a system displays a reversible wave, it is exhibiting fast electron transfer kinetics with the electrode suggesting that it will not interfere with the electrochemical step upon the addition of substrate.[9, 28] Bonding interactions between a substrate and catalyst are indicated via an irreversible multi-electron shape and an increase in current.[9] These features are associated with the chemical step associated with bond forming and breaking to generate reaction products. This process is defined as an *EC* (*E*= electron transfer, *C*= chemical reaction) mechanism.[28]

1.3 Intrinsic Parameters used to Define Catalytic Efficiency

Electrocatalysts are deemed efficient based on their redox potential (reversible system), high current efficiencies, and fast electron transfer and chemical kinetics.[8-9, 12] CV and CPE techniques (discussed above) are used to determine these parameters. An ideal electrocatalyst needs to be designed with low overpotential, high Faradaic efficiencies (FE) for the product of interest, and high turnover frequencies (TOF). Overpotential (η) is defined as the difference between the applied potential (E_{app}) and the standard reduction potential ($E^0_{substrate/products}$) of the target reaction.[8] More specifically, catalytic η can be defined as the difference between $E^0_{substrate/products}$ and the potential where half catalytic current height is observed ($E^0_{cat/2}$).[29-30] In terms of molecular catalysis, overpotential results from the added energy needed to drive bonds forming and/or breaking during the reaction.[24] Addition of a substrate results in a loss of reversibility and an observed increase in current, suggesting a chemical process (bonds breaking or forming) is occurring. This increase in current in comparison to the catalyst alone allows for extrapolation of the observed catalytic rate constant (k_{obs}) (eq 3).[31-33]

$$\frac{i_c}{i_p} = \frac{n}{0.4463}\sqrt{\frac{RTk_{obs}}{Fv}} \quad (3)$$

where i_p is the peak current of the catalyst (J(A/cm^2)), i_c is the catalytic peak current plateau (J (A/cm^2)), n is the number of electrons involved in the reaction, F is Faraday's constant (96485 C·mol^{-1}), v is the scan rate (V·s^{-1}), R is the universal gas constant (8.314 J·K^{-1}·mol^{-1}), and T is the temperature (K). Once k_{obs} is known, the maximum turn over frequency (TOF_{max}) can be determined by relating the overpotential according to eq 4.

$$TOF = \frac{k_{obs}}{1+exp\left[\frac{F}{RT}\left(E^0_{S/P}-E_{cat/2}\right)\right]exp\left(-\frac{F}{RT}\eta\right)} \quad (4)$$

where $E^0_{S/P}$ is the standard reduction potential of substrate to products and $E_{cat/2}$ is the potential taken at the half of the current observed for i_c. [9, 12, 33] Additional methods to examine the catalyst performance include CPE experiments which are used to assess the stability of the system and determine the turnover number (TON) of the catalyst.[25] The TON is simply the moles of product produced over the moles of catalyst used and can be determined by coupling quantification methods (gas, liquid or ion chromatography) with CPE. [25, 33] Catalysts that achieve high TONs are stable during the course of the reaction, while those exhibiting high FEs in a reaction demonstrate the ability to transfer the exact number of electrons to generate the product without concomitant loss of electrons to non-productive side reactions (eq 5).[12, 25]

$$FE(\%) = 100\ x\ \frac{nFmol_P}{Q} \quad (5)$$

where n is the number of electrons passed for a specific product, F is Faraday's constant (96485 C·mol^{-1}) and Q is the total charge passed. High TOF values reflect the activity of a catalyst. The parameters described above are used to benchmark molecular catalysts with

one another and used to optimize systems to achieve catalysis at low over potentials with high FE, TONs and TOFs.

1.3.1 Additives to Optimize Catalysis

To achieve lower overpotentials during small molecule activation it is common to couple protons with electron transfers (PCET).[34-35] PCET is a fundamental chemical phenomenon in numerous biological processes and offers important mechanistic insight towards understanding the active sites of various metalloenzymes responsible for energy conversion.[35-37] As shown in **Scheme 1.2**, electron and proton transfer processes can behave as elementary steps within a PCET mechanism. A proton and an electron can be transferred within the same step resulting in a concerted proton-electron transfer (CPET).[38] CPET processes are advantageous because they bypass the formation of a stable intermediate, thus minimizing the energy requirements of the reaction. [39-41] Incorporation of a proton source can involve the addition of a Brønsted acid or the integration of a pendent proton on the ligand framework.[8-9, 30] Although these systems offer lower thermodynamic driving forces, they result in observed sluggish kinetics or deactivation of the catalyst (in the case of strong acids as the proton source).[39] Therefore, to prevent deactivation its critical to screen the efficiency of a catalyst with various acids to determine the appropriate conditions for catalysis.

Scheme 1.2. Simple square-scheme showing the different mechanisms for proton coupled electron transfers.

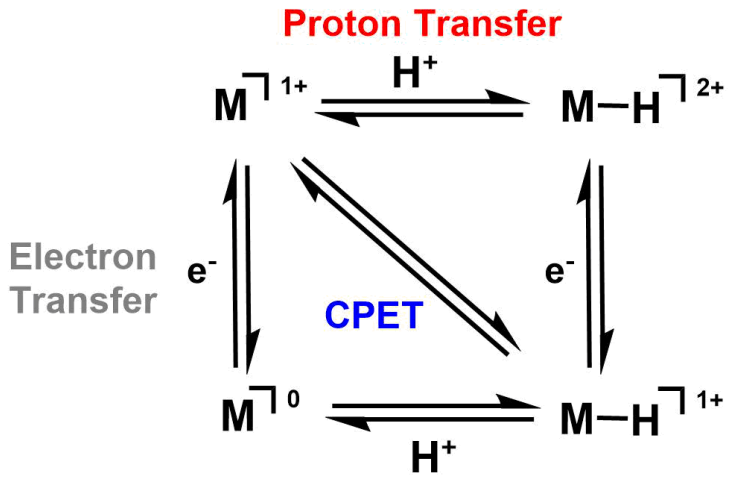

1.4 Challenges of Electrochemical Activation of CO_2

The activation of CO_2 poses a significant challenge due to its inherent stability. The one electron reduction of the linear molecule into the bent radical anion requires significant applied potential due to the large reorganization energy (–1.90 V vs NHE under aqueous conditions at pH = 7).[8] The direct reduction of CO_2 by an electrocatalyst often relies upon large overpotentials due to large kinetic barriers.[8-9, 15, 17] Commonly observed products include carbon monoxide and formic acid, generated by means of $2e^-/2H^+$ pathways. Other possible pathways include the $4e^-/4H^+$ product formaldehyde, the $6e^-/6H^+$ product methanol and the $8e^-/8H^+$ product methane (**Scheme 1.3).** In the presence of protons, the hydrogen evolution reaction (HER) can occur at the electrode due to its favorable thermodynamics (E^0 = –0.41 V vs NHE at pH = 7)[25] out competing the CO_2RR.[8]

Scheme 1.3. Selected reduction potentials[8, 25] of (pH = 7 aqueous media vs NHE under 1 atm and 25 °C) common products generated from the electrocatalytic reduction of CO_2 in the presence of a proton donor.

Reduction Process			$E_{1/2}$ (vs NHE)
$CO_2(g) + 2H^+ + 2e^-$	$\longrightarrow$	$H_2O(l) + CO(g)$	-0.53 V
$CO_2(g) + 2H^+ + 2e^-$	$\longrightarrow$	$HCO_2H(l)$	-0.61 V
$CO_2(g) + 4H^+ + 4e^-$	$\longrightarrow$	$H_2O(l) + HCHO(l)$	-0.48 V
$CO_2(g) + 6H^+ + 6e^-$	$\longrightarrow$	$CH_3OH(l) + H_2O(l)$	-0.38 V
$CO_2(g) + 8H^+ + 8e^-$	$\longrightarrow$	$CH_4(g) + 2H_2O(l)$	-0.24 V

1.4.1 Catalytic Design Based on Nature

As mentioned above, natural metalloenzymes have demonstrated their capability and efficiency for energy conversion in important biological processes. An important system to understand for CO_2RR is [Ni-Fe] CO dehydrogenases (CODHs), which can perform both CO oxidation and CO_2 reduction at its active site.[42] Crystallographic studies on enzymes from the anaerobic bacterium *Carboxydothermus hydrogenoformans* revealed the active catalyst to contain two metal centers, [Ni-Fe], supported by a Fe_3S_4 cluster.[42-43] Mechanistic investigations of reduced [NiFe] CO dehydrogenases revealed that CO_2 forms an adduct between the two metals with stabilization of intermediates occurring via hydrogen bonding interactions with a histidine ligand located in the first coordination sphere of the [NiFe] active site.[42, 44] Another noteworthy metalloenzyme responsible for reducing O_2 to water during cellular respiration is cytochrome *c* oxidase (C*c*O).[45] The enzyme contains four redox active metal centers (Fe and Cu) and uses a proton gradient to catalyze multi-electron/multi-proton conversions.[45-46] Both of these biological processes have become inspiration for catalytic designs discussed in this chapter.

1.4.2 Examples of Inorganic Electrocatalysts for CO_2 Reduction

There are several noteworthy transition metal electrocatalysts capable of reducing CO_2 that have been grouped according to their ligand framework into three major families:

macrocyclic, phosphine, and polypyridyl.[8, 15, 47-51] Many of these reported catalysts reduce CO_2 selectively and at low overpotentials, but utilize precious metals such as Os, Ru, and Rh. [52-54] Recently, there has been interest in the development of molecular electrocatalysts utilizing cost-effective and earth abundant first row transition metals (Co, Fe, Ni, etc.).[55-57] The most widely studied earth-abundant transition metal catalysts for the selective reduction of CO_2 to CO with high Faradaic efficiencies and TOF values are manganese(2,2'-bipyridine)$(CO)_3X$)([Mn(bpy)$(CO)_3X$])[58], nickel(II)(1,4,8,11-tetraazacyclotetradecane ([Ni(cyclam)]$^{2+}$) [8, 56, 59] and iron(porphyrins).[50, 60-66] In order to overcome the kinetic barriers for small molecule activation, ligand frameworks can be modulated to create a cooperative effect together with the metal center for the stabilization of high energy intermediates.[9] For example, [Ni(cyclam)]$^{2+}$ is known to exist in aqueous solutions in five possible conformational isomers, but CO_2 reduction to CO with high activity is attributed to the stabilizing effect of all four of the *trans*-I isomer's hydrogens interacting with bound CO_2.[59, 67] One recent study by Neri and co-workers[57] altered the cyclam backbone with a pendent carboxylic acid that, despite an acidic aqueous media (pH = 2) where HER is anticipated, the system remained selective for generating CO. Similarly, Savéant and co-workers[63] modified iron tetraphenylporphyrin to include phenolic moieties and found through experimental and computational studies that the added phenolic moiety facilitated the C–O bond cleavage through H-bonding stabilization of the transition state. Within the ([Mn(bpy)$(CO)_3X$] family, one study by Sampson and Kubiak[52] showed that modification of the bpy backbone to include steric bulk and the addition of magnesium as a Lewis acid improved the overpotential significantly. Several of the alterations to the ligand backbone mentioned above have been inspired by mimicking secondary sphere

effects of metalloenzymes such as C*c*O and CODHs.[30] Currently, three major challenges in catalyst design include developing and understanding the crucial relationship between a metal center and a ligand that enables efficient performance for the reduction of CO_2, activation of the metal center and mechanistically understanding multi-electron conversion of substrates to products.[8-9]

1.4.3 Pre-activation of CO_2 by Organic Molecules

Other methodologies have demonstrated the lowering of the energetic barrier for CO_2 activation using an organic molecule capable of "pre-activating" CO_2 for more facile reduction by a transition metal electrocatalyst. N-heterocyclic carbenes (NHCs) are a well-known ligand class.[68-69] The unique electronic properties of these compounds make them capable of activating various main group molecules even in the absence of a metal center.[70] Additionally, studies have found carbenes capable of reversibly binding CO_2 to form a zwitterionic imidazolium carboxylate.[71-73] Since this discovery, Luca and co-workers[74] reported forming a zwitterionic imidazolium carboxylate species that in the presence of $[Ni(cyclam)]^{2+}$ and an acid can undergo further electrochemical reduction to generate methane. Inspiration from this work inspired the research discussed in Chapter 3 where we studied the electrochemical properties of cyclic alkyl amino carbenes and their possible use towards CO_2RR.

1.5 The Oxygen Reduction Reaction (ORR)

The reduction of dioxygen (O_2) to water remains a crucial process towards the eventual implementation of carbon-neutral energy sources. A viable approach to cleaner energy involves storing energy from renewable resources (solar or wind) in chemical bonds via an electrochemical water splitting reaction. Water splitting converts two equivalents of

H_2O to one of O_2 (through an oxidation half-reaction) and two of H_2 (through a reduction half-reaction). Reversing this conversion electrochemically is the basis for the simplest possible fuel cell, enabling the use of the stored renewable energy on demand.[75]

Scheme 1.4. Possible reduction pathways for the reduction O_2.[76]

Reduction Process			$E_{1/2}$ (vs SHE)
$O_2(g) + 4H^+ + 4e^-$	$\longrightarrow$	$2H_2O$	+1.229 V
$O_2(g) + 2H^+ + 2e^-$	$\longrightarrow$	H_2O_2	+0.695 V
$H_2O_2(aq) + 2H^+ + 2e^-$	$\longrightarrow$	$2H_2O$	+1.763 V

In aqueous solutions the reduction of O_2 can proceed either by a $2e^-/2H^+$ pathway to yield hydrogen peroxide, a $4e^-/4H^+$ pathway to yield water or by a stepwise (2+2) mechanism which yields H_2O via reduction of the intermediate H_2O_2.[14] It is important to develop a mechanistic understanding to assess what aspects of a catalyst make it selective for one of the three pathways.[15] In fuel cell technology its desirable to tune the catalyst towards the production of H_2O and not H_2O_2. The generation of peroxide and reactive oxygen radical species can degrade proton exchange membranes, damaging the cell and deactivating the system.[77] There remains a lack of understanding for the reduction of O_2 at the cathode of fuels cells. In a fuel cell, the O_2 molecule is adsorbed onto the cathode to undergo the transformation, if a sluggish electron transfer results often the generation of reactive intermediates that destroy the fuel cells membranes occurs.[78] The current state-of-the-art catalyst for this process is heterogeneous Platinum metal, which is cost-prohibitive and not abundant enough to meet global energy demands.[79] Therefore, catalyst design based on the cheap and earth abundant first row transition metals has become a major focus in energy relevant catalysis.

1.5.1 Mechanistic Considerations

There are two primary reaction modes for ORR catalysts: an outer-sphere ET (electron-transfer) to O_2 to form superoxide or a bonding interaction forming a metal oxygen adduct via an inner-sphere ET.[14] Most molecular catalysts follow an inner-sphere ET with the formation of products dependent on the metal center, solvent, proton source, or presence of additives such as Lewis acids.[14] Monomeric homogenous catalysts can support $1e^-$ and $2e^-$ reductions at the metal center resulting in η^1-superoxo and η^2-peroxo binding modes, as shown in **Scheme 1.5**. In the case of bimetallic species, a $2e^-$ reduction can occur (**Scheme 1.5**).[80] The redox potential of the metal center and a vacant coordination site drive the reversible binding of O_2 with a catalyst and dictate its binding mode.[14]

In order to selectively generate H_2O with high TOF values, catalysts frequently operate at large overpotentials.[14] For example, Nocera and co-workers[81] determined the selectivity for H_2O by dicobalt metal complexes is largely dependent on a substantial overpotential with the use of strong acids. The major challenge in ORR catalysis is developing a system that produces H_2O at low effective overpotentials while maintaining a high TOF. Understanding the relationship between these three parameters (overpotential, TOF, and selectivity) is critical for designing efficient catalytic systems. To better understand TOF and overpotential, Mayer and co-workers[82] reported on the adjustment of $E_{1/2}$ values for a series of iron porphyrin catalysts through the use of different ancillary ligands, altering solvents and adjusting the solution acidity, and manipulating the protonation state of the catalyst. They found the overpotential to relate to the catalysts $E_{1/2}$'s and consequently high TOF values resulted from high overpotentials. Building on these results, Mayer and co-workers[83] later found that instead of modifying the catalyst, reaction

conditions such as acid concentration, pK_a of the acid, and partial pressures of reactants can also dictate the relationship between overpotential and TOF values. For example, they reported that by changing the pK_a of the acid versus acid concentration for the reduction of ORR by iron porphyrin in DMF lowers the effective overpotential while closely maintaining high TOF values.[83] There remains a need in this field to develop a catalyst that can operate at low overpotentials yet remain selective for H_2O and not H_2O_2.

Scheme 1.5. Common coordination modes for O_2 with a monomeric metal center.

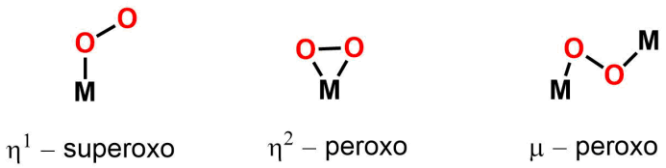

1.5.2 ORR Molecular Catalyst Design

Due to the highly selective nature of O_2 reduction to water by the iron porphyrin active site in C*c*O, porphyrin-based ligand scaffolds have been developed in order to mimic this type of biological activity.[84] The N_4 macrocyclic dianionic porphyrin ligand binds to metal ions via the N atoms allowing for O_2 coordination in the vacant axial positions. Critical to selectivity for H_2O is the choice of metal center, a key step in the generation of H_2O as a product is the formation of a terminal oxo indetermediate.[14, 84] Considering the *d* electron count in late transition metals, they are less likely to form terminal oxo intermediates and instead undergo a bimetallic mechanism while earlier transition metal are more prone towards stabilizing an oxo ligand.[84] While heme systems are frequently studied due to their mimicry of C*c*O, there have also been several studies on non-heme systems. For example, Nocera[81] and co-workers developed a series of bimetallic cobalt complexes supported by the six-coordinate ligand dipyridylethane naphthyridine (DPEN) to study the effect of acid strength on selectivity to H_2O or H_2O_2. Other approaches in

molecular design that optimize selectivity for H_2O is referred to a "push" effect and this is discussed further in Chapter 5.

1.6 Thesis Overview

This thesis discusses research towards the electrochemical reduction of CO_2 and O_2 by transition metal catalysts and organic molecules. The investigation discussed in Chapter 2 studies a polypyridyl complex with a nickel metal center for the reduction of CO_2 in the presence of a weak proton source. Although carbon monoxide (CO) was determined as the main reduction product, this complex decomposed to nickel tetracarbonyl under catalytic conditions. Despite the addition of a CO scavenger, these studies have shown that a polypyridyl ligand platform remains unstable for this process. Chapter 3 investigates the metal-free reductive disproportionation of CO_2 to CO and carbonate by zwitterionic adducts of CO_2 with cyclic(alkyl)(amino) carbenes (CAACs). Chapter 4 discusses the electrochemical characterization of manganese(III) *meso*-tetra(N-methylpyridinium-4-yl)porphyrin pentachloride ([Mn(TMPyP)Cl[Cl]$_4$) via CV and UV-Vis SEC in an universal buffer. Rotating-ring disc electrode experiments show that the Mn porphyrin is competent towards reduction O_2 to H_2O under acidic conditions. Chapter 5 discusses future directions for the electrochemical reduction of CO_2 and O_2 as well as concluding remarks.

1.7 References

1. Lewis, N. S.; Nocera, D. G., *PNAS*, **2006,** *103*, 15729.
2. Denman, K. L., G. Brasseur, A. Chidthaisong, P. Ciais, P.M. Cox, R.E. Dickinson, D. Hauglustaine, C. Heinze, E. Holland, D. Jacob, U.; Lohmann, S. R., P.L. da Silva Dias, S.C. Wofsy and X. Zhang, Couplings Between Changes in the Climate System and Biogeochemistry. In *Climate Change 2007: The Physical Science*

Basis. Contribution of Working Group I to the Fourth Assessment Report of the Intergovernmental Panel on Climate Change, Solomon, S., D. Qin, M. Manning, Z. Chen, M. Marquis, K.B. Averyt, M.Tignor; Miller, a. H. L., Eds. Cambridge University Press: Cambridge, United Kingdom and New York, NY, USA, 2007.

3. Adminstration, N. O. a. A. *Trends in Atmospheric Carbon Dioxide* 2019.
4. Fabry, V. J.; Seibel, B. A.; Feely, R. A.; Orr, J. C., *ICES J. Mar. Sci.* **2008,** *65*, 414.
5. Allen, M. R., O.P. Dube, W. Solecki, F. Aragón-Durand, W. Cramer, S. Humphreys, M. Kainuma, J. Kala, N. Mahowald, Y. Mulugetta, R. Perez, M. Wairiu, and K. Zickfeld, Framing and Context. In *Global Warming of 1.5°C. An IPCC Special Report on the impacts of global warming of 1.5°C above pre-industrial levels and related global greenhouse gas emission pathways, in the context of strengthening the global response to the threat of climate change, sustainable development, and efforts to eradicate poverty*, Masson-Delmotte, V., P. Zhai, H.-O. Pörtner, D. Roberts, J. Skea, P.R. Shukla, A. Pirani, W. Moufouma-Okia, C. Péan, R. Pidcock, S. Connors, J.B.R. Matthews, Y. Chen, X. Zhou, M.I. Gomis, E. Lonnoy, T. Maycock, M. Tignor, and T. Waterfield (eds.), Ed. In Press: 2018.
6. Rogelj, J., D. Shindell, K. Jiang, S. Fifita, P. Forster, V. Ginzburg, C. Handa, H. Kheshgi, S. Kobayashi, E. Kriegler, L. Mundaca, R. Séférian, and M.V. Vilariño, Mitigation Pathways Compatible with 1.5°C in the Context of Sustainable Development. In *Global Warming of 1.5°C. An IPCC Special Report on the impacts of global warming of 1.5°C above pre-industrial levels and related global greenhouse gas emission pathways, in the context of strengthening the global*

response to the threat of climate change, sustainable development, and efforts to eradicate poverty, [Masson-Delmotte, V., P. Zhai, H.-O. Pörtner, D. Roberts, J. Skea, P.R. Shukla, A. Pirani, W. Moufouma-Okia, C. Péan, R. Pidcock, S. Connors, J.B.R. Matthews, Y. Chen, X. Zhou, M.I. Gomis, E. Lonnoy, T. Maycock, M. Tignor, and T. Waterfield (eds.)], Ed. In Press 2018.

7. Qiao, J.; Liu, Y.; Hong, F.; Zhang, J., *Chem. Soc. Rev.* **2014,** *43*, 631.
8. Benson, E. E.; Kubiak, C. P.; Sathrum, A. J.; Smieja, J. M., *Chem. Soc. Rev.* **2009,** *38*, 89.
9. Francke, R.; Schille, B.; Roemelt, M., *Chem. Rev.* **2018,** *118*, 4631.
10. Kumar, B.; Brian, J. P.; Atla, V.; Kumari, S.; Bertram, K. A.; White, R. T.; Spurgeon, J. M., *Catal. Today* **2016,** *270*, 19.
11. Kauffman, D. R.; Thakkar, J.; Siva, R.; Matranga, C.; Ohodnicki, P. R.; Zeng, C.; Jin, R., *ACS Appl. Mater. Interfaces* **2015,** *7*, 15626.
12. Costentin, C.; Robert, M.; Savéant, J.-M., *Chem. Soc. Rev.* **2013,** *42*, 2423.
13. Lim, R. J.; Xie, M.; Sk, M. A.; Lee, J.-M.; Fisher, A.; Wang, X.; Lim, K. H., *Catal. Today* **2014,** *233*, 169.
14. Pegis, M. L.; Wise, C. F.; Martin, D. J.; Mayer, J. M., *Chem. Rev.* **2018,** *118*, 2340.
15. Savéant, J.-M., *Chem. Rev.* **2008,** *108*, 2348.
16. Li, W.; Wang, H.; Jiang, X.; Zhu, J.; Liu, Z.; Guo, X.; Song, C., *RSC Adv.* **2018,** *8*, 7651.
17. Sathrum, A. J.; Kubiak, C. P., *J. Phys. Chem. Lett.* **2011,** *2*, 2372.
18. Boutin, E.; Wang, M.; Lin, J. C.; Mesnage, M.; Mendoza, D.; Lassalle-Kaiser, B.; Hahn, C.; Jaramillo, T. F.; Robert, M., *Angew. Chem. Int. Ed.* **2019,** *58*, 16172.

19. Kuhl, K. P.; Hatsukade, T.; Cave, E. R.; Abram, D. N.; Kibsgaard, J.; Jaramillo, T. F., *J. Am. Chem. Soc.* **2014,** *136*, 14107.

20. Wu, J.; Sharifi, T.; Gao, Y.; Zhang, T.; Ajayan, P. M., *Adv. Mater.* **2019,** *31*, 1804257.

21. Zhao, G.; Huang, X.; Wang, X.; Wang, X., *J. Mater. Chem. A* **2017,** *5*, 21625.

22. Connelly, N. G.; Geiger, W. E., *Chem. Rev.* **1996,** *96*, 877.

23. Elgrishi, N.; Rountree, K. J.; McCarthy, B. D.; Rountree, E. S.; Eisenhart, T. T.; Dempsey, J. L., *J. Chem. Ed.* **2018,** *95*, 197.

24. Single Electron Transfer at an Electrode. In *Elements of Molecular and Biomolecular Electrochemistry*, pp 1.

25. Dalle, K. E.; Warnan, J.; Leung, J. J.; Reuillard, B.; Karmel, I. S.; Reisner, E., *Chem. Rev.* **2019,** *119*, 2752.

26. Machan, C. W.; Sampson, M. D.; Chabolla, S. A.; Dang, T.; Kubiak, C. P., *Organometallics* **2014,** *33*, 4550.

27. Kaim, W.; Fiedler, J., *Chem. Soc. Rev.* **2009,** *38*, 3373.

28. Savéant, J. M., *Elements of Molecular and Biomolecular Electrochemistry*. 2006; p 108.

29. Appel, A. M.; Helm, M. L., *ACS Catal.* **2014,** *4*, 630.

30. Nichols, A. W.; Machan, C. W., *Front. Chem.* **2019,** *7*.

31. Pool, D. H.; DuBois, D. L., *J. Organomet. Chem.* **2009,** *694*, 2858.

32. Thoi, V. S.; Sun, Y.; Long, J. R.; Chang, C. J., *Chem. Soc. Rev.* **2013,** *42*, 2388.

33. Costentin, C.; Drouet, S.; Robert, M.; Savéant, J.-M., *J. Am. Chem. Soc.* **2012,** *134*, 11235.

34. Costentin, C.; Robert, M.; Savéant, J. M., *Chem. Soc. Rev.* **2013,** *42*, 2423.

35. Chang, C. J.; Chang, M. C. Y.; Damrauer, N. H.; Nocera, D. G., *Biochim. Biophys. Acta, (BBA) - Bioenerg.* **2004,** *1655*, 13.

36. Weinberg, D. R.; Gagliardi, C. J.; Hull, J. F.; Murphy, C. F.; Kent, C. A.; Westlake, B. C.; Paul, A.; Ess, D. H.; McCafferty, D. G.; Meyer, T. J., *Chem. Rev.* **2012,** *112*, 4016.

37. Mayer, J. M., *Annu. Rev. Phys. Chem.* **2004,** *55*, 363.

38. Costentin, C.; Robert, M.; Savéant, J.-M., *J. Electroanal. Chem.* **2006,** *588*, 197.

39. Costentin, C.; Robert, M.; Savéant, J.-M., *Acc. Chem. Res.* **2010,** *43*, 1019.

40. Hammes-Schiffer, S., *Acc. Chem. Res.* **2009,** *42*, 1881.

41. Costentin, C., *Chem. Rev.* **2008,** *108*, 2145.

42. Jeoung, J.-H.; Dobbek, H., *Science* **2007,** *318*, 1461.

43. Dobbek, H.; Svetlitchnyi, V.; Gremer, L.; Huber, R.; Meyer, O., *Science* **2001,** *293*, 1281.

44. Appel, A. M.; Bercaw, J. E.; Bocarsly, A. B.; Dobbek, H.; DuBois, D. L.; Dupuis, M.; Ferry, J. G.; Fujita, E.; Hille, R.; Kenis, P. J. A.; Kerfeld, C. A.; Morris, R. H.; Peden, C. H. F.; Portis, A. R.; Ragsdale, S. W.; Rauchfuss, T. B.; Reek, J. N. H.; Seefeldt, L. C.; Thauer, R. K.; Waldrop, G. L., *Chem. Rev.* **2013,** *113*, 6621.

45. Blomberg, M. R. A., *Biochem.* **2016,** *55*, 489.

46. Yoshikawa, S.; Shimada, A., *Chem. Rev.* **2015,** *115*, 1936.

47. DuBois, D. L.; Miedaner, A.; Haltiwanger, R. C., *J. Am. Chem. Soc.* **1991,** *113*, 8753.

48. Raebiger, J. W.; Turner, J. W.; Noll, B. C.; Curtis, C. J.; Miedaner, A.; Cox, B.; DuBois, D. L., *Organometallics* **2006,** *25*, 3345.

49. Dubois, D. L., *Comments on Inorg. Chem.* **1997,** *19*, 307.

50. Costentin, C.; Drouet, S.; Robert, M.; Savéant, J.-M., *Science*, **2012,** *338*, 90.

51. Franco, F.; Cometto, C.; Nencini, L.; Barolo, C.; Sordello, F.; Minero, C.; Fiedler, J.; Robert, M.; Gobetto, R.; Nervi, C., *Chem. Eur. J.* **2017,** *23*, 4782.

52. Sampson, M. D.; Kubiak, C. P., *J. Am. Chem. Soc.* **2016,** *138*, 1386.

53. Bolinger, C. M.; Story, N.; Sullivan, B. P.; Meyer, T. J., *Inorg. Chem.* **1988,** *27*, 4582.

54. Bruce, M. R. M.; Megehee, E.; Sullivan, B. P.; Thorp, H.; O'Toole, T. R.; Downard, A.; Meyer, T. J., *Organometallics* **1988,** *7*, 238.

55. Fisher, B. J.; Eisenberg, R., *J. Am. Chem. Soc.***1980,** *102*, 7361.

56. Beley, M.; Collin, J.-P.; Ruppert, R.; Sauvage, J.-P., *J. Chem. Soc., Chem. Comm.* **1984**, 1315.

57. Neri, G.; Aldous, I. M.; Walsh, J. J.; Hardwick, L. J.; Cowan, A. J., *Chem. Sci.* **2016,** *7*, 1521.

58. Stanbury, M.; Compain, J.-D.; Chardon-Noblat, S., *Coord. Chem. Rev.* **2018,** *361*, 120.

59. Froehlich, J. D.; Kubiak, C. P., *Inorg. Chem.* **2012,** *51*, 3932.

60. Bhugun, I.; Lexa, D.; Savéant, J.-M., *J. Am. Chem. Soc.***1994,** *116*, 5015.

61. Bhugun, I.; Lexa, D.; Savéant, J.-M., *J. Phys. Chem.* **1996,** *100*, 19981.

62. Costentin, C.; Passard, G.; Robert, M.; Savéant, J.-M., *PNAS* **2014,** *111*, 14990.

63. Costentin, C.; Passard, G.; Robert, M.; Savéant, J.-M., *J. Am. Chem. Soc.* **2014,** *136*, 11821.

64. Costentin, C.; Robert, M.; Savéant, J.-M.; Tatin, A., *PNAS* **2015,** *112*, 6882.

65. Takeda, H.; Cometto, C.; Ishitani, O.; Robert, M., *ACS Catal.* **2017,** *7*, 70.

66. Costentin, C.; Robert, M.; Savéant, J.-M., *Acc.Chem. Res.* **2015,** *48*, 2996.

67. Schneider, J.; Jia, H.; Kobiro, K.; Cabelli, D. E.; Muckerman, J. T.; Fujita, E., *Energy Environ. Sci.* **2012,** *5*, 9502.

68. Peris, E., *Chem. Rev.* **2018,** *118*, 9988.

69. Franco, F.; Pinto, M. F.; Royo, B.; Lloret-Fillol, J., *Angew. Chem. Int. Ed.* **2018,** *57*, 4603.

70. Nesterov, V.; Reiter, D.; Bag, P.; Frisch, P.; Holzner, R.; Porzelt, A.; Inoue, S., *Chem. Rev.* **2018,** *118*, 9678.

71. Duong, H. A.; Tekavec, T. N.; Arif, A. M.; Louie, J., *Chem. Comm.* **2004**, 112.

72. Voutchkova, A. M.; Feliz, M.; Clot, E.; Eisenstein, O.; Crabtree, R. H., *J. Am. Chem. Soc.* **2007,** *129*, 12834.

73. Luca, O. R.; Fenwick, A. Q., *J. Photochem. Photobiol., B* **2015,** *152*, 26.

74. Luca, O. R.; McCrory, C. C. L.; Dalleska, N. F.; Koval, C. A., *J. Electrochem. Soc.* **2015,** *162*, H473.

75. Lewis, N. S.; Nocera, D. G., *PNAS.* **2006,** *103*, 15729.

76. Bratsch, S. G., *J. Phys. Chem. Ref. Data* **1989,** *18*, 1.

77. Collier, A.; Wang, H.; Zi Yuan, X.; Zhang, J.; Wilkinson, D. P., *Int. J. Hydrogen Energy* **2006,** *31*, 1838.

78. Ge, X.; Sumboja, A.; Wuu, D.; An, T.; Li, B.; Goh, F. W. T.; Hor, T. S. A.; Zong, Y.; Liu, Z., *ACS Catal.* **2015,** *5*, 4643.

79. Shimizu, K.; Sepunaru, L.; Compton, R. G., *Chem. Sci.* **2016,** *7*, 3364.

80. Momenteau, M.; Reed, C. A., *Chem. Rev.* **1994,** *94*, 659.

81. Passard, G.; Ullman, A. M.; Brodsky, C. N.; Nocera, D. G., *J. Am. Chem. Soc.* **2016,** *138*, 2925.

82. Pegis, M. L.; McKeown, B. A.; Kumar, N.; Lang, K.; Wasylenko, D. J.; Zhang, X. P.; Raugei, S.; Mayer, J. M., *ACS Cen. Sci.* **2016,** *2*, 850.

83. Pegis, M. L.; Wise, C. F.; Koronkiewicz, B.; Mayer, J. M., *J. Am. Chem. Soc.* **2017,** *139*, 11000.

84. Zhang, W.; Lai, W.; Cao, R., *Chem. Rev.* **2017,** *117*, 3717.

CHAPTER TWO

Electrochemical Reduction of Carbon Dioxide with a Molecular Polypyridyl Nickel Complex

This chapter is modified from published work "L. E. Lieske, Arnold L. Rheingold and C. W. Machan, *Sustainable Energy Fuels*, **2018,** *2,* 1269."

2.1 Abstract

The synthesis and reactivity of a molecular nickel(II) complex (**1**) with the polypyridyl ligand framework *N*,*N*,*N′*,*N′*-tetrakis(2-pyridylmethyl)ethylenediamine (TPEN) under electrochemically reducing conditions in the presence of CO_2 is reported. Cyclic voltammetry (CV), infrared spectroelectrochemistry (IR-SEC) and electrolysis experiments suggest this Ni complex is competent at mediating the two-electron reduction of CO_2 to CO and H_2O with phenol as an added proton donor, but is subsequently prone to rapid degradation as $Ni(CO)_4$. This deleterious pathway was shown to be mitigated by the inclusion of the CO scavenger $[Ni(TMC)]^{2+}$, although this requires stoichiometric inclusion for each catalyst turnover and does not significantly improve the observed catalytic current densities.

2.2 Introduction

There have been several reports utilizing polypyridyl catalysts towards hydrogen evolution, CO_2 reduction, and thermal activation of oxygen.[1-9,10-12] Polydentate ligands with flexible linkers allow structural changes under reducing conditions, enabling for stability across a large range of potentials.[11, 13-20] Although, N,N,N′,N′-tetrakis(2-pyridylmethyl) ethylenediamine (TPEN) is a hexadentate ligand, this ligand framework has been reported to have variable coordination modes to metal centers, which led us to believe CO_2 would bind readily with Ni.[21] Herein, the electrochemical behavior of a Ni-based complex with a polypyridyl framework, TPEN, with respect to added CO_2 and phenol (PhOH) is reported. In initial studies, cyclic voltammetry and infrared spectroelectrochemistry establish that $[Ni(TPEN)][PF_6]_2$ (**1**) reacts quite readily with CO_2 upon a one-electron reduction to a Ni(I) state, generating CO. Prolonged electrolysis experiments proved substantial formation of the degradation product $Ni(CO)_4$; this

deleterious pathway can be circumvented through the use of a CO scavenger, [Ni(1,4,8,11-tetramethyl-1,4,8,11-tetraazacyclotetradecane)][PF_6]$_2$ (1,4,8,11-tetramethyl-1,4,8,11-tetraazacyclotetradecane = TMC), prolonging the lifetime of [Ni(TPEN)][PF_6]$_2$ (**Figure 2.1**).[22]

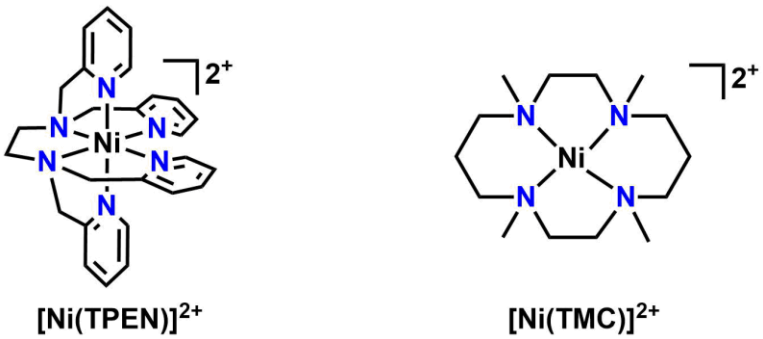

Figure 2.1. Structures of the molecular Ni species relevant to this report. Two hexafluorophosphate (PF_6^-) counter anions (not pictured) are present for both species [Ni(TPEN)][PF_6]$_2$ (**1**) and [Ni(TMC)][PF_6]$_2$ (**2**).

2.3 Results and Discussion

2.3.1 Characterization of [Ni(TPEN)][PF_6]$_2$ (1)

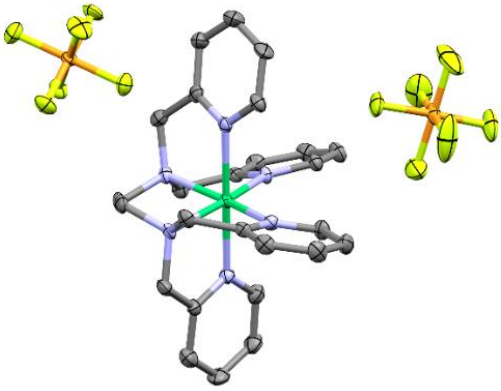

Figure 2.2. Crystal structure of (**1**). Hydrogen atoms omitted for clarity; thermal ellipsoids at 50%. C = dark grey, purple = nitrogen, orange = phosphorus, yellow = fluorine and green = Ni. CCDC 1816890.

To determine the preferred coordination of TPEN to the Ni metal center, ^{1}H NMR spectroscopy and crystallographic techniques were used (**Figure SI 2.4, Figure 2.2 and Table SI 2.4**). The ^{1}H NMR in CD_3CN was consistent with a paramagnetic species and Evans method measurements gave an effective magnetic moment of 3.1 Bohr magnetons, consistent with a Ni(II) d^8 octahedral compound (**See Section 2.5.1**).[23-24] Single crystals suitable for diffraction were obtained through vapor diffusion of CH_2Cl_2 into a solution of (**1**) in methanol (MeOH). The molecular structure shown in **Figure 2.2** confirmed octahedral geometry with two 2-methyl-pyridyl moieties in the axial positions and the tetrakis-2-methylpyridine-substituted ethylenediamine fragment in the equatorial plane. At the axial positions, Ni–N bond distances of 2.092(3) and 2.085(3) Å are observed. By comparison, the equatorial pyridyl fragments exhibit Ni–N distances of 2.077(3) and 2.085(3) Å. Slightly longer bond distances for the alkyl amine fragments of 2.102(3) and 2.098(3) Å are observed crystallographically. Based on these data, use of TPEN in an abbreviated coordination complex formulation refers to a κ^6-coordination mode unless otherwise explicitly stated.

2.3.2 Electrochemical Characterization

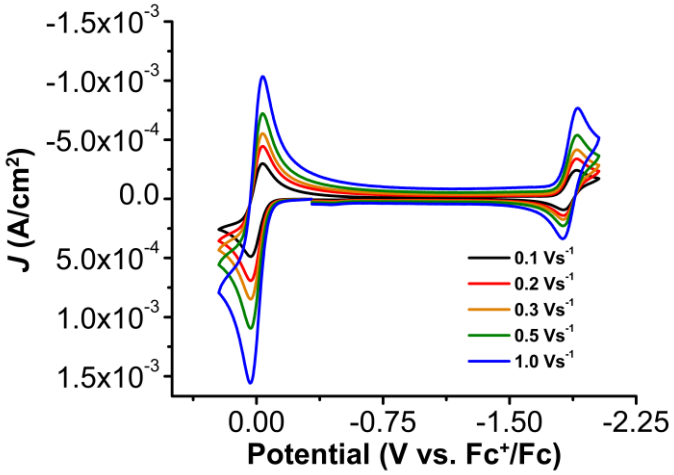

Figure 2.3. CVs of (**1**), obtained under Ar saturation conditions. Conditions: 1 mM analyte, 0.1 M $TBAPF_6$/MeCN, glassy carbon working electrode, Pt wire counter electrode, Ag/AgCl pseudoreference electrode; varied scan rate; referenced to internal ferrocene standard.

The electrochemical properties of (**1**) were studied utilizing cyclic voltammetry (CV) in acetonitrile (MeCN) with tetrabutylammonium hexafluorophosphate ($TBAPF_6$) supporting electrolyte. Under an Ar atmosphere, CVs revealed a reversible Ni(II)/(I) reduction feature ($E_{1/2} = -1.86$ V vs Fc^+/Fc (ferricenium /ferrocene)) and a peak current ratio (i_{pc}/i_{pa}) of 0.93 (**Table SI 2.1**).Variable scan rate studies demonstrated a diffusion-limited redox response, defining the electrochemical process as homogeneous (**Figure 2.3 and Figure SI 2.10**).[25] Under CO_2 saturation conditions (0.28 M for CO_2 in MeCN)[26], the

Ni(II/I) feature became irreversible and displayed an increase in current, suggestive of CO_2 binding and possible catalytic behavior of (**1**) in solution (**Figure 2.4**).

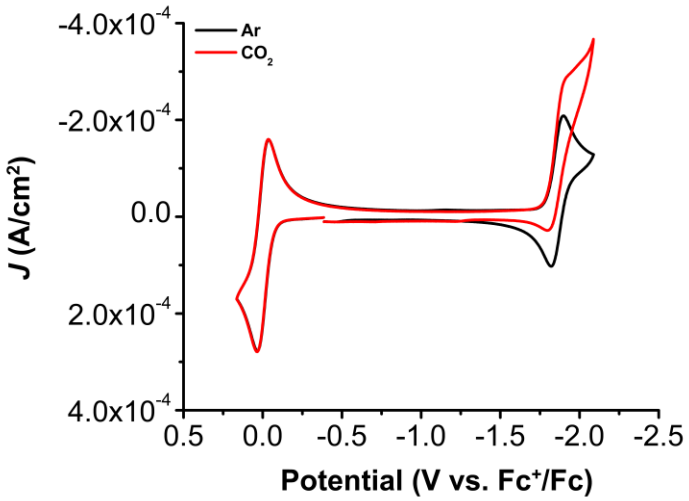

Figure 2.4. CVs of (**1**), obtained under Ar saturation conditions (black) and CO_2 saturation conditions (red). Conditions: 1 mM analyte, 0.1 M $TBAPF_6$/MeCN glassy carbon working electrode, glassy carbon counter electrode, Ag/AgCl pseudoreference electrode; scan rate 100 mVs^{-1}; referenced to internal ferrocene standard.

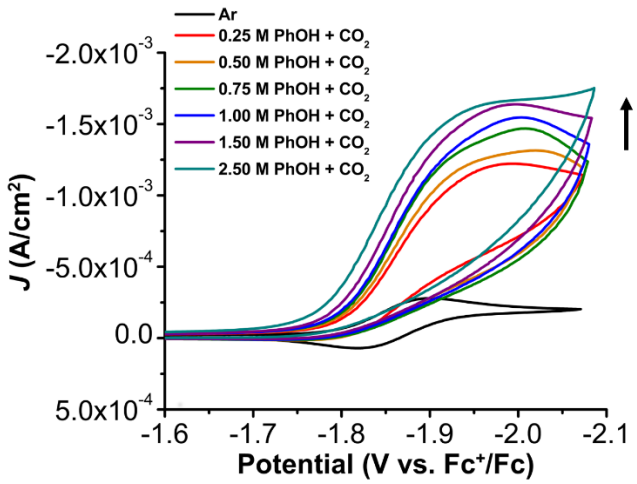

Figure 2.5. CV's of (**1**) under CO_2 saturation conditions with variable PhOH concentration. Conditions: 1 mM analyte 0.1 M $TBAPF_6$/MeCN, glassy carbon working electrode, glassy carbon counter electrode, Ag/AgCl pseudoreference electrode; scan rate 100 mVs^{-1}, referenced to internal ferrocene standard.

Next, phenol (PhOH) was added as a Brønsted acid to accelerate the CO bond cleavage

(**Figure 2.5**).[27] Increasing PhOH concentrations caused a corresponding increase in current and a shift towards more positive potentials at the Ni(II/I) reduction (**Figure 2.5**). Plotting the $E_{1/2}$ of the catalytic wave (half peak current density) vs. log[PhOH] showed a Nernstian dependence for the process, with a slope of 40 mV/log[PhOH] (**Figure SI 2.11**).[28-32] When plotting the log[J (A/cm^2)] vs. log[substrate] or [(**1**)], a half-order, first order, and first order dependence were observed for PhOH, CO_2, and (**1**), respectively (**Figure SI 2.12-2.16**).[33] This suggests that under a CO_2 atmosphere with PhOH as a proton source, a reduced Ni–CO_2 adduct is formed and subsequently protonated for the generation of CO and H_2O as the products.

2.3.3 Foot-of-the-Wave Analysis (FOWA)

In order to determine the rate constant of the reaction (k_{obs}), foot-of-the-wave analysis (FOWA) was used to find the theoretical maximum Turn Over Frequency (TOF_{max}).[3, 34-35] FOWA uses the Tafel relationship of the initial part of the catalytic wave, which provides a better approximation than the use of peak current plateaus, where the consumption of substrate or long-lived intermediates can result in deviations from an ideal catalytic response.[35] FOWA indicated that the highest k_{cat} ($k_{cat} = k_{obs}$[(**1**)]) occurs at 2.50 M PhOH as 1.15 x 10^{10} $M^{-2}s^{-1}$ with a TOF_{max} of 7.72 x 10^8 s^{-1} (**Figure SI 2.21 and Table SI 2.2**). Steady-state conditions could not be located by CV through variable scan-rate dependence studies with CO_2 saturation and 0.5 M PhOH up to 1 V·s^{-1} (**Figure SI 2.18- SI 2.20**).[3] The TOF_{max} values at higher concentrations show the effects of the Nernstian equilibrium as exemplified by the non-linear increase with greater PhOH concentrations. The TOF_{max} values obtained by this method (**Table SI 2.2**) show the effects of the Nernstian equilibrium observed by CV ($E_{1/2(cat)}$ shifts 40 mV/log[PhOH]); a non-linear

increase in TOF_{max} occurs at higher concentrations of PhOH as the Tafel relationship between catalytic and non-catalytic current shifts to increasingly positive potentials.

2.3.4 Product and Mechanistic Characterization by Controlled Potential Experiments (CPE)

To establish a better understanding of the mechanism of CO_2 reduction by (**1**), infrared spectroelectrochemistry (IR-SEC) and controlled potential electrolysis (CPE) experiments were conducted. IR-SEC is a technique that allows for observation of generated species as the potential is varied over time.[36-38] In this system, we were interested in observing the IR absorbance stretches of the Ni–CO_2 adduct and any reduction products present with and without a proton donor. In the absence of PhOH, decreasing the potential from −1.6 to −2.1 V vs. Fc^+/Fc, IR bands consistent with the formation of bicarbonate grew in at 1671 and 1638 cm^{-1} (**Figure SI 2.22**), suggesting a reductive disproportionation reaction of two equivalents of CO_2 to CO and CO_3^{2-} is occurring (**Figure 2.6 B)**). In addition, an IR band at 1986 cm^{-1} appeared, suggesting the presence of a [Ni(κ^5 -TPEN)(CO)]$^+$ species **(Figure 2.6 A**). However, in the presence of a proton donor, the known degradation product for Ni-based molecular electrocatalysts, $Ni(CO)_4$, was observed at 2043 cm^{-1} at potentials more negative than −1.7 V vs Fc^+/Fc suggesting that this pathway was competitive with catalysis (**Figure 2.7**). [22, 39] Minor species are also observed near 1910 and 1888 cm^{-1} , which we attribute either to an intermediate in the pathway between (**1**) and $Ni(CO)_4$, different charge state of a [Ni(TPEN)(CO)]$^{x+}$ adduct, or a different conformer of Ni(TPEN)(CO); at prolonged exposure to potentials of −2.1 V vs. Fc^+/Fc and more negative, substantial accumulation of $Ni(CO)_4$ occurs (**Figure 2.7**).

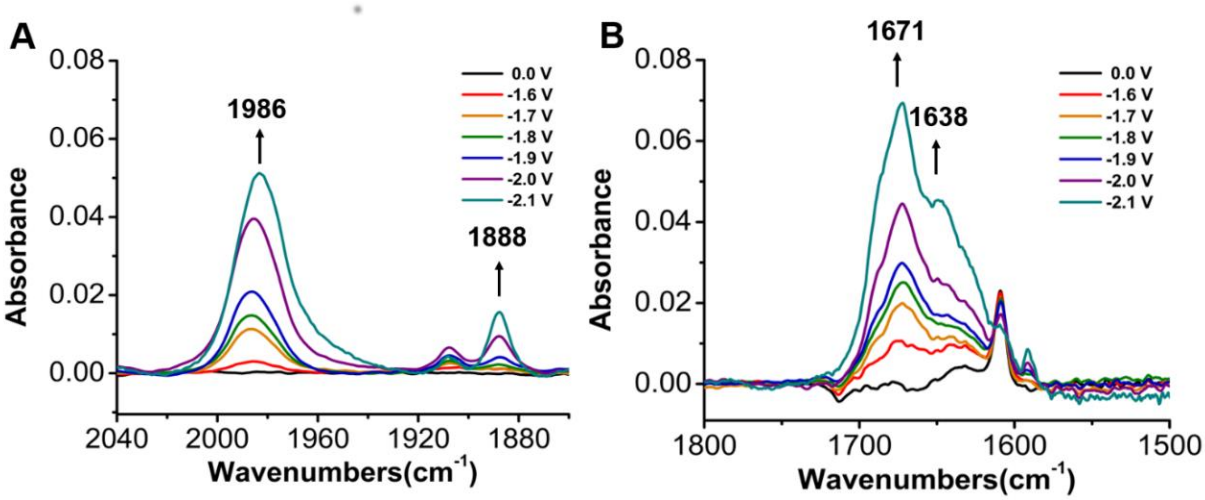

Figure 2.6. IR-SEC spectra of a 3 mM solution of (**1**) in the presence of CO_2 **(A)** Ni–CO stretch grows in at 1986 cm^{-1} and a CO adduct attributed to a minor species grows in at 1888 cm^{-1} from the applied potentials of −1.6 V to −2.1 V **(B)** the formation of CO_3^{2-} observed at 1671 cm^{-1} and 1638 cm^{-1}. Conditions: 0.1 M $TBAPF_6$/MeCN and CO_2 sparged into solution for ~ 30 s; the cell was referenced to an internal ferrocene standard.

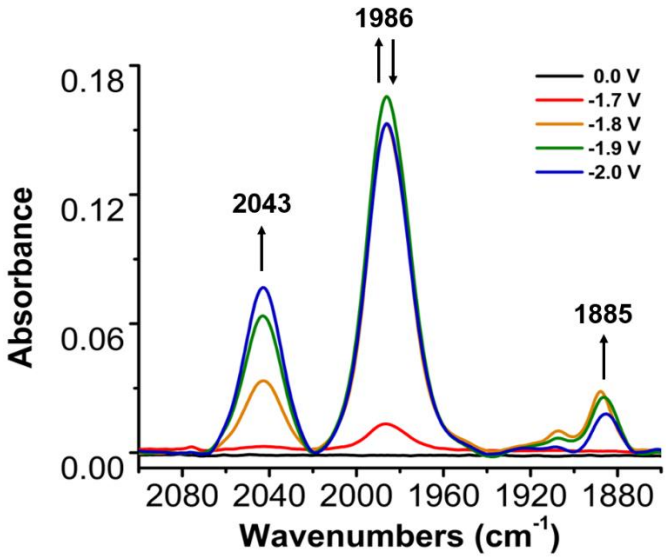

Figure 2.7. IR-SEC spectra of a 3 mM solution of **(1)** with the addition of 0.3 M PhOH and CO_2 sparged into solution for ~30 s. Conditions: 0.1 M $TBAPF_6$/MeCN; the cell was referenced to an internal ferrocene standard.

To confirm the identity of the proposed Ni–CO species, $^{13}CO_2$ was substituted for CO_2. To determine the experimental carbonyl shifts expected, the harmonic oscillator solution to Schrodinger's equation was used, assuming that only the C–O bond is involved

in the IR modes (**See Section 2.5.2**). The observed isotopic shifts were consistent with CO_2 being the source of all CO related species observed in these experiments (**Figure SI 2.23**). To further support the proposed species, these experiments were repeated using CO as the gas (**Figure SI 2.24**). At −1.8 V vs. Fc^+/Fc, a CO-saturated solution with (**1**) present showed the growth of a band consistent with the assigned $[Ni(\kappa^5\text{-TPEN})(CO)]^+$ species at 1982 cm^{-1}, as well as the minor carbonyl-containing species at 1888 cm^{-1}.

CPE experiments were conducted to assess the catalytic efficiency of this system, which demonstrated that under 0.5 M PhOH and CO_2 saturation in MeCN, only trace amounts of CO were observed, indicating that the decomposition pathway hinders electrocatalysis (**Figure SI 2.25-SI 2.26).** Detectable amounts of CO and H_2 were not observed with prolonged electrolysis at −2.05 V vs. Fc^+/Fc under nominally anhydrous and added PhOH conditions, respectively; CO was only observed in trace amounts with (**1**) after 8.66 electron equivalents per molecule of catalyst were passed during 10 hours of electrolysis. We believe this is a result of the decomposition of the catalyst to $Ni(CO)_4$, which can be observed in the post bulk electrolysis solution via IR (**Figure SI 2.26**). This is consistent with the IR-SEC data showing degradation products accumulating (**Figure 2.7**). The control electrolysis conducted at the same potential under CO_2 saturation and 0.5 M PhOH without catalyst present was observed to generate H_2. A Student's *t*-test assuming equal variances (determined using an *F*-test) between this control electrolysis and (**1**) under catalytic conditions resulted in a *P* value of 1.15 x 10^{-6} between the two data sets, indicating that the control generated significantly more H_2 than (**1)** under comparable conditions.[40] These results suggest that the degradation of (**1)** occurs rapidly and prevents any substantial catalytic activity.

2.3.5 Addition of CO Scavenger

In order to prevent the formation of $Ni(CO)_4$ and observe the true catalytic behavior of (**1**), we utilized a CO scavenger, [Ni(1,4,8,11-tetramethyl-1,4,8,11-tetraazacyclotetradecane)]$[PF_6]_2$ - [Ni(TMC)]$[PF_6]_2$, to improve the catalytic behavior and lifetime of (**1**).[22] Performing CV experiments in the presence of (**1**) and PhOH with the titration of $[Ni(TMC)]^{2+}$, FOWA calculations showed that k_{cat} was no longer dependent on PhOH concentration (**Figure SI 2.27 and Table SI 2.3**). The proportional relationship between k_{cat} and $[Ni(TMC)]^{2+}$ concentration suggests that the degradation pathway is the main contributor to the rate of (**1**) towards catalysis. IR-SEC experiments showed that $[Ni(TMC)]^{2+}$ captured CO under these conditions: a band appeared and grew in intensity at 1964 cm^{-1} from −1.5 V to −1.9 V vs. Fc^+/Fc (**Figure 2.8**).

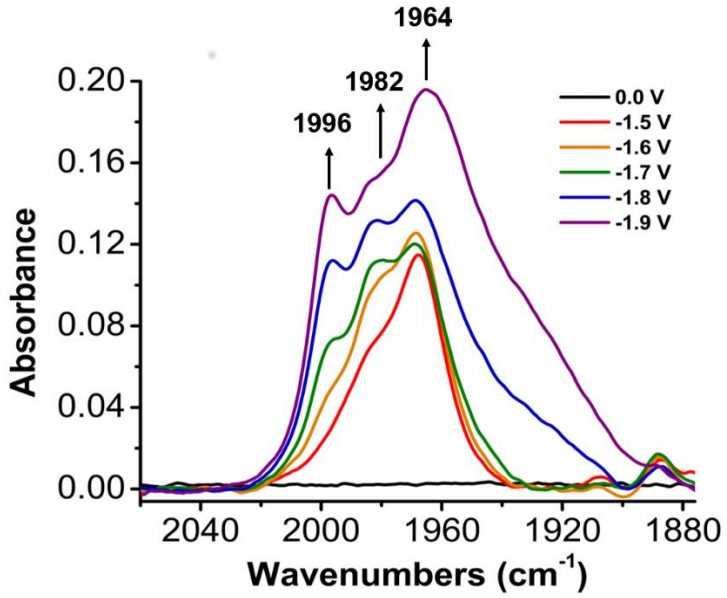

Figure 2.8. IR-SEC spectra of a 3 mM solution of **(1)** and 20 mM solution of $[Ni(TMC)]^{2+}$ with 0.1 M PhOH and CO_2 sparged into solution for ~ 30 s. Conditions: 0.1 M $TBAPF_6$/MeCN; the cell was referenced to an internal ferrocene standard.

The Ni–CO adduct of (**1**) was also observed as a shoulder at 1982 cm^{-1} (**Figure 2.8**).[22] However, when $[Ni(TMC)]^{2+}$ was added to mitigate the formation of $Ni(CO)_4$ during CPE experiments, only trace amounts of CO were observed (**Figure SI 2.28 and SI 2.30**). Therefore, to quantify CO generated by (**1**), a calibration curve was created using IR-SEC by varying the concentration (1-3 mM) of $[Ni(TMC)]^{2+}$ under CO saturation conditions (**Figure SI 2.33**). At −1.9 V vs. Fc^+/Fc after 60 s with 3 mM of (**1**) (30 s CO_2 sparge, 0.1 M PhOH, 20 mM $[Ni(TMC)]^{2+}$ an estimated concentration of 5.9 mM CO scavenger product was present, which corresponds to less than two turnovers per equivalent of complex (**1**).

2.3.6 DFT Calculations and the Proposed Mechanism

Scheme 2.6. Proposed mechanism for the electrochemical reduction of CO_2 to CO as well as the formation of $Ni(CO)_4$.

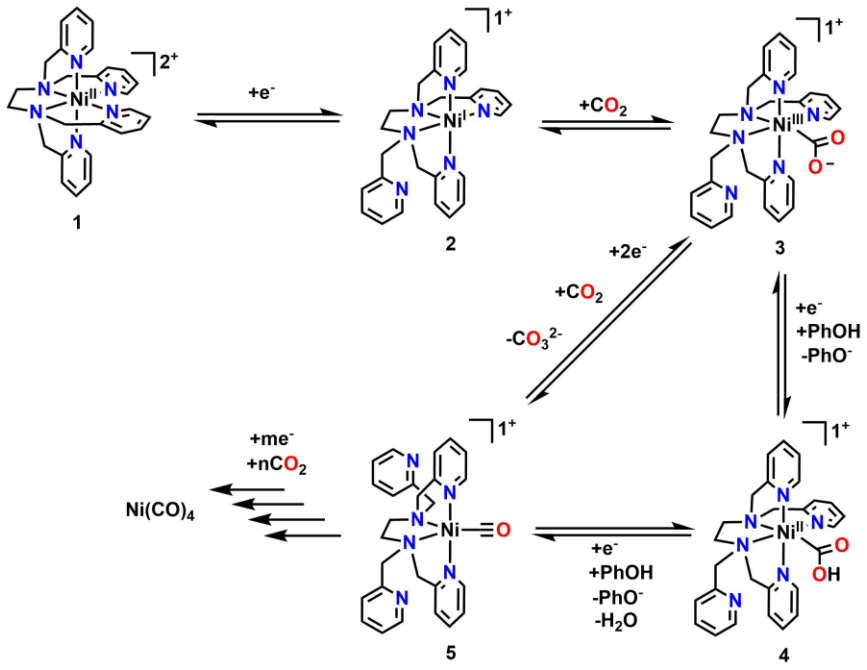

To supplement the experimental studies, the electronic structure of probable intermediates from the proposed reaction mechanism were examined computationally. In

the ground state, the calculated structure of the $[Ni(TPEN)]^{2+}$ parent species is consistent with that determined by X-ray crystallography (**Figure SI 2.36**). Kohn–Sham orbital plots of the orbital energy levels with two unpaired electrons, as well as a visualization of unpaired spin density, are consistent with the high-spin Ni^{2+} metal center observed by the Evans method (**Figure SI 2.37**). Geometry optimizations of the one-electron reduction product only produced a species at a minimum on the potential energy surface when one of the axial 2-pyridylmethyl arms had dissociated from the Ni center $[Ni(\kappa^5\text{-TPEN})]^+$ (**2, see Scheme 2.1**).

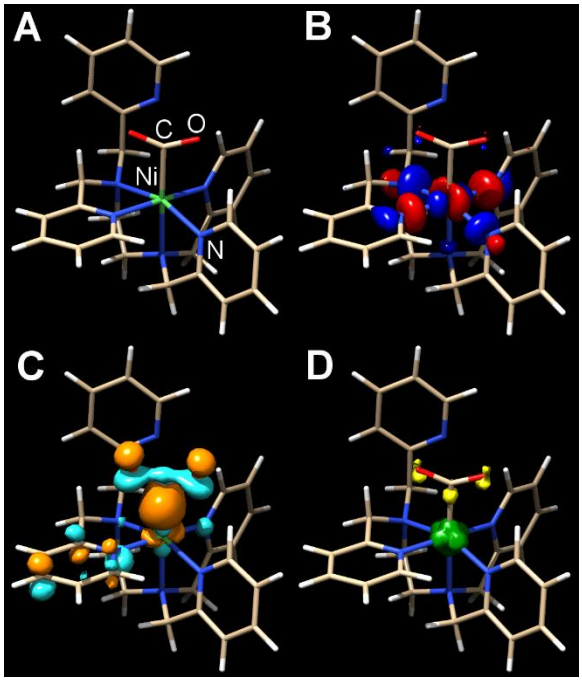

Figure 2.9. Kohn–Sham orbital representations of $[Ni(\kappa^5\text{-TPEN})(\eta^1\text{-}CO_2)]^+$ **3** (A); SOMO (B); LUMO (C); spin density (D). ORCA 4.0; B3LYP/G; ZORA; def2-TZVP; CPCM(Acetonitrile), 2S + 1 = 2.

Although there are two options for the dissociation of a 2-pyridylmethyl arm, the only pathway through which all presumptive intermediate species were verifiable minima through numerical frequency calculations (or lowest in energy according to this level of

theory) was one where this dissociation occurred in the equatorial plane of the starting material, shown as **Scheme 2.1**. The presumptive initial CO_2 adduct was calculated as a low spin monocationic octahedral Ni(III) complex $[Ni(\kappa^5\text{-TPEN})(\eta^1\text{-}CO_2)]^+$ (**3**) (**Figure 2.9**). Further reduction and protonation is presumed to result in a species similar to $[Ni(\kappa^5\text{-TPEN})(\eta^1\text{-}CO_2H)]^+$ (**4**). With further protonation and C–O bond cleavage, a monocationic monocarbonyl $[Ni(\kappa^4\text{-TPEN})(CO)]^+$ (**5**) species would result (**Figure SI 2.38**). The predicted IR frequency of $[Ni(\kappa^4\text{-TPEN})(CO)]^+$ (**5**), 2005 cm^{-1}, qualitatively compares with that observed experimentally by IRSEC (1986 cm^{-1}); error correction was achieved using calculated frequencies for $Ni(CO)_4$ at this level of theory compared to the experimentally observed value. The complete proposed mechanism for the reactivity of (**1**) with CO_2 at reducing potentials is shown in **Scheme 2.1**. Consistent with our experimental observations, there are two routes to the cationic Ni monocarbonyl species $[Ni(\kappa^4\text{-TPEN})(CO)]^+$ (**5**) that are observed by IR-SEC under protic and aprotic conditions. Under aprotic conditions, further reduction and a second $[Ni(TMC)]^{2+}$ present, $Ni(CO)_4$ formation is almost completely suppressed, with the stoichiometric CO capture product $[Ni(TMC)(CO)]^+$ observed by IR-SEC (**Figure 2.9**).

2.4 Conclusions

The electrochemical reduction of CO_2 by a molecular nickel(II) complex has been characterized by IR-SEC, CPE, and CV experiments. Under aprotic and protic conditions (where PhOH is a proton donor), CO is formed as a two-electron reduction product. Once CO is formed, degradation to $Ni(CO)_4$ occurs rapidly. This deleterious reaction can be suppressed by stoichiometric CO capture by the CO sponge $[Ni(TMC)]^{2+}$. These results

suggest that although CO_2 activation is rapid and efficient with this ligand framework, modification to improve stability is a requirement for practical application.

2.5 Experimental Section

2.5.1 Evans Method

The Evans method for determining paramagnetic susceptibility was performed by making a 1 x 10^{-3} M solution of (**1**) in acetonitrile (MeCN). A capillary insert was then made with a 50% v/v mixture of MeCN and MeCN-d_3. The insert was flame sealed, and then placed in an NMR tube containing the solution of (**1**). ^{1}H NMR spectra with 64 scans were then taken using a 600 MHz Varian NMR Spectrometer. Paramagnetic moment was then determined using the following eqns[23-24]:

$$\chi_D(\text{TPEN}) = 46.5\chi_D(\text{en}) + 49\chi_D(\text{pyr}) + 49\chi_D(\text{pyr}) + 49\chi_D(\text{pyr}) + 49\chi_D(\text{pyr}) + 6\chi_D(\text{C}) + 6\chi_D(\text{C}) + 6\chi_D(\text{C}) + 6\chi_D(\text{C}) = 267.00 \times 10^{-6}\ \text{emu}\cdot\text{mol}^{-6}$$

$$\chi^{dia} = \chi^{ligand} + \chi^{Ni\ 2+}$$

$$\chi^{dia} = [-267.00 + (-12.0)] \times 10^{-6}\ \text{emu}\cdot\text{mol}^{-1} = -279.00 \times 10^{-6}\ \text{emu}\cdot\text{mol}^{-1}$$

$$\delta\nu^{p} = (2.22-1.99)*600\ \text{Hz}$$

$$\chi^{para} = \frac{(138\ \text{Hz})*(770\ \text{g/mol})}{(600\ \text{Hz})*(1.33\pi)*(1.06 \times 10^{-2}\ \text{g/mL})} - \chi^{dia} = 4.27 \times 10^{-3}\ \text{emu}\cdot\text{mol}^{-1}$$

μ_{eff} = 3.1 Bohr Magnetons

2.5.2 Determination of $^{13}CO_2$ Shift [41]

The harmonic oscillator approximation for diatomic molecules in Schrodinger's equation was used to derive eqn (1).

$$\tilde{\nu} = \frac{1}{2\pi c}\sqrt{\frac{k}{\mu}} \qquad (1)$$

where is $\tilde{\nu}$ the frequency in cm^{-1}, k is the force constant of the bond, c is the speed of light (3×10^8 $m \cdot s^{-1}$) and μ is the reduced mass ($\mu = \frac{m_1 m_2}{m_1 + m_2}$). This equation describes the amount of energy required to vibronically excite a molecule by one energy level. The IR stretching frequencies from the naturally abundant sample can be used for $\tilde{\nu}$ in order to solve for k. This k value can be used to derive the anticipated isotopic shift for the $^{13}CO_2$ samples.

2.5.3 Materials and Methods

General. All chemicals and solvents (ACS or HPLC grade) were commercially available and used as received unless otherwise indicated. For all air-sensitive reactions and electrochemical experiments, solvents were obtained as anhydrous and air-free from a PPT Glass Contour Solvent Purification System. Gas cylinders were obtained from Praxair (Ar as 5.0; CO_2 as 4.0) and passed through molecular sieves prior to use. Gas mixing for variable concentration experiments was accomplished using a gas proportioning rotameter from Omega Engineering; concentration values were determined according to Henry's Law using a saturation concentration of 0.28 M for CO_2 in MeCN.[26] NMR spectra were obtained on either a Varian 600 MHz or 500 MHz instrument and referenced to the residual solvent signal. IR absorbance spectra were obtained on a Vertex V80 IR instrument from Bruker and UV-vis absorbance spectra on a Cary 60 from Agilent. GC experiments were performed using an Agilent 7890B Gas Chromatograph with an Agilent J&W Select Permanent Gases/CO_2 column; eluent retention times and product characterization were determined by standard injections. HRMS data were obtained by the Mass Spectrometry Lab at the University of Illinois at Urbana-Champaign and elemental analyses were performed by Midwest Microlab.

2.5.4 Synthetic Procedures

N,N,N′,N′-tetrakis(2-pyridylmethyl)ethylenediamine (TPEN).

The ligand framework, TPEN, was prepared according to a modified literature procedure.[42] A round-bottom flask equipped with a stir bar was charged with 2-picolyl chloride hydrochloride (15.99 g, 0.098 mol) and ethylenediamine (1.6 mL, 1.44 g, 0.024 mol). The resulting solution was heated to 70 °C and NaOH (aq) (10 M, 85 mL) was added dropwise over the course of an hour. During this addition, the solution turned a deep red color. The solution was allowed to cool to room temperature and extracted with dichloromethane (3 x 25 mL). The organic layers were combined, dried over $MgSO_4$, and filtered before the solvent was removed under reduced pressure, leaving a red oil. An aliquot of hexanes (20 mL) was added to the oil and the resulting suspension was stored overnight at 0 °C. After this time, a red brown precipitate was collected via vacuum filtration; 8.38 g isolated (80% yield). ^{1}H NMR (600 MHz; CD_3CN; Me_4Si), δ 8.43(4H, *d*, ArH), δ 7.62 (4H, *t*_ArH), δ 7.44 (4H, *d* ArH), δ 7.16 (4H, *t* ArH), δ 3.70 (8H, *s* -CH_2-), δ 2.68 (4H, *s* -CH_2-); **Figures SI 2.1, SI 2.2, and SI 2.3**. CHN Analysis; Found: C, 71.20; H, 6.46; N, 19.24. Calc for $C_{26}H_{28}N_6$: C, 73.56; H; 6.65; N, 19.80 %; ESI-MS (m/z) Calc'd $(M + H^+)^+$: 424.2454 Found: 425.2451.

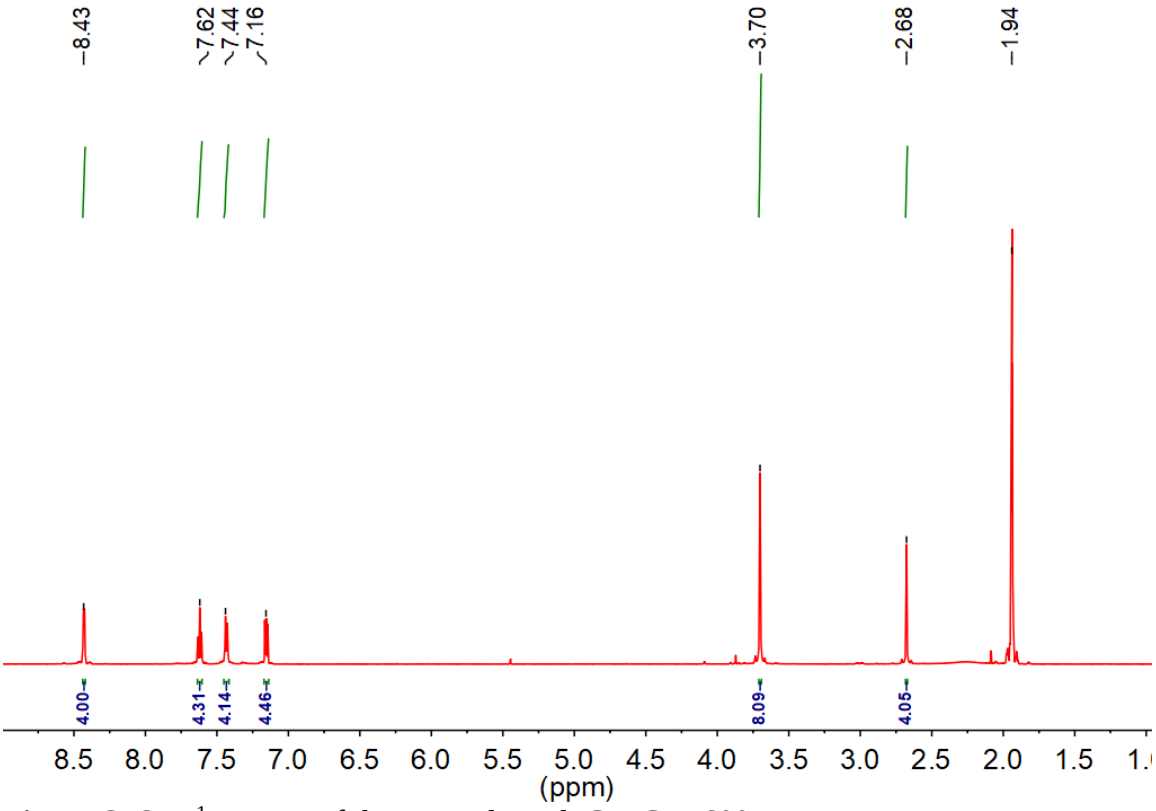

Figure SI 2.1. ^{1}H NMR of the TPEN ligand; CD_3CN; 600 MHz Varian.

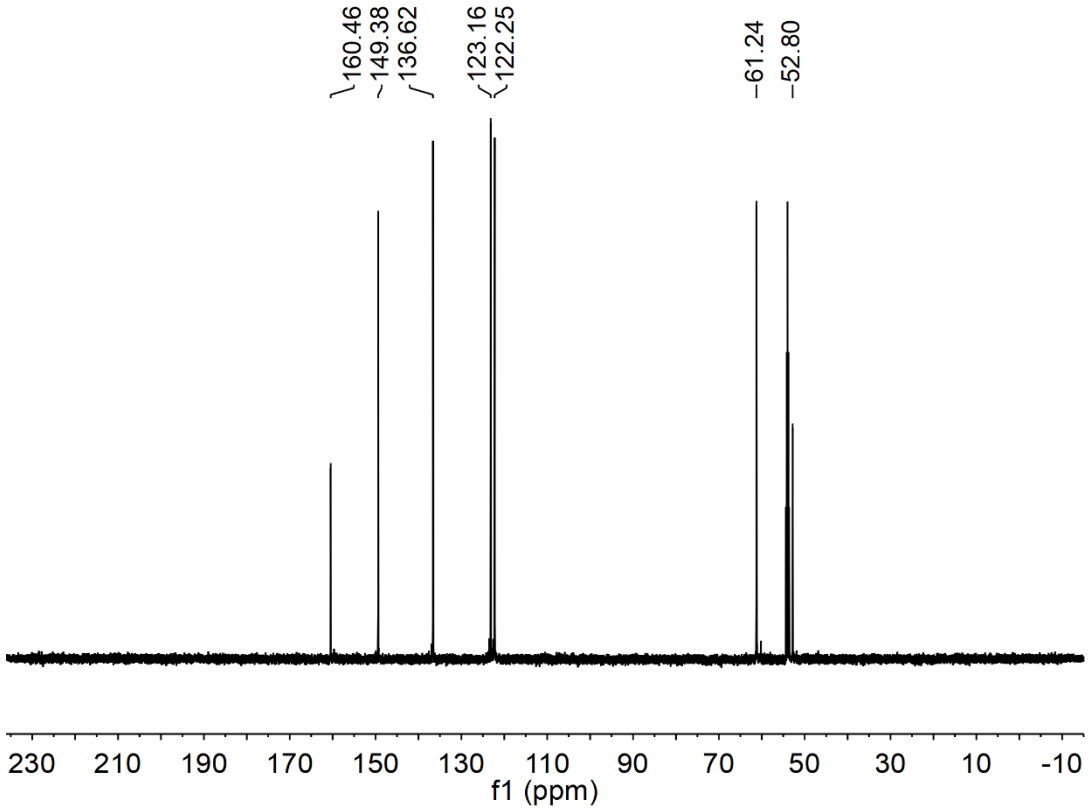

Figure SI 2.2. $^{13}C\{^{1}H\}$ NMR of the TPEN ligand; CD_2Cl_2; 600 MHz Varian.

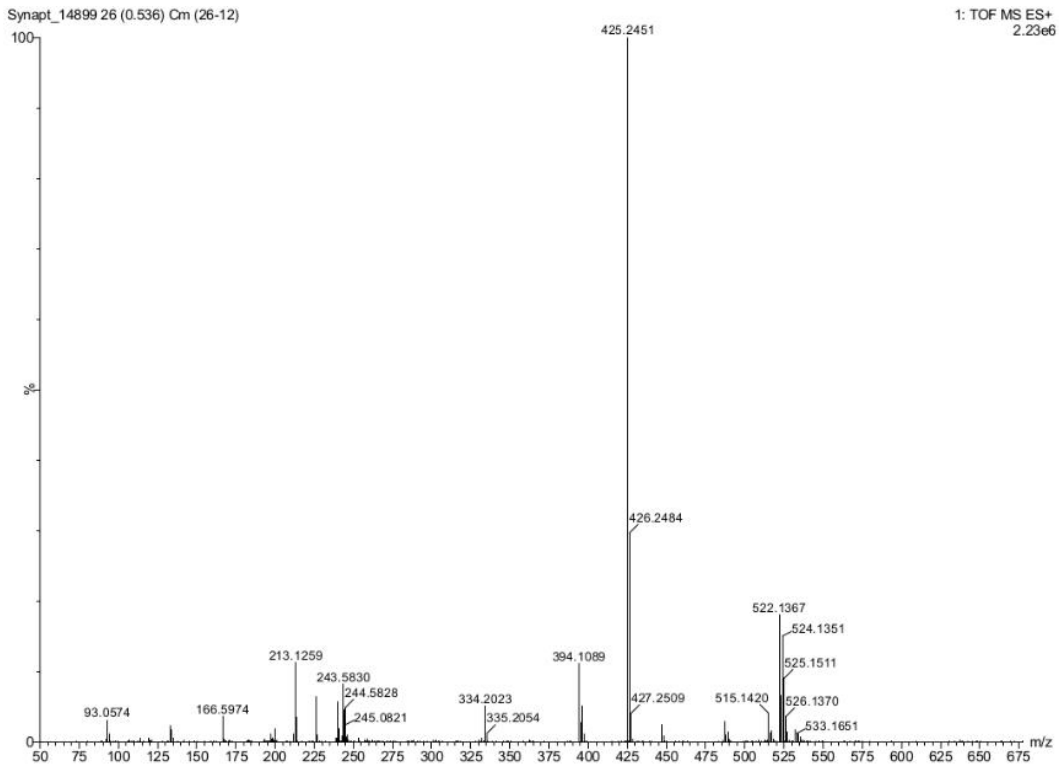

Figure SI 2.3. ESI-MS of TPEN.

[Ni(TPEN)][PF$_6$]$_2$ 1

A round-bottom flask equipped with a stir bar was charged with nickel (II) chloride hexahydrate (0.123 g, 0.473 mmol), TPEN (0.203 g, 0.478 mmol), and ethanol (50 mL). The resulting mixture was stirred for 30 min at room temperature. A portion of ammonium hexafluorophosphate (0.309 g, 1.9 mmol) was then added to the mixture with continued stirring for an additional 30 minutes, during which time a precipitate formed from the suspension. The precipitate was collected via vacuum filtration as a pale pink solid; 0.357 g isolated (97%). ^{1}H NMR was paramagnetic in CD$_3$CN (**Figure SI 2.4**). CHN Analysis; Found C, 40.08; H, 3.73; N, 10.39. Calc. for C$_{26}$H$_{28}$N$_6$:C, 40.39; H, 3.65; N, 10.87. ESI-MS (m/z) Calc'd (M - 2[PF$_6$])$^{2+}$: 241.0865 Found: 241.0868 (**Figure SI 2.5**)

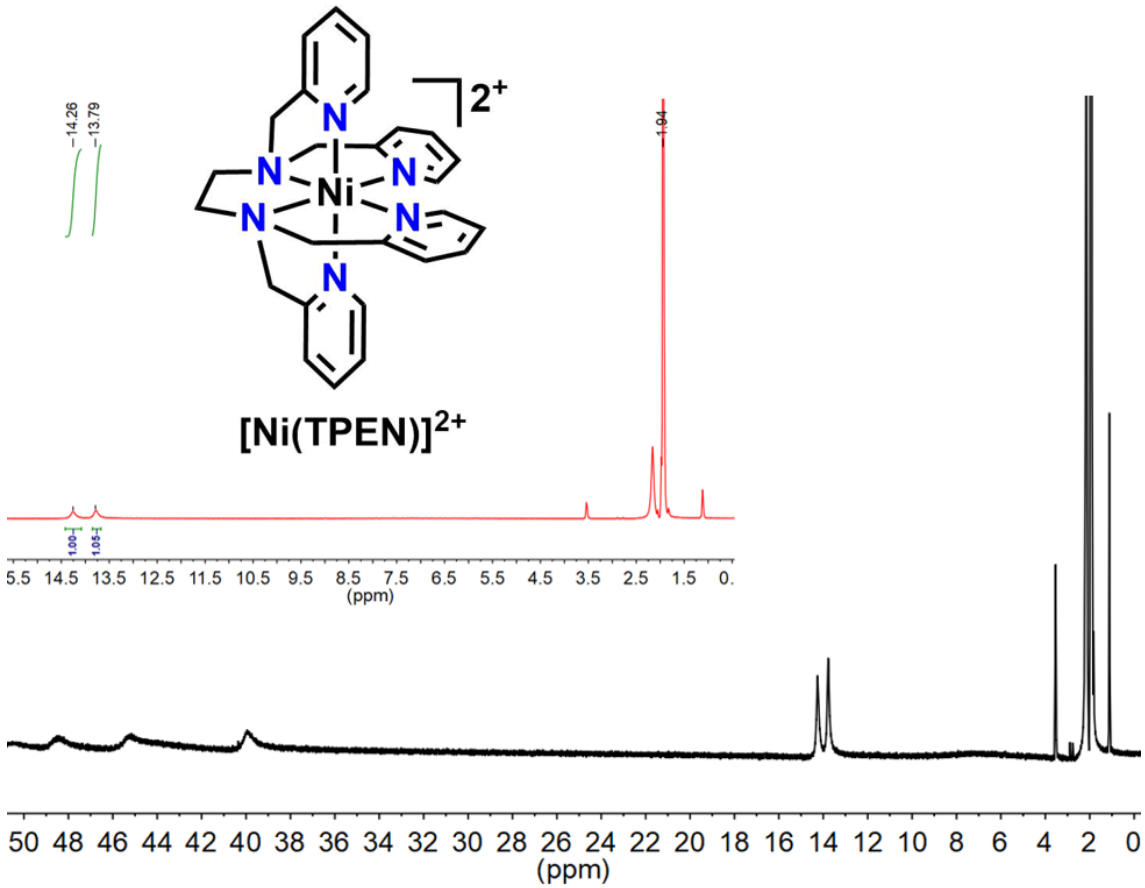

Figure SI 2.4. ^{1}H NMR of (**1**); CD_3CN; 600 MHz Varian. Residual ethanol peaks at 3.54 and 1.11 ppm. Insert: zoom in of the ^{1}H NMR.

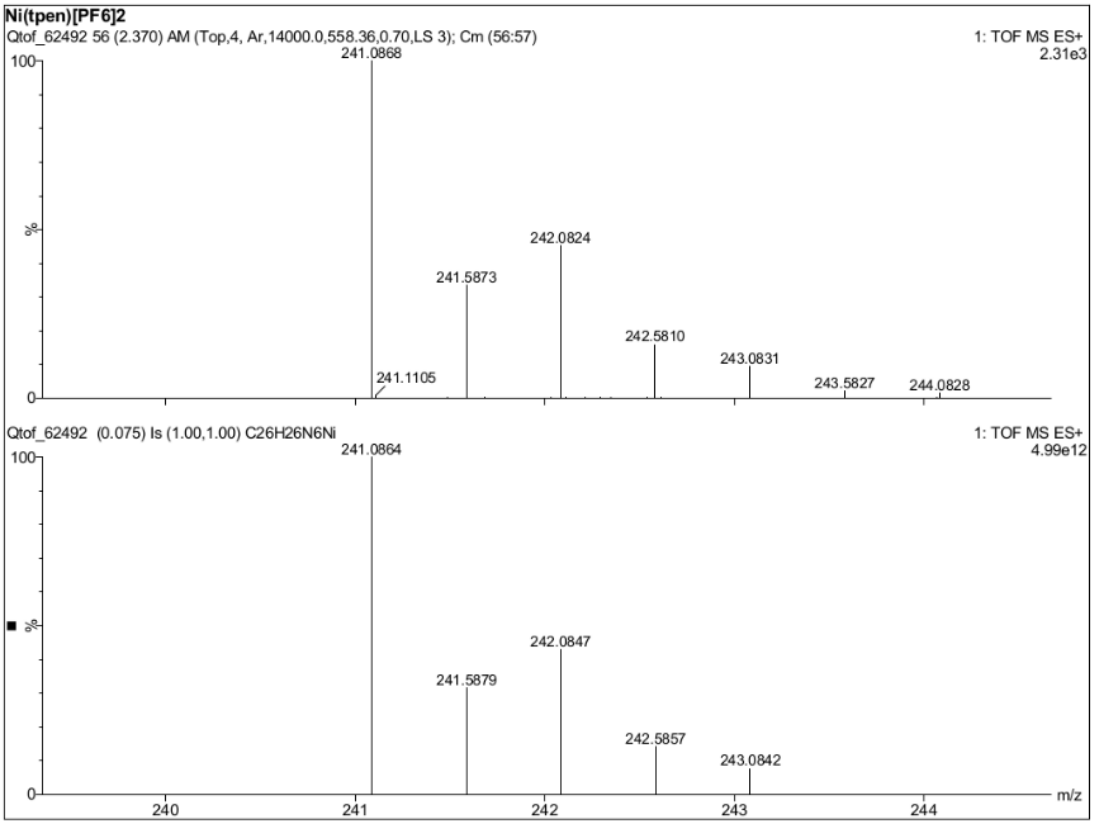

Figure SI 2.5. ESI-MS of $[Ni(TPEN)][PF_6]_2$ (**1**).

Synthesis of 1,4,8,11-tetramethyl-1,4,8,11-tetraazacyclotetradecane (TMC)

TMC was synthesized according to a modified literature procedure.[43-44] A round-bottom flask with stir bar was charged with a solution of 1,4,8,11-tetraazacylcotetradecane (1.500 g, 7.5 mmol), formaldehyde (6.6 mL, 37 % w/w aq solution), 8.5 ml formic acid (8.5 mL) and de-ionized water (5 mL) and brought to reflux (130 °C) for 24 hours. While still hot, the reaction mixture was diluted with de-ionized water (15 mL) and cooled in an ice water bath. The reaction mixture was placed in an ice bath and monitored to maintain temperatures below 22 °C while a concentrated solution of sodium hydroxide (11.90 g in 50 mL, 5.93 M) was slowly added dropwise over thirty minutes (the solution pH > 12 after this addition). Next, the solution was extracted with chloroform (5 x 50 mL), the organic

fractions combined and dried over magnesium sulfate. The solution was concentrated under reduced pressure and stored overnight at 0 °C; an oily yellow-brown solid was isolated, 0.890 g yield (46%). ^{1}H NMR (600 MHz; CD_2Cl_2; Me_4Si), δ 2.38 (16H, *m* -C*H*$_2$-), δ 2.15 (12H, *m* CH_3), and δ 1.57 (4H, *m* -C*H*$_2$-); **Figure SI 2.6**. CHN Analysis; Found C, 65.44; H, 12.52; N, 21.84. Calc. for $C_{14}H_{32}N_4$:C, 65.57; H, 12.58 N; 21.85; ESI-MS (m/z) Calc'd $(M + H)^+$: 257.270 Found: 257.2706 (**Figure SI 2.7**).

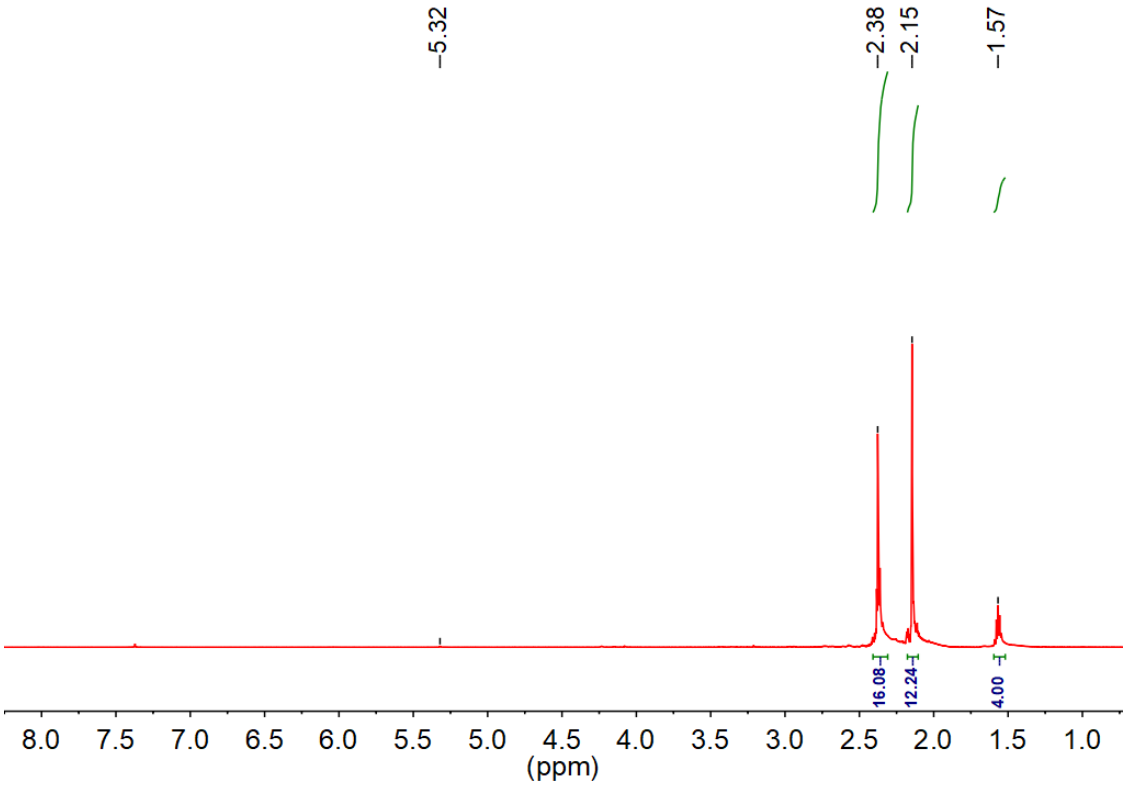

Figure SI 2.6. ^{1}H NMR of the TMC ligand; CD_2Cl_2; 600 MHz Varian.

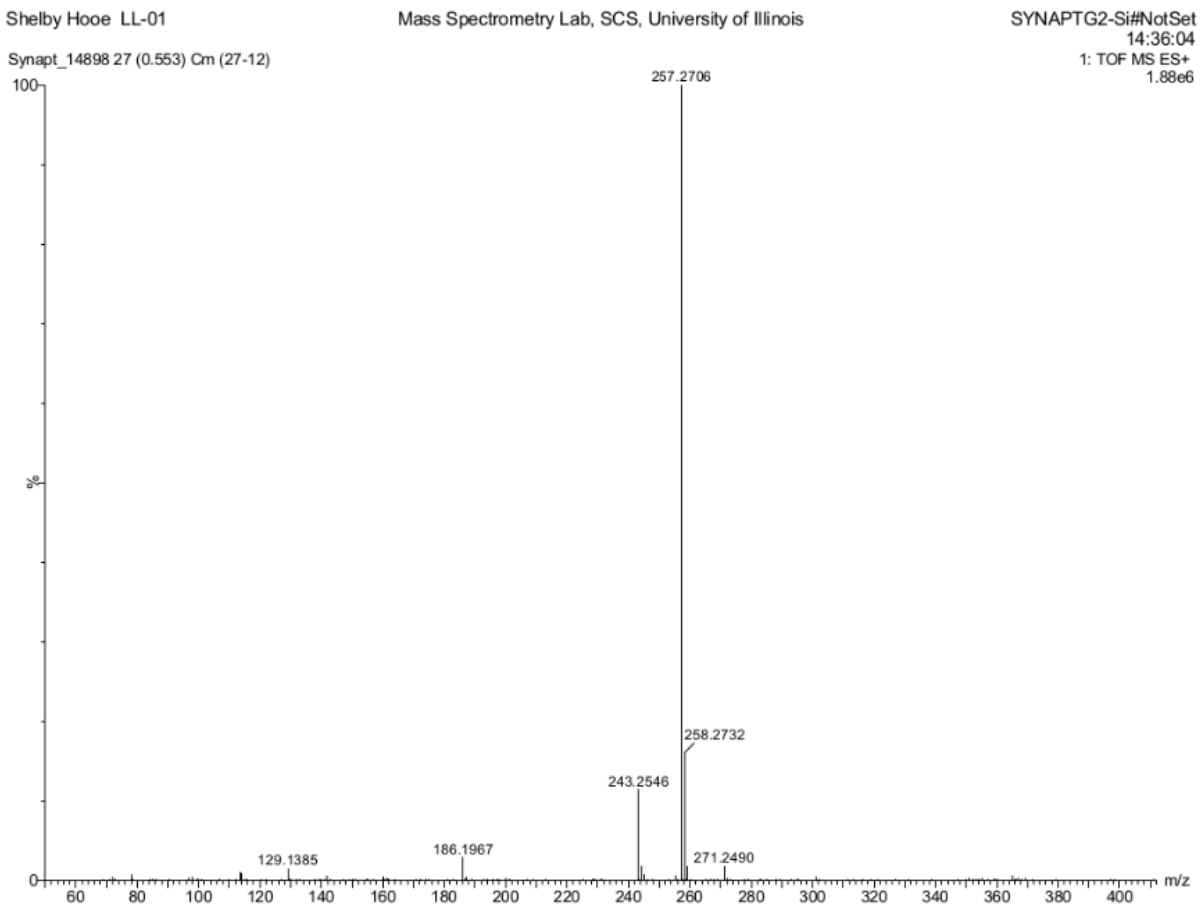

Figure SI 2.7. ESI-MS of TMC.

Synthesis of [Ni(TMC)][PF_6]$_2$

[Ni(TMC)](PF_6)$_2$ was synthesized according to a literature procedure.[22,45] A warm (40 °C) solution of nickel(II) chloride hexahydrate (0.249 g, 0.1 M) in ethanol (10 mL) was added to a solution of TMC ligand (0.21 M, 0.269 g) in ethanol (5 mL) in a round-bottom flask equipped with a stir bar. The reaction mixture was stirred at room temperature for thirty minutes. Next, the solvent was removed under reduced pressure and the precipitate was dissolved in de-ionized (DI) water (20 mL). To induce precipitation of the PF_6 salt, 4 equivalents of ammonium hexafluorophosphate were added (0.6489 g, 4 mol) and the solution stirred for an

additional thirty minutes. The resulting suspension was filtered to isolate a pink solid which was washed with ether (2 x 5 mL); 0.3869 g (61 %). ^{1}H NMR was paramagnetic in CD_3CN (**Figure SI 2.8**). CHN Analysis; Found C: 27.69 H: 9.36 N: 5.23. Calc. for $C_{14}H_{32}N_4$: C, 27.79; H, 9.26; N, 5.33. ESI-MS (m/z) Calc'd 349.1669 $(M - 2[PF_6] + Cl)^+$: Found: 349.1666 (**Figure SI 2.9**).

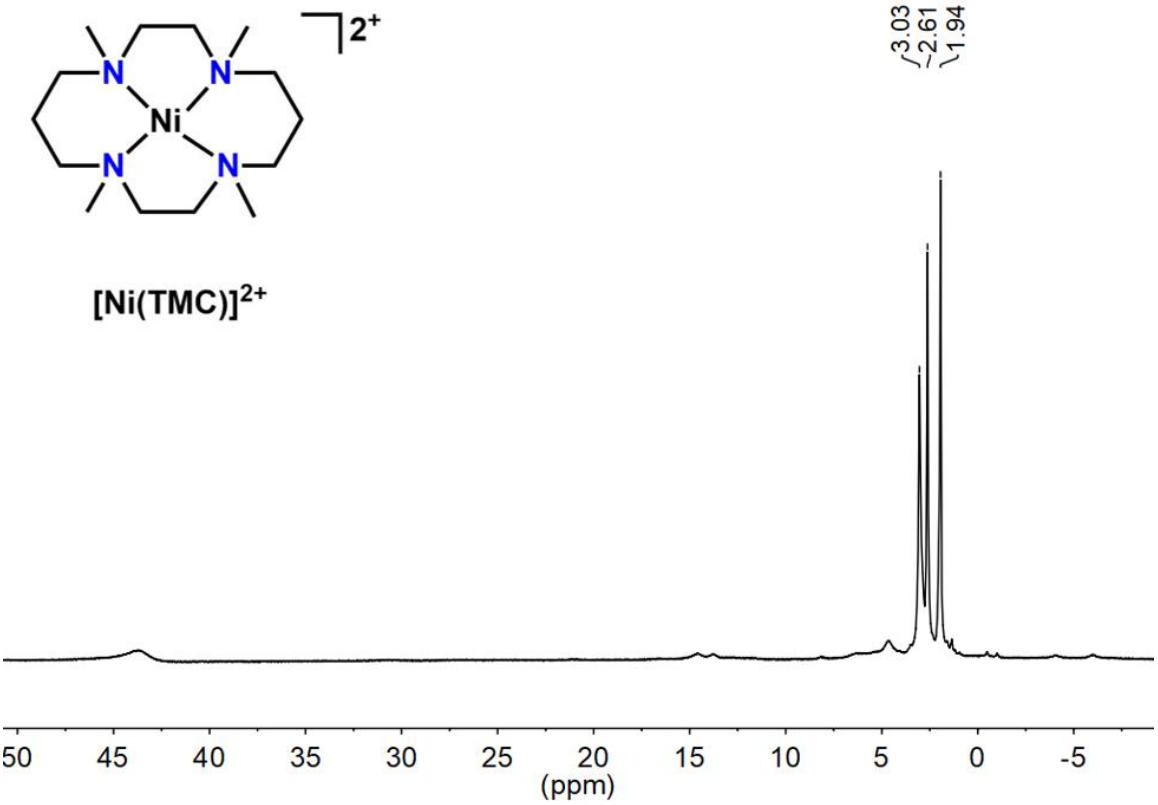

Figure SI 2.8. ^{1}H NMR of $[Ni(TMC)][PF_6]_2$; CD_3CN; 600 MHz Varian.

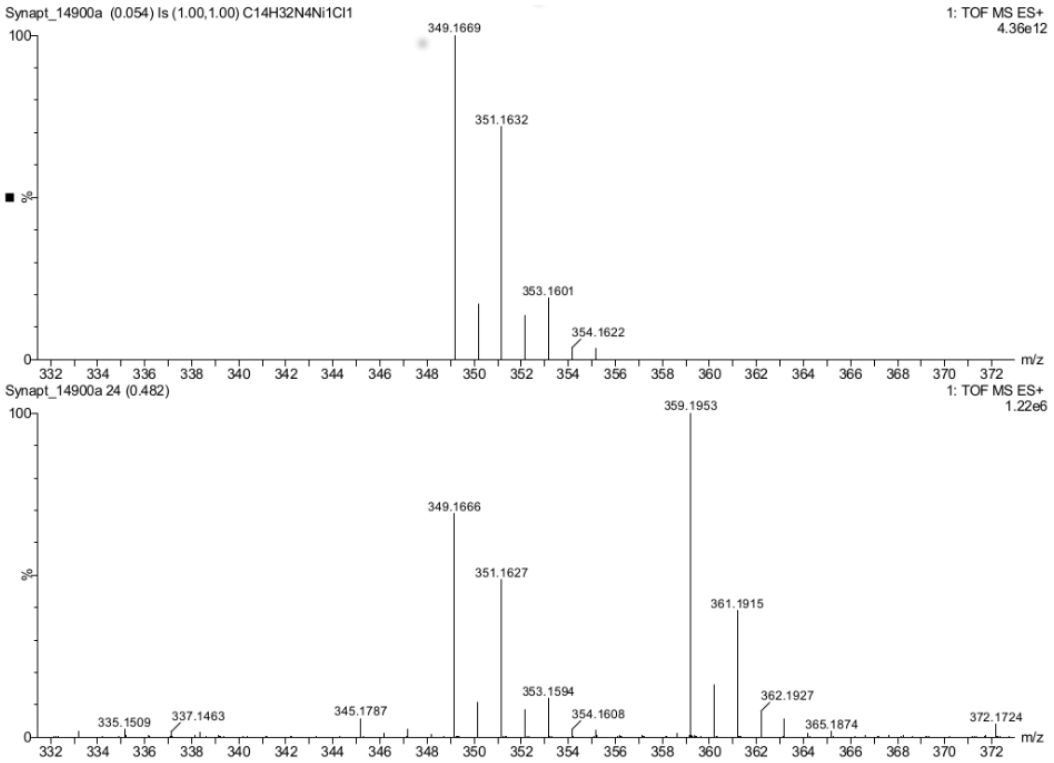

Figure SI 2.9. ESI-MS of $[Ni(TMC)]^{2+}$.

2.5.5 Electrochemistry

All electroanalytical experiments were performed using a Metrohm Autolab PGSTAT302N potentiostat or a BioLogic SP-50 potentiostat. Glassy carbon working (3 mm) electrode and non-aqueous silver wire pseudoreference electrode separated by PTFE tip were obtained from CH Instruments. The Ag/AgCl pseudoreference electrode were generated by depositing chloride on the bare silver wire in 10% HCl at oxidizing potentials and were stored in a 0.1 M tetrabutylammonium hexafluorophosphate/acetonitrile solution prior to use. The counter electrode was Pt wire (Alfa Aesar, 99.95%, 0.5 mm diameter) or glassy carbon rod (2 mm diameter), as noted. All cyclic voltammetry (CV) experiments were performed in a modified scintillation vial (20 mL volume) as a single-chamber cell with a cap modified with ports for all electrodes and a sparging needle.

Controlled potential electrolysis experiments were performed in an H-Cell from Pine Research Instrumentation (two ~25 mL chambers separated by glass frit), with the working electrode in one chamber separate from the pseudoreference and counter electrodes in the other chamber. Spectrographic grade carbon rods (Electron Microscopy Sciences, 6.35 mm diameter) were used as the working and counter electrodes with a silver/silver chloride pseudoreference electrode (CH Instruments) behind a PTFE frit. The cell was sealed with septa and electrical tape to allow head-space sampling and gas sparging via needles through the two septa using a y-splitter. Pressure balance was maintained by inserting a single section of AWG #14 standard wall PTFE tubing through each septum. Tetrabutylammonium hexafluorophosphate was purified by recrystallization from ethanol and dried in a vacuum oven overnight at 100 °C before being stored in a desiccator. All data were referenced to an internal ferrocene standard (ferricenium/ferrocene; Fc^+/Fc) redox potential under stated conditions unless otherwise specified.

2.5.6 IR Spectroelectrochemistry

All IR-SEC experiments were conducted using a custom cell based on a previously published design.[36-38] The three-electrode set-up consists of an inner glassy carbon working electrode disc (10 mm diameter), a central circular silver bare metal pseudoreference electrode, and an outer circular glassy carbon counter electrode embedded within a PEEK block. All data were referenced to an internal ferrocene standard (Fc^+/Fc reduction potential under stated conditions); obtained by taking a CV with the cell prior to injecting analyte for IR-SEC experiments unless otherwise specified. All spectra were processed by subtraction of a non-reactive/non-catalytic potential from those at which reactivity

occurred. For experiments with CO_2, gas was sparged into the solution containing $[Ni(TPEN)][PF_6]_2$ for ~30 s prior to injection into the assembled cell.

2.5.7 Product Analysis

The analysis for gas phase products was done by sampling the headspace of the H-cell containing the working electrode through syringe injections into an Agilent 7890B GC equipped with a specialty gas split column 5 Å mol sieve/Porabond Q column and thermal conductivity detector. The heads space within the tube connecting the other half of the cell as well as that headspace were accounted for in during calculations. Quantification was made from a calibration curve made from injections of known volumes of H_2 and CO into a flask containing MeCN which was degassed and sparged for 10 min with CO_2 while stirring. Manual injections were made using an SGE air-tight 1 mL syringe into a split inlet with a split ratio of 11.7:1. GC oven conditions were 50 °C for 10 minutes, followed by a 20 °C/min to 250 °C, with a final hold at 250 °C for 5 minutes. The column flow rate was set to 1.8 mL/min. The H-cell was calibrated using $Re(bpy)(CO)_3Cl$, with 1 mM catalyst, 0.5 M PhOH, and CO_2 saturation in 0.1 M $TBAPF_6$/MeCN, Faradaic efficiencies of CO could not be determined due to only trace amounts being present and the observed amount H_2 fell within the range of control electrolysis. Solution phase products measured by extracting 2 mL of bulk electrolysis solution with 2 mL of D_2O, and then washing the aqueous layer 1x with 2 mL of CH_2Cl_2 with the addition of a known amount of maleic acid as an internal standard. A ^1H NMR on a Varian 600 MHz NMR Spectrometer was taken of the extracted bulk solution and then acidified (with HCl(aq)), no downfield shift indicative of the protonation of formate to formic acid was observed.

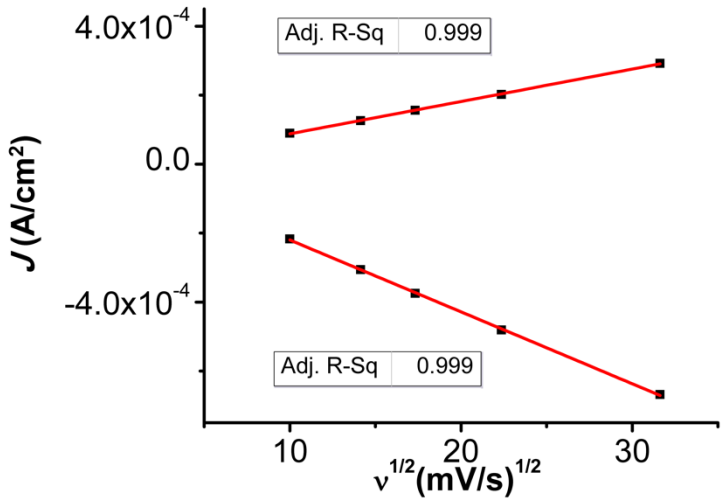

Figure SI 2.10. Linear Fit of variable scan rate data from **Figure 2.3** demonstrating that (**1**) shows a diffusion-limited current response. Conditions: 1 mM analyte; 0.1 M $TBAPF_6$/MeCN, glassy carbon working electrode, Pt wire counter electrode, Ag/AgCl pseudoreference electrode; varied scan rate; referenced to internal ferrocene standard.

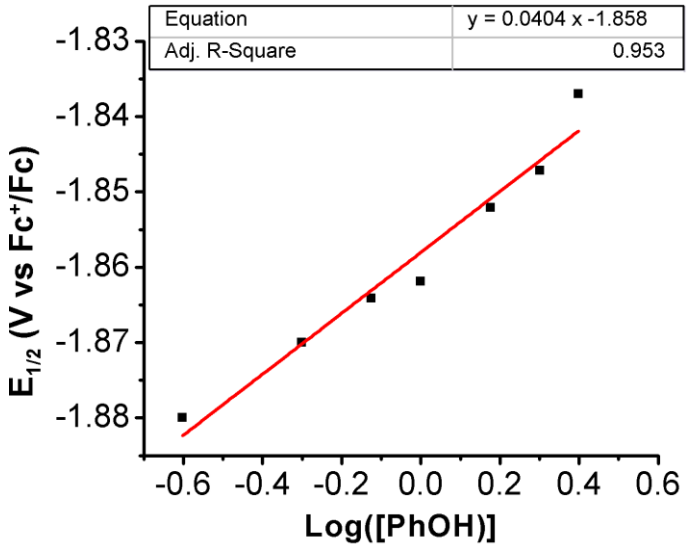

Figure SI 2.11. Plot displaying the Nernstian voltage dependence of (**1**) on the concentration of PhOH in MeCN under CO_2 saturation. Conditions: 0.1 M $TBAPF_6$/MeCN, glassy carbon working electrode, glassy carbon counter electrode, Ag/AgCl pseudoreference electrode; scan rate 100 mV/s; referenced to internal ferrocene standard. Uses data from **Figure 2.5** in main text.

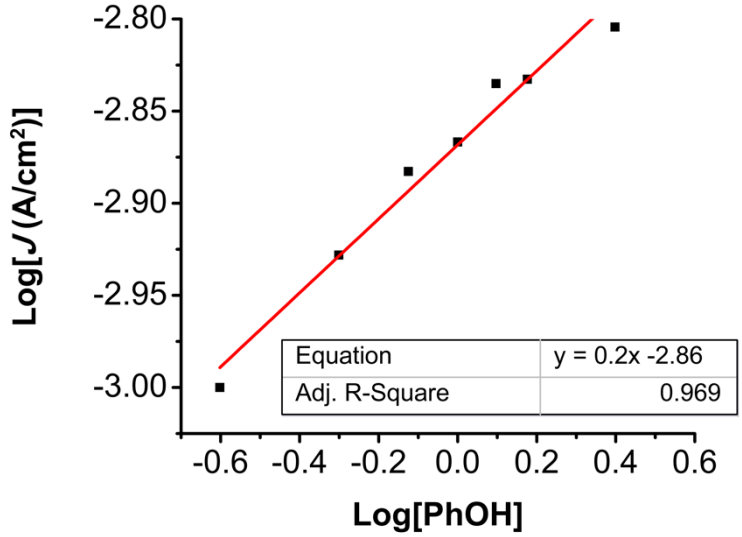

Figure SI 2.12. Log-log plot from data obtained from CVs **(Figure 2.5)** of complex (**1**), (1 mM) with variable PhOH concentrations and CO_2 saturation at −1.93 V vs Fc^+/Fc. Adapted from Sathrum and Kubiak J. Phys. Chem. Lett. **2011**, 2, 2372.[33] *F* is Faraday's constant, *A* is the electrode area, [*Q*] is the substrate concentration, k_{cat} is the catalytic rate, D is the diffusion constant of the catalyst, [*cat*] is the concentration of the catalyst, and n_{cat} is the number of electrons involved in the catalytic process. Uses data from **Figure 2.5** in main text.

$$i_{cat} = n_{cat}FA[cat](Dk_{cat}[Q]^{y})^{\frac{1}{2}} \qquad (2)$$

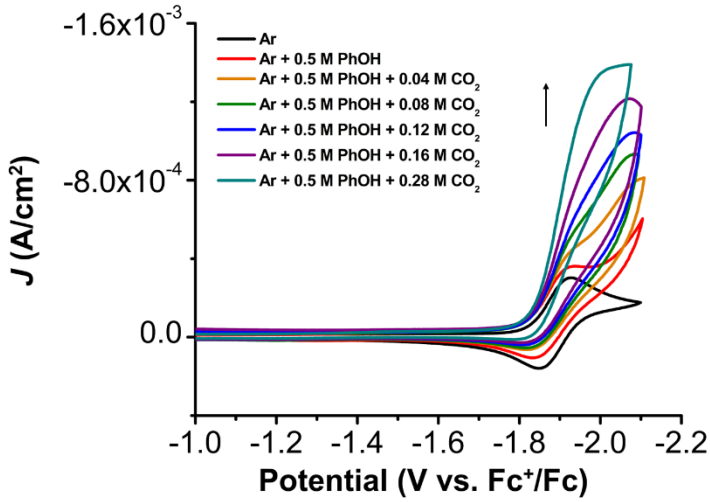

Figure SI 2.13. CVs of **(1)**, obtained under variable CO_2 concentrations with 0.5 M PhOH. Conditions: 1 mM analyte; 0.1 M $TBAPF_6$/MeCN, glassy carbon working electrode, glassy carbon counter electrode, Ag/AgCl pseudoreference electrode; scan rate 100 mV/s; referenced to internal ferrocene standard.

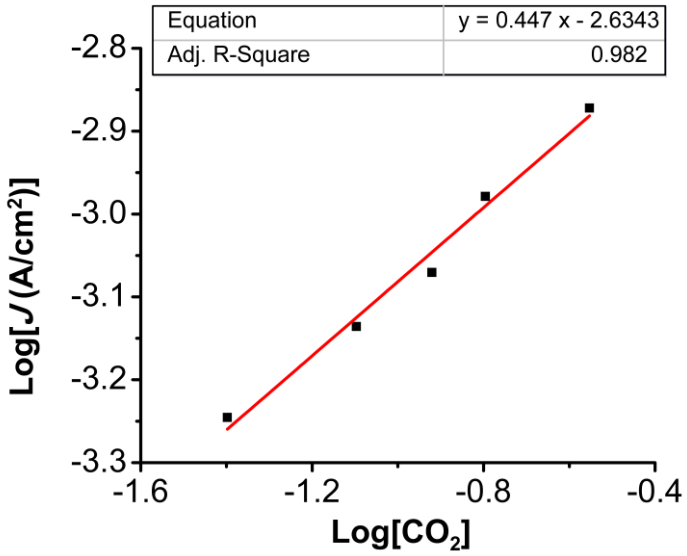

Figure SI 2.14. Log-log plot from data obtained from CVs of complex **(1)** (1 mM) under variable CO_2 concentration conditions with 0.5 M PhOH at −2.0 V vs Fc^+/Fc.

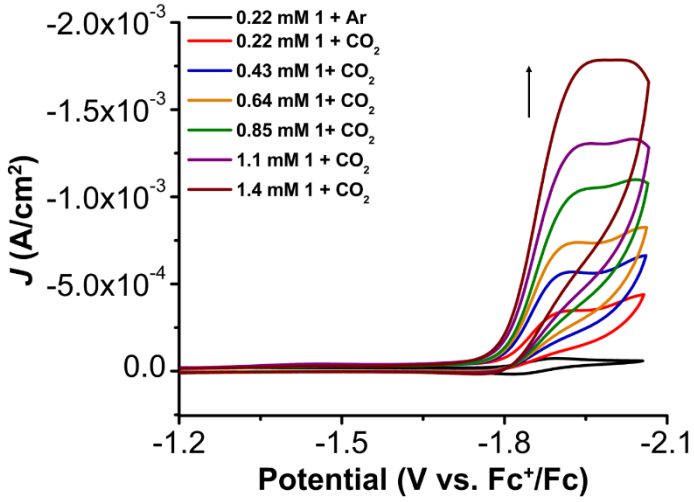

Figure SI 2.15. CVs of complex (**1**) at variable concentrations, obtained under CO_2 saturation and 0.5 M PhOH. Conditions: 0.1 M $TBAPF_6$/MeCN, glassy carbon working electrode, glassy carbon counter electrode, Ag/AgCl pseudoreference electrode; scan rate 100 mV/s; referenced to internal ferrocene standard.

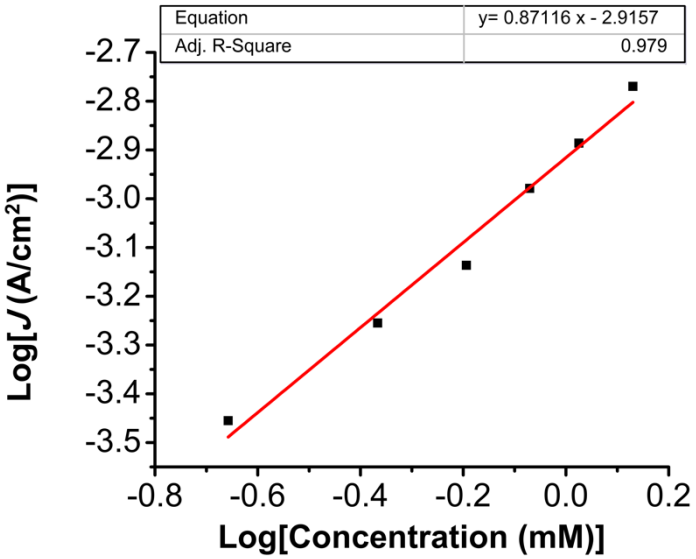

Figure SI 2.16. Log-log plot from data obtained from CVs of complex (**1**) under variable concentration conditions in mM with 0.5 M PhOH and CO_2 saturation at −1.93 V vs Fc^+/Fc.

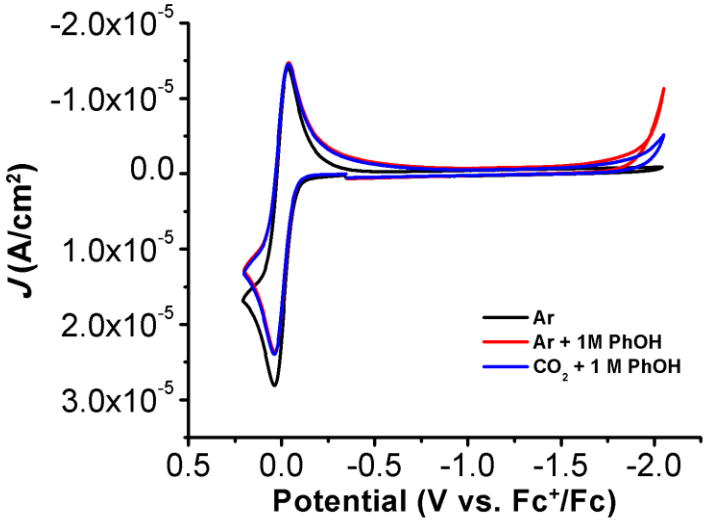

Figure SI 2.17. CVs showing CO_2 and PhOH control responses. Conditions: 0.1 M $TBAPF_6$/MeCN, glassy carbon working electrode, glassy carbon counter electrode, Ag/AgCl pseudoreference electrode; scan rate 100 mV/s; referenced to internal ferrocene standard.

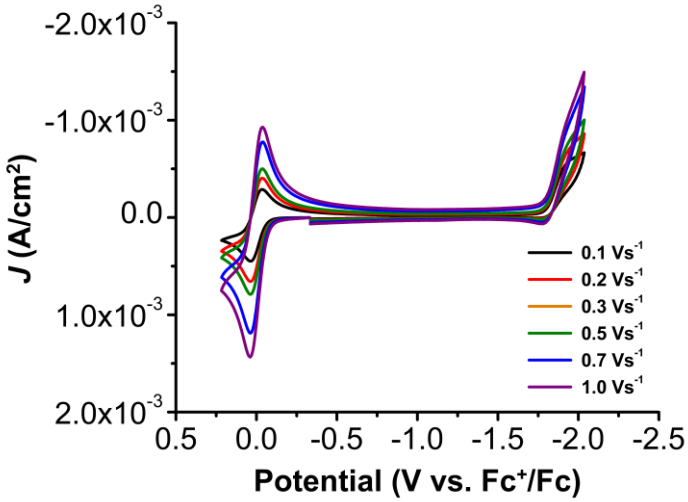

Figure SI 2.18. CVs of **(1)** (1 mM) under CO_2 saturation and 0.5 M PhOH. Conditions: 0.1 M $TBAPF_6$/MeCN; glassy carbon working electrode, glassy carbon counter electrode; Ag/AgCl pseudoreference electrode; varied scan rate; referenced to internal ferrocene standard.

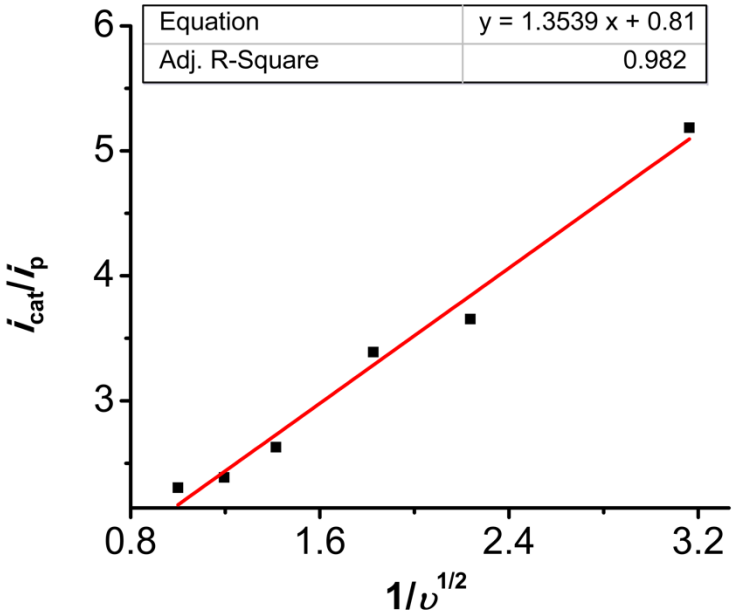

Figure SI 2.19. Linear fit between peak catalytic current over non-catalytic vs the inverse square root of the scan rate from the variable scan rate data in **Figure SI 2.18**. This establishes the validity of using the eqns for the FOWA.

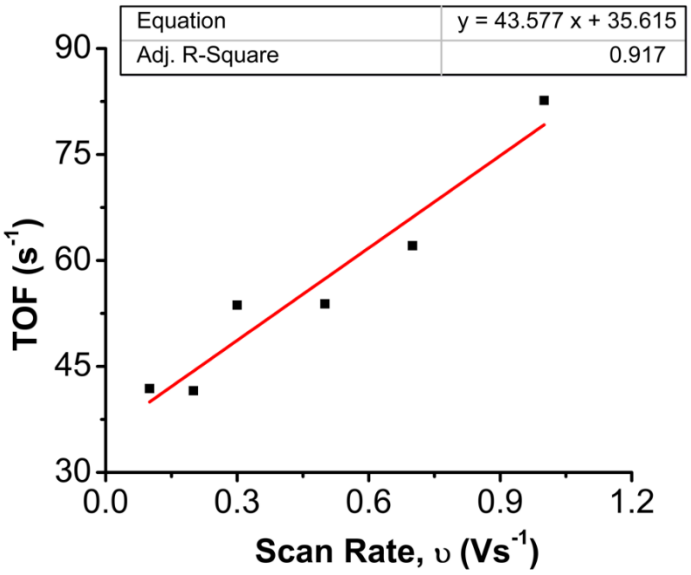

Figure SI 2.20. Linear fit plot of TOF (s^{-1}) vs scan rate of the variable scan rate data from **Figure SI 2.18** demonstrating that (**1**) can be analyzed by FOWA using these data.

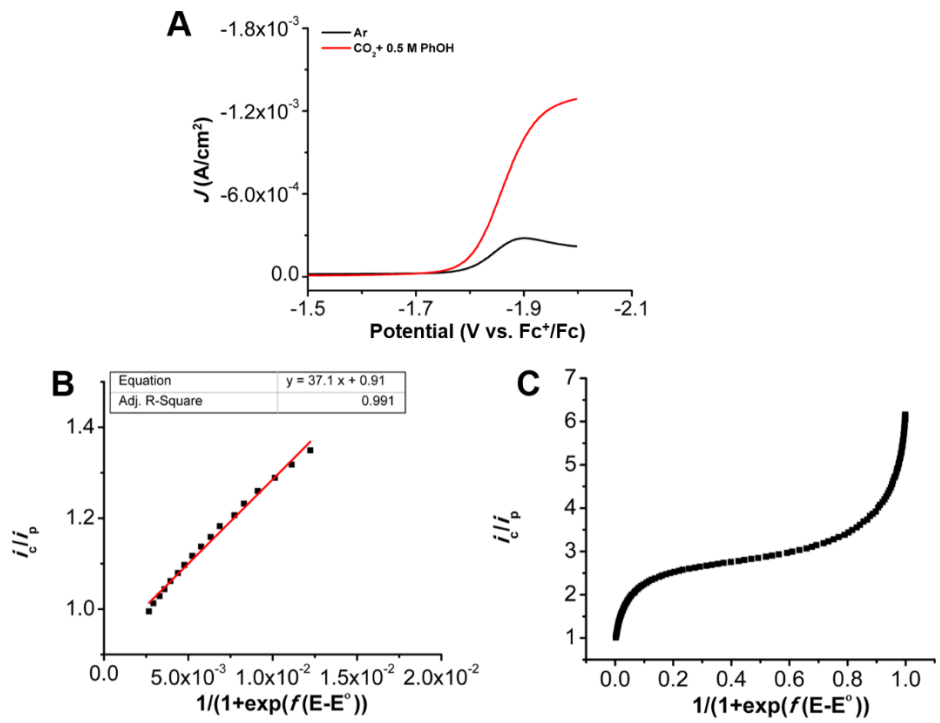

Figure SI 2.21. A) CV overlay between catalytic current of (**1**) under CO_2 and 0.5 M phenol (red trace) and (**1**) under Ar (black trace). **B)** Linear region from the FOWA. **C)** Entire region of i_c/i_p vs $1/(1+\exp(f\ (E-E^o))$. Conditions: 1 mM analyte; 0.1 M $TBAPF_6$/MeCN, glassy carbon working electrode, glassy carbon counter electrode, Ag/AgCl pseudoreference electrode; scan rate 100 mV/s; referenced to internal ferrocene standard.

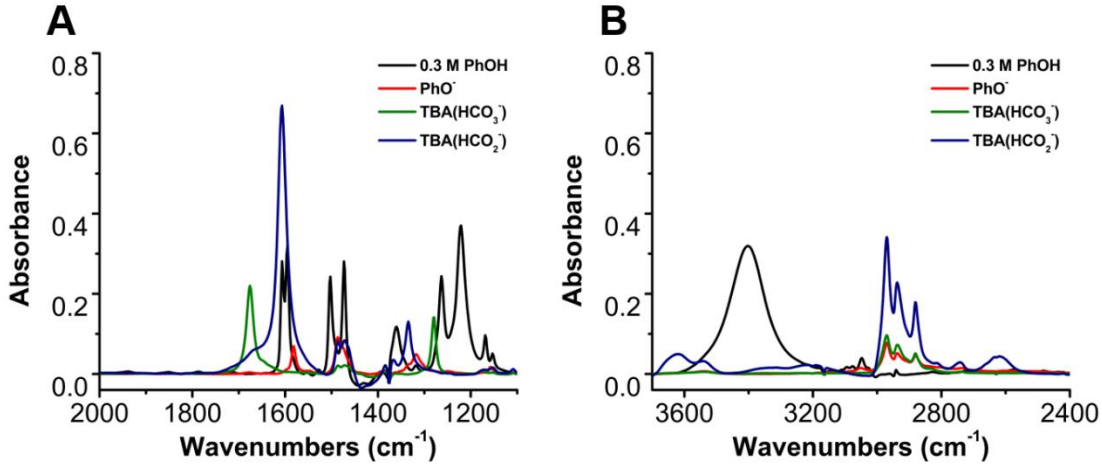

Figure SI 2.22. IR controls for the following with their corresponding v_{max}/cm^{-1} taken in MeCN: [TBA(HCO_2^-)] 1333 cm^{-1} and 1608 cm^{-1}, [TBA(HCO_3^-)] (1676 cm^{-1}), PhO^- (1589 cm^{-1}) and PhOH (3408 cm^{-1}) in MeCN.[46]

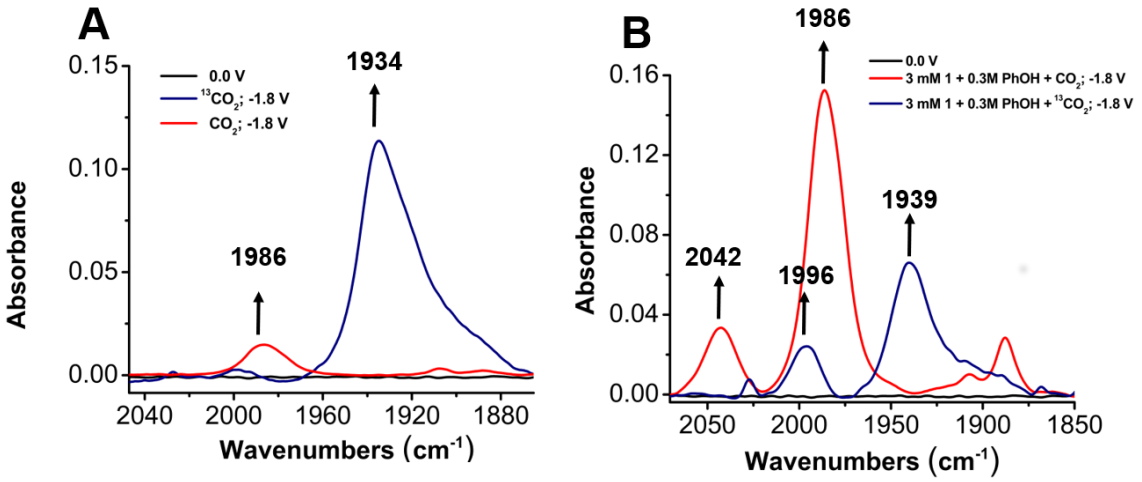

Figure SI 2.23. A comparison of the $[Ni(TPEN)(CO)]^+$ stretch with labeled CO_2 without **(A)** and with 0.3 M solution of PhOH **(B)**. Conditions: 3 mM solution of (**1**); $^{13}CO_2$ and CO_2 sparged for ~ 30s; 0.1 M $TBAPF_6$/MeCN; referenced to internal ferrocene standard.

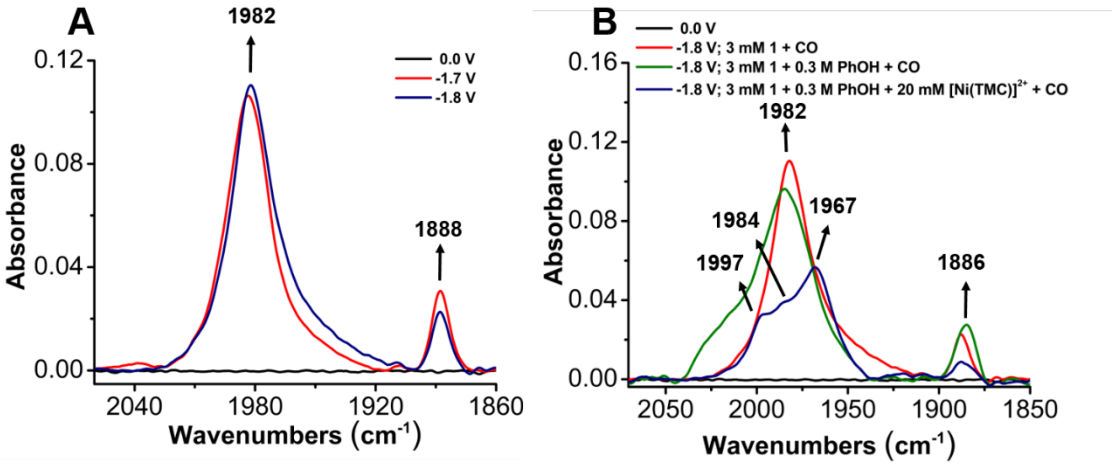

Figure SI 2.24. A) IR-SEC analysis of a 3 mM solution of (**1**) with CO sparged into solution for ~30 s. **B)** Different conditions with catalyst under CO. Ni–CO stretch from $[Ni(TMC)(CO)]^+$ grows in at 1967 cm^{-1} with a shoulder associated with Ni–CO stretch from $Ni(\kappa^4\text{-TPEN})(CO)]^+$ at 1984 cm^{-1}. Conditions: 0.1 M $TBAPF_6$/MeCN; referenced to internal ferrocene standard.

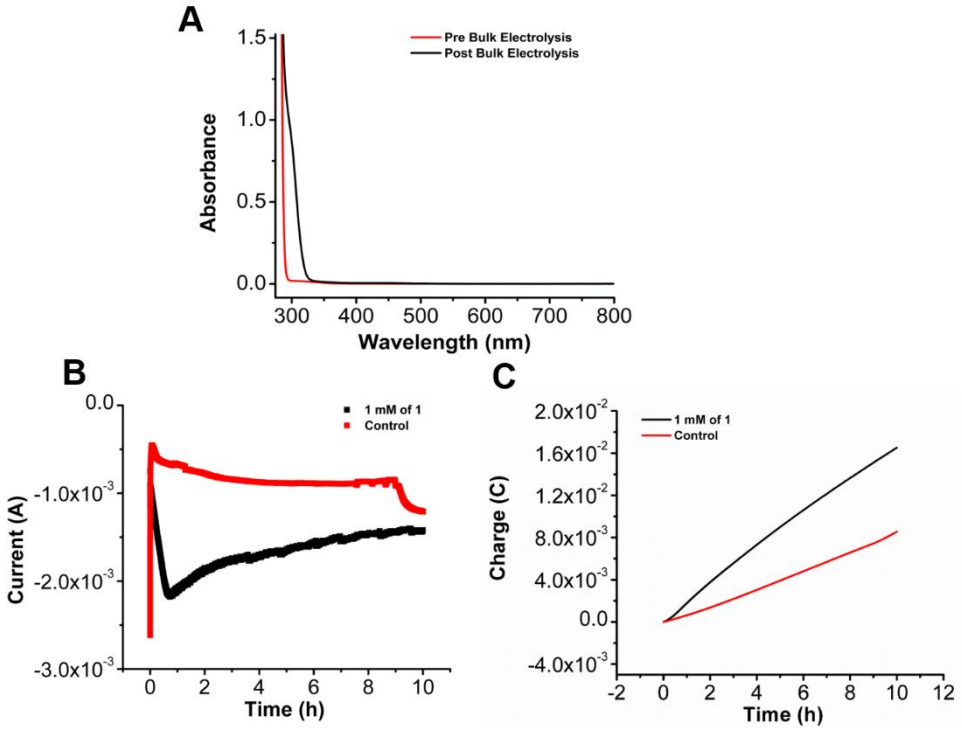

Figure SI 2.25. A) UV-Vis of the bulk solution before and after electrolysis. B) Current vs time plot of electrolysis experiment held at -2.05 V vs Fc^{+}/Fc. C) Charge passed during electrolysis experiment. Conditions: 1 mM of (**1**); 0.5 M PhOH; 0.1 M $TBAPF_6$/MeCN, graphite working electrode, graphite carbon counter electrode, Ag/AgCl pseudoreference electrode, and 0.5 M Fc was used as a sacrificial oxidant.

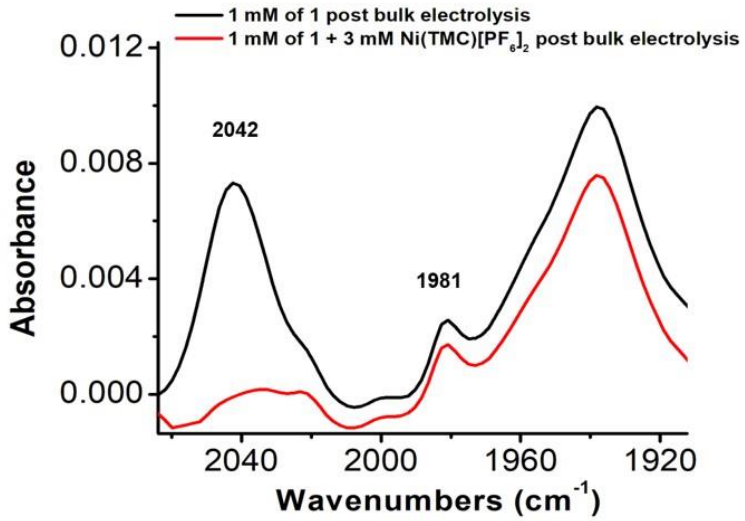

Figure SI 2.26. IR comparison between the post bulk electrolysis experiments of (**1**) with and without $[Ni(TMC)]^{2+}$. $Ni(CO)_4$ appears at 2042 cm^{-1} while the Ni–CO stretch is observed at 1981 cm^{-1} in both solutions.

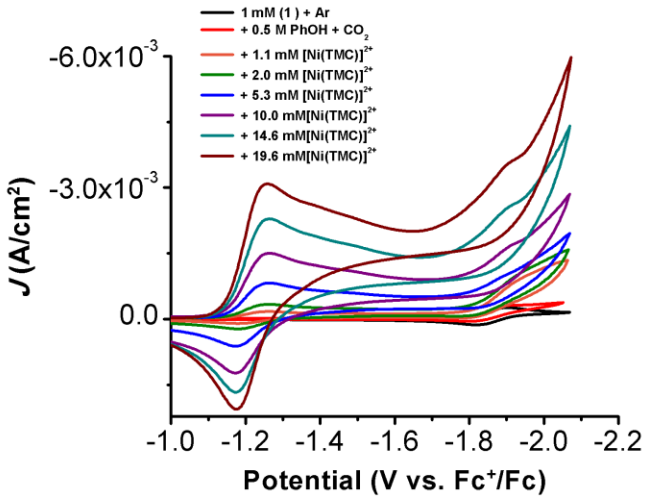

Figure SI 2.27. CVs of (**1**) at 1 mM, obtained under CO_2 saturation with 0.5 M PhOH and with $[Ni(TMC)]^{2+}$ titrations. Conditions: 1 mM analyte; 0.1 M $TBAPF_6$/MeCN glassy carbon working electrode, glassy carbon counter electrode, Ag/AgCl pseudoreference electrode; scan rate 100 mV/s; referenced to internal ferrocene standard.

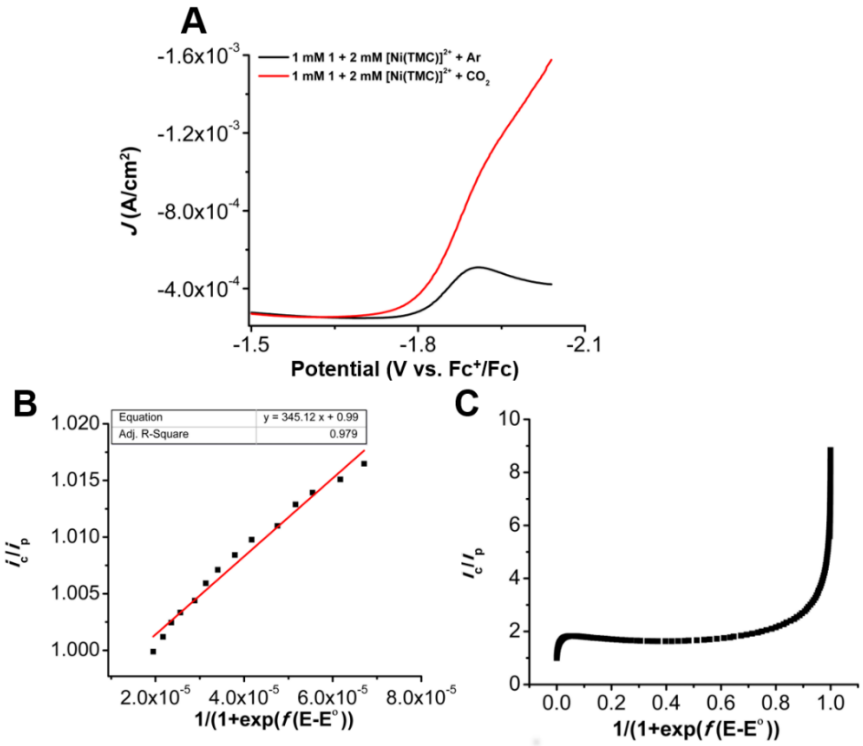

Figure SI 2.28. A.) CV overlay between catalytic current of (**1**) with 2 mM $[Ni(TMC)]^{2+}$ present under CO_2 with phenol (red trace) and under Ar (black trace) **B.)** Linear region from the FOWA. **C.)** Entire region of i_c/i_p vs $1/(1+\exp(f\,(E-E^o))$. Conditions: 1 mM (**1**), 2 mM $[Ni(TMC)]^{2+}$, 0.1 M $TBAPF_6$/MeCN, glassy carbon working electrode, glassy carbon counter electrode, Ag/AgCl pseudoreference electrode; scan rate 100 mV/s; referenced to internal ferrocene standard.

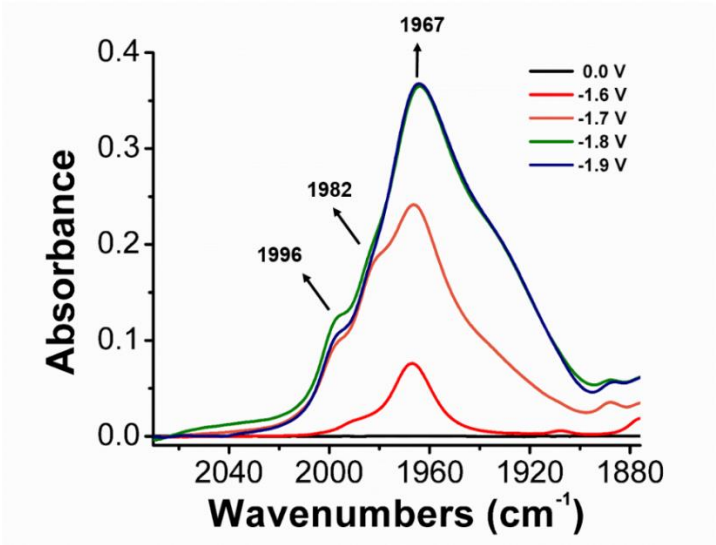

Figure SI 2.29. IR-SEC analysis of a 3 mM solution of (**1**) with CO_2 in a solution containing 20 mM of $[Ni(TMC)]^{2+}$. Ni–CO stretch from $[Ni(TMC)(CO)]^{+}$ grows in at 1967 cm^{-1} with a shoulder associated with Ni–CO stretch from $Ni(TPEN)(CO)]^{+}$ at 1982 cm^{-1}. Conditions: 0.1 M $TBAPF_6$/MeCN; referenced to internal ferrocene standard.

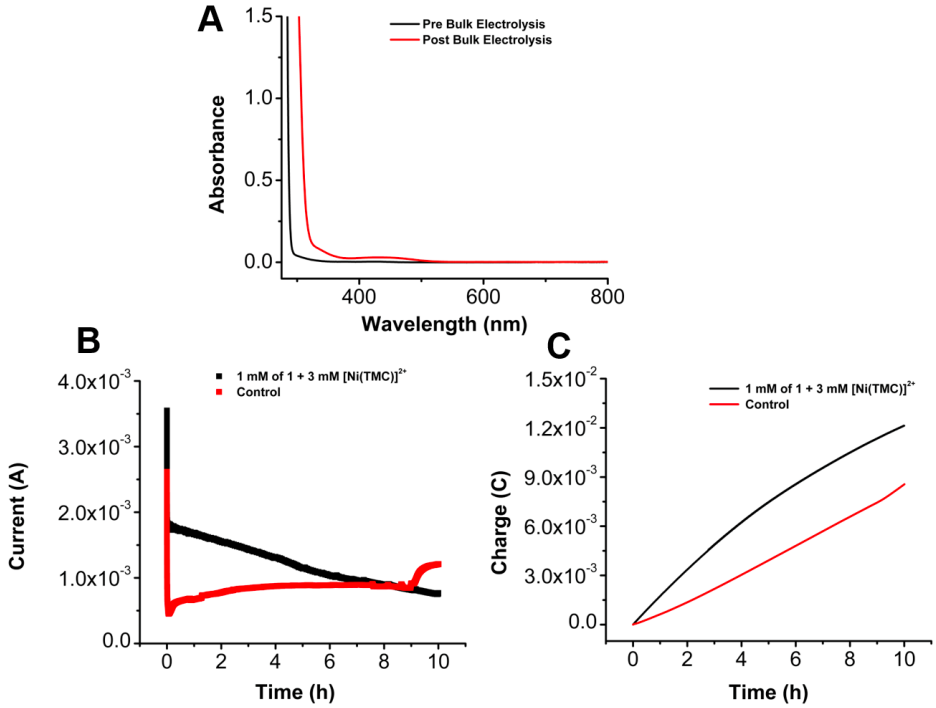

Figure SI 2.30. A) UV-Vis of the bulk solution before and after electrolysis. **B)** Current vs time plot of control electrolysis experiment held at −2.05 V vs Fc^{+}/Fc. **C)** Charge passed during control electrolysis experiment. Conditions: 1 mM of (**1**); 3 mM $[Ni(TMC)]^{2+}$; under Ar saturation conditions; 0.5 M PhOH; 0.1 M $TBAPF_6$/MeCN, graphite working electrode, graphite carbon counter electrode, Ag/AgCl pseudoreference electrode, and 0.5 M Fc was used as a sacrificial oxidant.

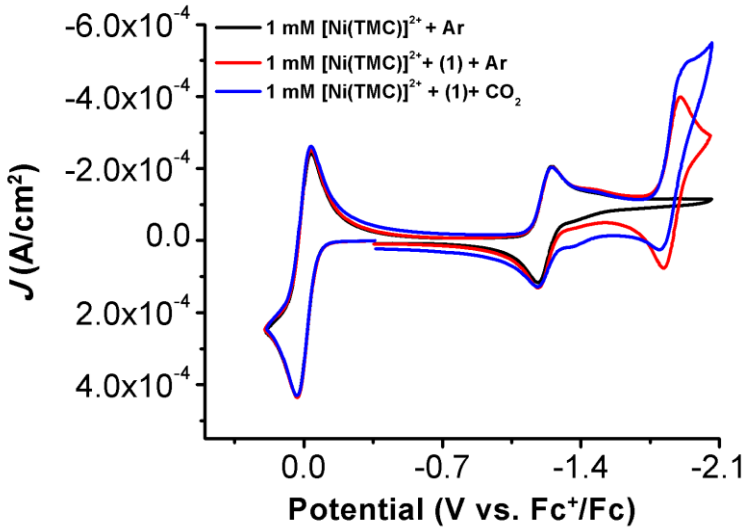

Figure SI 2.31. CVs of (**1**) obtained under Ar and then Ar and CO_2 upon the addition of 1 mM of $[Ni(TMC)]^{2+}$. Conditions: 0.1 M $TBAPF_6$/MeCN, glassy carbon working electrode, glassy carbon counter electrode, Ag/AgCl pseudoreference electrode; scan rate 100 mV/s; referenced to internal ferrocene standard.

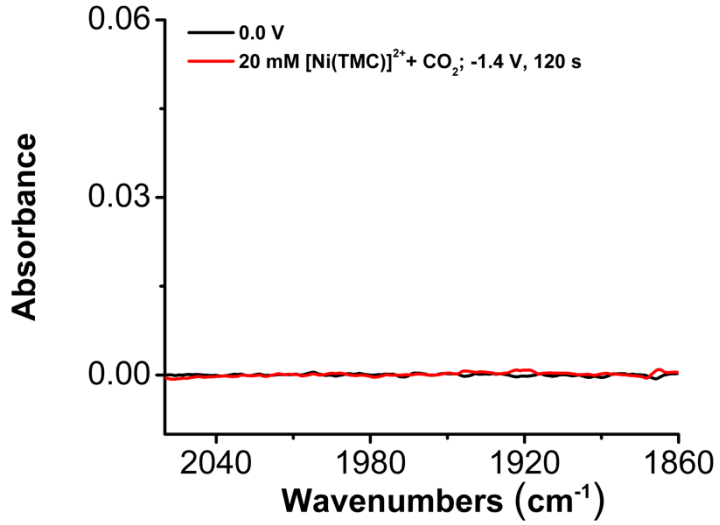

Figure SI 2.32. IR-SEC analysis of a 20 mM solution of $[Ni(TMC)]^{2+}$ with CO_2, without the addition of **(1)**. No carbonyl-containing species are observed. Conditions: 0.1 M $TBAPF_6$/MeCN; referenced to internal ferrocene standard.

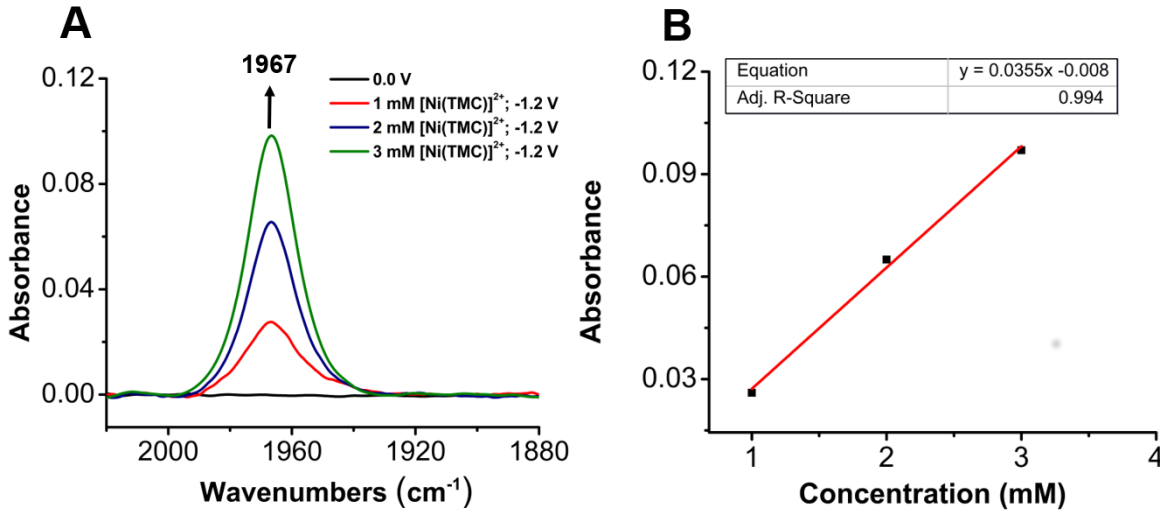

Figure SI 2.33. A) IR-SEC analysis of $[Ni(TMC)]^{2+}$ with CO sparged into solution for ~30 s to show the $[Ni(TMC)(CO)]^{+}$ stretch at 1967 cm^{-1}. Conditions: 0.1 M $TBAPF_6$/MeCN; referenced to internal ferrocene standard. **B)** Linear fit of $[Ni(TMC)(CO)]^{+}$ absorbance.

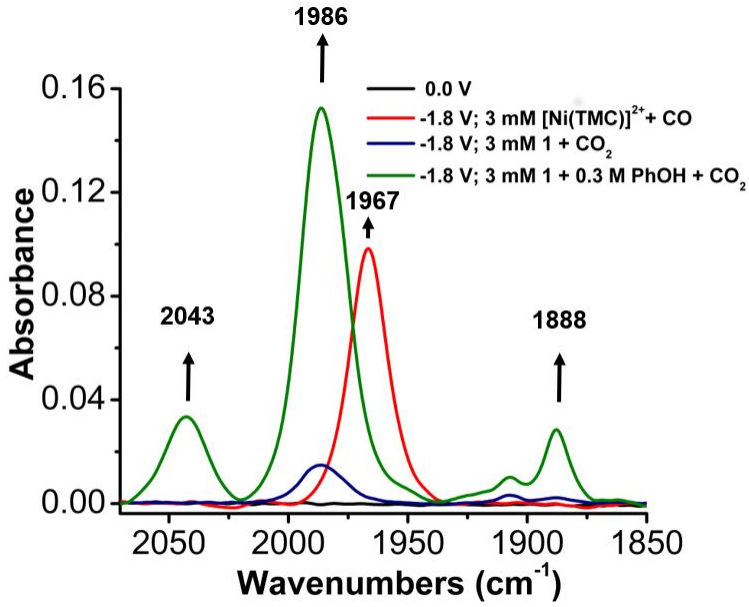

Figure SI 2.34 A comparison of the 3 mM solution of (**1**) with a 3 mM solution of $[Ni(TMC)]^{2+}$ to show the catalytic activity of $[Ni(TPEN)]^{2+}$.

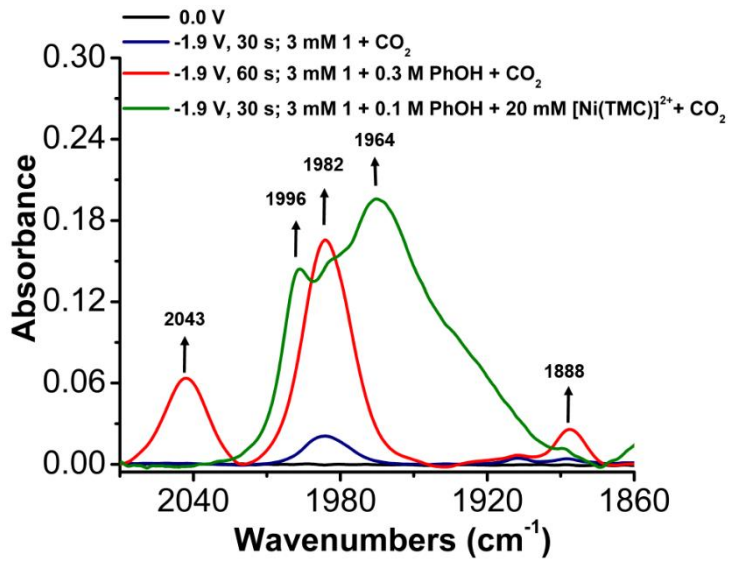

Figure SI 2.35. IR-SEC spectra overlaying of 3 mM **(1)** with the addition of 20 mM $[Ni(TMC)]^{2+}$ to show the loss of $Ni(CO)_4$ formation upon the addition of the CO scavenger. Timepoints: blue 60 s; red 30 s; green 60 s.

Table SI 2.1. The peak to peak separation as well as the peak current ratio for both **(1)** and the internal Fc^+/Fc reference at 100 mV/s.

Scan Rate (100mV/s)	i_{pa} **(*J*(A/cm^2)**	i_{pc} **(*J*(A/cm^2)**	E_{pa} **(V)**	E_{pc} **(V)**	$\|\Delta E\|$ **(V)**	$\|i_{pa}/i_{pc}\|$ **(*J*(A/cm^2)**
Fc^+/Fc	4.88×10^{-4}	-5.00×10^{-4}	0.035	−0.032	0.067	9.76×10^{-1}
(**1**)	2.06×10^{-4}	-2.23×10^{-4}	−1.82	−1.89	0.07	9.26×10^{-1}

2.5.8 Foot-of-the-Wave Analysis (FOWA) Calculations

FOWA provides an approximation of the true catalytic response by using the Tafel relationship of the initial part of the catalytic wave in order to avoid possible deviations caused by side products that form as the reaction progresses. To validate the use of FOWA, CV variable scan rate dependence studies (0.1-1.0 Vs^{-1}) with CO_2 saturation and 0.5 M PhOH did not locate steady state conditions in this regime (**Figures SI 2.18-2.20**).[3] By normalizing the catalytic current (i_c) to the non-Faradaic current (i_p) the following eqn is derived:

$$\frac{i_c}{i_p} = \frac{2.24 n_{cat}^{\sigma} \sqrt{\frac{RT}{F\nu} k_{obs} C_{substrate}}}{1 + \exp\left[\frac{F}{RT}(E - E^0)\right]}$$

where n_{cat}^{σ} = 2 , $\frac{RT}{F\nu}$ = 0.256796 s, $k_{obs} = k_{cat}$[catalyst]; $E^0 = E_{1/2}$(1 mM Ni(II)/Ni(I)) = −1.86 V vs Fc^+/Fc.

Table SI 2.2. FOWA analysis of **(1)** with PhOH titrations

Phenol Concentration (M)	**TOF_{max}** (s^{-1})	**[Ni(TPEN)]$^{2+}$** k_{cat} ($M^{-2}s^{-1}$)
0.24	2.18×10^2	3.24×10^3
0.5	2.67×10^2	3.97×10^3
0.75	4.02×10^3	6.00×10^4
1.0	3.60×10^4	5.36×10^5
1.48	1.02×10^5	1.51×10^6
1.98	3.70×10^5	5.51×10^6
2.49	7.72×10^8	1.15×10^{10}

Table SI 2.3. FOWA analysis of **(1)** with [Ni(TMC)]$^{2+}$ titrations at 0.5 M PhOH.

[Ni(TMC)]$^{2+}$ (mM)	**TOF_{max}** (s^{-1})	**[Ni(TPEN)]$^{2+}$** k_{cat} ($M^{-2}s^{-1}$)
1	7.96×10^5	4.02×10^9
2	2.31×10^4	1.17×10^8
5	2.74×10^4	1.39×10^8

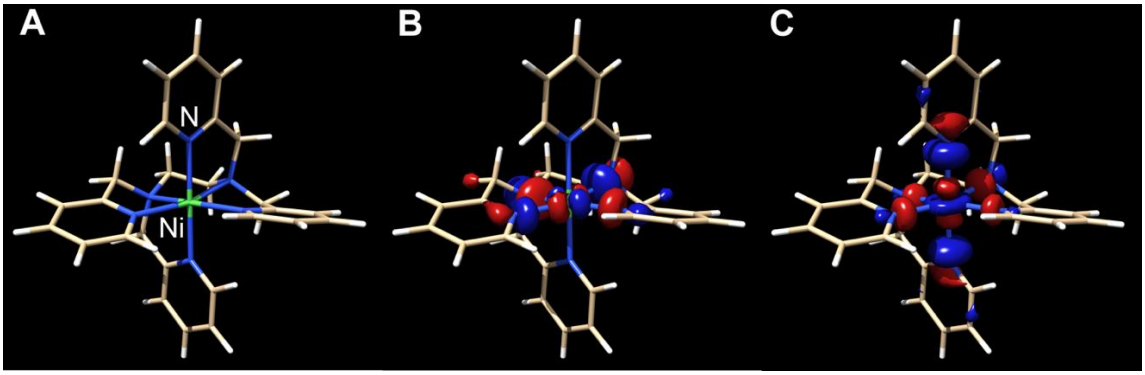

Figure SI 2.36. Kohn-Sham orbital representations of $[Ni(TPEN)]^{2+}$ (**1**) (A); SOMO-I (B); and SOMO-II (C). ORCA 4.0; B3LYP/G; ZORA; def2-TZVP; CPCM(Acetonitrile), 2S+1 = 3.

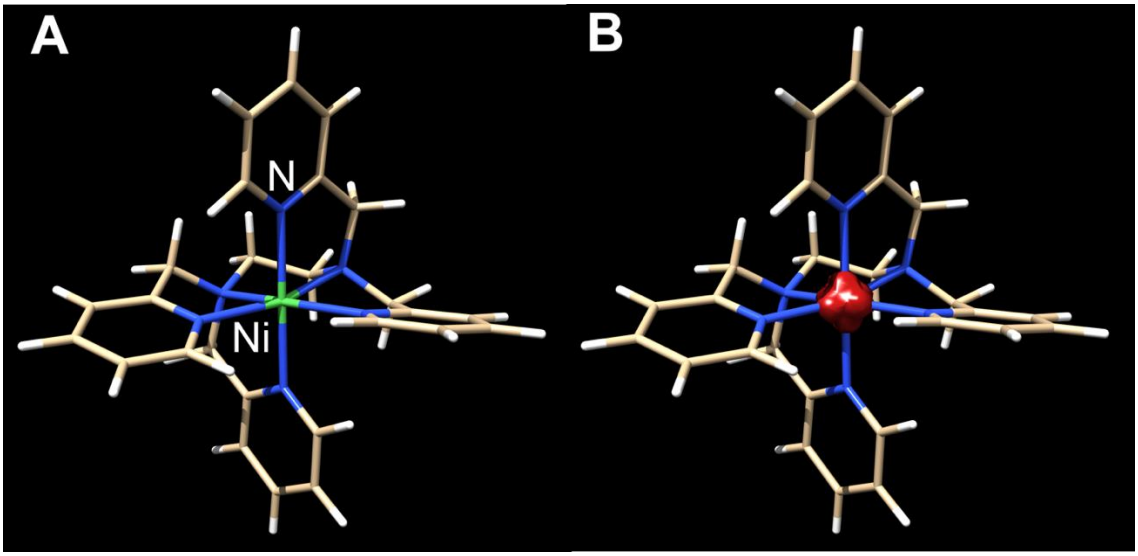

Figure SI 2.37. Calculated spin density localization of $[Ni(TPEN)]^{2+}$ (**1**). ORCA 4.0; B3LYP/G; def2-TZVP; CPCM(Acetonitrile), 2S+1 = 3.

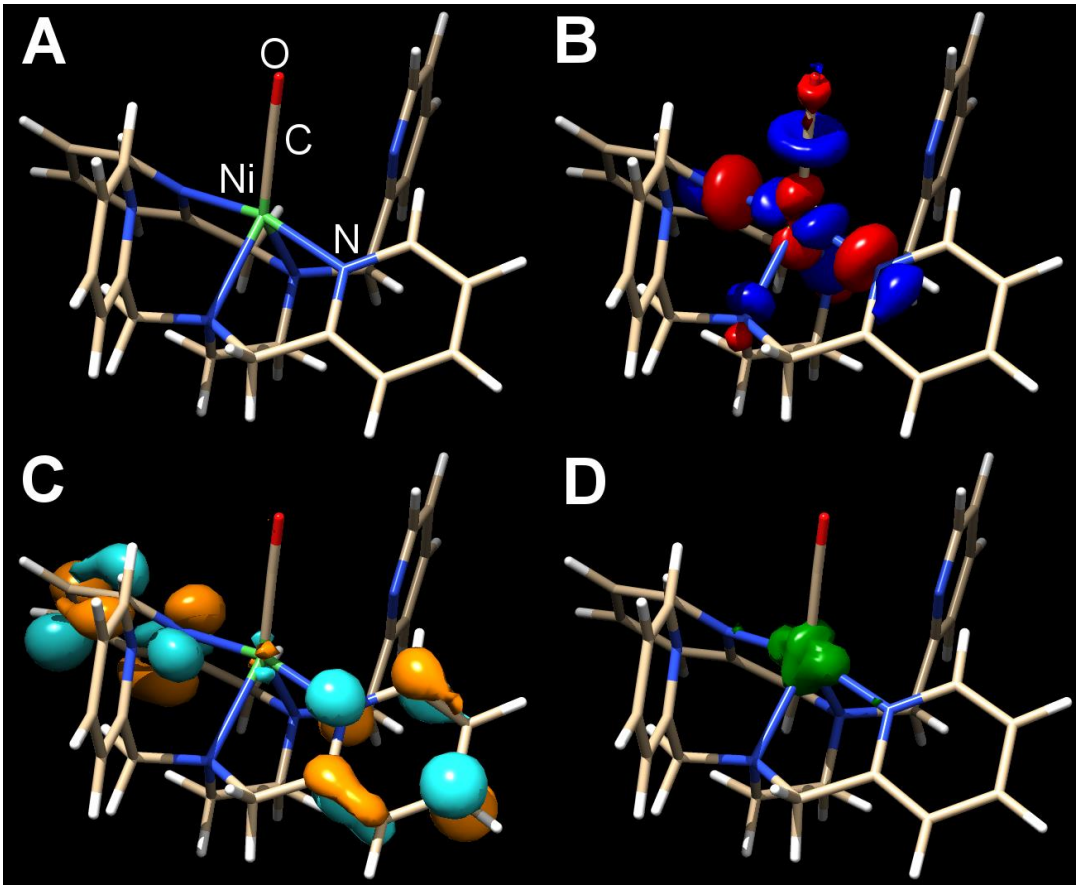

Figure SI 2.38. Kohn-Sham orbital representations of the SOMO (B) and LUMO (C) of $[Ni(TPEN)(CO)]^+$ 5 (A); spin density (D). ORCA 4.0; B3LYP/G; def2-TZVP; CPCM(Acetonitrile), 2S+1 = 2.

Table SI 2.4. Crystal data and structure refinement for machan02q.
CCDC 1816890

Identification code	CWM-002	
Empirical formula	C26 H28 F12 N6 Ni P2	
Formula weight	773.19	
Temperature	100.0 K	
Wavelength	0.71073 Å	
Crystal system	Monoclinic	
Space group	P 21/n	
Unit cell dimensions	a = 13.8699(6) Å	α = 90°.
	b = 17.1455(7) Å	β = 100.970(2)°.
	c = 14.2982(8)	γ = 90°.
Volume	3338.1(3) $Å^3$	
Z	4	
Density (calculated)	1.539 Mg/m^3	
Absorption coefficient	0.772 mm^{-1}	
F(000)	1568	

Crystal size	0.26 x 0.15 x 0.1 mm^3
Theta range for data collection	2.565 to 26.027°.
Index ranges	-11<=h<=17, -21<=k<=20, -17<=l<=12
Reflections collected	15877
Independent reflections	6314 [R(int) = 0.0550]
Completeness to theta = 25.242°	96.1 %
Absorption correction	Semi-empirical from equivalents
Max. and min. transmission	0.4293 and 0.3852
Refinement method	Full-matrix least-squares on F^2
Data / restraints / parameters	6314 / 0 / 424
Goodness-of-fit on F^2	1.011
Final R indices [I>2sigma(I)]	R1 = 0.0471, wR2 = 0.0906
R indices (all data)	R1 = 0.0902, wR2 = 0.1046
Extinction coefficient	n/a
Largest diff. peak and hole	0.516 and -0.424 e.$Å^{-3}$
SQUEEZE	154e/unit cell (roughly four hexane)

Geometry-Optimized DFT Coordinates

$[Ni(\kappa^6\text{-TPEN})]^{2+}$; 2S+1=3

Ni	6.271361	12.877217	12.070347
N	4.546489	11.748955	11.624644
N	7.936293	14.087427	12.527486
N	5.058258	13.480623	13.715087
N	7.024973	12.616755	10.126526
C	6.535656	11.845593	14.750365
N	6.833099	11.444606	13.501538
C	3.576296	11.831845	12.538833
N	5.618725	14.697368	11.155956
C	6.406484	13.416597	9.239812
C	5.907552	13.213023	14.886690
H	5.349323	13.281472	15.823029
H	6.692694	13.968886	14.918500
C	5.297967	14.290995	9.778850
H	5.142508	15.150513	9.123087
H	4.368197	13.722437	9.797535
C	7.900229	15.314867	12.002038
C	3.819018	12.675347	13.761941
H	2.958269	13.324167	13.932900
H	3.864995	12.003809	14.620573
C	9.017743	13.702631	13.221490
H	9.002092	12.699586	13.619779
C	8.011045	11.815257	9.715605
H	8.488527	11.207445	10.472294
C	4.460657	15.107491	11.977819
H	3.608520	14.492736	11.693341
H	4.191151	16.149349	11.789786
C	8.417213	11.759507	8.393091
H	9.219919	11.097748	8.101392
C	4.784874	14.910118	13.453637
H	5.672241	15.480456	13.725282
H	3.959857	15.273811	14.070922
C	6.702182	15.703772	11.177287
H	6.314867	16.659921	11.534054
H	7.044122	15.880644	10.156783
C	2.383279	11.130242	12.402149
H	1.615355	11.227172	13.157743
C	4.375841	10.952721	10.559385
H	5.191496	10.911660	9.852024
C	7.394720	10.248139	13.308788
H	7.597290	9.967393	12.284144
C	6.808396	11.045282	15.848836
H	6.547165	11.387638	16.840315
C	3.224207	10.217993	10.358707
H	3.130969	9.589368	9.484939
C	6.763936	13.420503	7.900419
H	6.257644	14.082718	7.211899
C	7.704542	9.399007	14.357726
H	8.159670	8.439790	14.159227
C	7.408749	9.808994	15.651119
H	7.631720	9.170171	16.494747
C	2.203276	10.314367	11.299258
H	1.283476	9.759379	11.174035
C	8.949450	16.212301	12.173973
H	8.884387	17.201677	11.742847
C	7.777435	12.575479	7.469279
H	8.072253	12.563805	6.428770
C	10.101926	14.532456	13.426588
H	10.952441	14.179189	13.991381
C	10.063463	15.817502	12.894195
H	10.891159	16.498708	13.038750

$[Ni(\kappa^5\text{-TPEN})]^+$; 2S+1=2

Ni	6.498403	12.830453	12.138965
N	4.779259	11.681902	11.833517
N	8.131724	13.971546	12.345123
N	5.026442	13.663898	13.802202
N	6.780289	12.497202	9.102165
C	6.392302	11.997532	14.954334
N	6.900211	11.562878	13.788527
C	3.813609	11.734480	12.758405
N	5.773472	14.606858	11.017891
C	6.298621	13.697707	8.761356
C	5.841937	13.407138	14.975108
H	5.298063	13.564475	15.915899
H	6.680947	14.106113	14.963860
C	5.254938	14.297484	9.666689
H	4.841067	15.196920	9.196696
H	4.444847	13.580913	9.796498
C	8.010086	15.244017	11.927687
C	3.799992	12.889507	13.746113
H	2.963656	13.540639	13.476973
H	3.554091	12.492016	14.735126
C	9.169738	13.661847	13.143815
C	7.720005	11.948849	8.333776
H	8.084334	10.975020	8.642128
C	4.665175	15.122519	11.851073
H	3.780032	14.533299	11.612826
H	4.440029	16.161237	11.580918
C	8.224510	12.557747	7.189704
H	8.989629	12.068675	6.602352
C	4.922775	15.044128	13.351952
H	5.853231	15.554358	13.602070
H	4.114879	15.587747	13.861264
C	6.897287	15.554525	10.961550
H	6.556220	16.583863	11.109851
H	7.333364	15.518926	9.962572
C	2.806738	10.774710	12.815549
H	2.044702	10.844316	13.581382
C	4.759607	10.690254	10.930272
C	7.395730	10.323970	13.720540
C	6.365889	11.188817	16.082491
H	5.933875	11.564696	16.999847
C	3.792498	9.700944	10.923720
C	6.736842	14.374668	7.626548
C	7.406612	9.457452	14.803552
C	6.880621	9.900726	16.009249
C	2.795348	9.742519	11.892148
C	8.904506	16.234631	12.314413
H	8.756657	17.249010	11.968569
C	7.714619	13.795822	6.826875
C	10.106862	14.589581	13.557753
C	9.970891	15.909695	13.139354
H	8.072703	14.305205	5.942067
H	6.322001	15.343042	7.381318
H	9.227701	12.632115	13.464528
H	10.676090	16.667421	13.453091
H	10.919834	14.282204	14.200860
H	7.812591	8.461554	14.696671
H	6.860492	9.252918	16.875622
H	7.791257	10.020003	12.759881
H	5.549988	10.724976	10.193507
H	3.823092	8.917869	10.178457
H	2.024007	8.983956	11.925911

$[Ni(\kappa^5\text{-TPEN})(CO_2)]^+$; 2S+1=2

Ni	6.651240	12.675429	12.287086
N	5.006555	11.488279	11.828454
N	8.074521	14.085183	12.746304
N	5.250869	13.482674	13.772450
N	6.154596	12.223867	8.550470
C	6.556162	11.967004	15.161011
N	7.069067	11.462233	14.025737
C	3.894818	11.785604	12.517488
N	5.868106	14.376693	11.044059
C	6.124314	13.555880	8.641062
C	5.924525	13.330799	15.065960
H	5.242075	13.490372	15.905253
H	6.703498	14.090897	15.135244
C	5.238747	14.138491	9.708197
H	4.825373	15.087520	9.350582
H	4.413266	13.451088	9.873179
C	7.980223	15.234278	12.066394
C	4.009896	12.693254	13.714629
H	3.136264	13.346734	13.768191
H	3.963137	12.054386	14.598336
C	9.012716	13.956323	13.692328
C	6.913952	11.666494	7.609032
H	6.915583	10.581988	7.572558
C	4.793233	14.970624	11.888383
H	3.873422	14.434027	11.660225
H	4.631769	16.014660	11.604034
C	7.672941	12.401218	6.706965
H	8.274005	11.898867	5.961234
C	5.057158	14.884017	13.376531
H	5.947807	15.443250	13.652231
H	4.213368	15.336156	13.908992
C	7.011641	15.295150	10.920679
H	6.673642	16.324181	10.766962
H	7.580921	15.000265	10.040948
C	2.666720	11.215992	12.204790
H	1.789009	11.496089	12.770828
C	4.936667	10.575306	10.849776
C	7.646515	10.256883	14.053628
C	6.614463	11.272606	16.360422
H	6.177930	11.703904	17.250494
C	3.754748	9.946815	10.501123
C	6.830351	14.372406	7.760213
C	7.747786	9.507032	15.215268
C	7.223414	10.025727	16.390801
C	2.592410	10.285875	11.180744
C	8.813718	16.310831	12.346086
H	8.700131	17.232356	11.792242
C	7.621928	13.786238	6.782383
C	9.889524	14.976007	14.012625
C	9.780879	16.181961	13.329514
C	8.045688	11.838936	10.917955
O	8.023349	10.624314	11.013539
O	8.642920	12.700869	10.307075
H	8.183821	14.399795	6.090323
H	6.755909	15.448950	7.837450
H	9.051212	13.005119	14.201938
H	10.439961	17.008146	13.560055
H	10.632078	14.826135	14.783191
H	8.221518	8.536314	15.190101
H	7.275885	9.465202	17.314525
H	8.025869	9.898217	13.108368
H	5.858095	10.361017	10.339625
H	3.750312	9.217652	9.703273
H	1.646631	9.829020	10.922196

$[Ni(\kappa^5\text{-TPEN})(CO_2H)]^+$; 2S+1=3

Ni	6.719180	12.560728	12.224117
N	4.932973	11.424931	11.818142
N	8.112603	14.148695	12.757103
N	5.271604	13.425537	13.768801
N	6.088724	12.223591	8.546930
C	6.586222	11.907447	15.173465
N	7.119290	11.399198	14.052880
C	3.840929	11.788348	12.499591
N	5.872136	14.391102	11.026507
C	6.112858	13.555641	8.637482
C	5.944456	13.267489	15.063029
H	5.260126	13.428285	15.901076
H	6.722762	14.027859	15.135227
C	5.237478	14.173582	9.694441
H	4.855110	15.133570	9.328424
H	4.390978	13.511043	9.855463
C	7.973987	15.285681	12.068729
C	4.018030	12.653047	13.722507
H	3.155823	13.314503	13.835366
H	3.998462	11.980474	14.582261
C	9.032831	14.070438	13.722294
C	6.836076	11.634353	7.615865
H	6.792910	10.550627	7.580185
C	4.819447	14.966383	11.901140
H	3.889566	14.450477	11.665411
H	4.666214	16.023650	11.658980
C	7.637030	12.335305	6.723636
H	8.225597	11.807633	5.985445
C	5.088982	14.833739	13.387822
H	5.982691	15.381542	13.673394
H	4.248562	15.281995	13.929779
C	7.030485	15.287975	10.898544
H	6.711490	16.312373	10.678928
H	7.619857	14.938675	10.050474
C	2.579269	11.315864	12.157179
H	1.712814	11.645337	12.714177
C	4.820023	10.550015	10.812272
C	7.726827	10.210331	14.092154
C	6.649133	11.224854	16.380605
H	6.198588	11.654168	17.264741
C	3.602329	10.012457	10.433096
C	6.865421	14.341189	7.765793
C	7.835107	9.472884	15.261029
C	7.285177	9.991912	16.425875
C	2.457906	10.416186	11.109112
C	8.746415	16.405693	12.358422
H	8.600322	17.318162	11.797145
C	7.643537	13.721454	6.798082
C	9.850150	15.135344	14.059185
C	9.695119	16.330373	13.366021
C	8.081565	11.783654	10.904251
O	8.089254	10.404827	10.748888
O	8.924024	12.404655	10.273540
H	8.239232	14.310514	6.113001
H	6.835401	15.420011	7.841829
H	9.106689	13.122835	14.238018
H	10.304447	17.190942	13.607803
H	10.580485	15.028960	14.848608
H	8.331898	8.513462	15.251280
H	7.341656	9.441333	17.355362
H	8.125980	9.851407	13.153086
H	5.736009	10.295938	10.305670
H	3.555059	9.306507	9.615931
H	1.486263	10.033287	10.826925
H	8.796432	10.186530	10.111160

Ni(κ^5-TPEN)(CO)]$^+$; 2S+1=2

Ni	6.709516	12.554690	11.854048
N	4.903527	11.515842	11.580364
N	8.138192	14.022629	12.305718
N	5.501650	13.244079	13.679174
N	6.627046	12.549895	8.584806
C	6.728044	11.940737	15.423525
N	7.704959	11.377684	14.704833
C	3.948905	11.678901	12.501354
N	5.763633	14.406812	10.903894
C	6.146113	13.795163	8.508895
C	6.229540	13.287348	14.969032
H	5.587502	13.715429	15.747850
H	7.078608	13.954964	14.835667
C	5.156506	14.214314	9.564670
H	4.655563	15.135790	9.245891
H	4.397005	13.441389	9.666565
C	7.919995	15.257172	11.843463
C	4.322333	12.372516	13.781647
H	3.458604	12.921575	14.171762
H	4.538576	11.584517	14.503385
C	9.180222	13.801807	13.119627
C	7.521246	12.155267	7.680526
H	7.890258	11.140294	7.780535
C	4.692775	14.754011	11.859440
H	3.844381	14.102431	11.659055
H	4.351122	15.782384	11.690309
C	7.976279	12.971128	6.650661
H	8.705537	12.601940	5.942363
C	5.119210	14.621679	13.308755
H	5.971257	15.268722	13.507952
H	4.297939	14.973472	13.945341
C	6.799207	15.449066	10.859065
H	6.362854	16.445889	10.983471
H	7.257792	15.434328	9.870141
C	2.666714	11.167928	12.325205
H	1.915062	11.334223	13.085163
C	4.623974	10.821720	10.468176
C	8.155733	10.179691	15.072393
C	6.187886	11.321656	16.547997
H	5.400841	11.809329	17.107178
C	3.379359	10.267712	10.229222
C	6.535520	14.675847	7.502735
C	7.670500	9.485989	16.175608
C	6.668102	10.075958	16.931802
C	2.377221	10.450826	11.176114
C	8.737474	16.324763	12.201465
H	8.523152	17.314435	11.822000
C	7.464660	14.257610	6.558376
C	10.045760	14.808148	13.507736
C	9.815608	16.098261	13.041176
C	7.869607	11.276959	11.292266
O	8.636975	10.512763	10.920372
H	7.784796	14.926222	5.770140
H	6.120662	15.674076	7.467621
H	9.279990	12.789886	13.484293
H	10.463898	16.914215	13.331398
H	10.872025	14.585575	14.168057
H	8.073071	8.515933	16.431749
H	6.263336	9.576401	17.801916
H	8.945483	9.755280	14.461607
H	5.425087	10.753711	9.746280
H	3.199698	9.716600	9.317066
H	1.387409	10.043707	11.019303

IR Frequencies Calibration: 2077 cm^{-1} by calculation, 2043 cm^{-1} by experiment, 0.983

$[Ni(CO)_4]^0$; 2S+1=1

Ni	-6.263080	7.635617	-0.398814
O	-6.238815	6.641085	-3.200318
O	-9.015277	8.467393	0.356204
O	-4.466348	9.989314	-0.124617
O	-5.346613	5.462036	1.410211
C	-6.247694	7.023147	-2.131169
C	-7.965909	8.146801	0.065024
C	-5.149117	9.088720	-0.232440
C	-5.698459	6.293252	0.721472

2.6. References

1. Fisher, B. J.; Eisenberg, R., *J. Am. Chem. Soc.* **1980,** *102*, 7361.
2. Roy, S.; Sharma, B.; Pécaut, J.; Simon, P.; Fontecave, M.; Tran, P. D.; Derat, E.; Artero, V., *J. Am. Chem. Soc.* **2017,** *139*, 3685.
3. Ngo, K. T.; McKinnon, M.; Mahanti, B.; Narayanan, R.; Grills, D. C.; Ertem, M. Z.; Rochford, J., *J. Am. Chem. Soc.* **2017,** *139*, 2604.
4. Chan, S. L.-F.; Lam, T. L.; Yang, C.; Yan, S.-C.; Cheng, N. M., *Chem. Commun.* **2015,** *51*, 7799.
5. Chapovetsky, A.; Do, T. H.; Haiges, R.; Takase, M. K.; Marinescu, S. C., *J. Am. Chem. Soc.* **2016,** *138*, 5765.
6. Elgrishi, N.; Chambers, M. B.; Fontecave, M., *Chem. Sci.* **2015,** *6*, 2522.
7. Haines, R. J.; Wittrig, R. E.; Kubiak, C. P., *Inorg. Chem.* **1994,** *33*, 4723.
8. Machan, C. W.; Kubiak, C. P., *Dalton Trans.* **2016,** *45*, 17179.
9. Rakowski Dubois, M.; Dubois, D. L., *Acc. Chem. Res.* **2009,** *42*, 1974.
10. Khnayzer, R. S.; Thoi, V. S.; Nippe, M.; King, A. E.; Jurss, J. W.; El Roz, K. A.; Long, J. R.; Chang, C. J.; Castellano, F. N., *Energy Environ. Sci.* **2014,** *7*, 1477.

11. Elgrishi, N.; Chambers, M. B.; Wang, X.; Fontecave, M., *Chem. Soc. Rev.* **2017,** *46*, 761.

12. Ammon, U.; Chiorboli, C.; Dümler, W.; Grampp, G.; Scandola, F.; Kisch, H., *J. Phys. Chem. A* **1997,** *101*, 6876.

13. Bourrez, M.; Molton, F.; Chardon-Noblat, S.; Deronzier, A., *Angew. Chem. Int. Ed.* **2011,** *50*, 9903.

14. Machan, C. W.; Chabolla, S. A.; Yin, J.; Gilson, M. K.; Tezcan, F. A.; Kubiak, C. P., *J. Am. Chem. Soc.* **2014,** *136*, 14598.

15. Sullivan, B. P.; Bolinger, C. M.; Conrad, D.; Vining, W. J.; Meyer, T. J., *J. Chem. Soc., Chem. Commun.* **1985**, 1414.

16. Bruce, M. R. M.; Megehee, E.; Sullivan, B. P.; Thorp, H. H.; O'Toole, T. R.; Downard, A.; Pugh, J. R.; Meyer, T. J., *Inorg. Chem.* **1992,** *31*, 4864.

17. Elgrishi, N.; Chambers, M. B.; Artero, V.; Fontecave, M., *Phys. Chem. Chem. Phy.* **2014,** *16*, 13635.

18. Ishida, H.; Tanaka, H.; Tanaka, K.; Tanaka, T., *J. Chem. Soc., Chem. Comm.* **1987**, 131.

19. Smieja, J. M.; Kubiak, C. P., *Inorg. Chem.* **2010,** *49*, 9283.

20. Wong, K.-Y.; Chung, W.-H.; Lau, C.-P., *J. Electroanal. Chem.* **1998,** *453*, 161.

21. Blindauer, C. A.; Razi, M. T.; Parsons, S.; Sadler, P. J., *Polyhedron* **2006,** *25*, 513.

22. Froehlich, J. D.; Kubiak, C. P., *J. Am. Chem. Soc.* **2015,** *137*, 3565.

23. Bain, G. A.; Berry, J. F., *J. Chem. Ed.* **2008,** *85*, 532.

24. Piguet, C., *J. Chem. Ed.* **1997,** *74*, 815.

25. Elgrishi, N.; Rountree, K. J.; McCarthy, B. D.; Rountree, E. S.; Eisenhart, T. T.; Dempsey, J. L., *J. Chem. Ed.* **2018,** *95*, 197.

26. Gennaro, A.; Isse, A. A.; Vianello, E., *J. Electroanal. Chem. Interfacial Electrochem.* **1990,** *289*, 203.

27. Bhugun, I.; Lexa, D.; Savéant, J.-M., *J. Am. Chem. Soc.* **1996,** *118*, 1769.

28. Appel, A. M.; Helm, M. L., *ACS Catal.* **2014,** *4*, 630.

29. Horvath, S.; Fernandez, L. E.; Appel, A. M.; Hammes-Schiffer, S., *Inorg. Chem.* **2013,** *52*, 3643.

30. Machan, C. W.; Sampson, M. D.; Kubiak, C. P., *J. Am. Chem. Soc.* **2015,** *137*, 8564.

31. McCarthy, B. D.; Dempsey, J. L., *Inorg. Chem.* **2017,** *56*, 1225.

32. Solis, B. H.; Hammes-Schiffer, S., *Inorg. Chem.* **2014,** *53*, 6427.

33. Sathrum, A. J.; Kubiak, C. P., *J. Phys. Chem. Lett.* **2011,** *2*, 2372.

34. Franco, F.; Pinto, M. F.; Royo, B.; Lloret-Fillol, J., *Angew. Chem. Int. Ed.* **2018,** *57*, 4603.

35. Costentin, C.; Drouet, S.; Robert, M.; Savéant, J.-M., *J. Am. Chem. Soc.* **2012,** *134*, 11235.

36. Machan, C. W.; Sampson, M. D.; Chabolla, S. A.; Dang, T.; Kubiak, C. P., *Organometallics* **2014,** *33*, 4550.

37. Zavarine, I. S.; Kubiak, C. P., *J. Electroanal. Chem.* **2001,** *495*, 106.

38. Nichols, A. W.; Chatterjee, S.; Sabat, M.; Machan, C. W., *Inorg. Chem.* **2018,** *57*, 2111.

39. Balazs, G. B.; Anson, F. C., *J. Electroanal. Chem.* **1993,** *361*, 149.

40. Harris, D. C., *Quantitative Chemical Analysis*. seventh ed.; W. H. Freeman and Company: New York, 2007.

41. Atkins, P. D. P., J.; Friedman, R. , *Quanta matter, and change: a molecular approach to physical chemistry*. Oxford University Press: 2009.

42. Mandel, J. B.; Maricondi, C.; Douglas, B. E., *Inorg. Chem.* **1988,** *27*, 2990.

43. Barefield, E. K.; Wagner, F., *Inorg. Chem.* **1973,** *12*, 2435.

44. Evangelio, E.; Rath, N. P.; Mirica, L. M., *Dalton Trans.* **2012,** *41*, 8010.

45. Bosnich, B.; Tobe, M. L.; Webb, G. A., *Inorg. Chem.* **1965,** *4*, 1109.

46. Cheng, S.C.; Blaine, C.A.; Hill, M.G.; Mann, K.R., *Inorg. Chem.* **1996,** *35*, 7704.

CHAPTER 3

Metal-Free Electrochemical Reduction of Carbon Dioxide Mediated by Cyclic(Alkyl)(Amino) Carbenes

Published as "Lieske, L.E; Freeman, L.A.; Wang, G.; Dickie, D.A.; Gilliard, R.J.; Machan, C.W. *Chem. Eur. J.* **2019,** *25,* 6098."

*Equal contribution between Lieske, L.E and Freeman, L.A.

Lieske, L.E. co-wrote this paper and conducted all electrochemical experiments

3.1 Abstract

Carbenes are known to activate carbon dioxide to form zwitterionic adducts. Their inherent metal-free redox activity remains understudied. Herein, we demonstrate that zwitterionic adducts of carbon dioxide formed with cyclic(alkyl)(amino) carbenes are not only redox active, but they can mediate the stoichiometric reductive disproportionation of carbon dioxide to carbon monoxide and carbonate. Infrared spectroelectrochemical experiments show that the reaction proceeds through an intermediate radical anion formed by one-electron reduction, ultimately generating a ketene product and carbonate in the absence of additional organic or inorganic reagents.

3.2 Introduction

Carbenes, particularly cyclic(alkyl)(amino) carbenes (CAACs), have unique reactivity with transition metals, organic small molecules and main group elements.[1-10] These properties have been harnessed to stabilize low-coordinate organic and inorganic species, and mediate organocatalytic transformations.[7-8, 11] While both N-heterocyclic carbenes (NHCs) and cyclic(alkyl)(amino)carbenes (CAACs) are known to stabilize carbon dioxide (CO_2) adducts as a zwitterion, only the more nucleophilic and electrophilic CAAC forms a ketene species with carbon monoxide (CO).[12-13] Previous reports have demonstrated that NHC–CO_2 complexes can act as a source of activated CO_2 for electrocatalytic reduction by transition metal compounds.[14] Additionally, NHC–CO_2 adducts can participate in organically mediated transformations of CO_2 to form methanol equivalents, further hinting at the potential utility of these molecules for CO_2 reduction chemistry.[15] Roesky et al. treated a Zn biradicaloid with CO_2 to form CAAC–CO_2 and Zn metal, however, the reactivity of the adduct toward reduction was not investigated.[16] Based

on these precedents, we were interested in examining the electrochemical behavior of CAAC–CO_2 adducts. Herein, we describe the synthesis, molecular structure, and electrochemical behavior of ^{Cy}CAAC–CO_2 adduct (**1**). Notably, compound **1** demonstrates reversible one-electron redox properties at $E_{1/2} = -2.15$ V versus Fc^+/Fc under Ar saturation conditions and can mediate the stoichiometric reductive disproportionation to CO and carbonate (CO_3^{2-}) under CO_2 saturation *without any additional organic or inorganic reagents*.

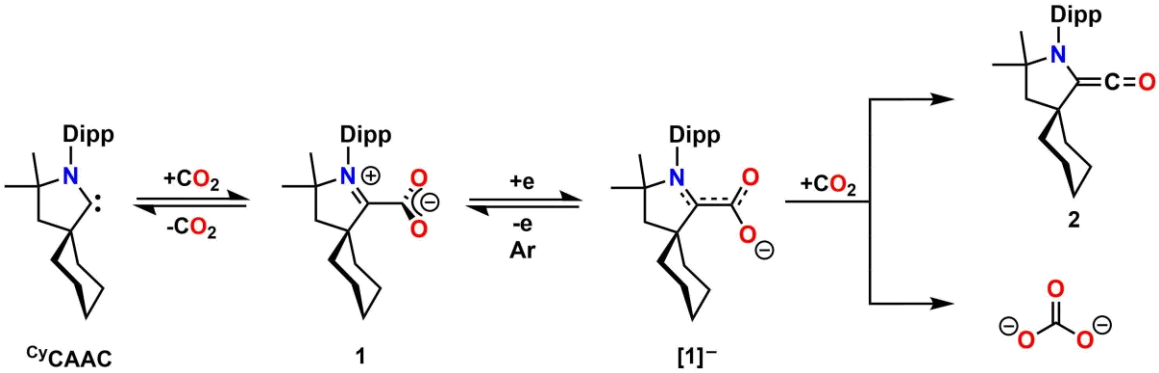

Figure 3.1. Complexes observed and the proposed electrochemical reaction pathway.

3.3 Results and Discussion

Bubbling CO_2 through a solution of ^{Cy}CAAC[9] in anhydrous THF or Et_2O resulted in immediate precipitation of a white solid which was isolated via filtration and determined to be the zwitterionic CO_2 adduct, compound **1** (**Figure 3.1**). Characterization by ^{1}H and ^{13}C NMR spectroscopy (**Figure SI 3.2 and SI 3.3**) was consistent with the molecular structure in **Figure 3.2**. Colorless block-shaped crystals of **1** suitable for a single crystal X-ray diffraction study were grown from a saturated THF solution at −37 °C (**Figure 3.2**).

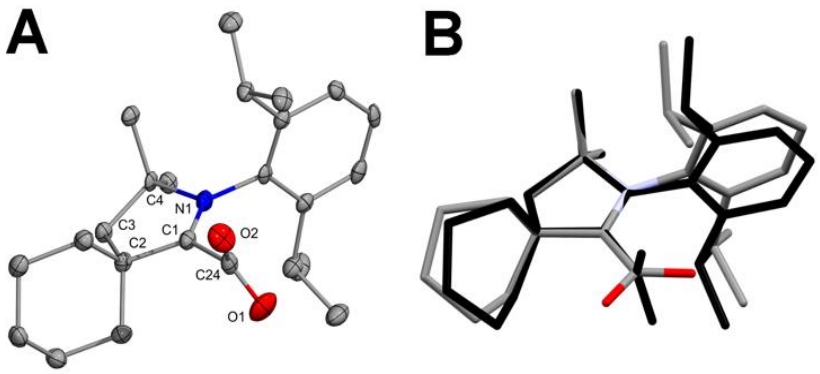

Figure 3.2. (A) Molecular structure of compound **1** (thermal ellipsoids at 40% probability; only one of the two chemically equivalent but crystallographically distinct molecules is shown). H atoms and co-crystallized THF solvent molecules omitted for clarity. Selected bond distances (Å) bond angles (°) and torsion angles (°): C1–C24: 1.526(4); C1–N1: 1.297(4); O1–C24 1.236(4); O2–C24: 1.234(4); N1–C1–C24: 123.9(3); O2–C24–O1: 131.5(3); O1–C24–C1: 113.7(3); N1–C1–C24–O2: 101.2(4). **(B)** Stick representations of the DFT optimized structures of **1** (black) and **[1]**$^-$ (gray, blue and red). ORCA 4.0.1 B3LYP/G, def2-TZVP, CPCM (THF).

Cyclic voltammetry (CV) experiments conducted in acetonitrile (MeCN; **Figures SI 3.4–SI 3.6**) and tetrahydrofuran (THF; **Figures 3.3 and SI 3.7**) showed reversible one-electron redox behavior under Ar saturation with $E_{1/2}$ at −2.08 V and −2.15 V versus Fc^+/Fc, respectively. Under CO_2 saturation conditions, this reduction wave became irreversible, and a new oxidation feature was observed on the return sweep at E_{pa}= −1.50 V versus Fc^+/Fc in THF and -1.40 V versus Fc^+/Fc in MeCN. The shift to irreversible redox behavior is suggestive of an EC mechanism, with an initial reduction of **1** preceding a chemical reaction step with free CO_2.[17] Importantly, these results also suggest that in the absence of inorganic components, the organic CO_2 adduct was capable of electrochemically mediating a reduction reaction of unquantified efficiency. CVs taken in blank solutions show no redox

response under Ar or CO_2 saturation in the absence of **1** in this potential range for both MeCN and THF (**Figure SI 3.8**).

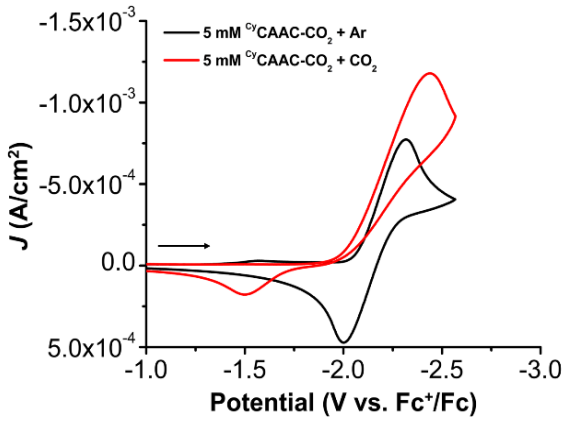

Figure 3.3. CV response of **1** at reducing potentials under an inert atmosphere (black) and CO_2 saturation (red) in THF. Conditions: 5 mM **1**, 0.1 M $TBAPF_6$/THF glassy carbon working electrode, glassy carbon counter electrode, Ag/AgCl pseudoreference electrode, referenced to internal ferrocene standard

Infrared spectroelectrochemical[18-19] (IR-SEC) and electrolysis experiments were undertaken to elucidate the products of this electrochemical reaction under Ar and CO_2 saturation (**Figure 3.4; Table SI 3.2**). At resting potentials under Ar saturation in THF, a strong IR absorbance mode corresponding to the CO_2 adduct is observed at 1670 cm^{1}. If the cell potential is moved stepwise to more reducing potentials, this absorbance mode disappears with the concomitant appearance of weaker modes at 1660 and 1603 cm^{-1}, which peak in intensity around −1.9 V versus Fc^+/Fc. A weaker absorbance mode at 1531cm^{-1} also forms upon the initial reduction of **1** but disappears at potentials more negative than −1.8 V versus Fc^+/Fc (**Figure SI 3.9**). Although the CV data are consistent with a reversible redox process, on the relatively longer time frame of the microscale electrolysis occurring during IR-SEC, there is sufficient time for the reduced species to undergo a chemical reaction. To analyze and quantify any gaseous products produced,

controlled potential electrolysis experiments were conducted (**Figures SI 3.10; Table SI 3.2).** Applying a potential of −2.4 V versus Fc^+/Fc with 5 mm of **1** in THF under Ar saturation showed CO in the headspace when analyzed by GC, corresponding to a Faradaic efficiency of 0.44% with the passage of 0.83 per electron equivalents per molecule of **1** (**Table SI 3.2**). These results suggest that the electrochemical reduction reaction is stoichiometric in nature under Ar saturation conditions.

Assignment of the new species is possible through literature precedent[20] and DFT calculations. The calculated IR spectrum for the one-electron reduction product [**1**]$^-$ in THF predicts a value of 1525 cm^{-1} for an asymmetric vibration mode of the bent CO_2 moiety, in agreement with the absorbance mode observed experimentally at 1531 cm^{-1} (def2-TZVP/B3LYP/G; **Figure 3.4 A**). New IR absorbance modes are observed experimentally at 1660 and 1603 cm^{-1}, which are not predicted by DFT calculations for [**1**]$^-$. One possible product of the reduction reaction is the ketene **2** (**Figure 3.1**). DFT calculations predict an intense absorbance mode at 2127 cm^{-1} in THF (2097cm^{-1}, 0.986 scaling factor)[21] for **2**, corresponding to the CO group. Direct synthesis of **2** showed an in-situ IR absorbance of 2064 cm^{-1} in THF (**Figure SI 3.11**). No IR absorbance more consistent with the ketene species is observed under Ar saturation experimentally. Given the observed instability of **2** (**Figures SI 3.1 and SI 3.11**), it is possible that the CO moiety is more activated in THF than predicted in the DFT methods using CPCM. Direct synthesis of tetrabutylammoniumoxalate [$(TBA)_2(ox)$] as an additional experimental control shows two absorbance modes at 1550 and 1286 cm^{-1}; we propose that the absence of a correlation with the experimentally observed modes at 1660 and 1603 cm^{-1} is consistent with these absorbances corresponding to degradation products of [**1**]$^-$ or **2**.

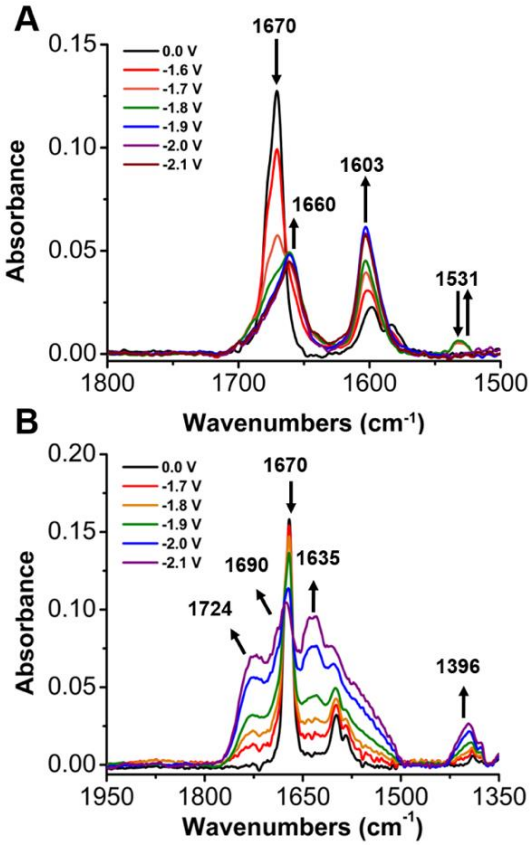

Figure 3.4. (A) Disappearance of the CO_2 adduct at 1670 cm^{-1} as the reduced species **[1]**$^-$ grows in and disappears at 1531 cm^{-1} at reducing conditions under Ar saturation monitored by IR-SEC. Presumptive ketene **2** degradation products appear at 1660 and 1603 cm^{-1}. **(B)** Comparable experiments under CO_2 saturation conditions show the loss of the CO_2 adduct upon the formation of CO_3^{2-} (1690 and 1635 cm^{-1}).

In MeCN, the loss of the zwitterionic CO_2 adduct **1** also occurs at reducing potentials under Ar saturation conditions, similar to the results obtained in THF (**Figure SI 3.12**). An absorbance mode consistent with the radical intermediate [**1**]$^-$ is observed at 1224 cm^{-1} upon initial reduction in the IR-SEC experiment, with subsequent loss in absorbance intensity with the appearance of the presumptive ketene product **2** at 2118 cm^{-1} (2121 cm^{-1} predicted). Although an asymmetric wagging IR absorption mode is predicted at ≈ 1500 cm^{-1}, similar to the transient species observed and predicted in THF above, the strong background solvent absorbances in MeCN preclude its observation. DFT

calculations suggest the experimentally absorbance mode at 1224 cm^{-1} corresponds to weak symmetric rocking by the CO_2 group (1227 cm^{-1} predicted), with contributions from scissoring of the ^{Cy}CAAC core. An IR absorption mode suggestive of the decomposition of [**1**]$^{-}$ or **2** is again observed at 1603 cm^{-1}.

Repeating IR-SEC experiments under CO_2 saturation conditions in THF resulted in several noteworthy differences from the data obtained with Ar. Neither the radical anion intermediate [**1**]$^{-}$, nor the ketene **2** were observed; instead, two bands at 1635 and 1690 cm^{-1} appeared and grew in intensity upon the disappearance of the symmetric CO_2 stretch of **1** at 1670 cm^{-1} (**Figure 3.4B**). Electrolysis experiments at −2.4 V versus Fc^{+}/Fc showed CO with 0.2% Faradaic efficiency (**Figure SI 3.13, Table SI 3.2**). Although CO dissociation from **2** could facilitate additional CO_2 binding and electrochemical reduction cycles, it is clear that the degradation products of **2** do not involve regeneration of the free carbene or CO release, rendering the process stoichiometric in nature. The directly prepared control compound TBA(HCO_3) shows good agreement (1675 and 1636 cm^{-1}) with the IR absorption bands observed experimentally by IR-SEC at 1690 and 1635 cm^{-1} (**Figure SI 3.14**). Previous characterization of a $(TBA)_2CO_3^{2-}$ in MeCN[22] showed similar IR absorption bands at 1682 and 1645 cm^{-1}, suggesting carbonate or bicarbonate formation is occurring with CO_2 present. Analogous IR-SEC and electrolysis experiments in MeCN under CO_2 saturation show that carbonate is again observed at 1686 and 1647 cm^{-1} across the same potential range (**Figures SI 3.15– SI 3.19**). If $^{13}CO_2$ is introduced to a THF solution of **1**, rapid exchange of the predominantly $^{12}CO_2$ from the as synthesized adduct with the isotopically labeled substrate occurs; upon reduction, the decomposition products

are shifted to lower wavenumbers as well, confirming that these arise from reactions involving the CO_2 moiety (**Figure SI 3.20**).

To better understand the results of the IR-SEC and electrolysis studies, spectrochemical experiments with the in situ generated carbene–CO adduct were conducted. In order to prepare ^{Cy}CAAC–CO, a THF solution of free ^{Cy}CAAC was generated in a Schlenk pressure tube under an Ar atmosphere. The head space of the reaction vessel was evacuated and subsequently refilled with $CO_{(g)}$, immediately generating an intensely colored royal blue solution. The color of this solution is consistent with the distinctive color observed for the ^{Menthyl}CAAC–CO adduct reported by Bertrand et al.[12] In contrast to the stability observed for the bulkier menthyl analogue, the diminished steric protection afforded by ^{Cy}CAAC (absence of *i*Pr and Me groups) was insufficient to stabilize the ketene, and this blue product was observed to decompose rapidly above −78 °C. Rapid decomposition was observed in all attempts to isolate **2** in the solid state, even under rigorously air-free conditions under a headspace of CO (**Figure SI 3.1**). As a result, the putative ketene species could only be studied in situ immediately after preparation. Monitoring a solution of ^{Cy}CAAC–CO by IR spectroscopy over the course of an hour revealed that the IR absorbance band corresponding to **2** at 2064 cm^{-1} diminishes in intensity (**Figure SI 3.11**), with an estimated half-life of ≈ 8min.

The DFT-optimized structure of [**1**]$^-$ showed several important differences with the starting species **1**. There is a lengthening of the N–C bond distance of the carbene core (1.292 to 1.388 Å), consistent with a decrease in double-bond character. The bent CO_2 is predicted to rotate ≈ 90º to be in plane with the central ring of the CAAC (NCCO dihedral 94.98 to 171.17). A shortening of the ^{CAAC}C–CO_2 bond length also occurs with this rotation

(1.518 to 1.462 Å), suggestive of a π-symmetric interaction. Significant radical character is also predicted on the central C atom of the carbene in [**1**]$^{-}$ (**Figure 3.2B**). Natural bond order (NBO) analysis[23-24] is consistent with double bond character between the N–C atoms of the carbene in **1**, which diminishes to a single bond upon reduction to [**1**]$^{-}$. Lengthening of both C–O bond lengths is also predicted for [**1**]$^{-}$ relative to **1** (1.242 to 1.270 Å), consistent with a decreased bond order. NBO analyses in MeCN show a minimal difference with the results obtained for THF.

These data allow us to propose a mechanism for the electrochemical reduction of CO_2 mediated by ^{Cy}CAAC. The electronic structure of the CO_2 adduct is best described as a zwitterion, with double bond character between the carbene N and C atoms and anionic charge on the O atoms of the CO_2 moiety, made equivalent by resonance. Upon one-electron reduction, the added electron density populates the vacant *p* orbital on the carbene C atom (**Figure SI 3.21**). The net result predicted by DFT methods is a lengthening of the N–C bond length and a shortening of the carbene–CO_2 bond length. There is a concomitant shift in the N–C–C–O dihedral bond angle as the activated CO_2 group rotates in plane with the carbene core from the starting perpendicular arrangement. The radical anion [**1**]$^{-}$ is observable by IR-SEC at reducing potentials. Conceptually, it is useful to think of this species as a carbene-stabilized pseudo-CO_2 radical anion, as this explains the observed products: (free CO), ketene **2**, and CO_3^{2-}. The net reaction results in a reductive disproportionation of two equivalents of [**1**]$^{-}$, generating one equivalent each of CO and CO_3^{2-}. The propensity of the ketene **2** to decompose via further side reactions is reflected in the observation of minimal CO in the reaction headspace.

NBO analysis of ketene **2** suggests that this instability is the result of two different contributing resonance structures. Natural resonance theory (NRT) calculations show a 2:1 contribution of structures, with the larger contributor best described as a ketene. The lesser contributor is best described as the carbene accepting the CO lone pair, with triple bond character retained; the electron balance is satisfied by π-symmetric lone pair on the carbene C atom. The ^{Cy}CAAC–CO adduct is intensely colored, the lowest energy absorbance is predicted to correspond to a HOMO–LUMO transition according to TD-DFT (**Figures SI 3.22 and SI 3.23**); the LUMO is antibonding with respect to the carbene–CO interaction (**Figure SI 3.22**).

3.4 Conclusion

This system represents a promising example of CAACs acting as organic mediators for the stoichiometric electrochemical reduction of CO_2. The observed instability of the resulting reaction products suggests further development may access a catalytic system in future studies. New derivatives and co-catalysts are currently being explored to control the destabilization of the CO adduct and decrease the required reduction potential.

3.5 Experimental

3.5.1 Supporting Information

General All manipulations were carried out under an atmosphere of purified nitrogen or argon using standard Schlenk techniques or in a MBRAUN LABmaster glovebox equipped with a −37 °C freezer. Solvents were purchased from commercial sources and purified by distillation over sodium/benzophenone prior to use. Glassware was oven-dried at 190 °C overnight and cooled under vacuum before use. The NMR spectra were recorded at the room temperature on a Bruker Avance 800 MHz spectrometer (^{1}H: 800.13 MHz and ^{13}C:

201.193 MHz). Proton and carbon chemical shifts are reported in ppm and are referenced using the residual proton and carbon signals of the deuterated solvent (^{1}H; THF-d_8, δ 3.58, 1.72, ^{13}C; THF-d_8, δ 67.21, 25.31; ^{1}H; CD_2Cl_2, δ 5.32, ^{13}C; CD_2Cl_2, δ 53.84). Deuterated solvents were purchased from Cambridge Isotope Laboratories and dried before use using either NaK amalgam (THF-d_8) or distillation over CaH_2 (CD_2Cl_2). Elemental analyses were performed at Robertson Microlit Laboratories, Ledgewood, NJ, USA. The ^{Cy}CAAC (CAAC = cyclic alkyl(amino)carbene),[9] was prepared according to the literature procedure.

Electrochemistry. All electroanalytical experiments were performed using a Metrohm Autolab PGSTAT302N potentiostat or a BioLogic SP-50 potentiostat. All solvents (ACS or HPLC grade) were commercially available and used as received unless otherwise indicated. For all air-sensitive electrochemical experiments, solvents were obtained as anhydrous and air-free from a PPT Glass Contour Solvent Purification System. Gas cylinders were obtained from Praxair (Ar as 5.0; CO_2 as 4.0) and passed through molecular sieves prior to use. Glassy carbon working (3 mm diameter) electrode and non-aqueous silver wire pseudoreference electrode separated by PTFE tip were obtained from CH Instruments. The Ag/AgCl pseudoreference electrode were generated by depositing chloride on the bare silver wire in 10% HCl at oxidizing potentials and were stored in a 0.1 M tetrabutylammonium hexafluorophosphate/acetonitrile solution prior to use. The counter electrode was a glassy carbon rod (2 mm diameter). All cyclic voltammetry (CV) experiments were performed in a modified scintillation vial (20 mL volume) as a single-chamber cell with a cap modified with ports for all electrodes and a sparging needle.

Controlled potential electrolysis experiments were performed in an H-Cell from Pine Research Instrumentation (two ~25 mL chambers separated by glass frit), with the

working electrode in one chamber separate from the pseudoreference and counter electrodes in the other chamber. Spectrographic grade carbon rods (Electron Microscopy Sciences, 6.35 mm diameter) were used as the working and counter electrodes with a silver/silver chloride pseudoreference electrode (CH Instruments) behind a PTFE frit). The cell was sealed with septa and electrical tape to allow head-space sampling and gas sparging via needles through the two septa using a y-splitter. Pressure balance was maintained by inserting a single section of AWG #14 standard wall PTFE tubing through each septum. Tetrabutylammonium hexafluorophosphate ($TBAPF_6$) was purified by recrystallization from ethanol and dried in a vacuum oven overnight at 100 °C before being stored in a desiccator. All data were referenced to an internal ferrocene standard (ferricenium/ferrocene; Fc^+/Fc) redox potential under stated conditions unless otherwise specified.

IR Spectroelectrochemistry. All IR-SEC experiments were conducted using a custom cell based on a previously published design.[18-19, 25] The three-electrode set-up consists of an inner glassy carbon working electrode disc (10 mm diameter), a central circular silver bare metal pseudoreference electrode, and an outer circular glassy carbon counter electrode embedded within a PEEK block. All data were referenced to an internal ferrocene standard (Fc^+/Fc) reduction potential under stated conditions; obtained by taking a CV with the cell prior to injecting analyte for IR-SEC experiments unless otherwise specified. All spectra were processed by subtraction of a non-reactive/non-catalytic potential from those at which reactivity occurred. For experiments with Ar, CO_2 and $^{13}CO_2$, gas was sparged into the solution containing ^{Cy}CAAC–CO_2 for ~30 s prior to injection into the assembled cell.

Synthesis of Compound 1 - ^{Cy}CAACCO$_2$

In a Schlenk round bottomed flask under argon, a solution of ^{Cy}CAAC (0.500 g, 1.54 mmol) was prepared in freshly distilled Et_2O (20 mL) to yield a clear, colorless solution. The flask sidearm was opened to a flow of argon. CO_2 was allowed to bubble rapidly into the solution for 30 minutes via a balloon fitted with a needle adapter, which was purged with argon 3 times prior to being filled. The flask sidearm remained open to the Schlenk manifold during the entire reaction to maintain approximately 1 atm of pressure and air-free conditions. White precipitate immediately began to form upon the initial introduction of CO_2 and continued over the course of the reaction. The resulting white solids were filtered via cannula, washed with hexanes (20 mL) and dried under vacuum to yield **1** as a bright white solid. Single crystals suitable for X-ray diffraction were obtained by cooling a saturated THF solution of the product to –37 °C (0.375 g, 66%). Note: during the synthesis of compound **1** it is imperative that water be excluded from the reaction. If trace water is present in the solvent it is possible to form a CAAC-activated water product. Therefore, solvents were freshly distilled prior to use. ^{1}H NMR (800 MHz, CD_2Cl_2) δ 7.44 (t, J = 7.8 Hz, 1H, C$\boldsymbol{H}_{para}$) 7.29 (d, J = 7.8 Hz, 2H, C$\boldsymbol{H}_{meta}$) 2.74 (hept, J = 6.4 Hz, 2H, C$\boldsymbol{H}_{methine}$) 2.33 (s, 2H, (C$\boldsymbol{H}_2$)$_{backbone}$) 2.16 (td, J = 13.3, 3.3 Hz, 2H, (C$\boldsymbol{H}_2$)$_{Cy}$) 1.88 (d, J = 12.2 Hz, 2H, (C$\boldsymbol{H}_2$)$_{Cy}$) 1.83 (dt, J = 13.2, 2.9 Hz, 2H, (C$\boldsymbol{H}_2$)$_{Cy}$) 1.73 (d, J = 12.4 Hz, 1H, (C$\boldsymbol{H}_2$)$_{Cy}$) 1.46 (s, 6H, (C$\boldsymbol{H}_3$)$_{backbone}$) 1.41 (m, 2H, (C$\boldsymbol{H}_2$)$_{Cy}$) 1.36 (m, 1H, (C$\boldsymbol{H}_2$)$_{Cy}$) 1.32 (d, J = 6.5 Hz, 6H, (C$\boldsymbol{H}_3$)$_{Dipp}$) 1.29 (d, J = 6.7 Hz, 6H, (C$\boldsymbol{H}_3$)$_{Dipp}$) ^{13}C{^{1}H} NMR (201 MHz, CD_2Cl_2) δ 193.4 ($\mathbf{C}_{C=N}$), 158.6 ($\mathbf{C}_{CO2}$), 146.3 ($\mathbf{C}_{ipso}$), 130.9, 129.5, 125.9, 79.6, 53.8, 53.1, 45.5, 36.2, 30.1, 29.6, 26.5, 25.0, 24.5, 22.2. Anal. Calcd. for CyCAACCO$_2$·0.5THF: C, 76.99; H, 9.69; N, 3.45. Found: C, 76.84; H, 9.48; N, 3.65.

Synthesis of Compound 2 and Decay Experiment

A solution of ^{Cy}CAAC (30 mg, 92 μmol) in THF (1 mL) was prepared in a Schlenk pressure tube under an argon atmosphere. The clear solution was completely frozen in a bath of liquid N_2, and the flask headspace was evacuated. A balloon of CO was attached to the sidearm via a glass three-way valve, allowing rigorously air-free conditions to be maintained during the introduction of CO. The balloon and flask sidearm were opened, allowing the CO to refill the evacuated headspace of the pressure tube. Once pressure had equilibrated, the pressure tube was sealed completely, and the cold bath removed. No reaction was observed until the contents of the tube had thawed, at which point the solution rapidly gained a deep blue color, which exactly matched that of the reported ^{menthyl}CAAC[12] of compound **2** (a photograph of this solution immediately after thawing is shown in **Figure SI 3.1A**). At temperatures above the freezing point of THF (–108.4 °C), the blue color is extremely short lived, and fades over the course of minutes. This short lifetime precluded the isolation of a pure sample of **2**, so its presence was confirmed, and decay monitored, via solution-phase IR spectroscopy. The solution of **2** was immediately brought into a glovebox and transferred to an Omnicell with CaF_2 windows and PTFE spacer. The IR spectrum of this solution showed a characteristic band was observed for the C=O stretch of **2** at 2064 cm^{-1}, the disappearance of which was monitored over the course of 8 min at intervals of 2 min. (**Figure SI 3.11**). ^{1}H NMR of the decay products in THF-d_8 showed multiple carbene-containing products, none of which were free ^{Cy}CAAC, further supporting the existence of multiple active decomposition pathways for **2**.

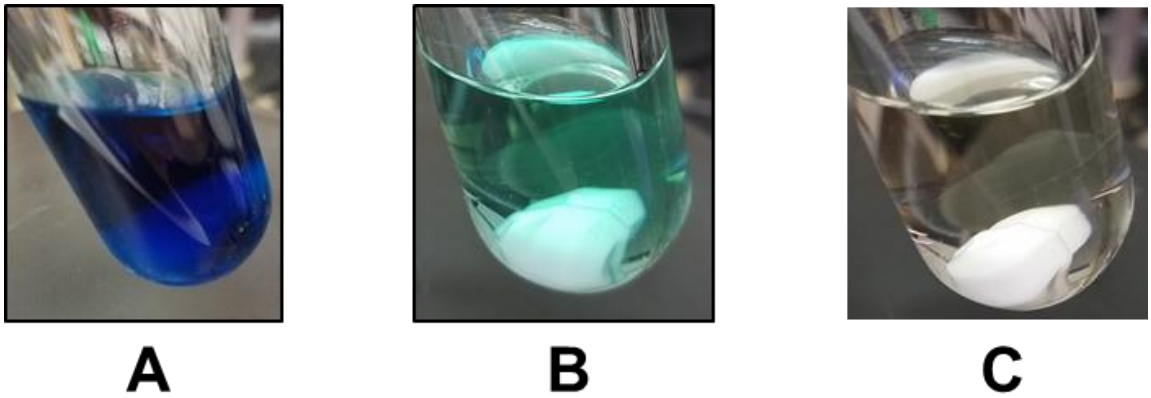

Figure SI 3.1. (**A**) Solution of **2** in THF under a CO atmosphere at t = 0 min after preparation. (**B**) The same solution of **2** in THF at t = 4 min after preparation. (**C**) Same solution of **2** in THF at t = 10 min after preparation.

Synthesis of tetrabutyl-*n*-ammonium oxalate [(TBA)$_2$(ox)]

A round bottom flask equipped with a stir bar was charged with 1.00 g of oxalic acid dihydrate and 10.4 ml of tetrabutylammonium hydroxide and stirred for 45 minutes. The resulting solution was condensed under reduced pressure at 65-70 ˚C for 30 mins and then dried under vacuum at 70 ˚C for 48 hours to yield a white solid. Due to the hygroscopic nature of this material a yield was not obtained. The acetonitrile solution IR spectrum gave strong absorbances at 1552 cm^{-1} and 1288 cm^{-1} and the THF solution IR gave absorbances at 1550 cm^{-1} and 1286 cm^{-1}. ^{13}C{^{1}H} NMR (600 MHz, $(CD_3)_2SO$) δ 174.8 (**C**$_{C=O}$), 57.3, 23.1, 19.0 (**C**$_{-CH2-}$), 13.3 (**C**$_{-CH3}$), Anal. Calc'd. for [(TBA)$_2$(ox)]: C, 71.21; H, 12.67; N, 4.89. Found: C, 70.99; H, 12.48; N, 4.29.

Synthesis of tetrabutyl-*N*-ammonium bicarbonate TBA(HCO_3)

TBA(bicarbonate) was synthesized and characterized following a literature procedure from Cheng et at.[26] (shown in **Figures SI 3.14 and SI 3.17** below).

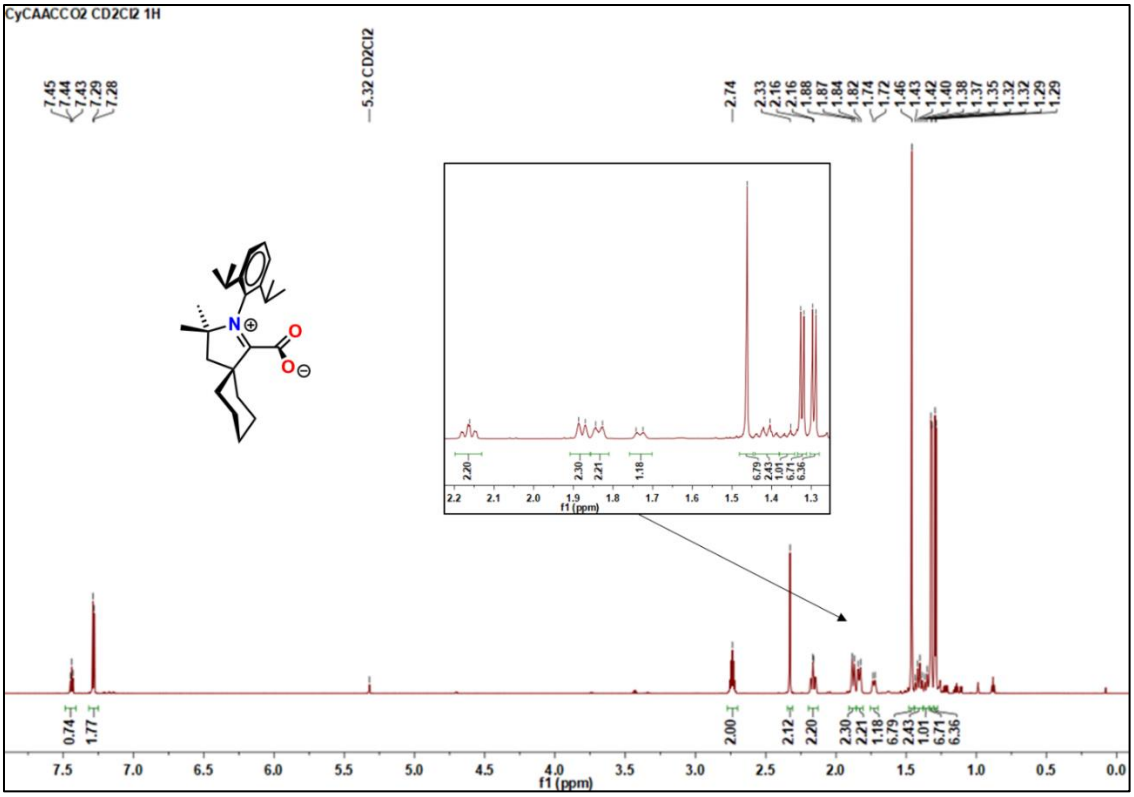

Figure SI 3.2. ^{1}H NMR of compound **1** in CD_2Cl_2 taken at 298.15 K.

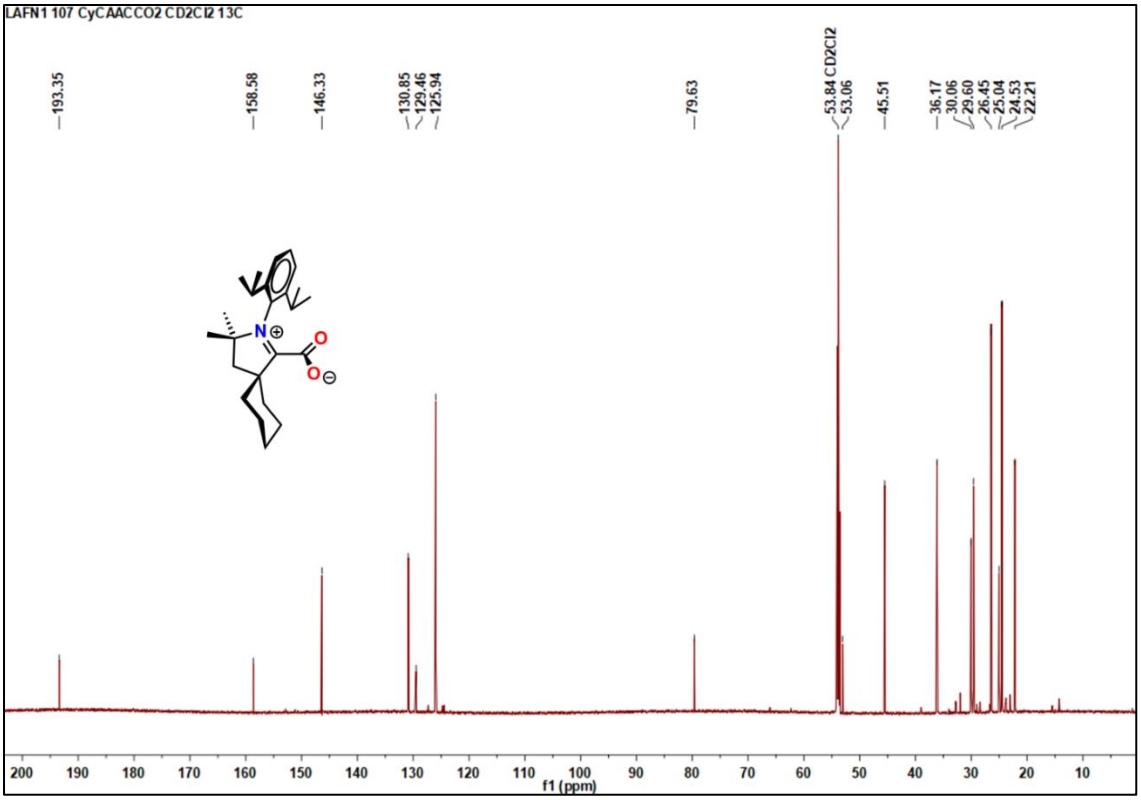

Figure SI 3.3. $^{13}C\{^{1}H\}$ NMR of compound **1** in CD_2Cl_2 taken at 298.15 K.

Table SI 3.1. Crystallographic Information.

Compound	1
CCDC number	1885398
Formula	$C_{32}H_{51}NO_4$
FW (g/mol)	513.73
Temp (K)	100(2)
λ (Å)	0.71073
Size (mm)	0.238 x 0.464 x 0.714
Crystal habit	colorless block
Crystal system	monoclinic
Space group	$P2_1/n$
a (Å)	17.518(7)
b(Å)	21.299(11)
c (Å)	17.819(8)
β (°)	116.624(15)
Volume ($Å^3$)	5944.(5)
Z	8
Density (g/cm^3)	1.148
μ (mm^{-1})	0.074
θ range (°)	1.60-26.64
Data / restraints / parameters	12189/0/685
GOF on F^2	1.044
Largest diff. peak/hole ($Å^{-3}$)	0.547/-0.348
R_1 ($I>2\sigma(I)$)	0.0624
wR_2 (all data)	0.1946

Colorless block-like crystals of **1** were coated with Paratone oil and mounted on a MiTeGen MicroLoop. The X-ray intensity data were measured on a Bruker Kappa APEXII Duo system equipped with a graphite monochromator and a Mo K_α fine focus sealed-tube (λ = 0.71073 Å). The frames were integrated with the Bruker SAINT software package[27] using a narrow-frame algorithm. Using CELL_NOW,[28] a three-domain twin was identified in **1**. Starting with 1302 reflections, 1233 reflections were fit to the first domain, 590 to the second domain (36 exclusively), and 1011 to the third domain (24 exclusively). There were 9 unindexed reflections. The first twin law, a 178.9º rotation about the reciprocal axis -0.507 0.012 1.000, was -0.980 0.006 -1.005 / -0.029 -1.000 0.009 / -0.040 0.016 0.980. The second twin law, a 179.5º rotation about the reciprocal axis -0.489 -0.003 1.000, was -1.007 0.013 -0.981 / -0.013 -1.000 -0.021 / 0.015 -0.013 1.007. Data for the structure was corrected for absorption effects using the Multi-Scan method (TWINABS for **1**).[27] The structure was solved and refined using the Bruker SHELXTL Software Package[29] within APEX3[27] and OLEX2.[30] The structure of **1** was refined on HKLF5, and the BASF for the twin domains converged at 0.1796 and 0.30036. Non-hydrogen atoms **1** were refined anisotropically. Hydrogen atoms were placed in geometrically calculated positions with $U_{iso} = 1.2U_{equiv}$ of the parent atom ($U_{iso} = 1.5\ U_{equiv}$ for methyl). In **1**, one carbon atom in a THF solvent molecule was disordered over two positions. The relative occupancies were freely refined, and a constraint was used on the anisotropic displacement parameters of the disordered atoms.

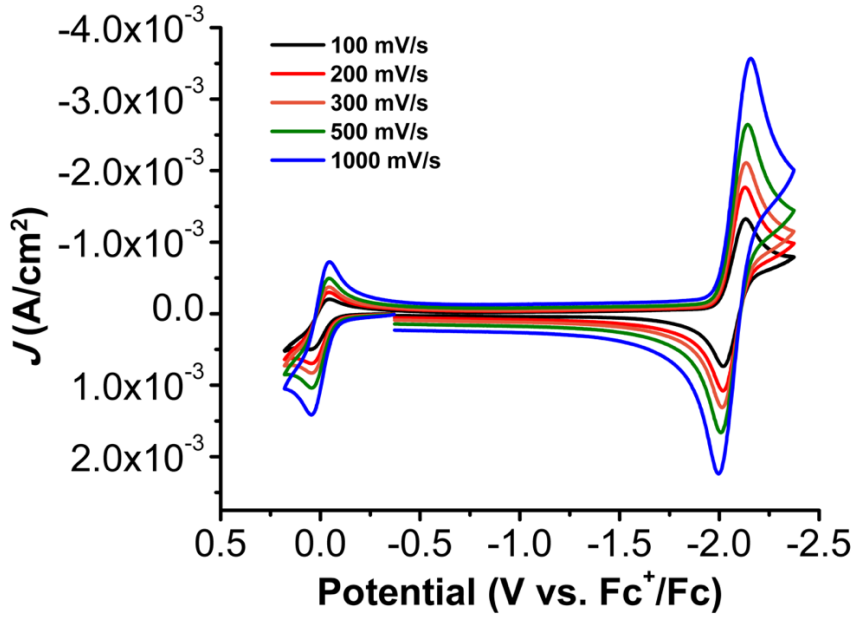

Figure SI 3.4. Variable scan rate CVs of **[1]** in MeCN under Ar. Conditions: 5 mM analyte; 0.1 M $TBAPF_6$/MeCN, glassy carbon working electrode, glassy carbon counter electrode, Ag/AgCl pseudoreference electrode; varied scan rate; referenced to internal ferrocene standard.

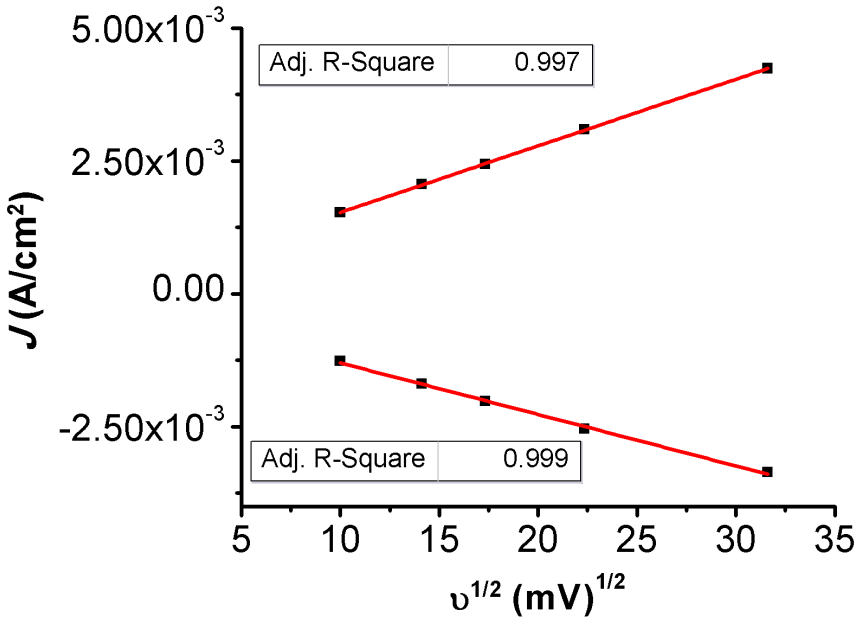

Figure SI 3.5. The linear fit of the variable scan data from **Figure SI 3.4** demonstrating the diffusion-limited current response. Conditions: 5 mM analyte; 0.1 M $TBAPF_6$/MeCN, glassy carbon working electrode, glassy carbon counter electrode, Ag/AgCl pseudoreference electrode; varied scan rate; referenced to internal ferrocene standard.

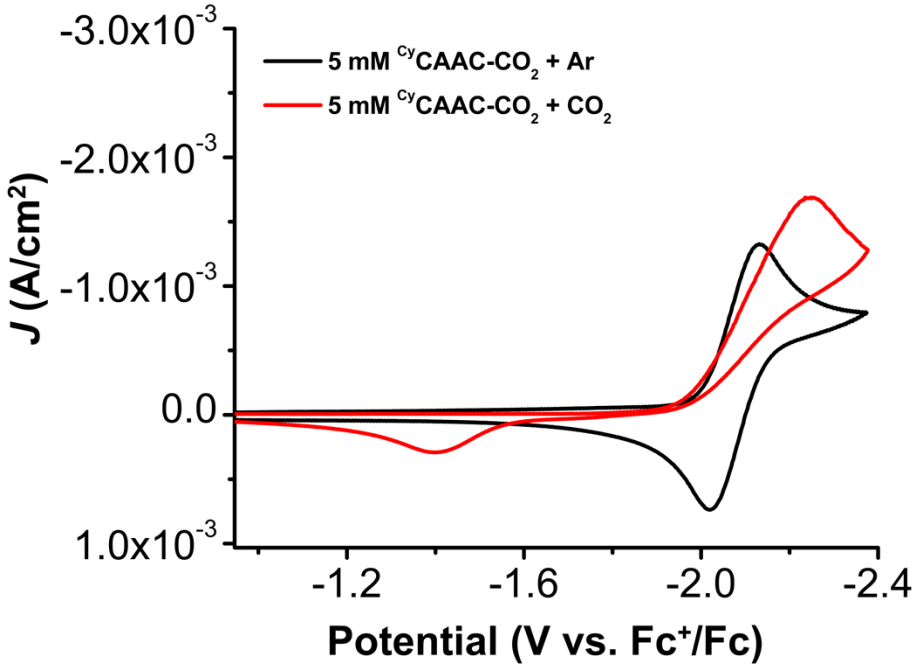

Figure SI 3.6. CV response of **[1]** at reducing potentials under and inert atmosphere (black) and CO_2 saturation (red) in MeCN. Conditions: 5 mM 1, 0.1 M $TBAPF_6$/MeCN glassy carbon working electrode, glassy carbon counter electrode, Ag/AgCl pseudoreference electrode, referenced to internal ferrocene standard.

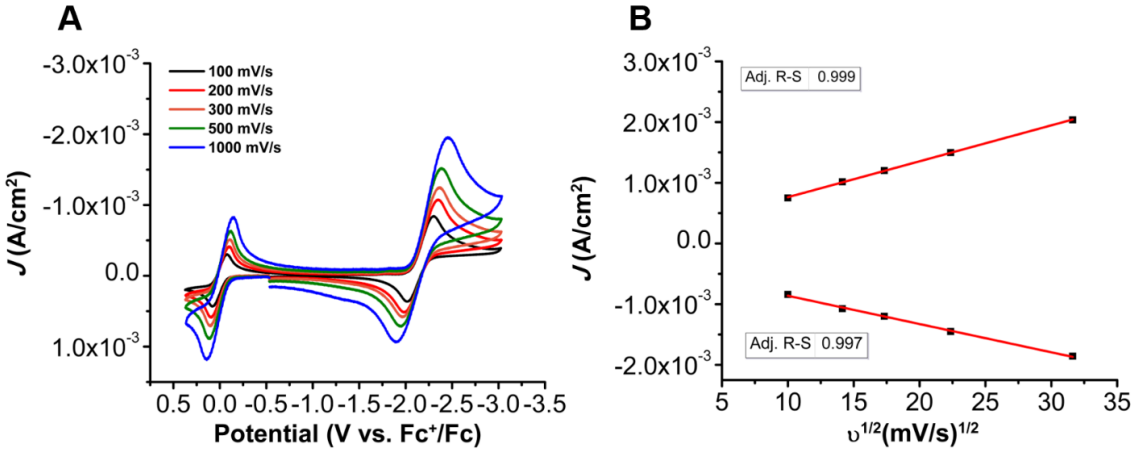

Figure SI 3.7. (A) Variable scan rate CVs of **[1]** in THF **(B)** the linear fit of the scans demonstrates the diffusion-limited current response. Conditions: 5 mM analyte; 0.1 M $TBAPF_6$/THF, glassy carbon working electrode, glassy carbon counter electrode, Ag/AgCl pseudoreference electrode; standard.

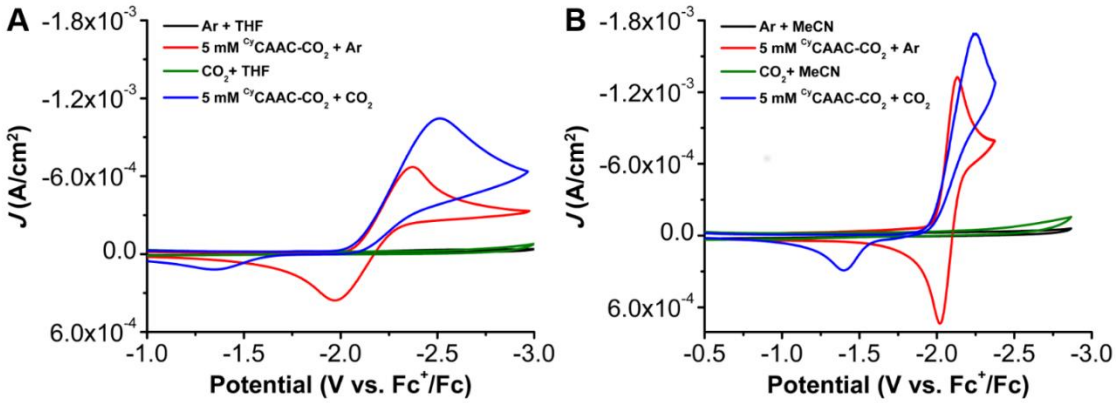

Figure SI 3.8. Control CVs of 5 mM CyCAAC-CO_2 in **(A)** THF and **(B)** MeCN. Conditions: 5 mM analyte; in 0.1 M $TBAPF_6$/THF or in 0.1 M $TBAPF_6$/MeCN, glassy carbon working electrode, glassy carbon counter electrode, Ag/AgCl pseudoreference electrode; varied scan rate; referenced to internal ferrocene standard.

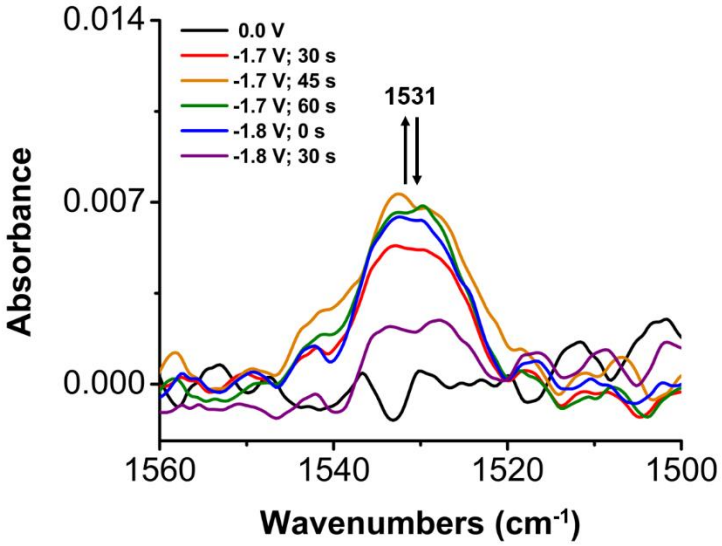

Figure SI 3.9. IR-SEC analysis of a 5 mM solution of **[1]** with a ~ 30 s Ar sparge in THF. Disappearance of the CO_2 adduct occurs at 1670 cm^{-1} with the growth of the transient radical species at 1531 cm^{-1} occurs from –1.7 to –1.8 V vs Fc^+/Fc.

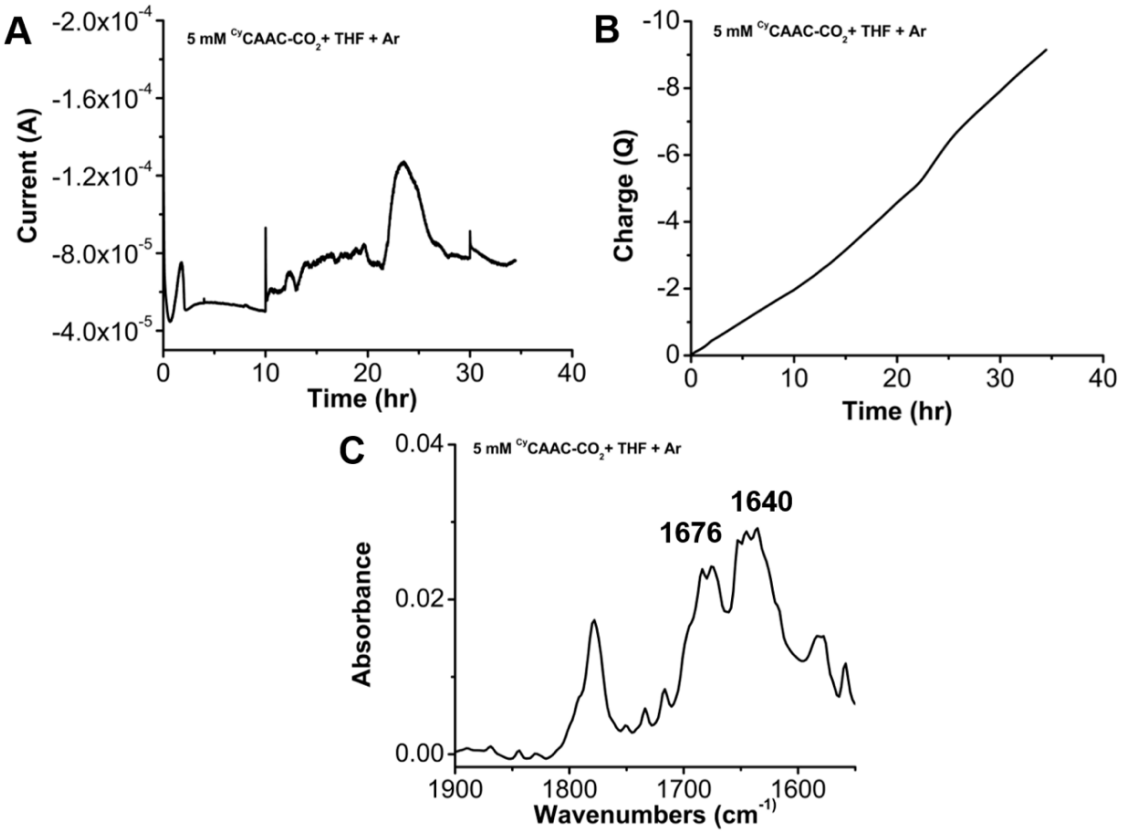

Figure SI 3.10. (A) Current vs time plot of electrolysis experiment of **[1]** under inert conditions. **(B)** Charge passed during electrolysis experiment. **(C)** IR of the bulk solution post electrolysis. Conditions: 5 mM of ^{Cy}CAAC–CO_2; 0.1 M $TBAPF_6$/THF; Ar sparge; graphite working electrode, graphite carbon counter electrode, Ag/AgCl pseudoreference electrode, and 0.5 M Fc was used as a sacrificial oxidant.

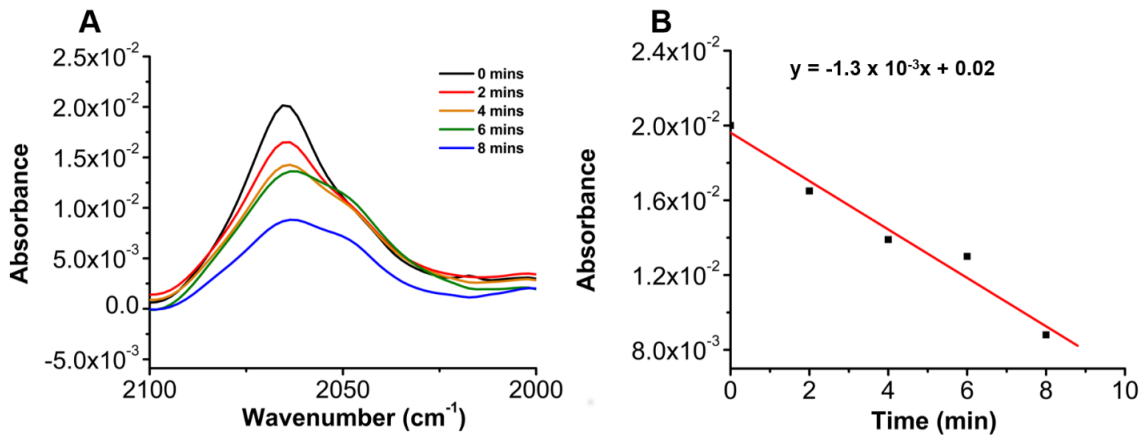

Figure SI 3.11. (A) IR absorbance from the ketene (2064 cm^{-1}) in THF at –70 C°. **(B)** The decay of the ketene overtime as the solution is warmed to room temperature showing a zero-order dependence. This species is highly unstable at room temperature and not observable in IR-SEC analysis.

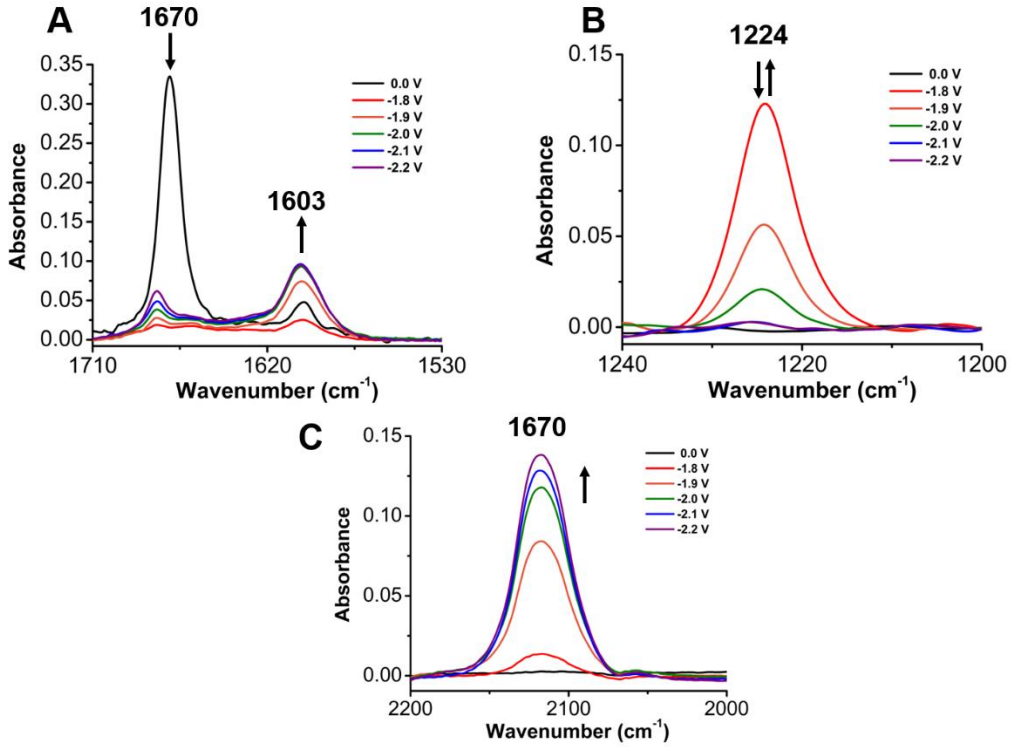

Figure SI 3.12. IR-SEC analysis of a 5 mM solution of **[1]** with an Ar sparge in MeCN. **(A)** Disappearance of the CO_2 adduct occurs at 1670 cm^{-1} with the growth of a feature at 1603 cm^{-1} associated with an unknown species. **(B)** A transient radical not observed with the initial CO_2 adduct disappears while **(C)** a feature grows in at 2118 cm^{-1} believed to be the ketene in MeCN supported by computational and literature results. Applied potential is given versus Fc^+/Fc for these IR-SEC experiments.

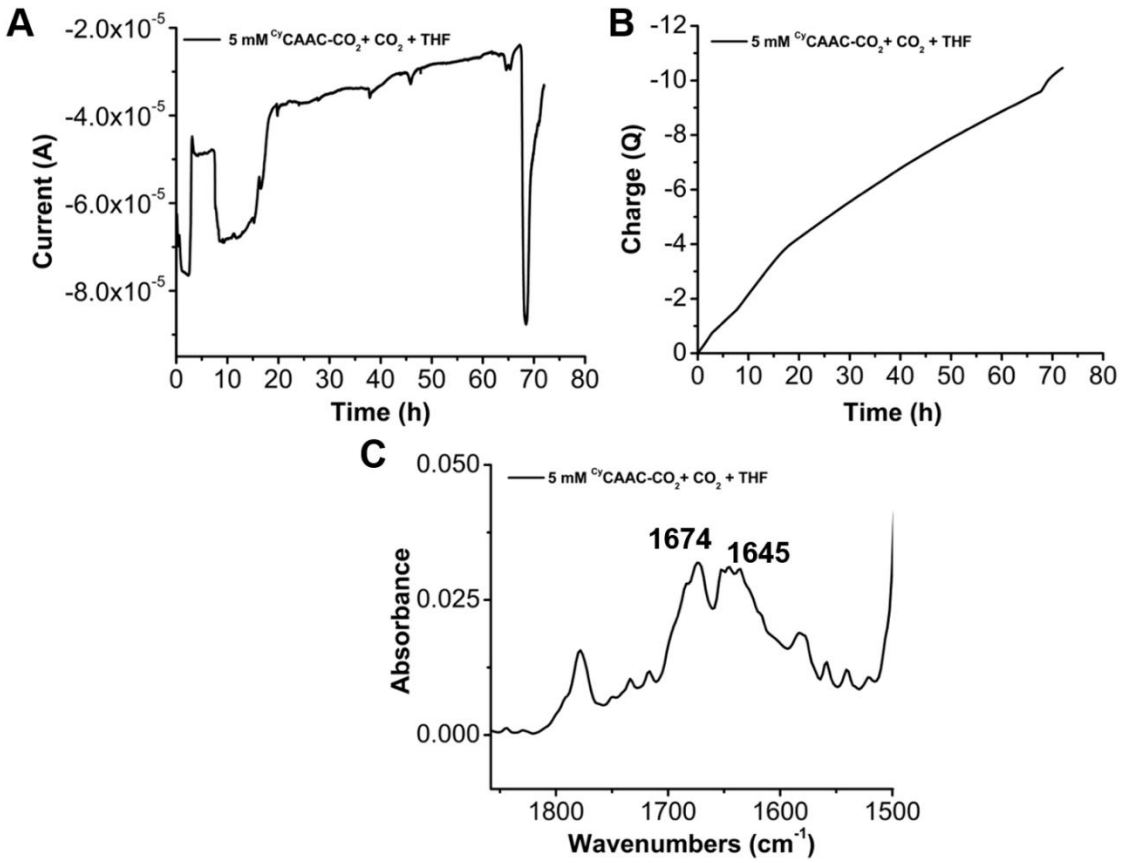

Figure SI 3.13. (A) Current vs time plot of electrolysis experiment of **[1]** under inert conditions **(B)** Charge passed during electrolysis experiment. **(C)** IR of the bulk solution post electrolysis. Conditions: 5 mM of ^{Cy}CAAC–CO_2; 0.1 M $TBAPF_6$/THF; CO_2 sparge; graphite working electrode, graphite carbon counter electrode, Ag/AgCl pseudoreference electrode, and 0.5 M Fc was used as a sacrificial oxidant.

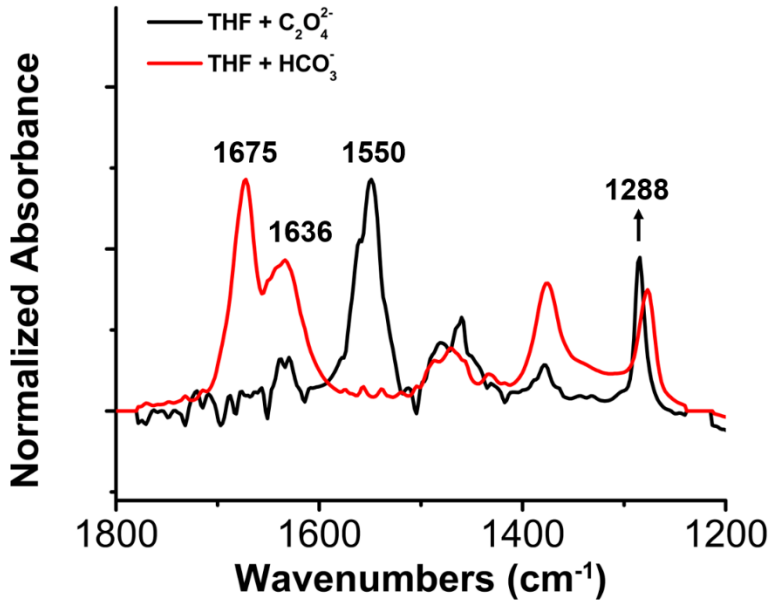

Figure SI 3.14. IR analysis of TBA(HCO_3) and [(TBA)$_2$(ox)] in THF with two absorbances from $C_2O_2^{2-}$ at 1550 and 1288 cm^{-1} (black trace) and two bands from HCO_3^- at 1675 and 1636 cm^{-1} (red trace).

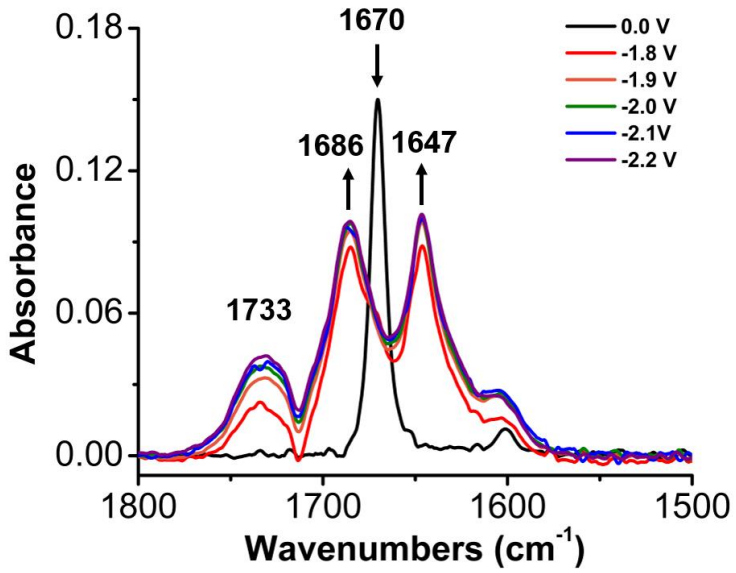

Figure SI 3.15. IR-SEC analysis of a 5 mM solution of **[1]** with a CO_2 sparge in MeCN. Disappearance of the CO_2 adduct occurs at 1670 cm^{-1} with the growth of carbonate from the appearance of stretches at 1686 and 1647 cm^{-1} as well as, an unknown species at 1733 cm^{-1}.

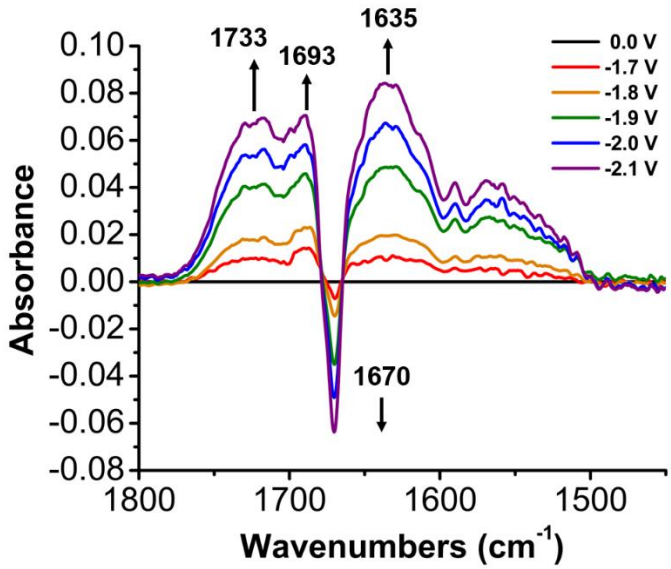

Figure SI 3.16. IR-SEC analysis of a 5 mM solution of **[1]** with a CO_2 sparge in THF. Disappearance of the CO_2 adduct occurs at 1670 cm^{-1} with the growth of carbonate from the appearance of stretches at 1693 and 1635 cm^{-1}. Difference spectra were used to high light the band at 1693 cm^{-1}.

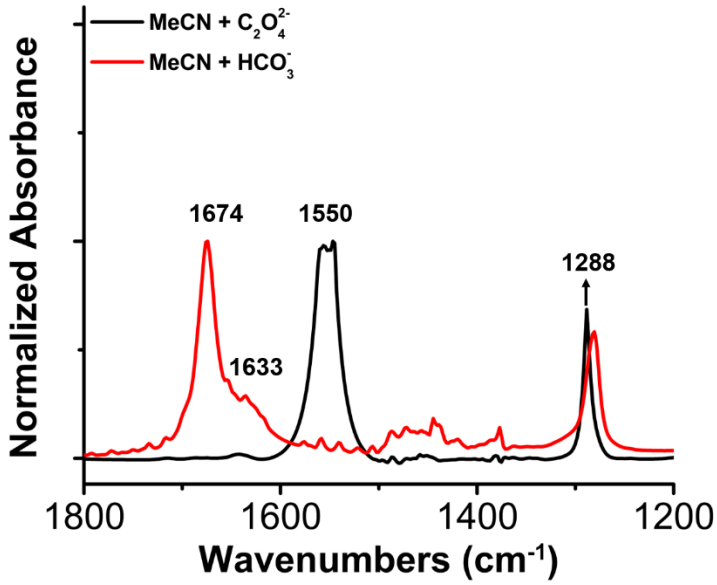

Figure SI 3.17. IR analysis of TBA(HCO_3) and [(TBA)$_2$(ox)] in MeCN with two bands from $C_2O_2^{2-}$ at 1550 and 1288 cm^{-1} (black trace) and two bands at 1674 and 1633 $cm^{-1}$from HCO_3^-.

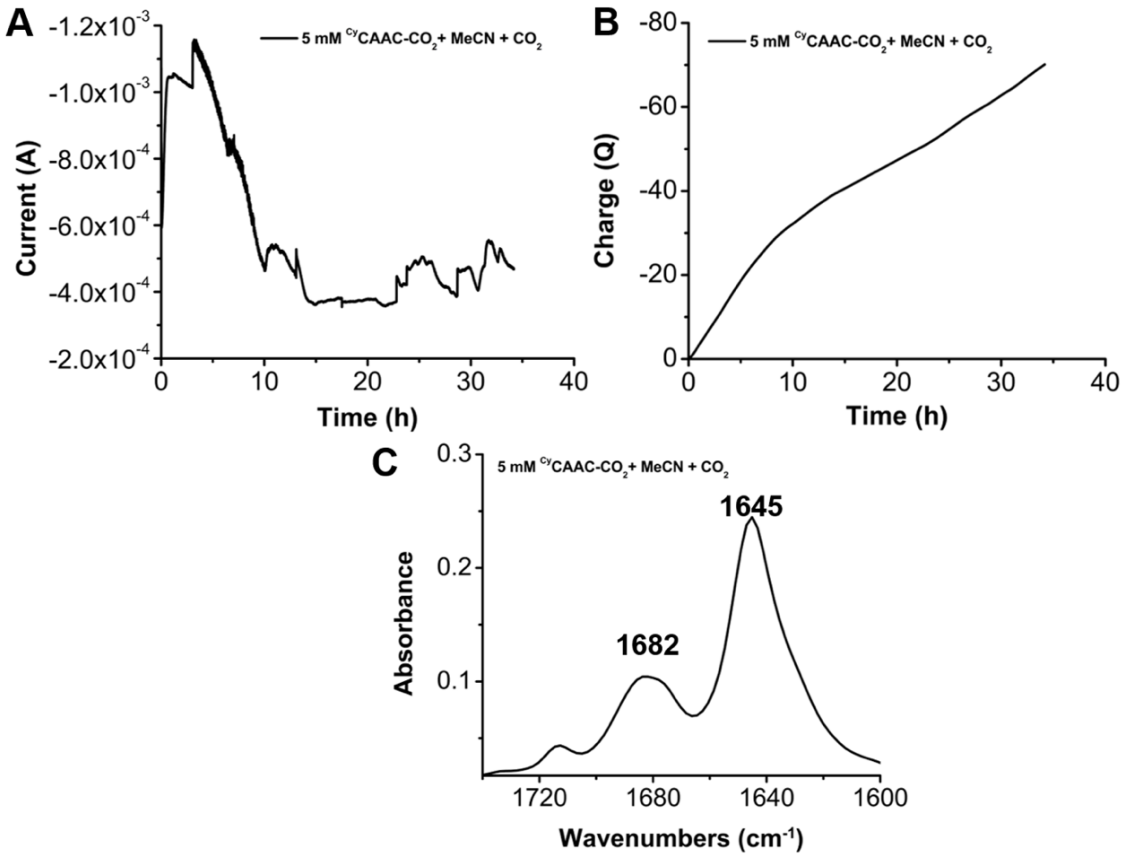

Figure SI 3.18. (A) Current vs time plot of electrolysis experiment. **(B)** Charge passed during electrolysis experiment. **(C)** IR of the bulk solution post electrolysis. Conditions: 5 mM of ^{Cy}CAAC–CO_2; 0.1 M $TBAPF_6$/MeCN; CO_2 sparge; graphite working electrode, graphite carbon counter electrode, Ag/AgCl pseudoreference electrode, and 0.5 M Fc was used as a sacrificial oxidant.

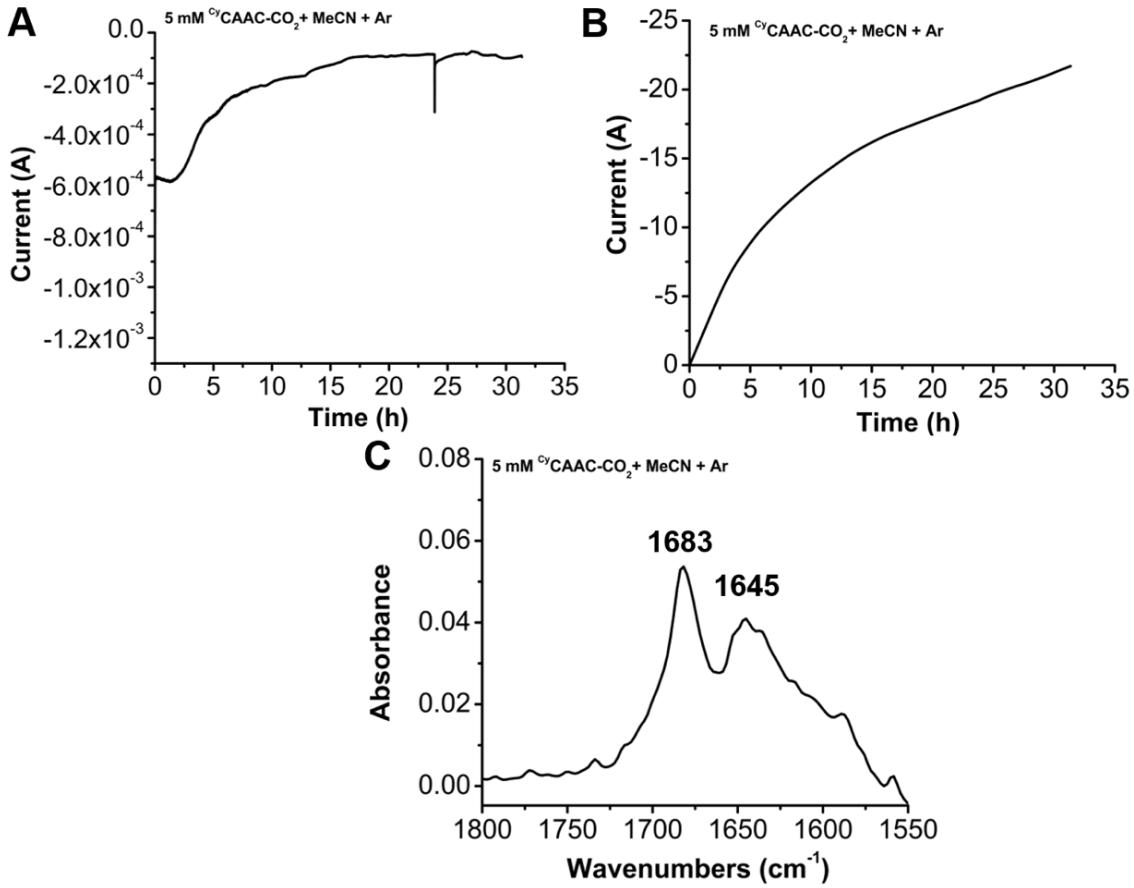

Figure SI 3.19. (A) Current vs time plot of electrolysis experiment of **[1]** under inert conditions **(B)** Charge passed during electrolysis experiment. **(C)** IR of the bulk solution post electrolysis. Conditions: 5 mM of ^{Cy}CAAC–CO_2; 0.1 M $TBAPF_6$/MeCN; Ar sparge; graphite working electrode, graphite carbon counter electrode, Ag/AgCl pseudoreference electrode, and 0.5 M Fc was used as a sacrificial oxidant.

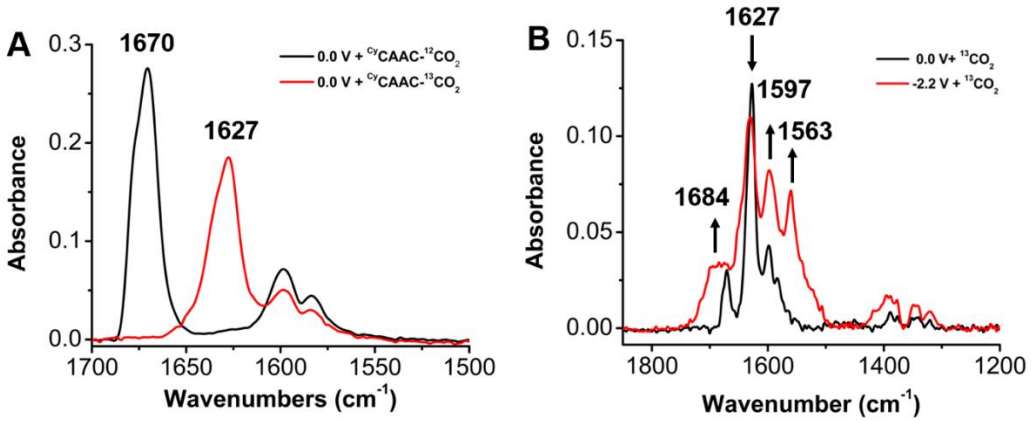

Figure SI 3.20. (A) IR-SEC comparison of a 5 mM solution of **[1]** with a CO_2 sparge (black trace) in THF versus a sparge in $^{13}CO_2$ (red trace). This shows the rapid (~less than 1 minute) between the $^{12}CO_2$ adduct with the $^{13}CO_2$ atmosphere**. (B)** IR-SEC analysis of a 5 mM solution of **[1]** in THF under a $^{13}CO_2$ atmosphere showing the reaction does not go to completion. Potentials measured against an internal Fc^+/Fc reference.

Table SI 3.2 Summarized results of the electrolysis experiments under different conditions.[a]

Solvent	**Gas**	**CO FE (%)**	**Duration (hrs)**	**mol e^- per mol ^{Cy}CAAC–CO_2**
THF	CO_2	0.2	72	0.95
THF	Ar	0.44	34.5	0.83

[a] All experiments were held at the $E_{1/2}$ values of –2.1 V (MeCN) and –2.4 (THF) vs. ferrocene with 0.1 M $TBAPF_6$ supporting electrolyte, and 0.5 M Ferrocene was used as a sacrificial oxidant. An H-Cell was utilized and equipped with Graphite electrodes from Electron Microscopy Sciences (2.5” Length x 0.120” and 1/8” Diameter) as the working and reference electrodes, and a Ag/AgCl pseudoreference electrode.

DFT calculations were performed on the Rivanna High-Performance Computing Cluster at the University of Virginia using ORCA 4.0.1.[31] Geometry optimizations were performed unrestricted with the B3LYP/G[32-34] functional and def2-TZVP[35-38] basis set with CPCM[39] to model the acetonitrile abd THF solvents. Numerical frequency calculations at the same level of theory were performed to validate the optimized geometries as minima on the potential energy surface and to generate thermochemical data. NBO and NRT analysis were performed on the optimized coordinates using NBO 6.0.[40] Molecular graphics and analyses were performed with the UCSF Chimera package. Chimera is developed by the Resource for Biocomputing, Visualization, and Informatics at the University of California, San Francisco (supported by NIGMS P41-GM103311).[41]

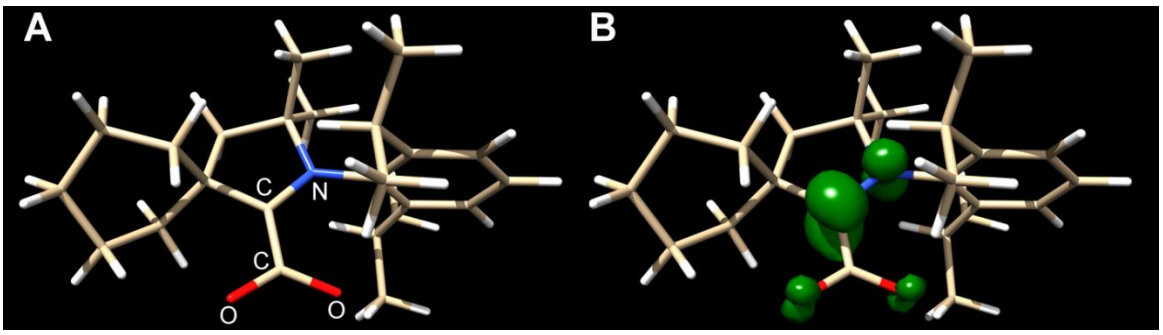

Figure SI 3.21. Spin density map showing the localization of the added electron density for **[1]**$^{-}$. ORCA 4.0.1 B3LYP/G def2-TZVP/J CPCM (THF).

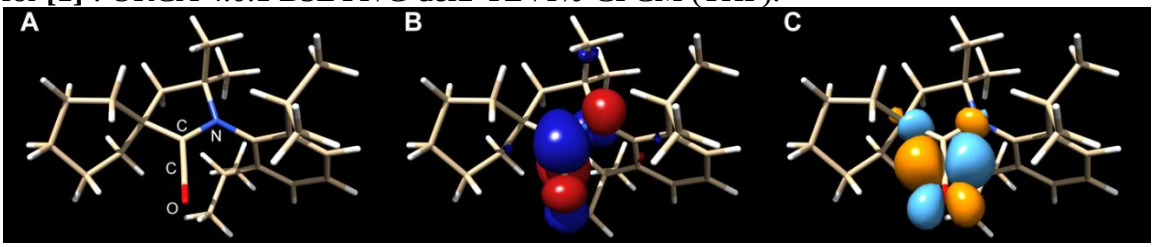

Figure SI 3.22. HOMO **(B)**-LUMO **(C)** orbitals of Natural Transition Orbital for the predicted electronic absorbance of **2** at 622 nm by TD-DFT methods. ORCA 4.0.1 B3LYP/G def2-TZVP/J CPCM (THF).

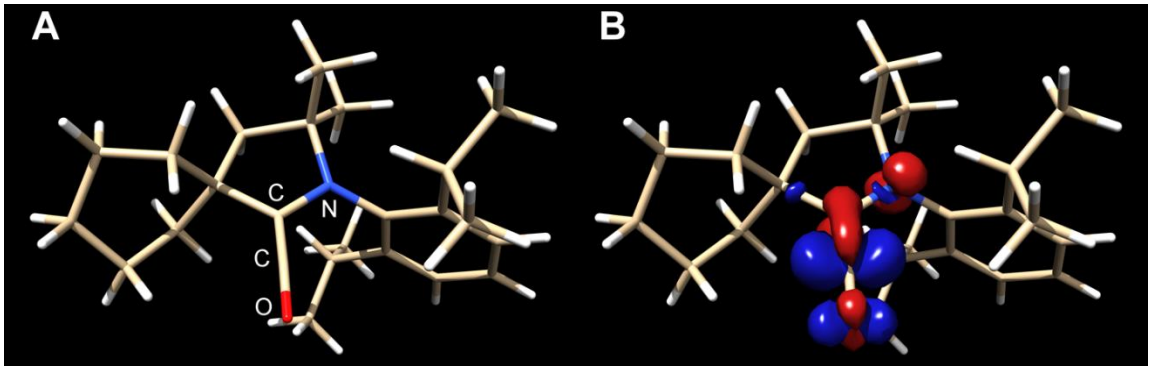

Figure SI 3.23. Difference density plot for the predicted electronic absorbance of **2** at 622 nm by TD-DFT methods; red = ground state, blue = excited state. ORCA 4.0.1 B3LYP/G def2-TZVP/J CPCM (THF).

3.5.2 DFT Coordinates

[CyCAAC–CO_2] in THF

Optimized Coordinates

1.	C	-1.577523	5.190832	-0.836061
2.	C	-2.585578	4.349179	-0.032428
3.	C	-2.373178	2.857726	-0.272407
4.	H	-3.607275	4.620391	-0.303004
5.	H	-2.484556	4.558410	1.036131
6.	C	-0.998920	2.400087	0.309628
7.	H	-2.402063	2.650877	-1.342491
8.	H	-3.169641	2.273581	0.185339
9.	C	0.046345	3.539215	0.168440
10.	C	-0.236610	4.455269	-1.017482
11.	H	1.046095	3.108971	0.103852
12.	H	0.012824	4.123730	1.091013
13.	H	-0.251558	3.866712	-1.936700
14.	H	0.577061	5.173334	-1.129437
15.	H	-1.414058	6.141464	-0.323455
16.	H	-1.994228	5.429760	-1.816374
17.	C	-1.096382	1.903180	1.765977
18.	C	-1.246313	0.375397	1.713466
19.	H	-1.921718	2.368887	2.300147
20.	H	-0.174739	2.152311	2.292219
21.	N	-0.683648	0.089181	0.313583
22.	C	-0.567235	1.155044	-0.408080
23.	C	-0.048451	1.171346	-1.834135
24.	O	-0.926703	1.129539	-2.710905
25.	O	1.185497	1.280335	-1.919909
26.	C	-0.350153	-1.247875	-0.151428
27.	C	-1.323880	-2.006873	-0.824996
28.	C	-0.978911	-3.303207	-1.207367
29.	C	0.278152	-3.822718	-0.952296
30.	C	1.232689	-3.037776	-0.328028
31.	C	0.949926	-1.734955	0.078432
32.	H	0.520278	-4.832732	-1.256050
33.	H	2.223469	-3.437407	-0.161411
34.	H	-1.709958	-3.908911	-1.724921
35.	C	2.077911	-0.918442	0.687298
36.	C	3.192675	-0.677786	-0.342070
37.	H	2.800329	-0.180042	-1.224958
38.	H	3.656031	-1.620812	-0.638296
39.	H	3.968265	-0.046833	0.097704
40.	C	2.664975	-1.588705	1.937725
41.	H	1.688881	0.057344	0.970593
42.	H	3.396172	-0.926395	2.405059
43.	H	3.179985	-2.513994	1.674040
44.	H	1.900518	-1.830647	2.673755
45.	C	-2.703317	-1.499711	-1.209600
46.	C	-2.862324	-1.450377	-2.736131
47.	H	-3.839091	-1.032383	-2.989627
48.	H	-2.806126	-2.451361	-3.167372
49.	H	-2.095491	-0.823287	-3.183817
50.	C	-3.820938	-2.358722	-0.600821
51.	H	-2.815378	-0.481639	-0.845913
52.	H	-4.791396	-1.899979	-0.799407
53.	H	-3.713335	-2.476172	0.476291
54.	H	-3.828127	-3.354921	-1.045147
55.	C	-2.694900	-0.091280	1.800903
56.	H	-3.084994	0.201530	2.775504
57.	H	-2.757147	-1.174479	1.727198
58.	H	-3.325653	0.352157	1.035844
59.	C	-0.434631	-0.323508	2.790629
60.	H	0.591594	0.030474	2.816242
61.	H	-0.442735	-1.404700	2.657358
62.	H	-0.891869	-0.100582	3.75

[CyCAAC–CO_2] in THF

IR SPECTRUM

Mode	freq (cm**-1)	T**2
6:	17.56	1.667872
7:	38.82	0.174874
8:	47.72	6.072454
9:	63.13	0.118946
10:	78.94	1.366368
11:	90.38	2.150729
12:	107.52	16.304328
13:	122.49	0.004634
14:	128.61	0.474493
15:	139.27	6.302747
16:	146.33	1.202509
17:	151.20	3.137978
18:	162.01	7.104874
19:	166.76	20.188404
20:	190.51	1.905400
21:	199.23	5.805822
22:	204.95	17.870045
23:	216.02	3.701315
24:	227.38	3.512934
25:	238.93	0.919415
26:	243.34	0.133626
27:	253.48	0.084282
28:	264.48	5.677376
29:	269.68	0.444332
30:	274.16	0.500153
31:	279.45	4.098586
32:	293.40	2.490015
33:	307.71	3.058697
34:	320.17	4.707971
35:	324.56	2.166600
36:	326.95	8.449230
37:	343.05	3.585840
38:	374.48	1.186673
39:	397.22	1.726045
40:	412.55	5.823889
41:	426.67	1.078515
42:	444.51	2.987537
43:	452.34	0.410434
44:	481.42	23.160143
45:	503.44	2.278376
46:	510.98	6.738358
47:	553.78	0.967634
48:	577.80	22.401288
49:	583.52	4.674539
50:	598.00	1.456280
51:	623.35	9.876442
52:	631.10	2.681329
53:	650.94	1.553056
54:	688.20	35.960817
55:	736.80	6.084434
56:	757.38	13.486758
57:	768.30	38.707223
58:	775.49	6.528988
59:	786.17	2.129845
60:	807.05	21.376071
61:	823.22	1.747073
62:	830.08	53.392924
63:	837.78	8.195177
64:	844.65	3.281691
65:	863.38	1.531583
66:	895.66	7.399568
67:	905.23	3.628740
68:	916.19	30.611492
69:	921.26	27.857414
70:	941.33	7.631497
71:	944.03	6.674726
72:	947.04	2.946622
73:	952.70	19.324347
74:	955.94	8.739215
75:	966.09	0.336467
76:	966.73	0.535921
77:	971.10	7.276662
78:	975.76	1.016679
79:	983.33	3.990790
80:	1000.56	9.007888
81:	1005.06	5.172704
82:	1029.45	0.658692
83:	1036.09	1.616322
84:	1065.06	19.433251
85:	1067.85	6.522901
86:	1075.01	12.027088
87:	1087.17	2.819211
88:	1098.56	0.339928
89:	1117.30	5.166862
90:	1119.21	8.416585
91:	1126.66	0.534287
92:	1139.36	17.277687
93:	1163.91	53.781262
94:	1173.93	44.397735
95:	1179.78	1.446653
96:	1184.99	16.371691
97:	1191.18	1.594507
98:	1196.45	7.414515
99:	1206.76	27.835898
100:	1220.50	11.729251
101:	1235.38	5.351399
102:	1262.03	20.755272
103:	1267.13	1.532245
104:	1280.39	1.420912
105:	1281.93	2.140671
106:	1297.86	6.058787
107:	1302.13	8.332140
108:	1304.88	2.169446
109:	1319.35	9.285775
110:	1338.67	0.816269
111:	1342.01	2.046131
112:	1350.88	3.195546
113:	1352.72	8.595881
114:	1358.24	25.567631
115:	1369.25	3.905523
116:	1377.11	3.326021
117:	1385.86	41.343512
118:	1386.27	5.088447
119:	1387.63	31.703451
120:	1389.37	14.081467
121:	1393.63	199.190026
122:	1398.21	2.849252
123:	1409.15	16.285581
124:	1410.17	1.341678
125:	1417.61	12.248242
126:	1424.69	21.959632
127:	1472.48	5.381115
128:	1475.49	14.212787
129:	1476.76	6.834297
130:	1480.07	6.413113
131:	1480.84	3.342520
132:	1481.59	1.946074
133:	1482.54	3.093320
134:	1484.78	3.071650
135:	1486.18	5.285443
136:	1489.19	13.891431
137:	1491.16	6.191598
138:	1493.37	12.167407
139:	1494.23	18.759268
140:	1496.60	4.824682
141:	1497.60	11.535226
142:	1502.33	1.626608
143:	1504.65	59.678809
144:	1508.16	5.056874
145:	1513.70	11.443793
146:	1517.00	20.392027
147:	1622.00	126.120374
148:	1624.77	8.671546
149:	1637.81	125.700354
150:	1689.16	743.818976
151:	3023.58	27.746345
152:	3032.64	45.732189
153:	3032.82	36.175704
154:	3033.37	54.657028
155:	3038.84	45.050449
156:	3039.73	71.569592
157:	3044.13	399.411651
158:	3049.23	27.979371
159:	3057.32	17.280744
160:	3058.56	38.755119
161:	3062.79	17.715480
162:	3064.86	12.653079
163:	3067.48	31.868452
164:	3077.53	45.358305
165:	3079.75	124.400955
166:	3084.98	89.905324
167:	3085.99	37.763242
168:	3088.56	256.523503
169:	3090.48	49.710907
170:	3092.78	9.394247
171:	3103.66	202.057063
172:	3106.81	30.317024
173:	3112.98	43.062745
174:	3115.96	24.948854
175:	3119.09	67.967598
176:	3119.82	72.629694
177:	3121.30	54.891789
178:	3132.93	5.286184
179:	3140.91	5.027806
180:	3145.63	2.876844
181:	3154.74	50.747190
182:	3155.76	67.734281
183:	3179.81	19.388569
184:	3196.09	99.388037
185:	3208.28	456.838395

[CyCAAC–CO_2] in THF

NRT Analysis

```
  Atom
   -----
  1.  C
  2.  C
  3.  C
  4.  H
  5.  H
  6.  C
  7.  H
  8.  H
  9.  C
 10.  C
 11.  H
 12.  H
 13.  H
 14.  H
 15.  H
 16.  H
 17.  C
 18.  C
 19.  H
 20.  H
 21.  N
 22.  C
 23.  C
 24.  O
 25.  O
 26.  C
 27.  C
 28.  C
 29.  C
 30.  C
 31.  C
 32.  H
 33.  H
 34.  H
 35.  C
 36.  C
 37.  H
 38.  H
 39.  H
 40.  C
 41.  H
 42.  H
 43.  H
 44.  H
 45.  C
 46.  C
 47.  H
 48.  H
 49.  H
 50.  C
 51.  H
 52.  H
 53.  H
 54.  H
 55.  C
 56.  H
 57.  H
 58.  H
 59.  C
 60.  H
 61.  H
 62.  H

$NRTSTRA
STR       ! Wgt = 44.14%
LONE 24 2 25 3 END
BOND S 1 2 S 1 10 S 1 15 S 1 16 S 2 3 S 2 4 S 2 5 S 3 6 S 3 7
S 3 8 S 6 9 S 6 17 S 6 22 S 9 10 S 9 11 S 9 12 S 10 13 S 10 14
S 17 18 S 17 19 S 17 20 S 18 21 S 18 55 S 18 59 D 21 22 S 21
26 S 22 23 D 23 24 S 23 25 D 26 27 S 26 31 S 27 28 S 27 45
D 28 29 S 28 34 S 29 30 S 29 32 D 30 31 S 30 33 S 31 35 S 35
36 S 35 40 S 35 41 S 36 37 S 36 38 S 36 39 S 40 42 S 40 43 S
40 44 S 45 46 S 45 50 S 45 51 S 46 47 S 46 48 S 46 49 S 50
52 S 50 53 S 50 54 S 55 56 S 55 57 S 55 58 S 59 60 S 59 61 S
59 62 END
END
STR       ! Wgt = 44.06%
LONE 24 3 25 2 END
BOND S 1 2 S 1 10 S 1 15 S 1 16 S 2 3 S 2 4 S 2 5 S 3 6 S 3 7
S 3 8 S 6 9 S 6 17 S 6 22 S 9 10 S 9 11 S 9 12 S 10 13 S 10 14
S 17 18 S 17 19 S 17 20 S 18 21 S 18 55 S 18 59 D 21 22 S 21
26 S 22 23 S 23 24 D 23 25 D 26 27 S 26 31 S 27 28 S 27 45
D 28 29 S 28 34 S 29 30 S 29 32 D 30 31 S 30 33 S 31 35 S 35
36 S 35 40 S 35 41 S 36 37 S 36 38 S 36 39 S 40 42 S 40 43 S
40 44 S 45 46 S 45 50 S 45 51 S 46 47 S 46 48 S 46 49 S 50
52 S 50 53 S 50 54 S 55 56 S 55 57 S 55 58 S 59 60 S 59 61 S
59 62 END
END
$END

$NRTSTRB
 STR       ! Wgt = 44.14%
 LONE 24 2 25 3 END
 BOND S 1 2 S 1 10 S 1 15 S 1 16 S 2 3 S 2 4 S 2 5 S 3 6 S 3 7
S 3 8 S 6 9 S 6 17 S 6 22 S 9 10 S 9 11 S 9 12 S 10 13 S 10 14
S 17 18 S 17 19 S 17 20 S 18 21 S 18 55 S 18 59 D 21 22 S 21
26 S 22 23 D 23 24 S 23 25 D 26 27 S 26 31 S 27 28 S 27 45
D 28 29 S 28 34 S 29 30 S 29 32 D 30 31 S 30 33 S 31 35 S 35
36 S 35 40 S 35 41 S 36 37 S 36 38 S 36 39 S 40 42 S 40 43 S
40 44 S 45 46 S 45 50 S 45 51 S 46 47 S 46 48 S 46 49 S 50
52 S 50 53 S 50 54 S 55 56  S 55 57 S 55 58 S 59 60 S 59 61 S
59 62 END
END
STR       ! Wgt = 44.06%
LONE 24 3 25 2 END
BOND S 1 2 S 1 10 S 1 15 S 1 16 S 2 3 S 2 4 S 2 5 S 3 6 S 3 7
S 3 8 S 6 9 S 6 17 S 6 22 S 9 10 S 9 11 S 9 12 S 10 13 S 10 14
S 17 18 S 17 19 S 17 20 S 18 21 S 18 55 S 18 59 D 21 22 S 21
26 S 22 23 S 23 24 D 23 25 D 26 27 S 26 31 S 27 28 S 27 45
D 28 29 S 28 34 S 29 30 S 29 32 D 30 31 S 30 33 S 31 35 S 35
36 S 35 40 S 35 41 S 36 37 S 36 38 S 36 39 S 40 42 S 40 43 S
40 44 S 45 46 S 45 50 S 45 51 S 46 47 S 46 48 S 46 49 S 50
52 S 50 53 S 50 54 S 55 56 S 55 57 S 55 58 S 59 60 S 59 61 S
59 62 END
END
$END
```

[CyCAAC–CO_2] in THF

NATURAL BOND ORBITALS (Summary):

```
        NBO              Occupancy    Energy
========================================
==========
Molecular unit  1  (C24H35NO2)
------ Lewis -----------------------------------
   1. CR ( 1) C  1           0.99999   -12.00327
   2. CR ( 1) C  2           0.99999   -12.00800
   3. CR ( 1) C  3           0.99999   -12.01701
   4. CR ( 1) C  6           0.99999   -12.05314
   5. CR ( 1) C  9           0.99999   -12.01542
   6. CR ( 1) C 10           0.99999   -12.00394
   7. CR ( 1) C 17           0.99999   -12.02570
   8. CR ( 1) C 18           0.99999   -12.08771
   9. CR ( 1) N 21           0.99999   -16.58068
  10. CR ( 1) C 22           0.99999   -12.10982
  11. CR ( 1) C 23           0.99999   -12.12012
  12. CR ( 1) O 24           1.00000   -21.58370
  13. CR ( 1) O 25           1.00000   -21.58367
  14. CR ( 1) C 26           0.99999   -12.07308
  15. CR ( 1) C 27           0.99999   -12.03914
  16. CR ( 1) C 28           0.99999   -12.01880
  17. CR ( 1) C 29           0.99999   -12.02292
  18. CR ( 1) C 30           0.99999   -12.01886
  19. CR ( 1) C 31           0.99999   -12.03878
  20. CR ( 1) C 35           0.99999   -12.02477
  21. CR ( 1) C 36           0.99999   -11.99241
  22. CR ( 1) C 40           0.99999   -12.00105
  23. CR ( 1) C 45           0.99999   -12.02422
  24. CR ( 1) C 46           0.99999   -11.99262
  25. CR ( 1) C 50           0.99999   -12.00121
  26. CR ( 1) C 55           0.99999   -12.01482
  27. CR ( 1) C 59           0.99999   -12.01424
  28. LP ( 1) O 24           0.98778    -1.20718
  29. LP ( 2) O 24           0.92170    -0.86133
  30. LP ( 1) O 25           0.98767    -1.20754
  31. LP ( 2) O 25           0.91990    -0.86117
  32. LP ( 3) O 25           0.78910    -0.86186
  33. BD ( 1) C  1- C  2     0.99381    -0.99708
  34. BD ( 1) C  1- C 10     0.99366    -0.99476
  35. BD ( 1) C  1- H 15     0.99119    -0.89386
  36. BD ( 1) C  1- H 16     0.99127    -0.89382
  37. BD ( 1) C  2- C  3     0.99138    -1.01117
  38. BD ( 1) C  2- H  4     0.98886    -0.89904
  39. BD ( 1) C  2- H  5     0.99046    -0.89908
  40. BD ( 1) C  3- C  6     0.97488    -1.00615
  41. BD ( 1) C  3- H  7     0.98799    -0.90897
  42. BD ( 1) C  3- H  8     0.98950    -0.91279
  43. BD ( 1) C  6- C  9     0.98124    -1.01329
  44. BD ( 1) C  6- C 17     0.98395    -1.02155
  45. BD ( 1) C  6- C 22     0.97928    -1.08110
  46. BD ( 1) C  9- C 10     0.99329    -1.00975
  47. BD ( 1) C  9- H 11     0.98921    -0.90745
  48. BD ( 1) C  9- H 12     0.98721    -0.90404
  49. BD ( 1) C 10- H 13     0.98969    -0.89724
  50. BD ( 1) C 10- H 14     0.98915    -0.89586
  51. BD ( 1) C 17- C 18     0.98482    -1.03712
  52. BD ( 1) C 17- H 19     0.98804    -0.92285
  53. BD ( 1) C 17- H 20     0.98854    -0.91838
  54. BD ( 1) C 18- N 21     0.98445    -1.17899
  55. BD ( 1) C 18- C 55     0.98739    -1.04606
  56. BD ( 1) C 18- C 59     0.98919    -1.05022
  57. BD ( 1) N 21- C 22     0.99174    -1.39168
  58. BD ( 2) N 21- C 22     0.97797    -0.88267
  59. BD ( 1) N 21- C 26     0.99008    -1.24810
  60. BD ( 1) C 22- C 23     0.98578    -1.08622
  61. BD ( 1) C 23- O 24     0.99649    -1.49590
  62. BD ( 2) C 23- O 24     0.99221    -0.90633
  63. BD ( 1) C 23- O 25     0.99469    -1.48034
  64. BD ( 1) C 26- C 27     0.98461    -1.13028
  65. BD ( 2) C 26- C 27     0.83749    -0.68903
  66. BD ( 1) C 26- C 31     0.98445    -1.12927
  67. BD ( 1) C 27- C 28     0.98601    -1.11652
  68. BD ( 1) C 27- C 45     0.98595    -1.03284
  69. BD ( 1) C 28- C 29     0.99088    -1.12153
  70. BD ( 2) C 28- C 29     0.82856    -0.66285
  71. BD ( 1) C 28- H 34     0.98792    -0.93129
  72. BD ( 1) C 29- C 30     0.99083    -1.12097
  73. BD ( 1) C 29- H 32     0.98959    -0.93214
  74. BD ( 1) C 30- C 31     0.98611    -1.11745
  75. BD ( 2) C 30- C 31     0.81863    -0.66788
  76. BD ( 1) C 30- H 33     0.98793    -0.93153
  77. BD ( 1) C 31- C 35     0.98587    -1.03278
  78. BD ( 1) C 35- C 36     0.98679    -0.99854
  79. BD ( 1) C 35- C 40     0.98911    -1.00467
  80. BD ( 1) C 35- H 41     0.98440    -0.90944
  81. BD ( 1) C 36- H 37     0.99410    -0.89607
  82. BD ( 1) C 36- H 38     0.99437    -0.89518
  83. BD ( 1) C 36- H 39     0.99299    -0.89233
  84. BD ( 1) C 40- H 42     0.99349    -0.89972
  85. BD ( 1) C 40- H 43     0.99442    -0.90233
  86. BD ( 1) C 40- H 44     0.99478    -0.90565
  87. BD ( 1) C 45- C 46     0.98703    -0.99900
  88. BD ( 1) C 45- C 50     0.98892    -1.00433
  89. BD ( 1) C 45- H 51     0.98450    -0.91080
  90. BD ( 1) C 46- H 47     0.99306    -0.89234
  91. BD ( 1) C 46- H 48     0.99444    -0.89578
  92. BD ( 1) C 46- H 49     0.99415    -0.89599
  93. BD ( 1) C 50- H 52     0.99352    -0.89965
  94. BD ( 1) C 50- H 53     0.99443    -0.90609
  95. BD ( 1) C 50- H 54     0.99446    -0.90232
  96. BD ( 1) C 55- H 56     0.98874    -0.91447
  97. BD ( 1) C 55- H 57     0.99226    -0.92164
  98. BD ( 1) C 55- H 58     0.99302    -0.92477
  99. BD ( 1) C 59- H 60     0.99322    -0.92265
 100. BD ( 1) C 59- H 61     0.99232    -0.91863
 101. BD ( 1) C 59- H 62     0.98827    -0.9138
```

[CyCAAC–CO_2]$^-$ in THF

Optimized Coordinates

1.	C	-1.998485	5.236221	-0.543249
2.	C	-2.879388	4.110897	0.043298
3.	C	-2.406083	2.730010	-0.410444
4.	H	-3.924777	4.260070	-0.238701
5.	H	-2.852613	4.151611	1.136273
6.	C	-0.986903	2.397251	0.124051
7.	H	-2.370410	2.687647	-1.499667
8.	H	-3.110990	1.964583	-0.084574
9.	C	-0.087074	3.666712	-0.010832
10.	C	-0.623815	4.712138	-0.983586
11.	H	0.918483	3.358619	-0.300267
12.	H	-0.001016	4.130292	0.978182
13.	H	-0.689771	4.247545	-1.965478
14.	H	0.081827	5.543976	-1.063461
15.	H	-1.872336	6.026496	0.202956
16.	H	-2.500131	5.695335	-1.399191
17.	C	-1.016315	1.954434	1.603788
18.	C	-1.066897	0.420986	1.638670
19.	H	-1.843186	2.399361	2.157953
20.	H	-0.091919	2.278888	2.084406
21.	N	-0.481027	0.077929	0.312068
22.	C	-0.438316	1.161192	-0.554530
23.	C	0.065306	1.092376	-1.925027
24.	O	-0.117438	2.121228	-2.655422
25.	O	0.651062	0.035181	-2.316166
26.	C	-0.285767	-1.287548	-0.062248
27.	C	-1.308198	-2.003298	-0.713130
28.	C	-1.120067	-3.362794	-0.959357
29.	C	0.053748	-4.005262	-0.596719
30.	C	1.077865	-3.276057	-0.011295
31.	C	0.934864	-1.914655	0.250018
32.	H	0.179160	-5.063292	-0.792332
33.	H	2.013191	-3.768398	0.223214
34.	H	-1.900924	-3.924470	-1.456598
35.	C	2.138569	-1.126419	0.731530
36.	C	3.149497	-0.970531	-0.415465
37.	H	2.658142	-0.530205	-1.282300
38.	H	3.563264	-1.941141	-0.702593
39.	H	3.978194	-0.329741	-0.103172
40.	C	2.812474	-1.735954	1.964454
41.	H	1.793290	-0.127563	0.985073
42.	H	3.619576	-1.086436	2.311231
43.	H	3.252254	-2.709128	1.735976
44.	H	2.107501	-1.871917	2.785007
45.	C	-2.560484	-1.333903	-1.248954
46.	C	-2.496304	-1.239793	-2.780774
47.	H	-3.351154	-0.674795	-3.160510
48.	H	-2.523069	-2.235561	-3.230333
49.	H	-1.578688	-0.744934	-3.094506
50.	C	-3.852443	-2.036268	-0.815254
51.	H	-2.582221	-0.316481	-0.870527
52.	H	-4.719901	-1.461718	-1.148714
53.	H	-3.911564	-2.143510	0.267888
54.	H	-3.929391	-3.031740	-1.256396
55.	C	-2.497287	-0.110271	1.803645
56.	H	-2.877481	0.188782	2.782074
57.	H	-2.511996	-1.199181	1.753494
58.	H	-3.172913	0.278311	1.047059
59.	C	-0.236068	-0.129241	2.798965
60.	H	0.779736	0.258181	2.780348
61.	H	-0.196836	-1.218439	2.775424
62.	H	-0.697418	0.171442	3.741615

[CyCAAC–CO_2]$^-$ in THF

IR SPECTRUM

Mode	freq (cm**-1)	T**2
6:	11.95	1.661405
7:	36.46	5.155182
8:	46.93	3.283782
9:	66.71	1.555173
10:	92.45	2.394601
11:	97.43	1.690958
12:	106.51	8.343784
13:	111.95	4.388933
14:	116.23	5.078365
15:	125.18	6.054347
16:	136.41	1.870824
17:	142.56	5.926538
18:	147.25	2.793340
19:	180.43	21.458690
20:	190.47	1.973965
21:	208.69	7.933821
22:	214.96	3.649460
23:	228.23	1.598548
24:	238.09	2.904967
25:	244.52	3.988984
26:	255.83	1.630248
27:	265.66	1.928595
28:	267.73	4.938665
29:	273.93	0.496411
30:	280.62	2.315420
31:	288.98	3.354375
32:	296.90	0.707789
33:	306.21	2.114472
34:	320.52	1.158877
35:	330.46	2.386378
36:	340.72	3.164670
37:	361.48	3.368845
38:	369.62	8.776888
39:	394.69	2.099627
40:	421.37	2.550534
41:	431.38	2.266231
42:	451.52	3.695218
43:	464.06	1.324595
44:	471.10	4.017045
45:	486.91	13.383559
46:	496.79	17.422619
47:	548.73	9.389106
48:	558.00	5.593438
49:	566.64	6.391215
50:	591.70	0.125561
51:	604.57	5.174657
52:	622.37	1.747757
53:	626.01	1.493754
54:	654.46	5.160982
55:	710.21	45.888770
56:	753.51	16.419945
57:	760.50	10.683274
58:	766.61	17.016739
59:	771.57	3.976127
60:	798.22	15.863771
61:	818.00	15.225446
62:	820.53	21.128973
63:	833.02	9.606686
64:	843.70	5.176102
65:	858.34	2.053340
66:	894.34	3.200052
67:	907.78	5.126116
68:	911.82	1.908596
69:	923.62	3.457312
70:	933.40	8.409502
71:	939.58	3.029193
72:	945.41	4.537608
73:	955.61	5.601741
74:	956.09	16.979741
75:	960.17	2.779032
76:	966.17	0.821198
77:	966.54	8.541031
78:	968.06	3.224746
79:	973.73	2.979810
80:	991.37	7.512991
81:	1003.33	15.423113
82:	1019.93	1.537024
83:	1029.43	6.569788
84:	1054.75	1.344045
85:	1064.03	7.527884
86:	1077.10	27.329109
87:	1082.89	4.520763
88:	1098.01	3.430992
89:	1118.64	8.569307
90:	1124.83	7.080312
91:	1136.19	17.504593
92:	1143.67	1.183961
93:	1159.53	18.271712
94:	1173.19	27.620262
95:	1175.68	4.781226
96:	1184.68	4.579405
97:	1185.57	44.432503
98:	1202.71	23.607486
99:	1209.90	80.463756
100:	1226.59	77.275507
101:	1233.32	5.816698
102:	1245.69	198.484762
103:	1267.19	8.758148
104:	1275.46	13.656597
105:	1278.17	16.642835
106:	1281.78	45.861911
107:	1283.40	1.295596
108:	1295.32	6.230207
109:	1307.63	48.498059
110:	1335.56	306.432825
111:	1342.75	5.138212
112:	1345.88	23.566304
113:	1350.94	25.564115
114:	1355.73	38.535715
115:	1362.06	8.999687
116:	1364.62	3.191709
117:	1365.57	0.709237
118:	1373.53	17.430468
119:	1376.82	3.155530
120:	1379.96	6.978734
121:	1383.98	5.217253
122:	1389.39	4.548899
123:	1394.14	23.850144
124:	1408.62	23.793600
125:	1411.09	16.922197
126:	1415.79	16.155043
127:	1463.02	107.554494
128:	1470.60	3.821101
129:	1474.28	3.568066
130:	1476.34	9.878306
131:	1478.96	4.625353
132:	1480.39	5.798056
133:	1481.48	0.395132
134:	1481.96	15.141147
135:	1485.07	20.466961
136:	1487.84	10.215826
137:	1488.70	40.773446
138:	1490.27	8.014107
139:	1490.67	12.213063
140:	1493.79	9.741838
141:	1494.93	12.456462
142:	1496.74	10.214721
143:	1499.59	21.909723
144:	1505.46	60.441382
145:	1507.89	116.897418
146:	1512.49	40.896904
147:	1512.75	26.699706
148:	1525.17	784.843123
149:	1616.19	8.400590
150:	1628.14	0.891256
151:	2994.86	63.684428
152:	3004.57	28.769168
153:	3011.22	81.610930
154:	3016.40	88.009997
155:	3017.29	28.470403
156:	3027.05	133.899735
157:	3027.26	35.027623
158:	3027.74	108.137524
159:	3030.70	65.424720
160:	3038.58	15.608494
161:	3040.82	65.106873
162:	3046.74	34.235453
163:	3049.07	91.897825
164:	3059.03	105.291297
165:	3064.43	56.524823
166:	3068.42	54.573660
167:	3070.14	56.635098
168:	3075.64	29.295996
169:	3080.13	70.398999
170:	3086.79	23.663205
171:	3089.40	61.725043
172:	3095.55	14.989002
173:	3098.07	101.988396
174:	3100.23	43.853371
175:	3104.53	80.029912
176:	3107.51	34.860290
177:	3110.24	28.773986
178:	3115.39	9.035795
179:	3118.50	25.516934
180:	3124.84	25.683916
181:	3132.06	50.129087
182:	3146.53	36.812419
183:	3158.25	1.639629
184:	3171.37	34.019261
185:	3182.30	47.855842

[CyCAAC–CO_2]$^-$ in THF

NRT Analysis

```
 Atom
  -----
  1.  C
  2.  C
  3.  C
  4.  H
  5.  H
  6.  C
  7.  H
  8.  H
  9.  C
 10.  C
 11.  H
 12.  H
 13.  H
 14.  H
 15.  H
 16.  H
 17.  C
 18.  C
 19.  H
 20.  H
 21.  N
 22.  C
 23.  C
 24.  O
 25.  O
 26.  C
 27.  C
 28.  C
 29.  C
 30.  C
 31.  C
 32.  H
 33.  H
 34.  H
 35.  C
 36.  C
 37.  H
 38.  H
 39.  H
 40.  C
 41.  H
 42.  H
 43.  H
 44.  H
 45.  C
 46.  C
 47.  H
 48.  H
 49.  H
 50.  C
 51.  H
 52.  H
 53.  H
 54.  H
 55.  C
 56.  H
 57.  H
 58.  H
 59.  C
 60.  H
 61.  H
 62.  H
$NRTSTRA
 STR       ! Wgt = 36.15%
 LONE 21 1 24 3 25 3 END
 BOND S 1 2 S 1 10 S 1 15 S 1 16 S 2 3 S 2 4 S 2 5 S 3 6 S
3 7 S 3 8 S 6 9 S 6 17 S 6 22 S 9 10 S 9 11 S 9 12 S 10 13 S
10 14 S 17 18 S 17 19 S 17 20 S 18 21 S 18 55 S 18 59 S 21
22 S 21 26 D 22 23 S 23 24 S 23 25 D 26 27 S 26 31 S 27 28
S 27 45 D 28 29 S 28 34 S 29 30 S 29 32 D 30 31 S 30 33 S
31 35 S 35 36 S 35 40 S 35 41 S 36 37 S 36 38 S 36 39 S 40
42 S 40 43 S 40 44 S 45 46 S 45 50 S 45 51 S 46 47 S 46 48
S 46 49 S 50 52 S 50 53 S 50 54 S 55 56 55 57 S 55 58 S 59
60 S 59 61 S 59 62 END
STR       ! Wgt = 28.68%
LONE 21 1 22 1 24 3 25 2 END
BOND S 1 2 S 1 10 S 1 15 S 1 16 S 2 3 S 2 4 S 2 5 S 3 6 S 3
7 S 3 8 S 6 9 S 6 17 S 6 22 S 9 10 S 9 11 S 9 12 S 10 13 S 10
14 S 17 18 S 17 19 S 17 20 S 18 21 S 18 55 S 18 59 S 21 22
S 21 26 S 22 23 S 23 24 D 23 25 D 26 27 S 26 31 S 27 28 S
27 45 D 28 29 S 28 34 S 29 30 S 29 32 D 30 31 S 30 33 S 31
35 S 35 36 S 35 40 S 35 41 S 36 37 S 36 38 S 36 39 S 40 42
S 40 43 S 40 44 S 45 46 S 45 50 S 45 51 S 46 47 S 46 48 S
46 49 S 50 52 S 50 53 S 50 54 S 55 56 S 55 57 S 55 58 S 59
60 S 59 61 S 59 62
END
STR       ! Wgt = 28.62%
LONE 21 1 22 1 24 2 25 3 END
BOND S 1 2 S 1 10 S 1 15 S 1 16 S 2 3 S 2 4 S 2 5 S 3 6 S 3
7 S 3 8 S 6 9 S 6 17 S 6 22 S 9 10 S 9 11 S 9 12 S 10 13 S 10
14 S 17 18 S 17 19 S 17 20 S 18 21 S 18 55 S 18 59 S 21 22
S 21 26 S 22 23 D 23 24 S 23 25 D 26 27 S 26 31 S 27 28 S
27 45 D 28 29 S 28 34 S 29 30 S 29 32 D 30 31 S 30 33 S 31
35 S 35 36 S 35 40 S 35 41 S 36 37 S 36 38 S 36 39 S 40 42
S 40 43 S 40 44 S 45 46 S 45 50 S 45 51 S 46 47 S 46 48 S
46 49 S 50 52 S 50 53 S 50 54 S 55 56 S 55 57 S 55 58 S 59
60 S 59 61 S 59 62 END
$END

$NRTSTRB
STR       ! Wgt = 49.16%
LONE 24 3 25 2 END
BOND S 1 2 S 1 10 S 1 15 S 1 16 S 2 3 S 2 4 S 2 5 S 3 6 S 3
7 S 3 8 S 6 9 S 6 17 S 6 22 S 9 10 S 9 11 S 9 12 S 10 13 S 10
14 S 17 18 S 17 19 S 17 20 S 18 21 S 18 55 S 18 59 D 21 22
S 21 26 S 22 23 S 23 24 D 23 25 D 26 27 S 26 31 S 27 28 S
27 45 D 28 29 S 28 34 S 29 30 S 29 32 D 30 31 S 30 33 S 31
35 S 35 36 S 35 40 S 35 41 S 36 37 S 36 38 S 36 39 S 40 42
S 40 43 S 40 44 S 45 46 S 45 50 S 45 51 S 46 47 S 46 48 S
46 49 S 50 52 S 50 53 S 50 54 S 55 56 S 55 57 S 55 58 S 59
60 S 59 61 S 59 62
END
STR       ! Wgt = 42.82%
 LONE 24 2 25 3 END
 BOND S 1 2 S 1 10 S 1 15 S 1 16 S 2 3 S 2 4 S 2 5 S 3 6 S 3
7 S 3 8 S 6 9 S 6 17 S 6 22 S 9 10 S 9 11 S 9 12 S 10 13 S 10
14 S 17 18 S 17 19 S 17 20 S 18 21 S 18 55 S 18 59 D 21 22
S 21 26 S 22 23 D 23 24 S 23 25 D 26 27 S 26 31 S 27 28 S
27 45 D 28 29 S 28 34S 29 30 S 29 32 D 30 31 S 30 33 S 31
35 S 35 36 S 35 40 S 35 41 S 36 37 S 36 38 S 36 39 S 40 42
S 40 43 S 40 44 S 45 46 S 45 50 S 45 51 S 46 47 S 46 48 S
46 49 S 50 52 S 50 53 S 50 54 S 55 56  S 55 57 S 55 58 S 59
60 S 59 61 S 59 62
END
$END
```

[CyCAAC–CO_2]$^-$ in THF

NATURAL BOND ORBITALS (Summary):

```
        NBO              Occupancy    Energy
=========================================
======
Molecular unit  1  (C24H35NO2)
----- Lewis -----------------------------------
  1. CR ( 1) C  1           0.99999   -11.98088
  2. CR ( 1) C  2           0.99999   -11.98215
  3. CR ( 1) C  3           0.99999   -11.97545
  4. CR ( 1) C  6           0.99999   -11.99821
  5. CR ( 1) C  9           0.99999   -11.97552
  6. CR ( 1) C 10           0.99999   -11.96996
  7. CR ( 1) C 17           0.99999   -11.98373
  8. CR ( 1) C 18           0.99999   -12.03815
  9. CR ( 1) N 21           0.99999   -16.47193
 10. CR ( 1) C 22           0.99999   -11.98481
 11. CR ( 1) C 23           0.99999   -12.04567
 12. CR ( 1) O 24           1.00000   -21.50819
 13. CR ( 1) O 25           1.00000   -21.50794
 14. CR ( 1) C 26           0.99999   -12.02669
 15. CR ( 1) C 27           0.99999   -11.99867
 16. CR ( 1) C 28           0.99999   -11.98908
 17. CR ( 1) C 29           0.99999   -11.99331
 18. CR ( 1) C 30           0.99999   -11.98895
 19. CR ( 1) C 31           0.99999   -11.99758
 20. CR ( 1) C 35           0.99999   -11.99383
 21. CR ( 1) C 36           0.99999   -11.97097
 22. CR ( 1) C 40           0.99999   -11.98153
 23. CR ( 1) C 45           0.99999   -11.99519
 24. CR ( 1) C 46           0.99999   -11.97338
 25. CR ( 1) C 50           0.99999   -11.98190
 26. CR ( 1) C 55           0.99999   -11.98164
 27. CR ( 1) C 59           0.99999   -11.98227
 28. LP ( 1) O 24           0.98832    -1.14481
 29. LP ( 2) O 24           0.94826    -0.79324
 30. LP ( 3) O 24           0.79047    -0.76525
 31. LP ( 1) O 25           0.98814    -1.14245
 32. LP ( 2) O 25           0.94440    -0.79120
 33. BD ( 1) C  1- C  2      0.99381    -0.96946
 34. BD ( 1) C  1- C 10      0.99392    -0.96969
 35. BD ( 1) C  1- H 15      0.99187    -0.87124
 36. BD ( 1) C  1- H 16      0.99154    -0.87137
 37. BD ( 1) C  2- C  3      0.99225    -0.97649
 38. BD ( 1) C  2- H  4      0.99005    -0.87383
 39. BD ( 1) C  2- H  5      0.99065    -0.87367
 40. BD ( 1) C  3- C  6      0.97876    -0.96030
 41. BD ( 1) C  3- H  7      0.98789    -0.86604
 42. BD ( 1) C  3- H  8      0.98872    -0.87440
 43. BD ( 1) C  6- C  9      0.98317    -0.95692
 44. BD ( 1) C  6- C 17      0.98487    -0.96902
 45. BD ( 1) C  6- C 22      0.98255    -0.98413
 46. BD ( 1) C  9- C 10      0.99347    -0.97265
 47. BD ( 1) C  9- H 11      0.98937    -0.86578
 48. BD ( 1) C  9- H 12      0.98913    -0.86543
 49. BD ( 1) C 10- H 13      0.98945    -0.86411
 50. BD ( 1) C 10- H 14      0.98900    -0.86509
 51. BD ( 1) C 17- C 18      0.98457    -0.98962
 52. BD ( 1) C 17- H 19      0.98980    -0.88354
 53. BD ( 1) C 17- H 20      0.98851    -0.87780
 54. BD ( 1) C 18- N 21      0.98487    -1.12762
 55. BD ( 1) C 18- C 55      0.98728    -0.99502
 56. BD ( 1) C 18- C 59      0.98853    -0.99909
 57. BD ( 1) N 21- C 22      0.98938    -1.20123
 58. BD ( 2) N 21- C 22      0.95487    -0.74005
 59. BD ( 1) N 21- C 26      0.99032    -1.18335
 60. BD ( 1) C 22- C 23      0.99013    -1.02352
 61. BD ( 1) C 23- O 24      0.99651    -1.39228
 62. BD ( 1) C 23- O 25      0.99699    -1.39827
 63. BD ( 2) C 23- O 25      0.98236    -0.81301
 64. BD ( 1) C 26- C 27      0.98368    -1.08379
 65. BD ( 2) C 26- C 27      0.81548    -0.64171
 66. BD ( 1) C 26- C 31      0.98403    -1.08269
 67. BD ( 1) C 27- C 28      0.98664    -1.08338
 68. BD ( 1) C 27- C 45      0.98554    -0.99912
 69. BD ( 1) C 28- C 29      0.99046    -1.08999
 70. BD ( 2) C 28- C 29      0.84290    -0.63451
 71. BD ( 1) C 28- H 34      0.98810    -0.90340
 72. BD ( 1) C 29- C 30      0.99043    -1.08942
 73. BD ( 1) C 29- H 32      0.98986    -0.90609
 74. BD ( 1) C 30- C 31      0.98717    -1.08372
 75. BD ( 2) C 30- C 31      0.82541    -0.63503
 76. BD ( 1) C 30- H 33      0.98820    -0.90342
 77. BD ( 1) C 31- C 35      0.98537    -0.99797
 78. BD ( 1) C 35- C 36      0.98640    -0.97135
 79. BD ( 1) C 35- C 40      0.99099    -0.98248
 80. BD ( 1) C 35- H 41      0.98311    -0.87783
 81. BD ( 1) C 36- H 37      0.99392    -0.87180
 82. BD ( 1) C 36- H 38      0.99482    -0.87246
 83. BD ( 1) C 36- H 39      0.99349    -0.87217
 84. BD ( 1) C 40- H 42      0.99402    -0.88046
 85. BD ( 1) C 40- H 43      0.99469    -0.88309
 86. BD ( 1) C 40- H 44      0.99476    -0.88392
 87. BD ( 1) C 45- C 46      0.98684    -0.97400
 88. BD ( 1) C 45- C 50      0.99049    -0.98212
 89. BD ( 1) C 45- H 51      0.98325    -0.88233
 90. BD ( 1) C 46- H 47      0.99356    -0.87367
 91. BD ( 1) C 46- H 48      0.99482    -0.87432
 92. BD ( 1) C 46- H 49      0.99433    -0.87488
 93. BD ( 1) C 50- H 52      0.99400    -0.88059
 94. BD ( 1) C 50- H 53      0.99473    -0.88473
 95. BD ( 1) C 50- H 54      0.99473    -0.88360
 96. BD ( 1) C 55- H 56      0.99125    -0.88370
 97. BD ( 1) C 55- H 57      0.99291    -0.88712
 98. BD ( 1) C 55- H 58      0.99333    -0.89277
 99. BD ( 1) C 59- H 60      0.99374    -0.88936
100. BD ( 1) C 59- H 61      0.99312    -0.88720
101. BD ( 1) C 59- H 62      0.99115    -0.88396
```

[CyCAAC-CO] in THF

Optimized Coordinates

1.	C	-0.743463	5.285104	-0.561489
2.	C	-1.915829	4.707233	0.253835
3.	C	-2.164943	3.249666	-0.124215
4.	H	-2.818154	5.299157	0.090124
5.	H	-1.698017	4.769924	1.323878
6.	C	-0.978051	2.341779	0.287433
7.	H	-2.309675	3.188506	-1.205850
8.	H	-3.084020	2.878812	0.328841
9.	C	0.341490	3.152303	0.224500
10.	C	0.315413	4.208919	-0.874021
11.	H	1.178479	2.466507	0.097789
12.	H	0.490043	3.651115	1.187662
13.	H	0.094591	3.730526	-1.832294
14.	H	1.299941	4.666192	-0.985306
15.	H	-0.283158	6.105473	-0.006210
16.	H	-1.118394	5.710332	-1.494909
17.	C	-1.154918	1.725413	1.700535
18.	C	-1.647155	0.273259	1.531179
19.	H	-1.832154	2.323518	2.309707
20.	H	-0.187726	1.704885	2.203149
21.	N	-1.017079	-0.079344	0.238873
22.	C	-0.917652	1.066159	-0.567022
23.	C	-0.891770	1.055708	-1.878571
24.	O	-0.723923	1.058571	-3.047376
25.	C	-0.471045	-1.333246	-0.147361
26.	C	-1.282572	-2.299366	-0.770240
27.	C	-0.721674	-3.528597	-1.119153
28.	C	0.618047	-3.793393	-0.886554
29.	C	1.424039	-2.818963	-0.314560
30.	C	0.902936	-1.582084	0.057546
31.	H	1.038683	-4.752350	-1.162019
32.	H	2.474934	-3.024603	-0.157822
33.	H	-1.340566	-4.282214	-1.588812
34.	C	1.827287	-0.521330	0.618829
35.	C	2.694010	0.078450	-0.496551
36.	H	2.075448	0.480210	-1.299801
37.	H	3.354881	-0.679246	-0.923611
38.	H	3.314937	0.887339	-0.104861
39.	C	2.698871	-1.034796	1.768308
40.	H	1.202535	0.277541	1.009929
41.	H	3.276602	-0.212164	2.194342
42.	H	3.406063	-1.794680	1.429888
43.	H	2.091763	-1.471613	2.562760
44.	C	-2.733870	-2.026051	-1.109496
45.	C	-2.970236	-2.074640	-2.624734
46.	H	-4.005470	-1.812002	-2.852906
47.	H	-2.782536	-3.073158	-3.024784
48.	H	-2.318454	-1.373457	-3.147380
49.	C	-3.679373	-2.986227	-0.380191
50.	H	-2.958108	-1.015507	-0.779385
51.	H	-4.720063	-2.712728	-0.567695
52.	H	-3.510725	-2.968325	0.697961
53.	H	-3.536677	-4.013551	-0.722191
54.	C	-3.180958	0.214286	1.471546
55.	H	-3.608130	0.666163	2.368969
56.	H	-3.529668	-0.815727	1.415567
57.	H	-3.564858	0.751013	0.604558
58.	C	-1.154053	-0.633892	2.651059
59.	H	-0.072152	-0.581092	2.760999
60.	H	-1.433202	-1.671812	2.464053
61.	H	-1.609449	-0.327513	3.593501

[CyCAAC–CO] in THF

IR SPECTRUM

Mode	freq (cm**-1)	T**2
6:	31.04	0.010390
7:	31.76	1.379723
8:	43.06	0.057559
9:	54.71	0.150783
10:	75.45	0.957231
11:	81.91	1.404793
12:	88.60	0.242263
13:	97.03	1.489893
14:	105.38	0.442444
15:	126.31	0.220780
16:	135.60	2.099672
17:	140.15	1.052690
18:	143.93	0.128561
19:	195.90	0.166902
20:	206.45	3.017201
21:	215.29	0.829614
22:	224.53	3.570533
23:	233.67	1.924897
24:	242.22	0.827035
25:	243.75	0.977721
26:	254.76	0.671650
27:	256.88	1.326401
28:	266.55	0.814836
29:	272.05	1.443762
30:	282.46	2.959618
31:	297.74	2.916177
32:	301.92	0.377691
33:	320.16	0.342076
34:	321.91	0.228047
35:	342.27	3.602228
36:	355.11	8.267802
37:	364.98	0.933754
38:	398.06	1.843695
39:	416.32	2.633799
40:	434.18	0.630534
41:	444.15	5.442281
42:	452.87	5.802710
43:	465.98	14.312509
44:	492.01	3.104197
45:	521.04	0.236004
46:	545.96	6.539867
47:	549.48	2.203375
48:	560.77	3.171179
49:	577.59	10.699887
50:	599.65	3.040312
51:	601.73	5.215008
52:	631.85	2.996561
53:	651.54	2.147941
54:	657.24	0.399394
55:	730.97	2.442016
56:	772.08	16.645910
57:	773.96	8.654235
58:	807.10	9.860807
59:	816.33	5.792583
60:	823.98	6.227564
61:	839.66	11.388952
62:	844.50	18.387362
63:	861.63	2.214509
64:	893.28	0.140467
65:	904.66	3.672797
66:	917.42	1.336001
67:	934.37	0.780887
68:	938.69	1.125263
69:	942.03	1.061060
70:	947.48	6.033280
71:	948.65	5.218837
72:	951.06	6.097540
73:	965.60	0.670479
74:	965.79	0.327463
75:	968.60	0.958722
76:	973.86	2.039510
77:	991.56	2.637631
78:	999.33	3.098960
79:	1015.39	1.844572
80:	1025.73	0.716502
81:	1036.54	3.122076
82:	1061.79	7.542025
83:	1066.22	7.563124
84:	1072.50	22.725657
85:	1084.08	0.617350
86:	1094.37	0.159412
87:	1122.00	1.178175
88:	1124.15	1.247364
89:	1130.80	7.678808
90:	1144.87	3.109122
91:	1159.62	2.895043
92:	1171.75	17.401359
93:	1174.93	1.072773
94:	1176.63	8.671283
95:	1186.24	1.528302
96:	1202.00	9.355992
97:	1207.48	117.860867
98:	1236.46	6.812254
99:	1238.10	17.845816
100:	1261.02	20.627065
101:	1264.87	55.986868
102:	1277.73	4.585705
103:	1278.96	10.547356
104:	1284.51	3.227592
105:	1291.89	6.339089
106:	1305.20	9.702279
107:	1318.83	23.358234
108:	1343.37	5.525848
109:	1345.78	2.437584
110:	1359.33	41.194621
111:	1362.95	22.224832
112:	1364.13	46.711562
113:	1366.25	20.158838
114:	1373.05	2.540946
115:	1375.15	0.903180
116:	1376.04	28.722646
117:	1382.79	1.084858
118:	1392.06	193.344711
119:	1393.67	15.456315
120:	1398.02	12.842476
121:	1400.88	2.323770
122:	1412.84	4.884769
123:	1414.20	11.101262
124:	1416.73	10.510021
125:	1473.78	4.920268
126:	1476.91	10.630538
127:	1477.27	16.512424
128:	1477.80	28.302549
129:	1480.49	4.459733
130:	1481.85	0.263058
131:	1482.78	0.993810
132:	1484.21	10.679390
133:	1485.13	4.320860
134:	1487.71	0.846750
135:	1488.63	23.715250
136:	1489.06	6.829991
137:	1491.25	1.634885
138:	1494.26	23.514095
139:	1495.86	12.141433
140:	1498.33	36.043011
141:	1498.63	3.917504
142:	1503.69	9.216223
143:	1505.10	2.161687
144:	1506.34	24.036821
145:	1615.65	11.101354
146:	1629.86	0.652403
147:	2127.27	874.448279
148:	3011.72	17.495770
149:	3022.92	31.810204
150:	3023.43	43.080623
151:	3024.35	80.012624
152:	3026.81	45.722468
153:	3027.15	69.695517
154:	3029.51	38.080580
155:	3035.23	43.781334
156:	3037.43	58.255270
157:	3038.54	37.992182
158:	3044.60	26.916193
159:	3055.12	36.540670
160:	3057.34	50.264355
161:	3067.64	79.223516
162:	3076.68	47.748980
163:	3077.67	144.058761
164:	3078.93	108.199279
165:	3083.34	4.103749
166:	3085.26	13.573572
167:	3087.56	55.458674
168:	3089.77	72.459412
169:	3093.57	41.565432
170:	3094.03	58.606393
171:	3097.99	46.999564
172:	3098.24	24.329314
173:	3100.60	26.326381
174:	3103.97	6.146963
175:	3107.91	78.664987
176:	3114.95	63.194528
177:	3122.63	46.444586
178:	3123.61	49.058267
179:	3128.09	16.883557
180:	3166.78	8.379345
181:	3180.46	95.732632
182:	3191.44	105.83896

[CyCAAC–CO] in THF

NRT Analysis

```
 Atom
  -----
  1.  C
  2.  C
  3.  C
  4.  H
  5.  H
  6.  C
  7.  H
  8.  H
  9.  C
 10.  C
 11.  H
 12.  H
 13.  H
 14.  H
 15.  H
 16.  H
 17.  C
 18.  C
 19.  H
 20.  H
 21.  N
 22.  C
 23.  C
 24.  O
 25.  C
 26.  C
 27.  C
 28.  C
 29.  C
 30.  C
 31.  H
 32.  H
 33.  H
 34.  C
 35.  C
 36.  H
 37.  H
 38.  H
 39.  C
 40.  H
 41.  H
 42.  H
 43.  H
 44.  C
 45.  C
 46.  H
 47.  H
 48.  H
 49.  C
 50.  H
 51.  H
 52.  H
 53.  H
 54.  C
 55.  H
 56.  H
 57.  H
 58.  C
 59.  H
 60.  H
 61.  H

$NRTSTRA
 STR       ! Wgt = 69.45%
 LONE 21 1 24 2 END
 BOND S 1 2 S 1 10 S 1 15 S 1 16 S 2 3 S 2 4 S 2 5 S 3 6 S 3 7
S 3 8 S 6 9 S 6 17 S 6 22 S 9 10 S 9 11 S 9 12 S 10 13 S 10 14
S 17 18 S 17 19 S 17 20 S 18 21 S 18 54 S 18 58 S 21 22 S 21
25 D 22 23 D 23 24 D 25 26 S 25 30 S 26 27 S 26 44 D 27 28
S 27 33 S 28 29 S 28 31 D 29 30 S 29 32 S 30 34 S 34 35 S 34
39 S 34 40 S 35 36  35 37 S 35 38 S 39 41 S 39 42 S 39 43 S
44 45 S 44 49 S 44 50 S 45 46 S 45 47 S 45 48 S 49 51 S 49
52 S 49 53 S 54 55 S 54 56 S 54 57 S 58 59 S 58 60 S 58 61
END
END
STR       ! Wgt = 23.02%
LONE 21 1 22 1 24 1 END
BOND S 1 2 S 1 10 S 1 15 S 1 16 S 2 3 S 2 4 S 2 5 S 3 6 S 3 7
S 3 8 S 6 9 S 6 17 S 6 22 S 9 10 S 9 11 S 9 12 S 10 13 S 10 14
S 17 18 S 17 19 S 17 20 S 18 21 S 18 54 S 18 58 S 21 22 S 21
25 S 22 23 T 23 24 D 25 26 S 25 30 S 26 27 S 26 44 D 27 28 S
27 33 S 28 29 S 28 31 D 29 30 S 29 32 S 30 34 S 34 35 S 34
39 S 34 40 S 35 36  S 35 37 S 35 38 S 39 41 S 39 42 S 39 43 S
44 45 S 44 49 S 44 50 S 45 46 S 45 47 S 45 48 S 49 51 S 49
52 S 49 53 S 54 55 S 54 56S 54 57 S 58 59 S 58 60 S 58 61
END
 END
 $END

$NRTSTRB
 STR       ! Wgt = 69.45%
 LONE 21 1 24 2 END
 BOND S 1 2 S 1 10 S 1 15 S 1 16 S 2 3 S 2 4 S 2 5 S 3 6 S 3 7
S 3 8 S 6 9 S 6 17 S 6 22 S 9 10 S 9 11 S 9 12 S 10 13 S 10 14
S 17 18 S 17 19 S 17 20 S 18 21 S 18 54 S 18 58 S 21 22 S 21
25 D 22 23 D 23 24 D 25 26 S 25 30 S 26 27 S 26 44 D 27 28
S 27 33 S 28 29 S 28 31 D 29 30 S 29 32 S 30 34 S 34 35 S 34
39 S 34 40 S 35 36 S 35 37 S 35 38 S 39 41 S 39 42 S 39 43 S
44 45 S 44 49 S 44 50 S 45 46 S 45 47 S 45 48 S 49 51 S 49
52 S 49 53 S 54 55 S 54 56 S 54 57 S 58 59 S 58 60 S 58 61
END
END
STR       ! Wgt = 23.02%
LONE 21 1 22 1 24 1 END
BOND S 1 2 S 1 10 S 1 15 S 1 16 S 2 3 S 2 4 S 2 5 S 3 6 S 3 7
S 3 8 S 6 9 S 6 17 S 6 22 S 9 10 S 9 11 S 9 12 S 10 13 S 10 14
S 17 18 S 17 19 S 17 20 S 18 21 S 18 54 S 18 58 S 21 22 S 21
25 S 22 23 T 23 24 D 25 26 S 25 30 S 26 27 S 26 44 D 27 28 S
27 33 S 28 29 S 28 31 D 29 30 S 29 32 S 30 34 S 34 35 S 34
39 S 34 40 S 35 36 S 35 37 S 35 38 S 39 41 S 39 42 S 39 43 S
44 45 S 44 49 S 44 50 S 45 46 S 45 47 S 45 48 S 49 51 S 49
52 S 49 53 S 54 55 S 54 56  S 54 57 S 58 59 S 58 60 S 58 61
END
END
$END
```

[CyCAAC–CO] in THF

NATURAL BOND ORBITALS (Summary):

```
        NBO              Occupancy    Energy
=========================================
=========
Molecular unit  1  (C24H35NO)
------ Lewis -----------------------------------
   1. CR ( 1) C  1           0.99999   -12.00087
   2. CR ( 1) C  2           0.99999   -12.00182
   3. CR ( 1) C  3           0.99999   -12.00420
   4. CR ( 1) C  6           0.99999   -12.03801
   5. CR ( 1) C  9           0.99999   -12.00418
   6. CR ( 1) C 10           0.99999   -12.00199
   7. CR ( 1) C 17           0.99999   -12.00745
   8. CR ( 1) C 18           0.99999   -12.05734
   9. CR ( 1) N 21           0.99999   -16.48734
  10. CR ( 1) C 22           0.99999   -12.04582
  11. CR ( 1) C 23           0.99999   -12.10732
  12. CR ( 1) O 24           1.00000   -21.66815
  13. CR ( 1) C 25           0.99999   -12.04762
  14. CR ( 1) C 26           0.99999   -12.01993
  15. CR ( 1) C 27           0.99999   -12.00892
  16. CR ( 1) C 28           0.99999   -12.01357
  17. CR ( 1) C 29           0.99999   -12.00894
  18. CR ( 1) C 30           0.99999   -12.02057
  19. CR ( 1) C 34           0.99999   -12.01534
  20. CR ( 1) C 35           0.99999   -11.99772
  21. CR ( 1) C 39           0.99999   -11.99832
  22. CR ( 1) C 44           0.99999   -12.01409
  23. CR ( 1) C 45           0.99999   -11.99657
  24. CR ( 1) C 49           0.99999   -11.99844
  25. CR ( 1) C 54           0.99999   -11.99555
  26. CR ( 1) C 58           0.99999   -12.00038
  27. LP ( 1) N 21           0.89985    -0.77331
  28. LP ( 1) O 24           0.98810    -1.24839
  29. LP ( 2) O 24           0.88712    -0.93349
  30. BD ( 1) C  1- C  2      0.99376    -0.99205
  31. BD ( 1) C  1- C 10      0.99363    -0.99121
  32. BD ( 1) C  1- H 15      0.99126    -0.89158
  33. BD ( 1) C  1- H 16      0.99143    -0.89164
  34. BD ( 1) C  2- C  3      0.99284    -1.00207
  35. BD ( 1) C  2- H  4      0.98994    -0.89411
  36. BD ( 1) C  2- H  5      0.99022    -0.89352
  37. BD ( 1) C  3- C  6      0.98638    -1.00165
  38. BD ( 1) C  3- H  7      0.98803    -0.89518
  39. BD ( 1) C  3- H  8      0.98955    -0.89939
  40. BD ( 1) C  6- C  9      0.98600    -1.00113
  41. BD ( 1) C  6- C 17      0.98274    -0.99748
  42. BD ( 1) C  6- C 22      0.96699    -1.01628
  43. BD ( 1) C  9- C 10      0.99340    -1.00376
  44. BD ( 1) C  9- H 11      0.98910    -0.89984
  45. BD ( 1) C  9- H 12      0.98720    -0.89357
  46. BD ( 1) C 10- H 13      0.98948    -0.89478
  47. BD ( 1) C 10- H 14      0.99008    -0.89432
  48. BD ( 1) C 17- C 18      0.98403    -1.00452
  49. BD ( 1) C 17- H 19      0.98845    -0.90466
  50. BD ( 1) C 17- H 20      0.98835    -0.90141
  51. BD ( 1) C 18- N 21      0.98471    -1.16093
  52. BD ( 1) C 18- C 54      0.99033    -1.01170
  53. BD ( 1) C 18- C 58      0.98937    -1.02311
  54. BD ( 1) N 21- C 22      0.98050    -1.21296
  55. BD ( 1) N 21- C 25      0.99075    -1.21814
  56. BD ( 1) C 22- C 23      0.99185    -1.21701
  57. BD ( 2) C 22- C 23      0.98077    -0.72435
  58. BD ( 1) C 23- O 24      0.99805    -1.63382
  59. BD ( 2) C 23- O 24      0.99361    -0.95918
  60. BD ( 1) C 25- C 26      0.98625    -1.10673
  61. BD ( 2) C 25- C 26      0.82633    -0.66552
  62. BD ( 1) C 25- C 30      0.98561    -1.10311
  63. BD ( 1) C 26- C 27      0.98750    -1.10437
  64. BD ( 1) C 26- C 44      0.98584    -1.02138
  65. BD ( 1) C 27- C 28      0.99076    -1.11111
  66. BD ( 2) C 27- C 28      0.83798    -0.65415
  67. BD ( 1) C 27- H 33      0.98860    -0.92261
  68. BD ( 1) C 28- C 29      0.99066    -1.10919
  69. BD ( 1) C 28- H 31      0.98983    -0.92417
  70. BD ( 1) C 29- C 30      0.98746    -1.10654
  71. BD ( 2) C 29- C 30      0.82533    -0.65645
  72. BD ( 1) C 29- H 32      0.98847    -0.92255
  73. BD ( 1) C 30- C 34      0.98589    -1.02259
  74. BD ( 1) C 34- C 35      0.98724    -0.99815
  75. BD ( 1) C 34- C 39      0.99025    -1.00238
  76. BD ( 1) C 34- H 40      0.98347    -0.90186
  77. BD ( 1) C 35- H 36      0.99434    -0.89863
  78. BD ( 1) C 35- H 37      0.99485    -0.89718
  79. BD ( 1) C 35- H 38      0.99361    -0.89668
  80. BD ( 1) C 39- H 41      0.99388    -0.89703
  81. BD ( 1) C 39- H 42      0.99473    -0.89951
  82. BD ( 1) C 39- H 43      0.99440    -0.89923
  83. BD ( 1) C 44- C 45      0.98840    -0.99789
  84. BD ( 1) C 44- C 49      0.98916    -1.00028
  85. BD ( 1) C 44- H 50      0.98367    -0.89983
  86. BD ( 1) C 45- H 46      0.99379    -0.89534
  87. BD ( 1) C 45- H 47      0.99489    -0.89732
  88. BD ( 1) C 45- H 48      0.99457    -0.89764
  89. BD ( 1) C 49- H 51      0.99401    -0.89694
  90. BD ( 1) C 49- H 52      0.99426    -0.89989
  91. BD ( 1) C 49- H 53      0.99473    -0.89879
  92. BD ( 1) C 54- H 55      0.99206    -0.89769
  93. BD ( 1) C 54- H 56      0.99348    -0.90296
  94. BD ( 1) C 54- H 57      0.99310    -0.90235
  95. BD ( 1) C 58- H 59      0.99331    -0.90559
  96. BD ( 1) C 58- H 60      0.99291    -0.90170
  97. BD ( 1) C 58- H 61      0.99120    -0.90065
```

[CyCAAC–CO_2] in MeCN

Optimized Coordinates

1.	C	-1.572343	5.196298	-0.831762
2.	C	-2.579328	4.355450	-0.026032
3.	C	-2.372445	2.863861	-0.270252
4.	H	-3.601368	4.629923	-0.291760
5.	H	-2.472885	4.561241	1.042479
6.	C	-0.997152	2.401578	0.305872
7.	H	-2.406987	2.660178	-1.340841
8.	H	-3.168531	2.281267	0.189642
9.	C	0.050394	3.538233	0.163091
10.	C	-0.233941	4.457656	-1.019914
11.	H	1.049423	3.106256	0.097260
12.	H	0.019945	4.120985	1.086586
13.	H	-0.254574	3.871604	-1.940974
14.	H	0.581164	5.174002	-1.133021
15.	H	-1.403723	6.144853	-0.317171
16.	H	-1.992172	5.438968	-1.809917
17.	C	-1.090831	1.903675	1.762011
18.	C	-1.247312	0.376955	1.709269
19.	H	-1.912307	2.372067	2.299470
20.	H	-0.166216	2.148665	2.284728
21.	N	-0.685337	0.089699	0.306989
22.	C	-0.570393	1.155668	-0.413478
23.	C	-0.057383	1.169686	-1.841517
24.	O	-0.937506	1.130530	-2.717700
25.	O	1.176693	1.276089	-1.939440
26.	C	-0.349195	-1.246657	-0.158841
27.	C	-1.321071	-2.007995	-0.832555
28.	C	-0.971890	-3.302430	-1.217981
29.	C	0.287060	-3.818467	-0.964355
30.	C	1.238597	-3.032381	-0.336628
31.	C	0.951582	-1.731377	0.072975
32.	H	0.532175	-4.827343	-1.269503
33.	H	2.229624	-3.430519	-0.167745
34.	H	-1.701792	-3.910178	-1.734788
35.	C	2.074858	-0.916309	0.692474
36.	C	3.198356	-0.672420	-0.326405
37.	H	2.813255	-0.171584	-1.210819
38.	H	3.663828	-1.614454	-0.622352
39.	H	3.970409	-0.043456	0.122336
40.	C	2.652179	-1.591281	1.944964
41.	H	1.683799	0.058264	0.976844
42.	H	3.377995	-0.929497	2.421233
43.	H	3.170371	-2.514780	1.681145
44.	H	1.881432	-1.836895	2.673044
45.	C	-2.704887	-1.507415	-1.209575
46.	C	-2.875826	-1.463657	-2.734967
47.	H	-3.856398	-1.050858	-2.982175
48.	H	-2.818534	-2.465667	-3.163580
49.	H	-2.114649	-0.835049	-3.190481
50.	C	-3.813889	-2.370154	-0.590302
51.	H	-2.819276	-0.489181	-0.847330
52.	H	-4.787594	-1.914917	-0.780696
53.	H	-3.695689	-2.485274	0.485857
54.	H	-3.820436	-3.366821	-1.033662
55.	C	-2.697582	-0.084038	1.795648
56.	H	-3.086305	0.214483	2.768928
57.	H	-2.763844	-1.167260	1.726970
58.	H	-3.326457	0.359559	1.029147
59.	C	-0.438187	-0.326490	2.784893
60.	H	0.588582	0.025525	2.813094
61.	H	-0.450038	-1.407419	2.649688
62.	H	-0.896509	-0.103943	3.748775

[CyCAAC–CO_2] in MeCN

IR SPECTRUM

Mode	freq (cm**-1)	T**2
6:	22.48	0.639133
7:	38.73	1.366982
8:	53.64	2.958388
9:	62.91	0.965395
10:	80.56	0.551855
11:	95.26	3.045975
12:	109.53	12.042806
13:	120.34	2.760889
14:	125.11	1.758519
15:	139.43	2.376703
16:	142.42	2.141289
17:	152.96	0.816504
18:	161.94	10.159009
19:	166.28	17.507499
20:	190.46	0.530773
21:	202.02	2.236242
22:	215.49	0.632114
23:	226.47	0.086959
24:	234.96	0.606381
25:	240.30	3.214699
26:	244.38	0.126910
27:	255.24	0.553202
28:	264.01	7.400661
29:	268.73	1.600919
30:	274.95	0.433445
31:	284.25	0.629316
32:	293.83	1.505534
33:	308.21	1.147494
34:	322.60	2.076453
35:	325.29	2.356814
36:	328.10	8.646291
37:	344.47	2.209841
38:	375.42	3.182765
39:	397.05	3.174256
40:	412.74	3.669675
41:	427.17	1.000766
42:	444.77	4.832797
43:	453.00	0.052598
44:	482.09	26.213020
45:	503.52	1.696914
46:	511.10	9.113944
47:	554.38	1.044375
48:	580.07	12.580583
49:	583.43	2.767487
50:	598.01	1.477490
51:	624.92	4.754494
52:	632.16	0.041179
53:	652.67	0.552880
54:	688.32	37.623738
55:	736.94	3.244592
56:	756.73	20.507631
57:	769.18	48.848036
58:	781.62	4.148465
59:	786.65	3.862188
60:	807.93	12.610101
61:	823.83	2.745534
62:	834.28	49.612460
63:	838.39	19.438238
64:	845.17	5.738021
65:	862.98	2.866438
66:	896.04	3.825507
67:	905.21	6.834914
68:	915.81	28.310097
69:	939.67	3.970011
70:	941.81	3.534339
71:	944.62	8.004253
72:	947.80	3.525674
73:	952.86	18.253314
74:	956.42	7.323447
75:	966.02	0.271474
76:	967.32	0.221316
77:	970.86	8.463441
78:	974.85	0.948545
79:	982.72	4.320863
80:	1003.64	7.053546
81:	1010.54	1.647794
82:	1029.88	0.446437
83:	1036.97	2.912448
84:	1063.91	10.414306
85:	1068.06	2.494820
86:	1076.05	24.177358
87:	1087.00	1.043909
88:	1097.84	0.083107
89:	1117.53	4.674767
90:	1119.77	4.540398
91:	1125.16	0.464359
92:	1135.23	11.493740
93:	1162.15	48.399531
94:	1172.53	53.525329
95:	1180.03	1.204320
96:	1184.30	20.733594
97:	1190.75	0.189962
98:	1194.51	13.224718
99:	1202.75	11.044113
100:	1219.22	16.346233
101:	1234.47	5.043116
102:	1261.61	22.895838
103:	1266.35	2.005911
104:	1278.79	1.935605
105:	1279.20	5.245540
106:	1297.05	3.658209
107:	1298.55	16.993799
108:	1303.29	1.908305
109:	1318.44	10.954837
110:	1339.08	0.731549
111:	1342.94	2.080530
112:	1351.04	4.695401
113:	1352.99	4.499794
114:	1358.62	12.094276
115:	1368.36	4.791178
116:	1373.21	7.146498
117:	1385.59	22.869506
118:	1386.62	29.955256
119:	1389.07	11.626690
120:	1394.61	189.406834
121:	1396.26	21.428472
122:	1398.11	68.660093
123:	1410.27	23.507421
124:	1414.64	4.230189
125:	1416.36	17.755940
126:	1425.56	26.794026
127:	1473.26	11.072643
128:	1475.41	2.295401
129:	1477.92	2.500203
130:	1479.28	10.385381
131:	1480.10	5.039036
132:	1481.13	2.307650
133:	1483.06	6.332604
134:	1484.89	2.277403
135:	1487.19	4.701663
136:	1488.88	1.575594
137:	1489.60	20.696273
138:	1492.13	21.328404
139:	1492.94	10.008882
140:	1494.98	9.305635
141:	1496.22	12.848800
142:	1500.71	1.282604
143:	1503.28	58.498302
144:	1507.22	5.963363
145:	1510.19	10.034923
146:	1513.95	21.039072
147:	1622.51	80.988443
148:	1624.13	11.525625
149:	1637.62	171.204233
150:	1678.21	859.175524
151:	3025.76	32.125044
152:	3031.30	51.165679
153:	3032.71	43.866648
154:	3033.16	59.249959
155:	3038.57	68.509316
156:	3039.53	47.637922
157:	3040.98	33.758726
158:	3046.57	33.217133
159:	3056.29	12.979105
160:	3058.54	41.639759
161:	3064.67	7.149494
162:	3065.22	30.850898
163:	3070.01	19.199220
164:	3077.18	40.482203
165:	3081.05	24.609244
166:	3083.64	118.103583
167:	3086.11	37.167511
168:	3088.63	3.393342
169:	3089.35	50.317011
170:	3093.26	10.397572
171:	3106.48	101.094923
172:	3109.12	32.018270
173:	3113.86	43.478811
174:	3116.33	21.825532
175:	3120.26	110.072101
176:	3122.48	10.646026
177:	3123.28	33.514646
178:	3136.80	10.986839
179:	3138.65	6.056143
180:	3143.65	5.306354
181:	3154.91	21.047932
182:	3155.60	36.093330
183:	3179.31	5.432629
184:	3192.92	12.548265
185:	3201.01	16.405058

[CyCAAC–CO_2] in MeCN

NRT Analysis

```
  Atom
  ------
  1.  C
  2.  C
  3.  C
  4.  H
  5.  H
  6.  C
  7.  H
  8.  H
  9.  C
 10.  C
 11.  H
 12.  H
 13.  H
 14.  H
 15.  H
 16.  H
 17.  C
 18.  C
 19.  H
 20.  H
 21.  N
 22.  C
 23.  C
 24.  O
 25.  O
 26.  C
 27.  C
 28.  C
 29.  C
 30.  C
 31.  C
 32.  H
 33.  H
 34.  H
 35.  C
 36.  C
 37.  H
 38.  H
 39.  H
 40.  C
 41.  H
 42.  H
 43.  H
 44.  H
 45.  C
 46.  C
 47.  H
 48.  H
 49.  H
 50.  C
 51.  H
 52.  H
 53.  H
 54.  H
 55.  C
 56.  H
 57.  H
 58.  H
 59.  C
 60.  H
 61.  H
 62.  H
```

```
$NRTSTRA
STR       ! Wgt = 44.24%
LONE 24 2 25 3 END
BOND S 1 2 S 1 10 S 1 15 S 1 16 S 2 3 S 2 4 S 2 5 S 3 6 S 3
7 S 3 8 S 6 9 S 6 17 S 6 22 S 9 10 S 9 11 S 9 12 S 10 13 S 10
14 S 17 18 S 17 19 S 17 20 S 18 21 S 18 55 S 18 59 D 21 22 S
21 26 S 22 23 D 23 24 S 23 25 D 26 27 S 26 31 S 27 28 S 27
45 D 28 29 S 28 34 S 29 30 S 29 32 D 30 31 S 30 33 S 31 35
S 35 36 S 35 40 S 35 41 S 36 37 S 36 38 S 36 39 S 40 42 S
40 43 S 40 44 S 45 46 S 45 50 S 45 51 S 46 47 S 46 48 S 46
49 S 50 52 S 50 53 S 50 54 S 55 56 S 55 57 S 55 58 S 59 60
S 59 61 S 59 62 END
STR       ! Wgt = 44.15%
LONE 24 3 25 2 END
BOND S 1 2 S 1 10 S 1 15 S 1 16 S 2 3 S 2 4 S 2 5 S 3 6 S 3
7 S 3 8 S 6 9 S 6 17 S 6 22 S 9 10 S 9 11 S 9 12 S 10 13 S 10
14 S 17 18 S 17 19 S 17 20 S 18 21 S 18 55 S 18 59 D 21 22
S 21 26 S 22 23 S 23 24 D 23 25 D 26 27 S 26 31 S 27 28 S
27 45 D 28 29 S 28 34 S 29 30 S 29 32 D 30 31 S 30 33 S 31
35 S 35 36 S 35 40 S 35 41 S 36 37 S 36 38 S 36 39 S 40 42
S 40 43 S 40 44 S 45 46 S 45 50 S 45 51 S 46 47 S 46 48 S
46 49 S 50 52 S 50 53 S 50 54 S 55 56 S 55 57 S 55 58 S 59
60 S 59 61 S 59 62 END
$END

$NRTSTRB
STR       ! Wgt = 44.24%
LONE 24 2 25 3 END
BOND S 1 2 S 1 10 S 1 15 S 1 16 S 2 3 S 2 4 S 2 5 S 3 6 S 3
7 S 3 8 S 6 9 S 6 17 S 6 22 S 9 10 S 9 11 S 9 12 S 10 13 S 10
14 S 17 18 S 17 19 S 17 20 S 18 21 S 18 55 S 18 59 D 21 22
S 21 26 S 22 23 D 23 24 S 23 25 D 26 27 S 26 31 S 27 28 S
27 45 D 28 29 S 28 34 S 29 30 S 29 32 D 30 31 S 30 33 S 31
35 S 35 36 S 35 40 S 35 41 S 36 37 S 36 38 S 36 39 S 40 42
S 40 43 S 40 44 S 45 46 S 45 50 S 45 51 S 46 47 S 46 48 S
46 49 S 50 52 S 50 53 S 50 54 S 55 56 S 55 57 S 55 58 S 59
60 S 59 61 S 59 62 END
STR       ! Wgt = 44.15%
LONE 24 3 25 2 END
BOND S 1 2 S 1 10 S 1 15 S 1 16 S 2 3 S 2 4 S 2 5 S 3 6 S 3
7 S 3 8 S 6 9 S 6 17 S 6 22 S 9 10 S 9 11 S 9 12 S 10 13 S 10
14 S 17 18 S 17 19 S 17 20 S 18 21 S 18 55 S 18 59 D 21 22
S 21 26 S 22 23 S 23 24 D 23 25 D 26 27 S 26 31 S 27 28 S
27 45 D 28 29 S 28 34 S 29 30 S 29 32 D 30 31 S 30 33 S 31
35 S 35 36 S 35 40 S 35 41 S 36 37 S 36 38 S 36 39 S 40 42
S 40 43 S 40 44 S 45 46 S 45 50 S 45 51 S 46 47 S 46 48 S
46 49 S 50 52 S 50 53 S 50 54 S 55 56 S 55 57 S 55 58 S 59
60 S 59 61 S 59 62 END
$END
```

[CyCAAC–CO_2] in MeCN

NATURAL BOND ORBITALS (Summary):

```
        NBO              Occupancy    Energy
=========================================
=========
Molecular unit  1  (C24H35NO2)
------ Lewis -----------------------------------
   1. CR ( 1) C  1           0.99999   -12.00273
   2. CR ( 1) C  2           0.99999   -12.00663
   3. CR ( 1) C  3           0.99999   -12.01626
   4. CR ( 1) C  6           0.99999   -12.05269
   5. CR ( 1) C  9           0.99999   -12.01505
   6. CR ( 1) C 10           0.99999   -12.00446
   7. CR ( 1) C 17           0.99999   -12.02331
   8. CR ( 1) C 18           0.99999   -12.08591
   9. CR ( 1) N 21           0.99999   -16.58136
  10. CR ( 1) C 22           0.99999   -12.11122
  11. CR ( 1) C 23           0.99999   -12.12484
  12. CR ( 1) O 24           1.00000   -21.58857
  13. CR ( 1) O 25           1.00000   -21.58843
  14. CR ( 1) C 26           0.99999   -12.07330
  15. CR ( 1) C 27           0.99999   -12.03918
  16. CR ( 1) C 28           0.99999   -12.01857
  17. CR ( 1) C 29           0.99999   -12.02261
  18. CR ( 1) C 30           0.99999   -12.01856
  19. CR ( 1) C 31           0.99999   -12.03882
  20. CR ( 1) C 35           0.99999   -12.02459
  21. CR ( 1) C 36           0.99999   -11.99373
  22. CR ( 1) C 40           0.99999   -11.99970
  23. CR ( 1) C 45           0.99999   -12.02405
  24. CR ( 1) C 46           0.99999   -11.99390
  25. CR ( 1) C 50           0.99999   -11.99991
  26. CR ( 1) C 55           0.99999   -12.01181
  27. CR ( 1) C 59           0.99999   -12.01119
  28. LP ( 1) O 24           0.98791    -1.21254
  29. LP ( 2) O 24           0.92354    -0.86653
  30. LP ( 1) O 25           0.98780    -1.21279
  31. LP ( 2) O 25           0.92217    -0.86633
  32. LP ( 3) O 25           0.79004    -0.86732
  33. BD ( 1) C  1- C  2     0.99382    -0.99617
  34. BD ( 1) C  1- C 10     0.99365    -0.99466
  35. BD ( 1) C  1- H 15     0.99116    -0.89321
  36. BD ( 1) C  1- H 16     0.99129    -0.89337
  37. BD ( 1) C  2- C  3     0.99132    -1.01004
  38. BD ( 1) C  2- H  4     0.98879    -0.89769
  39. BD ( 1) C  2- H  5     0.99040    -0.89760
  40. BD ( 1) C  3- C  6     0.97478    -1.00551
  41. BD ( 1) C  3- H  7     0.98808    -0.90859
  42. BD ( 1) C  3- H  8     0.98949    -0.91172
  43. BD ( 1) C  6- C  9     0.98118    -1.01299
  44. BD ( 1) C  6- C 17     0.98378    -1.02023
  45. BD ( 1) C  6- C 22     0.97926    -1.08144
  46. BD ( 1) C  9- C 10     0.99331    -1.00986
  47. BD ( 1) C  9- H 11     0.98922    -0.90733
  48. BD ( 1) C  9- H 12     0.98705    -0.90329
  49. BD ( 1) C 10- H 13     0.98979    -0.89803
  50. BD ( 1) C 10- H 14     0.98920    -0.89625
  51. BD ( 1) C 17- C 18     0.98477    -1.03538
  52. BD ( 1) C 17- H 19     0.98786    -0.92018
  53. BD ( 1) C 17- H 20     0.98846    -0.91586
  54. BD ( 1) C 18- N 21     0.98431    -1.17724
  55. BD ( 1) C 18- C 55     0.98724    -1.04386
  56. BD ( 1) C 18- C 59     0.98913    -1.04815
  57. BD ( 1) N 21- C 22     0.99174    -1.39302
  58. BD ( 2) N 21- C 22     0.97817    -0.88305
  59. BD ( 1) N 21- C 26     0.99010    -1.24843
  60. BD ( 1) C 22- C 23     0.98598    -1.08957
  61. BD ( 1) C 23- O 24     0.99650    -1.49965
  62. BD ( 2) C 23- O 24     0.99237    -0.91162
  63. BD ( 1) C 23- O 25     0.99470    -1.48386
  64. BD ( 1) C 26- C 27     0.98459    -1.13044
  65. BD ( 2) C 26- C 27     0.83775    -0.68925
  66. BD ( 1) C 26- C 31     0.98441    -1.12935
  67. BD ( 1) C 27- C 28     0.98600    -1.11641
  68. BD ( 1) C 27- C 45     0.98597    -1.03286
  69. BD ( 1) C 28- C 29     0.99090    -1.12126
  70. BD ( 2) C 28- C 29     0.82840    -0.66270
  71. BD ( 1) C 28- H 34     0.98789    -0.93080
  72. BD ( 1) C 29- C 30     0.99084    -1.12067
  73. BD ( 1) C 29- H 32     0.98957    -0.93153
  74. BD ( 1) C 30- C 31     0.98611    -1.11734
  75. BD ( 2) C 30- C 31     0.81865    -0.66788
  76. BD ( 1) C 30- H 33     0.98790    -0.93090
  77. BD ( 1) C 31- C 35     0.98590    -1.03275
  78. BD ( 1) C 35- C 36     0.98693    -0.99921
  79. BD ( 1) C 35- C 40     0.98896    -1.00382
  80. BD ( 1) C 35- H 41     0.98442    -0.90930
  81. BD ( 1) C 36- H 37     0.99418    -0.89790
  82. BD ( 1) C 36- H 38     0.99441    -0.89632
  83. BD ( 1) C 36- H 39     0.99305    -0.89349
  84. BD ( 1) C 40- H 42     0.99345    -0.89840
  85. BD ( 1) C 40- H 43     0.99441    -0.90101
  86. BD ( 1) C 40- H 44     0.99474    -0.90435
  87. BD ( 1) C 45- C 46     0.98718    -0.99957
  88. BD ( 1) C 45- C 50     0.98876    -1.00350
  89. BD ( 1) C 45- H 51     0.98454    -0.91059
  90. BD ( 1) C 46- H 47     0.99312    -0.89349
  91. BD ( 1) C 46- H 48     0.99447    -0.89686
  92. BD ( 1) C 46- H 49     0.99423    -0.89775
  93. BD ( 1) C 50- H 52     0.99348    -0.89837
  94. BD ( 1) C 50- H 53     0.99438    -0.90475
  95. BD ( 1) C 50- H 54     0.99444    -0.90107
  96. BD ( 1) C 55- H 56     0.98850    -0.91110
  97. BD ( 1) C 55- H 57     0.99222    -0.91873
  98. BD ( 1) C 55- H 58     0.99298    -0.92191
  99. BD ( 1) C 59- H 60     0.99318    -0.91984
 100. BD ( 1) C 59- H 61     0.99225    -0.91567
 101. BD ( 1) C 59- H 62     0.98804    -0.91046
```

[CyCAAC–CO_2]$^-$ in MeCN

Optimized Coordinates

1.	C	-2.015994	5.230396	-0.542077
2.	C	-2.888121	4.100659	0.049033
3.	C	-2.411799	2.721702	-0.407444
4.	H	-3.935527	4.244850	-0.227307
5.	H	-2.856013	4.141286	1.141591
6.	C	-0.987501	2.396828	0.117494
7.	H	-2.386484	2.678595	-1.497075
8.	H	-3.110080	1.953728	-0.073779
9.	C	-0.092557	3.668248	-0.027969
10.	C	-0.642522	4.713168	-0.994091
11.	H	0.911194	3.362933	-0.327193
12.	H	0.003629	4.132137	0.959486
13.	H	-0.715735	4.252120	-1.977241
14.	H	0.058735	5.548252	-1.077537
15.	H	-1.886950	6.019633	0.204249
16.	H	-2.525888	5.688945	-1.393391
17.	C	-1.007763	1.959939	1.598896
18.	C	-1.055878	0.426960	1.640465
19.	H	-1.832849	2.405000	2.154924
20.	H	-0.082146	2.288267	2.074095
21.	N	-0.476685	0.079614	0.309550
22.	C	-0.437507	1.159118	-0.558378
23.	C	0.064140	1.088466	-1.925739
24.	O	-0.128070	2.111184	-2.666902
25.	O	0.662186	0.036841	-2.318634
26.	C	-0.283938	-1.286985	-0.063439
27.	C	-1.306515	-1.997349	-0.720314
28.	C	-1.121058	-3.356479	-0.971293
29.	C	0.049923	-4.003465	-0.606904
30.	C	1.074070	-3.279023	-0.015418
31.	C	0.933970	-1.917993	0.250987
32.	H	0.172576	-5.061415	-0.804403
33.	H	2.006704	-3.774750	0.222368
34.	H	-1.902430	-3.914803	-1.471335
35.	C	2.138641	-1.137821	0.743999
36.	C	3.157810	-0.979417	-0.394958
37.	H	2.675592	-0.525224	-1.259773
38.	H	3.564882	-1.950349	-0.689922
39.	H	3.990185	-0.349486	-0.071015
40.	C	2.802949	-1.759053	1.976515
41.	H	1.797353	-0.138951	1.001973
42.	H	3.608840	-1.113977	2.333832
43.	H	3.241536	-2.731267	1.742397
44.	H	2.092031	-1.899958	2.790846
45.	C	-2.557289	-1.324364	-1.255513
46.	C	-2.494156	-1.228514	-2.787083
47.	H	-3.353719	-0.670316	-3.166026
48.	H	-2.512355	-2.223202	-3.239207
49.	H	-1.581109	-0.724356	-3.100080
50.	C	-3.850729	-2.023571	-0.821517
51.	H	-2.577213	-0.307270	-0.876426
52.	H	-4.716731	-1.446980	-1.154814
53.	H	-3.909160	-2.129008	0.261677
54.	H	-3.930424	-3.019274	-1.261519
55.	C	-2.483562	-0.107553	1.815447
56.	H	-2.857618	0.194398	2.795097
57.	H	-2.496347	-1.196598	1.770306
58.	H	-3.165952	0.276615	1.062723
59.	C	-0.217403	-0.115326	2.798418
60.	H	0.796132	0.277446	2.774378
61.	H	-0.173687	-1.204365	2.780925
62.	H	-0.676671	0.188184	3.740934

[CyCAAC–CO_2]$^-$ in MeCN

IR SPECTRUM

Mode	freq (cm**-1)	T**2
6:	12.83	0.828652
7:	49.88	8.890677
8:	55.55	0.219070
9:	69.69	1.641427
10:	92.89	2.071923
11:	96.87	2.191742
12:	108.06	6.613976
13:	113.20	5.825191
14:	119.08	3.659100
15:	125.70	11.049533
16:	138.36	0.823494
17:	142.42	6.676136
18:	150.71	4.203435
19:	182.63	19.352940
20:	191.00	2.915696
21:	217.21	3.074304
22:	229.67	0.928310
23:	239.96	5.261279
24:	244.84	0.470306
25:	257.10	1.426161
26:	263.17	3.577380
27:	271.28	3.633576
28:	277.12	0.721567
29:	279.59	1.319765
30:	288.12	0.582501
31:	295.90	0.931109
32:	309.80	3.109992
33:	315.58	0.980671
34:	329.25	0.274877
35:	333.86	0.434351
36:	341.13	4.307006
37:	362.76	4.794999
38:	367.09	1.954617
39:	396.06	2.160192
40:	430.43	3.280773
41:	433.47	1.820134
42:	449.72	3.200248
43:	461.62	4.770776
44:	473.58	3.286059
45:	486.77	10.758939
46:	498.61	8.949821
47:	550.88	8.260193
48:	564.41	2.814445
49:	569.27	6.536770
50:	592.98	1.124591
51:	606.46	4.556086
52:	622.49	3.429922
53:	627.72	3.166599
54:	655.27	4.556914
55:	714.26	22.370990
56:	753.04	20.639745
57:	759.46	11.410971
58:	766.63	18.816452
59:	773.98	3.040824
60:	798.47	10.522632
61:	818.93	16.281370
62:	821.56	32.244394
63:	835.45	13.040784
64:	845.21	6.067194
65:	857.07	4.224070
66:	895.14	3.521230
67:	907.94	9.197351
68:	918.00	1.854598
69:	923.94	3.701934
70:	935.35	15.658283
71:	941.50	3.360253
72:	948.24	4.575638
73:	954.93	11.592964
74:	957.37	10.328732
75:	959.70	2.889261
76:	966.42	23.805077
77:	968.06	4.188892
78:	968.95	1.476738
79:	983.09	1.789399
80:	990.28	14.327379
81:	1002.58	23.357374
82:	1021.45	2.144099
83:	1030.66	4.614309
84:	1053.38	0.387069
85:	1064.02	12.464407
86:	1076.78	24.918935
87:	1082.99	4.501321
88:	1097.70	4.058325
89:	1121.11	4.583677
90:	1125.36	6.685931
91:	1131.65	14.921163
92:	1144.45	6.672184
93:	1159.14	19.903139
94:	1171.43	45.760334
95:	1175.94	0.788857
96:	1185.25	72.464378
97:	1191.48	5.961636
98:	1206.01	11.120444
99:	1208.32	127.958016
100:	1227.68	133.527994
101:	1232.91	17.765285
102:	1243.84	229.260594
103:	1266.74	15.409221
104:	1275.04	15.318444
105:	1278.95	19.767923
106:	1281.79	60.037877
107:	1283.63	11.227752
108:	1294.92	8.806876
109:	1308.33	58.421560
110:	1335.04	341.612882
111:	1344.16	2.989803
112:	1348.78	22.010520
113:	1353.23	11.007639
114:	1356.24	42.820171
115:	1362.72	4.082991
116:	1364.25	8.150210
117:	1369.08	2.736752
118:	1378.33	3.153473
119:	1378.95	3.766264
120:	1382.02	4.113072
121:	1388.51	7.552899
122:	1394.16	21.771843
123:	1395.77	17.680684
124:	1409.23	22.397204
125:	1411.73	17.065466
126:	1414.08	10.527113
127:	1468.64	60.252428
128:	1475.53	22.041545
129:	1477.11	15.595957
130:	1477.93	14.382657
131:	1479.62	0.455218
132:	1480.59	1.348123
133:	1482.64	4.624538
134:	1484.82	55.462181
135:	1485.34	3.393134
136:	1488.38	16.633091
137:	1489.52	24.366042
138:	1489.84	2.402351
139:	1492.91	13.493574
140:	1493.83	21.335677
141:	1495.51	19.203715
142:	1499.22	31.074409
143:	1503.46	1.651763
144:	1506.18	764.048453
145:	1509.99	26.822026
146:	1511.49	23.183655
147:	1513.78	11.487803
148:	1517.26	240.600693
149:	1617.27	8.201552
150:	1627.37	1.240250
151:	2999.93	62.975738
152:	3008.19	29.854511
153:	3013.16	80.476988
154:	3019.10	95.413309
155:	3019.37	59.792218
156:	3028.89	70.196199
157:	3029.63	141.673627
158:	3031.15	56.891761
159:	3033.89	69.338585
160:	3040.64	20.179619
161:	3043.64	69.376384
162:	3048.66	21.438031
163:	3051.19	86.903510
164:	3060.63	129.638614
165:	3067.03	59.888440
166:	3067.65	47.897535
167:	3072.77	45.132538
168:	3078.56	31.161009
169:	3081.55	47.876679
170:	3088.67	36.656023
171:	3091.67	67.862176
172:	3098.40	29.056063
173:	3100.50	92.028096
174:	3102.46	58.293055
175:	3105.63	68.959485
176:	3106.11	46.964796
177:	3111.24	17.522188
178:	3116.89	20.170377
179:	3118.01	16.013290
180:	3127.18	32.841666
181:	3133.98	57.527306
182:	3146.08	40.483874
183:	3160.83	1.807371
184:	3173.42	32.890672
185:	3184.14	44.627052

[CyCAAC–CO_2]$^-$ in MeCN
NRT Analysis

```
   Atom
  -----
  1.  C
  2.  C
  3.  C
  4.  H
  5.  H
  6.  C
  7.  H
  8.  H
  9.  C
 10.  C
 11.  H
 12.  H
 13.  H
 14.  H
 15.  H
 16.  H
 17.  C
 18.  C
 19.  H
 20.  H
 21.  N
 22.  C
 23.  C
 24.  O
 25.  O
 26.  C
 27.  C
 28.  C
 29.  C
 30.  C
 31.  C
 32.  H
 33.  H
 34.  H
 35.  C
 36.  C
 37.  H
 38.  H
 39.  H
 40.  C
 41.  H
 42.  H
 43.  H
 44.  H
 45.  C
 46.  C
 47.  H
 48.  H
 49.  H
 50.  C
 51.  H
 52.  H
 53.  H
 54.  H
 55.  C
 56.  H
 57.  H
 58.  H
 59.  C
 60.  H
 61.  H
 62.  H
```

```
$NRTSTRA
STR       ! Wgt = 38.04%
LONE 21 1 24 3 25 3 END
BOND S 1 2 S 1 10 S 1 15 S 1 16 S 2 3 S 2 4 S 2 5 S 3 6 S 3
7 S 3 8 S 6 9 S 6 17 S 6 22 S 9 10 S 9 11 S 9 12 S 10 13 S 10
14 S 17 18 S 17 19 S 17 20 S 18 21 S 18 55 S 18 59 S 21 22
S 21 26 D 22 23 S 23 24 S 23 25 D 26 27 S 26 31 S 27 28 S
27 45 D 28 29 S 28 34 S 29 30 S 29 32 D 30 31 S 30 33 S 31
35 S 35 36 S 35 40 S 35 41 S 36 37 S 36 38 S 36 39 S 40 42
S 40 43 S 40 44 S 45 46 S 45 50 S 45 51 S 46 47 S 46 48 S
46 49 S 50 52 S 50 53 S 50 54 S 55 56 S 55 57 S 55 58 S 59
60 S 59 61 S 59 62 END
STR       ! Wgt = 30.17%
LONE 21 1 22 1 24 3 25 2 END
BOND S 1 2 S 1 10 S 1 15 S 1 16 S 2 3 S 2 4 S 2 5 S 3 6 S 3
7 S 3 8 S 6 9 S 6 17 S 6 22 S 9 10 S 9 11 S 9 12 S 10 13 S 10
14 S 17 18 S 17 19 S 17 20 S 18 21 S 18 55 S 18 59 S 21 22
S 21 26 S 22 23 23 24 D 23 25 D 26 27 S 26 31 S 27 28 S 27
45 D 28 29 S 28 34 S 29 30 S 29 32 D 30 31 S 30 33 S 31 35
S 35 36 S 35 40 S 35 41 S 36 37 S 36 38 S 36 39 S 40 42 S
40 43 S 40 44 S 45 46 S 45 50 S 45 51 S 46 47 S 46 48 S 46
49 S 50 52 S 50 53 S 50 54 S 55 56 S 55 57 S 55 58 S 59 60
S 59 61 S 59 62 END
STR       ! Wgt = 26.59%
LONE 21 1 22 1 24 2 25 3 END
BOND S 1 2 S 1 10 S 1 15 S 1 16 S 2 3 S 2 4 S 2 5 S 3 6 S 3
7 S 3 8 S 6 9 S 6 17 S 6 22 S 9 10 S 9 11 S 9 12 S 10 13 S 10
14 S 17 18 S 17 19 S 17 20 S 18 21 S 18 55 S 18 59 S 21 22
S 21 26 S 22 23 D 23 24 S 23 25 D 26 27 S 26 31 S 27 28 S
27 45 D 28 29 S 28 34 S 29 30 S 29 32 D 30 31 S 30 33 S 31
35 S 35 36 S 35 40 S 35 41 S 36 37 S 36 38 S 36 39 S 40 42
S 40 43 S 40 44 S 45 46 S 45 50  S 45 51 S 46 47 S 46 48 S
46 49 S 50 52 S 50 53 S 50 54 S 55 56 S 55 57 S 55 58 S 59
60 S 59 61 S 59 62 END
 $END

$NRTSTRB
STR       ! Wgt = 49.18%
LONE 24 3 25 2 END
BOND S 1 2 S 1 10 S 1 15 S 1 16 S 2 3 S 2 4 S 2 5 S 3 6 S 3
7 S 3 8 S 6 9 S 6 17 S 6 22 S 9 10 S 9 11 S 9 12 S 10 13 S 10
14 S 17 18 S 17 19 S 17 20 S 18 21 S 18 55 S 18 59 D 21 22
S 21 26 S 22 23 S 23 24 D 23 25 D 26 27 S 26 31 S 27 28 S
27 45 D 28 29 S 28 34 S 29 30 S 29 32 D 30 31 S 30 33 S 31
35 S 35 36 S 35 40 S 35 41 S 36 37 S 36 38 S 36 39 S 40 42
S 40 43 S 40 44 S 45 46 S 45 50 S 45 51 S 46 47 S 46 48 S
46 49 S 50 52 S 50 53 S 50 54 S 55 56 S 55 57 S 55 58 S 59
60 S 59 61 S 59 62 END
STR       ! Wgt = 42.48%
LONE 24 2 25 3 END
BOND S 1 2 S 1 10 S 1 15 S 1 16 S 2 3 S 2 4 S 2 5 S 3 6 S 3
7 S 3 8 S 6 9 S 6 17 S 6 22 S 9 10 S 9 11 S 9 12 S 10 13 S 10
14 S 17 18 S 17 19 S 17 20 S 18 21 S 18 55 S 18 59 D 21 22
S 21 26 S 22 23 D 23 24 S 23 25 D 26 27 S 26 31 S 27 28 S
27 45 D 28 29 S 28 34 S 29 30 S 29 32 D 30 31 S 30 33 S 31
35 S 35 36 S 35 40 S 35 41
 S 36 37 S 36 38 S 36 39 S 40 42 S 40 43 S 40 44 S 45 46 S
45 50 S 45 51 S 46 47 S 46 48 S 46 49 S 50 52 S 50 53 S 50
54 S 55 56 S 55 57 S 55 58 S 59 60 S 59 61 S 59 62
END
$END
```

[CyCAAC–CO_2]$^-$ in MeCN

NATURAL BOND ORBITALS (Summary):

```
          NBO              Occupancy    Energy

=========================================
=========
 Molecular unit  1  (C24H35NO2)
 ------ Lewis -----------------------------------
   1. CR ( 1) C  1            0.99999   -11.99137
   2. CR ( 1) C  2            0.99999   -11.99254
   3. CR ( 1) C  3            0.99999   -11.98839
   4. CR ( 1) C  6            0.99999   -12.00962
   5. CR ( 1) C  9            0.99999   -11.98834
   6. CR ( 1) C 10            0.99999   -11.98261
   7. CR ( 1) C 17            0.99999   -11.99410
   8. CR ( 1) C 18            0.99999   -12.04833
   9. CR ( 1) N 21            0.99999   -16.49524
  10. CR ( 1) C 22            0.99999   -12.01465
  11. CR ( 1) C 23            0.99999   -12.06346
  12. CR ( 1) O 24            1.00000   -21.53097
  13. CR ( 1) O 25            1.00000   -21.53007
  14. CR ( 1) C 26            0.99999   -12.03838
  15. CR ( 1) C 27            0.99999   -12.01114
  16. CR ( 1) C 28            0.99999   -12.00047
  17. CR ( 1) C 29            0.99999   -12.00463
  18. CR ( 1) C 30            0.99999   -12.00023
  19. CR ( 1) C 31            0.99999   -12.00995
  20. CR ( 1) C 35            0.99999   -12.00515
  21. CR ( 1) C 36            0.99999   -11.98359
  22. CR ( 1) C 40            0.99999   -11.99086
  23. CR ( 1) C 45            0.99999   -12.00668
  24. CR ( 1) C 46            0.99999   -11.98630
  25. CR ( 1) C 50            0.99999   -11.99139
  26. CR ( 1) C 55            0.99999   -11.99134
  27. CR ( 1) C 59            0.99999   -11.99152
  28. LP ( 1) N 21            0.93484    -0.79978
  29. LP ( 1) O 24            0.98862    -1.17579
  30. LP ( 2) O 24            0.94950    -0.81598
  31. LP ( 3) O 24            0.87526    -0.81206
  32. LP ( 1) O 25            0.98840    -1.17108
  33. LP ( 2) O 25            0.94531    -0.81367
  34. LP ( 3) O 25            0.86728    -0.81354
  35. BD ( 1) C  1- C  2      0.99382    -0.98000
  36. BD ( 1) C  1- C 10      0.99393    -0.98128
  37. BD ( 1) C  1- H 15      0.99184    -0.88175
  38. BD ( 1) C  1- H 16      0.99149    -0.88191
  39. BD ( 1) C  2- C  3      0.99351    -0.98847
  40. BD ( 1) C  2- H  4      0.99071    -0.88387
  41. BD ( 1) C  2- H  5      0.99058    -0.88412
  42. BD ( 1) C  3- C  6      0.98694    -0.97778
  43. BD ( 1) C  3- H  7      0.98823    -0.87942
  44. BD ( 1) C  3- H  8      0.98866    -0.88676
  45. BD ( 1) C  6- C  9      0.98692    -0.97248
  46. BD ( 1) C  6- C 17      0.98513    -0.98076
  47. BD ( 1) C  6- C 22      0.98308    -1.01382
  48. BD ( 1) C  9- C 10      0.99365    -0.98524
  49. BD ( 1) C  9- H 11      0.98995    -0.87919
  50. BD ( 1) C  9- H 12      0.98946    -0.87758
  51. BD ( 1) C 10- H 13      0.98969    -0.87741
  52. BD ( 1) C 10- H 14      0.98928    -0.87742
  53. BD ( 1) C 17- C 18      0.98455    -1.00034
  54. BD ( 1) C 17- H 19      0.98940    -0.89386
  55. BD ( 1) C 17- H 20      0.98841    -0.88827
  56. BD ( 1) C 18- N 21      0.98505    -1.15060
  57. BD ( 1) C 18- C 55      0.99096    -1.00721
  58. BD ( 1) C 18- C 59      0.99055    -1.01060
  59. BD ( 1) N 21- C 22      0.98987    -1.22746
  60. BD ( 1) N 21- C 26      0.99056    -1.20922
  61. BD ( 1) C 22- C 23      0.99025    -1.06765
  62. BD ( 2) C 22- C 23      0.96642    -0.66194
  63. BD ( 1) C 23- O 24      0.99645    -1.41082
  64. BD ( 1) C 23- O 25      0.99694    -1.41756
  65. BD ( 1) C 26- C 27      0.98651    -1.09797
  66. BD ( 2) C 26- C 27      0.81547    -0.65418
  67. BD ( 1) C 26- C 31      0.98611    -1.09690
  68. BD ( 1) C 27- C 28      0.98708    -1.09541
  69. BD ( 1) C 27- C 45      0.98557    -1.01099
  70. BD ( 1) C 28- C 29      0.99050    -1.10140
  71. BD ( 2) C 28- C 29      0.84203    -0.64624
  72. BD ( 1) C 28- H 34      0.98838    -0.91441
  73. BD ( 1) C 29- C 30      0.99047    -1.10090
  74. BD ( 1) C 29- H 32      0.98981    -0.91691
  75. BD ( 1) C 30- C 31      0.98716    -1.09543
  76. BD ( 2) C 30- C 31      0.82591    -0.64729
  77. BD ( 1) C 30- H 33      0.98837    -0.91433
  78. BD ( 1) C 31- C 35      0.98539    -1.00967
  79. BD ( 1) C 35- C 36      0.98664    -0.98368
  80. BD ( 1) C 35- C 40      0.99094    -0.99277
  81. BD ( 1) C 35- H 41      0.98346    -0.88949
  82. BD ( 1) C 36- H 37      0.99404    -0.88521
  83. BD ( 1) C 36- H 38      0.99486    -0.88498
  84. BD ( 1) C 36- H 39      0.99351    -0.88457
  85. BD ( 1) C 40- H 42      0.99397    -0.88982
  86. BD ( 1) C 40- H 43      0.99467    -0.89257
  87. BD ( 1) C 40- H 44      0.99471    -0.89335
  88. BD ( 1) C 45- C 46      0.98698    -0.98639
  89. BD ( 1) C 45- C 50      0.99046    -0.99278
  90. BD ( 1) C 45- H 51      0.98365    -0.89396
  91. BD ( 1) C 46- H 47      0.99360    -0.88634
  92. BD ( 1) C 46- H 48      0.99484    -0.88713
  93. BD ( 1) C 46- H 49      0.99438    -0.88853
  94. BD ( 1) C 50- H 52      0.99393    -0.89013
  95. BD ( 1) C 50- H 53      0.99467    -0.89411
  96. BD ( 1) C 50- H 54      0.99472    -0.89317
  97. BD ( 1) C 55- H 56      0.99144    -0.89280
  98. BD ( 1) C 55- H 57      0.99287    -0.89667
  99. BD ( 1) C 55- H 58      0.99329    -0.90229
 100. BD ( 1) C 59- H 60      0.99366    -0.89872
 101. BD ( 1) C 59- H 61      0.99303    -0.89678
 102. BD ( 1) C 59- H 62      0.99123    -0.89291
```

[CyCAAC–CO] in MeCN

Optimized Coordinates

1.	C	-0.745903	5.287044	-0.556980
2.	C	-1.919866	4.704469	0.252918
3.	C	-2.164181	3.246832	-0.128266
4.	H	-2.823337	5.293870	0.086518
5.	H	-1.706150	4.765572	1.323812
6.	C	-0.976091	2.341863	0.286122
7.	H	-2.304827	3.186731	-1.210538
8.	H	-3.083542	2.873253	0.321820
9.	C	0.341972	3.154775	0.224549
10.	C	0.314320	4.213184	-0.872249
11.	H	1.180636	2.470971	0.097875
12.	H	0.488234	3.652476	1.188496
13.	H	0.093506	3.736348	-1.831431
14.	H	1.298216	4.672036	-0.982658
15.	H	-0.286540	6.103974	0.004148
16.	H	-1.118776	5.717292	-1.488949
17.	C	-1.153790	1.725945	1.699152
18.	C	-1.647393	0.274412	1.530679
19.	H	-1.830629	2.325008	2.307649
20.	H	-0.186660	1.704896	2.201754
21.	N	-1.018096	-0.079361	0.237361
22.	C	-0.911737	1.065226	-0.567309
23.	C	-0.874011	1.054408	-1.878334
24.	O	-0.693269	1.055967	-3.046392
25.	C	-0.472259	-1.333491	-0.148345
26.	C	-1.284252	-2.299950	-0.770147
27.	C	-0.723371	-3.529240	-1.119569
28.	C	0.616927	-3.793571	-0.888559
29.	C	1.423341	-2.818716	-0.317256
30.	C	0.902137	-1.581912	0.055495
31.	H	1.037480	-4.752584	-1.164114
32.	H	2.474444	-3.023957	-0.161210
33.	H	-1.342631	-4.283245	-1.588206
34.	C	1.826676	-0.521357	0.617083
35.	C	2.694560	0.077627	-0.497875
36.	H	2.076834	0.478840	-1.302150
37.	H	3.356156	-0.680703	-0.922691
38.	H	3.314441	0.887086	-0.105848
39.	C	2.697818	-1.035391	1.766666
40.	H	1.202463	0.277833	1.008226
41.	H	3.275836	-0.212747	2.192207
42.	H	3.404218	-1.795891	1.427925
43.	H	2.090143	-1.470917	2.561415
44.	C	-2.736088	-2.027080	-1.107409
45.	C	-2.974151	-2.075617	-2.622453
46.	H	-4.009672	-1.813116	-2.849335
47.	H	-2.786481	-3.074321	-3.022093
48.	H	-2.322878	-1.374115	-3.145627
49.	C	-3.680466	-2.987806	-0.377450
50.	H	-2.960291	-1.016848	-0.776482
51.	H	-4.721231	-2.714599	-0.564988
52.	H	-3.511643	-2.968858	0.700668
53.	H	-3.537359	-4.015152	-0.719280
54.	C	-3.181070	0.215592	1.472127
55.	H	-3.606420	0.668711	2.369697
56.	H	-3.529804	-0.814553	1.417862
57.	H	-3.566019	0.751583	0.605174
58.	C	-1.153807	-0.632651	2.650429
59.	H	-0.071745	-0.580619	2.758972
60.	H	-1.434948	-1.670266	2.464400
61.	H	-1.607904	-0.324802	3.592946

[CyCAAC–CO] in MeCN

IR SPECTRUM

Mode	freq (cm**-1)	T**2
6:	28.57	1.021679
7:	30.57	0.433972
8:	41.79	0.090508
9:	55.02	0.069630
10:	75.00	1.064926
11:	81.83	1.794554
12:	89.79	0.206680
13:	97.18	1.449692
14:	106.20	0.484862
15:	125.27	0.389070
16:	135.35	2.375174
17:	140.30	1.099672
18:	143.78	0.303515
19:	195.74	0.169782
20:	206.80	2.844783
21:	214.17	1.736349
22:	222.86	3.700311
23:	232.13	3.311953
24:	241.70	0.983706
25:	242.74	0.482787
26:	254.66	0.561436
27:	256.84	1.336165
28:	266.25	1.193579
29:	271.34	1.855937
30:	281.34	2.583816
31:	296.69	3.380003
32:	301.94	0.576437
33:	319.73	0.395250
34:	321.83	0.239125
35:	338.85	4.018114
36:	353.46	6.931033
37:	364.30	0.868498
38:	398.12	1.841702
39:	415.83	3.112360
40:	433.91	0.830566
41:	444.27	4.822929
42:	453.23	6.038175
43:	466.25	14.840518
44:	491.89	2.987492
45:	521.97	0.313727
46:	545.94	8.031428
47:	549.97	2.178695
48:	560.52	3.495475
49:	577.86	11.697293
50:	599.82	4.494907
51:	602.11	4.692152
52:	632.17	2.668624
53:	651.10	2.436883
54:	657.84	0.315753
55:	730.71	3.134900
56:	772.70	11.895821
57:	773.85	14.802499
58:	807.45	10.814456
59:	816.23	6.595612
60:	824.07	7.767119
61:	839.71	11.935382
62:	844.61	23.269378
63:	861.74	2.613343
64:	893.17	0.463902
65:	904.66	4.588299
66:	917.47	1.559931
67:	935.28	1.386583
68:	938.64	1.113153
69:	942.01	1.094068
70:	947.58	8.788005
71:	948.50	4.877247
72:	952.54	7.074315
73:	965.16	0.890059
74:	965.97	0.263155
75:	967.69	0.718785
76:	973.77	2.216373
77:	991.19	3.148730
78:	1003.75	4.492856
79:	1015.19	2.307691
80:	1025.46	0.724577
81:	1035.83	3.348405
82:	1061.32	9.360255
83:	1065.62	7.908118
84:	1071.48	27.517105
85:	1083.81	0.708368
86:	1093.91	0.201333
87:	1121.71	2.273595
88:	1123.43	1.658259
89:	1130.36	7.466441
90:	1144.29	3.902850
91:	1159.35	3.063790
92:	1171.25	20.209537
93:	1174.49	1.202127
94:	1175.94	10.365736
95:	1185.36	2.203796
96:	1201.69	9.799429
97:	1206.11	140.615885
98:	1236.12	7.212165
99:	1237.69	20.355986
100:	1260.53	29.937591
101:	1264.33	55.488892
102:	1276.71	3.850825
103:	1278.67	12.548619
104:	1284.05	4.625729
105:	1291.40	7.416834
106:	1304.21	10.334465
107:	1318.41	26.119964
108:	1343.24	6.016211
109:	1345.15	2.527134
110:	1358.79	48.029145
111:	1361.95	20.839251
112:	1363.75	32.043817
113:	1365.38	44.221392
114:	1372.58	7.452077
115:	1374.21	1.208005
116:	1375.29	35.175708
117:	1381.94	1.845106
118:	1390.21	213.462095
119:	1392.06	14.613864
120:	1397.25	13.591138
121:	1398.79	3.640800
122:	1410.88	5.080677
123:	1412.98	10.051350
124:	1415.46	13.255467
125:	1471.49	4.538028
126:	1475.28	9.534127
127:	1475.93	11.633370
128:	1476.67	33.606652
129:	1479.06	5.206522
130:	1480.53	0.398681
131:	1481.68	0.300713
132:	1482.35	14.713107
133:	1483.41	2.788708
134:	1485.55	11.057869
135:	1486.75	14.350845
136:	1487.13	8.959513
137:	1489.63	1.150442
138:	1492.86	27.862608
139:	1494.09	12.901298
140:	1496.37	36.054112
141:	1496.66	5.672008
142:	1502.18	8.728422
143:	1503.19	3.806493
144:	1505.30	27.380161
145:	1614.86	12.633007
146:	1629.08	0.772247
147:	2121.33	1000.51217
148:	3012.60	19.416353
149:	3023.00	31.057530
150:	3023.25	59.179933
151:	3023.57	73.937339
152:	3025.45	39.719504
153:	3027.86	98.705864
154:	3029.19	33.323232
155:	3034.50	49.887350
156:	3035.23	87.538269
157:	3038.54	31.581304
158:	3044.49	28.881236
159:	3054.82	38.723480
160:	3057.98	46.990101
161:	3067.35	82.376893
162:	3076.41	60.439527
163:	3077.02	160.187756
164:	3078.56	121.593531
165:	3083.29	6.822862
166:	3085.16	32.775501
167:	3088.09	60.076441
168:	3089.45	74.649156
169:	3093.03	49.818658
170:	3093.48	58.723902
171:	3096.40	43.624020
172:	3097.47	43.292976
173:	3101.33	24.666686
174:	3104.63	9.745554
175:	3108.36	87.700855
176:	3115.36	66.367823
177:	3122.67	55.679877
178:	3123.65	47.908107
179:	3128.29	23.430031
180:	3166.82	11.918101
181:	3180.48	114.730993
182:	3191.41	127.007900

[CyCAAC–CO] in MeCN

NRT Analysis

```
   Atom
   ----  -
  1.  C
  2.  C
  3.  C
  4.  H
  5.  H
  6.  C
  7.  H
  8.  H
  9.  C
 10.  C
 11.  H
 12.  H
 13.  H
 14.  H
 15.  H
 16.  H
 17.  C
 18.  C
 19.  H
 20.  H
 21.  N
 22.  C
 23.  C
 24.  O
 25.  C
 26.  C
 27.  C
 28.  C
 29.  C
 30.  C
 31.  H
 32.  H
 33.  H
 34.  C
 35.  C
 36.  H
 37.  H
 38.  H
 39.  C
 40.  H
 41.  H
 42.  H
 43.  H
 44.  C
 45.  C
 46.  H
 47.  H
 48.  H
 49.  C
 50.  H
 51.  H
 52.  H
 53.  H
 54.  C
 55.  H
 56.  H
 57.  H
 58.  C
 59.  H
 60.  H
 61.  H
```

```
$NRTSTRA
STR       ! Wgt = 67.19%
LONE 21 1 24 2 END
 BOND S 1 2 S 1 10 S 1 15 S 1 16 S 2 3 S 2 4 S 2 5 S 3 6 S 3
7 S 3 8 S 6 9 S 6 17 S 6 22 S 9 10 S 9 11 S 9 12 S 10 13 S 10
14 S 17 18 S 17 S 19 S 17 20 S 18 21 S 18 54 S 18 58 S 21
22 S 21 25 D 22 23 23 24 D 25 26 S 25 30 S 26 27 S 26 44 D
27 28 S 27 33 S 28 29 S 28 31 D 29 30 S 29 32 S 30 34 S 34
35 S 34 39 S 34 40 S 35 36 S 35 37 S 35 38 S 39 41 S 39 42
S 39 43 S 44 45 S 44 49 S 44 50 S 45 46 S 45 47 S 45 48 S
49 51 S 49 52 S 49 53 S 54 55 S 54 56 S 54 57 S 58 59 S 58
60 S 58 61 END
END
STR       ! Wgt = 22.78%
LONE 21 1 22 1 24 1 END
BOND S 1 2 S 1 10 S 1 15 S 1 16 S 2 3 S 2 4 S 2 5 S 3 6 S 3
7 S 3 8 S 6 9 S 6 17 S 6 22 S 9 10 S 9 11 S 9 12 S 10 13 S 10
14 S 17 18 S 17 19 S 17 20 S 18 21 S 18 54 S 18 58 S 21 22
S 21 25 S 22 23 T 23 24 D 25 26 S 25 30 S 26 27 S 26 44 D
27 28 S 27 33 S 28 29 S 28 31 D 29 30 S 29 32 S 30 34 S 34
35 S 34 39 S 34 40 S 35 36  S 35 37 S 35 38 S 39 41 S 39 42
S 39 43 S 44 45 S 44 49 S 44 50 S 45 46 S 45 47 S 45 48 S
49 51 S 49 52 S 49 53 S 54 55 S 54 56 S 54 57 S 58 59 S 58
60 S 58 61 END
END
$END

$NRTSTRB
STR       ! Wgt = 67.19%
 LONE 21 1 24 2 END
 BOND S 1 2 S 1 10 S 1 15 S 1 16 S 2 3 S 2 4 S 2 5 S 3 6 S 3
7 S 3 8 S 6 9 S 6 17 S 6 22 S 9 10 S 9 11 S 9 12 S 10 13 S 10
14 S 17 18 S 17 19 S 17 20 S 18 21 S 18 54 S 18 58 S 21 22
S 21 25 D 22 23 D 23 24 D 25 26 S 25 30 S 26 27 S 26 44 D
27 28 S 27 33 S 28 29 S 28 31 D 29 30 S 29 32 S 30 34 S 34
35 S 34 39 S 34 40 S 35 36 S 35 37 S 35 38 S 39 41 S 39 42
S 39 43 S 44 45 S 44 49 S 44 50 S 45 46 S 45 47 S 45 48 S
49 51 S 49 52 S 49 53 S 54 55 S 54 56 S 54 57 S 58 59 S 58
60 S 58 61 END
END
STR       ! Wgt = 22.78%
LONE 21 1 22 1 24 1 END
BOND S 1 2 S 1 10 S 1 15 S 1 16 S 2 3 S 2 4 S 2 5 S 3 6 S 3
7 S 3 8 S 6 9 S 6 17 S 6 22 S 9 10 S 9 11 S 9 12 S 10 13 S 10
14 S 17 18 S 17 19 S 17 20 S 18 21 S 18 54 S 18 58 S 21 22
S 21 25 S 22 23 T 23 24 D 25 26 S 25 30 S 26 27 S 26 44 D
27 28 S 27 33 S 28 29 S 28 31 D 29 30 S 29 32 S 30 34 S 34
35 S 34 39 S 34 40 S 35 36 S 35 37 S 35 38 S 39 41 S 39 42
S 39 43 S 44 45 S 44 49 S 44 50 S 45 46 S 45 47 S 45 48 S
49 51 S 49 52 S 49 53 S 54 55 S 54 56S 54 57 S 58 59 S 58
60 S 58 61 END
  END
 $END
```

[CyCAAC–CO] in MeCN

NATURAL BOND ORBITALS (Summary):

```
        NBO              Occupancy    Energy
=========================================
=========
Molecular unit  1  (C24H35NO)
------ Lewis -----------------------------------
   1. CR ( 1) C  1          0.99999   -11.99993
   2. CR ( 1) C  2          0.99999   -12.00067
   3. CR ( 1) C  3          0.99999   -12.00334
   4. CR ( 1) C  6          0.99999   -12.03751
   5. CR ( 1) C  9          0.99999   -12.00337
   6. CR ( 1) C 10          0.99999   -12.00135
   7. CR ( 1) C 17          0.99999   -12.00622
   8. CR ( 1) C 18          0.99999   -12.05661
   9. CR ( 1) N 21          0.99999   -16.48752
  10. CR ( 1) C 22          0.99999   -12.04653
  11. CR ( 1) C 23          0.99999   -12.10806
  12. CR ( 1) O 24          1.00000   -21.66927
  13. CR ( 1) C 25          0.99999   -12.04795
  14. CR ( 1) C 26          0.99999   -12.02026
  15. CR ( 1) C 27          0.99999   -12.00916
  16. CR ( 1) C 28          0.99999   -12.01383
  17. CR ( 1) C 29          0.99999   -12.00915
  18. CR ( 1) C 30          0.99999   -12.02086
  19. CR ( 1) C 34          0.99999   -12.01504
  20. CR ( 1) C 35          0.99999   -11.99754
  21. CR ( 1) C 39          0.99999   -11.99756
  22. CR ( 1) C 44          0.99999   -12.01404
  23. CR ( 1) C 45          0.99999   -11.99691
  24. CR ( 1) C 49          0.99999   -11.99793
  25. CR ( 1) C 54          0.99999   -11.99442
  26. CR ( 1) C 58          0.99999   -11.99929
  27. LP ( 1) N 21          0.89923    -0.77341
  28. LP ( 1) O 24          0.98811    -1.25039
  29. LP ( 2) O 24          0.88880    -0.93489
  30. BD ( 1) C  1- C  2     0.99376    -0.99094
  31. BD ( 1) C  1- C 10     0.99362    -0.99049
  32. BD ( 1) C  1- H 15     0.99124    -0.89056
  33. BD ( 1) C  1- H 16     0.99144    -0.89077
  34. BD ( 1) C  2- C  3     0.99280    -1.00099
  35. BD ( 1) C  2- H  4     0.98993    -0.89296
  36. BD ( 1) C  2- H  5     0.99021    -0.89230
  37. BD ( 1) C  3- C  6     0.98634    -1.00102
  38. BD ( 1) C  3- H  7     0.98806    -0.89438
  39. BD ( 1) C  3- H  8     0.98954    -0.89849
  40. BD ( 1) C  6- C  9     0.98598    -1.00054
  41. BD ( 1) C  6- C 17     0.98266    -0.99675
  42. BD ( 1) C  6- C 22     0.96674    -1.01597
  43. BD ( 1) C  9- C 10     0.99340    -1.00300
  44. BD ( 1) C  9- H 11     0.98911    -0.89908
  45. BD ( 1) C  9- H 12     0.98714    -0.89262
  46. BD ( 1) C 10- H 13     0.98949    -0.89423
  47. BD ( 1) C 10- H 14     0.99008    -0.89365
  48. BD ( 1) C 17- C 18     0.98401    -1.00376
  49. BD ( 1) C 17- H 19     0.98833    -0.90328
  50. BD ( 1) C 17- H 20     0.98830    -0.90015
  51. BD ( 1) C 18- N 21     0.98467    -1.16018
  52. BD ( 1) C 18- C 54     0.99033    -1.01092
  53. BD ( 1) C 18- C 58     0.98935    -1.02220
  54. BD ( 1) N 21- C 22     0.98047    -1.21406
  55. BD ( 1) N 21- C 25     0.99074    -1.21830
  56. BD ( 1) C 22- C 23     0.99184    -1.21766
  57. BD ( 2) C 22- C 23     0.98100    -0.72529
  58. BD ( 1) C 23- O 24     0.99805    -1.63368
  59. BD ( 2) C 23- O 24     0.99368    -0.96029
  60. BD ( 1) C 25- C 26     0.98626    -1.10711
  61. BD ( 2) C 25- C 26     0.82633    -0.66593
  62. BD ( 1) C 25- C 30     0.98562    -1.10336
  63. BD ( 1) C 26- C 27     0.98751    -1.10462
  64. BD ( 1) C 26- C 44     0.98585    -1.02153
  65. BD ( 1) C 27- C 28     0.99077    -1.11133
  66. BD ( 2) C 27- C 28     0.83826    -0.65460
  67. BD ( 1) C 27- H 33     0.98858    -0.92265
  68. BD ( 1) C 28- C 29     0.99067    -1.10936
  69. BD ( 1) C 28- H 31     0.98982    -0.92423
  70. BD ( 1) C 29- C 30     0.98747    -1.10676
  71. BD ( 2) C 29- C 30     0.82532    -0.65679
  72. BD ( 1) C 29- H 32     0.98845    -0.92253
  73. BD ( 1) C 30- C 34     0.98591    -1.02254
  74. BD ( 1) C 34- C 35     0.98722    -0.99785
  75. BD ( 1) C 34- C 39     0.99019    -1.00180
  76. BD ( 1) C 34- H 40     0.98349    -0.90153
  77. BD ( 1) C 35- H 36     0.99436    -0.89867
  78. BD ( 1) C 35- H 37     0.99485    -0.89700
  79. BD ( 1) C 35- H 38     0.99360    -0.89639
  80. BD ( 1) C 39- H 41     0.99385    -0.89621
  81. BD ( 1) C 39- H 42     0.99473    -0.89878
  82. BD ( 1) C 39- H 43     0.99439    -0.89853
  83. BD ( 1) C 44- C 45     0.98840    -0.99795
  84. BD ( 1) C 44- C 49     0.98911    -1.00002
  85. BD ( 1) C 44- H 50     0.98369    -0.89975
  86. BD ( 1) C 45- H 46     0.99380    -0.89562
  87. BD ( 1) C 45- H 47     0.99490    -0.89757
  88. BD ( 1) C 45- H 48     0.99459    -0.89815
  89. BD ( 1) C 49- H 51     0.99399    -0.89638
  90. BD ( 1) C 49- H 52     0.99425    -0.89939
  91. BD ( 1) C 49- H 53     0.99473    -0.89833
  92. BD ( 1) C 54- H 55     0.99200    -0.89641
  93. BD ( 1) C 54- H 56     0.99347    -0.90187
  94. BD ( 1) C 54- H 57     0.99309    -0.90131
  95. BD ( 1) C 58- H 59     0.99330    -0.90459
  96. BD ( 1) C 58- H 60     0.99290    -0.90071
  97. BD ( 1) C 58- H 61     0.99114    -0.89943
```

3.5 Author Contributions

Lauren E. Lieske (co-lead author; equal), Lucas A. Freeman (co-lead author; equal) and Dr. Guocang Wang (supporting) synthesized and characterized all compounds reported here; Lauren E. Lieske (co-lead author; equal) performed all electrochemical and spectroelectrochemical experiments; Dr. Diane A. Dickie (supporting) performed all X-ray crystallographic studies; Prof. Dr. Robert J. Gilliard, Jr. (co-corresponding author; equal) and Prof. Dr. Charles W. Machan (co-corresponding author; equal) curated all data, acquired funding, conducted formal data analysis and experimental design, and supervised the project.

3.6 References

1. Welz, E.; Böhnke, J.; Dewhurst, R. D.; Braunschweig, H.; Engels, B., *J. Am. Chem. Soc.* **2018,** *140*, 12580.
2. Holzmann, N.; Andrada, D. M.; Frenking, G., *J. Organometallic Chem.* **2015,** *792*, 139.
3. Mondal, K. C.; Roesky, H. W.; Schwarzer, M. C.; Frenking, G.; Tkach, I.; Wolf, H.; Kratzert, D.; Herbst-Irmer, R.; Niepötter, B.; Stalke, D., *Angew. Chem. Int. Ed.* **2012,** *52*, 1801.
4. Rozenberg, I.; Eivgi, O.; Frenklah, A.; Butilkov, D.; Kozuch, S.; Goldberg, I.; Lemcoff, N. G., *ACS Catal.* **2018,** *8*, 8182.
5. Bawari, D.; Goswami, B.; R, S. V.; Thakur, S. K.; Varun Tej, R. V.; Roy Choudhury, A.; Singh, S., *Dalton Trans.* **2018,** *47*, 6274.
6. Eichhorn, A. F.; Kuehn, L.; Marder, T. B.; Radius, U., *Chem. Commun.* **2017,** *53*, 11694.

7. Soleilhavoup, M.; Bertrand, G., *Acc. Chem. Res.* **2015,** *48*, 256.

8. Melaimi, M.; Jazzar, R.; Soleilhavoup, M.; Bertrand, G., *Angew. Chem. Int. Ed.* **2017,** *56*, 10046.

9. Lavallo, V.; Canac, Y.; Präsang, C.; Donnadieu, B.; Bertrand, G., *Angew. Chem. Int. Ed* **2005,** *44*, 5705.

10. Riduan, S. N.; Zhang, Y.; Ying, J. Y., *Angew. Chem.* **2009,** *121*, 3372.

11. Nesterov, V.; Reiter, D.; Bag, P.; Frisch, P.; Holzner, R.; Porzelt, A.; Inoue, S., *Chem. Rev.* **2018,** *118*, 9678.

12. Lavallo, V.; Canac, Y.; Donnadieu, B.; Schoeller, W. W.; Bertrand, G., *Angew. Chem. Int. Ed.* **2006,** *45*, 3488.

13. Vincent, L.; Yves, C.; Bruno, D.; W., S. W.; Guy, B., *Angew. Chem.* **2006,** *118*, 3568.

14. Luca, O. R.; McCrory, C. C. L.; Dalleska, N. F.; Koval, C. A., *J. Electrochem. Soc.* **2015,** *162*, H473.

15. Riduan, S. N.; Zhang, Y.; Ying, J. Y., *Angew. Chem. Int. Ed.* **2009,** *48*, 3322.

16. Singh, A. P.; Samuel, P. P.; Roesky, H. W.; Schwarzer, M. C.; Frenking, G.; Sidhu, N. S.; Dittrich, B., *J. Am. Chem. Soc.* **2013,** *135*, 7324.

17. Savéant, J. M., Coupling of Electrode Electron Transfers with Homogeneous Chemical Reactions. In *Elements of Molecular and Biomolecular Electrochemistry*, John Wiley & Sons, Inc.: 2006.

18. Machan, C. W.; Sampson, M. D.; Chabolla, S. A.; Dang, T.; Kubiak, C. P., *Organometallics* **2014,** *33*, 4550.

19. Zavarine, I. S.; Kubiak, C. P., *J. Electroanal. Chem.* **2001,** *495*, 106.

20. Del Bene, J. E.; Alkorta, I.; Elguero, J., *J. Phys. Chem. A* **2017,** *121*, 4039.

21. Alecu, I. M.; Zheng, J.; Zhao, Y.; Truhlar, D. G., *J. Chem. Theory Comput.* **2010,** *6*, 2872.

22. Christensen, P. A.; Hamnett, A.; Muir, A. V. G.; Freeman, N. A., *J. Electroanal. Chem. Interfacial Electrochem.* **1990,** *288*, 197.

23. Glendening, E. D.; Landis, C. R.; Weinhold, F., NBO 6.0: Natural bond orbital analysis program **2013,** *34*, 1429.

24. Glendening E. D., B. J. K., Reed A. E., Carpenter J. E. , Bohmann J. A., Morales C. M., Landis C. R., and Weinhold F. *NBO 6.0* Theoretical Chemistry Institute: University of Wisconsin, Madison, WI, 2013.

25. Nichols, A. W.; Chatterjee, S.; Sabat, M.; Machan, C. W., *Inorg. Chem.* **2018,** *57*, 2111.

26. Cheng, S. C.; Blaine, C. A.; Hill, M. G.; Mann, K. R., *Inorg. Chem.* **1996,** *35*, 7704.

27. Bruker, *Saint; SADABS;APEX3* **2012**.

28. Sheldrick, G. M., *Cell_now* **2008**.

29. Sheldrick, G., *Acta Crystallogr., Sect. A* **2015,** *71*, 3.

30. Dolomanov, O. V.; Bourhis, L. J.; Gildea, R. J.; Howard, J. A. K.; Puschmann, H., *J. Appl. Crystallogr.* **2009,** *42*, 339.

31. Neese, F., *Wiley Interdiscip. Rev.: Comput. Mol. Sci.* **2012,** *2*, 73.

32. Vosko, S. H.; Wilk, L.; Nusair, M., *Can. J. Phys.* **1980,** *58*, 1200.

33. Lee, C.; Yang, W.; Parr, R. G., *Phys. Rev. B* **1988,** *37*, 785.

34. Stephens, P. J.; Devlin, F. J.; Chabalowski, C. F.; Frisch, M. J., *J. Phys. Chem.* **1994,** *98*, 11623.

35. Schäfer, A.; Horn, H.; Ahlrichs, R., *J. Chem. Phys.* **1992,** *97*, 2571.

36. Weigend, F.; Ahlrichs, R., *Phys. Chem. Chem. Phys.* **2005,** *7*, 3297.

37. Becke, A. D., *J. Chem. Phys.***1993,** *98*, 1372.

38. Becke, A. D., *J. Chem. Phys.* **1993,** *98*, 5648.

39. Cossi, M.; Rega, N.; Scalmani, G.; Barone, V., *J. Comput. Chem.* **2003,** *24*, 669.

40. Glendening, E. D.; Badenhoop, J. K.; Reed, A. E.; Carpenter, J. E.; Bohmann, J. A.; Morales, C. M.; Landis, C. R.; Weinhold, F. *NBO 6.0*, Theoretical Chemistry Institute, University of Wisconsin: Madison, WI, 2013.

41. Pettersen, E. F.; Goddard, T. D.; Huang, C. C.; Couch, G. S.; Greenblatt, D. M.; Meng, E. C.; Ferrin, T. E., *J. Comput. Chem.* **2004,** *25*, 1605.

CHAPTER FOUR

Electrocatalytic Reduction of Dioxygen by Mn(III) meso-tetra(N-methylpyridinium-4-yl)porphyrin in Universal Buffer

This chapter is reproduced from "L. E. Lieske, S. L. Hooe, A. W. Nichols and C. W. Machan, *Dalton Trans.*, **2019,** *48,* 8633."

4.1 Abstract

The electrochemical characterization of manganese(III) meso-tetra(N-methylpyridinium-4-yl)porphyrin pentachloride ([Mn(TMPyP)Cl][Cl]$_4$) via cyclic voltammetry (CV) and UV-vis spectroelectrochemistry (UV-vis SEC) was performed across the entire pH domain in aqueous buffered conditions. Assessment of the homogeneous electrocatalytic efficiency for the oxygen reduction reaction (ORR) from pH 3 to 6 using rotating-ring disk electrode experiments (RRDE) found it to be selective for water (82 to 93%). The observed efficiency for water is in contrast to previous reports on electrocatalytic ORR activity by Mn porphyrins in aqueous systems, which identified H_2O_2 as the primary product using indirect RDE methods only. The results described here are consistent with recent reports on the electrocatalytic behavior of Mn porphyrins under nonaqueous conditions, where the similar selectivity for water was also determined by RRDE methods. At pH 1, UV-vis SEC experiments also revealed that decomposition was occurring; free-base porphyrin was observed after the application of reducing potentials.

4.2 Introduction

Due to the highly selective nature of O_2 reduction to H_2O by the iron porphyrin active site in cytochrome c oxidase, porphyrin-based ligand scaffolds have been developed in order to study the reactivity of synthetic metal complexes with O_2.[1] To date, iron- and cobalt-based porphyrin systems have received significant attention for homogenous ORR catalytic studies, with comparatively less known about their manganese analogues.[2] Herein we report the electrochemical characterization of the water-soluble manganese(III) meso-tetra(N-methylpyridinium-4-yl)porphyrin pentachloride ([Mn(TMPyP)Cl]$^{4+}$) from pH 1–14 in aqueous buffered conditions via cyclic voltammetry (CV), UV-vis

spectroelectrochemistry (SEC), and rotating-ring disk electrode (RRDE) studies. Under acidic conditions (from pH 3–6) and in the presence of O_2, $[Mn(TMPyP)Cl]^{4+}$ functions as a competent electrocatalyst for the $4e^-$ pathway to water, with efficiencies from 82 to 93% established by rotating ring-disk electrode RRDE experiments. Previous studies on this catalyst reported that $[Mn(TMPyP)Cl]^{4+}$ was active for the electrocatalytic reduction of O_2 with H_2O_2 as the major product.[3-4] However, studies on the related $[Fe(TMPyP)]^{5+}$ system reported that selectivity for the four-electron reduction to water was dependent on low catalyst concentrations and the involvement of a heterogeneous response from catalyst adsorption on the electrode.[2, 5-7]

A recent report on the activity of $[Mn(porphyrin)]^+$ derivatives for the electrocatalytic reduction of O_2 to H_2O under non-aqueous conditions motivated us to re-examine $[Mn(TMPyP)Cl]^{4+}$ under aqueous conditions.[8] With $[Mn(TMPyP)Cl]^{4+}$ our results indicate catalytic selectivity for H_2O instead of H_2O_2 from pH 3 to 6 in Britton–Robinson buffer.[9] Unlike $[Fe(TMPyP)]^{5+}$, control testing showed electrode adsorption did not occur, meaning that the observed catalytic response for $[Mn(TMPyP)Cl]^{4+}$ is homogeneous in nature. The disparity between our results and those previously published appear to arise from experimental methodology: prior reports used indirect RDE methods,[3-4] while we have directly quantified H_2O_2 production using RRDE methods.

4.3 Results and Discussion

4.3.1 Electrochemical Characterization

In initial CV studies of $[Mn(TMPyP)Cl]^{4+}$ (**Figure 4.1**) under Ar saturation, the $E_{1/2}$ values for the Mn(III)/(II) reduction were determined from pH 1–14. Britton–Robinson buffer,[9-10] adjusted with a NaOH solution, (**Table SI 4.1**) was used as a universal buffer

system from pH 2–13 in order to maintain a similar reaction environment for each set of experimental conditions.[11] This necessitated a systematic comparison to previous reports, in order to establish that the behavior in the universal buffer system did not differ substantively. *Nota bene*, the equilibrium displacement reaction of Cl^- by H_2O is known to occur in aqueous solution, resulting in the formation of diaquo species $[Mn(III)(TMPyP)(OH_2)_2]^{5+}$.[12] Based on the reported pK_{a1} and pK_{a2} values of 8.0 and 10.6 for $[Mn(III)(TMPyP)(OH_2)_2]^{5+}$,[12-13] by pH 11 the aquo ligands should both be partially deprotonated to generate the Mn-dihydroxo species $[Mn(III)(TMPyP)(OH)_2]^{3+}$.[12, 14]

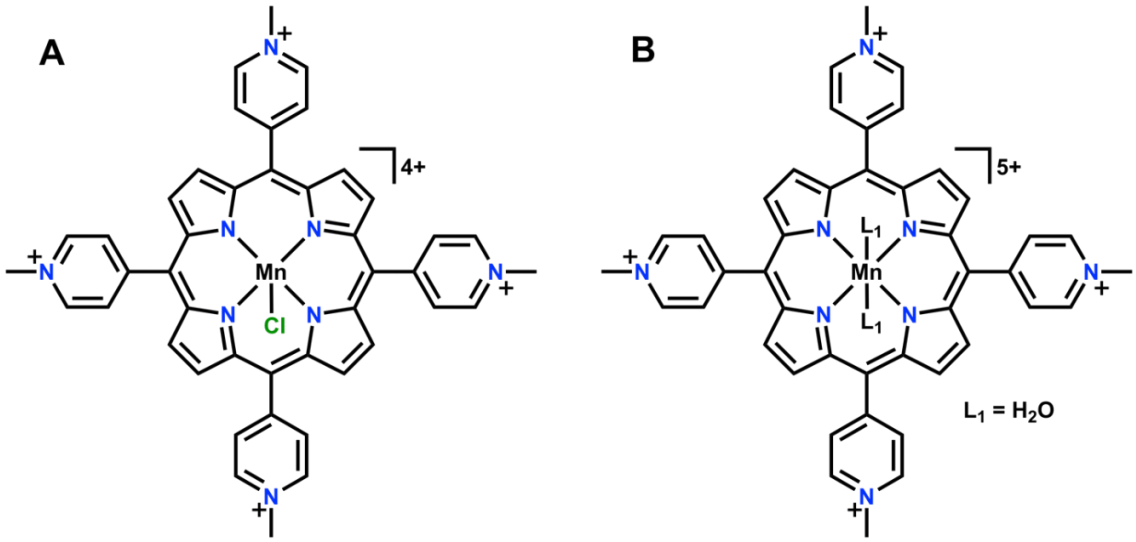

Figure 4.1. (A) Structure of the solid state water-soluble manganese (III) meso-tetra(N-methylpyridinium-4-yl) porphyrin pentachloride ($[Mn(TMPyP)Cl]^{4+}$) **(B)** Diaquo species expected to predominate in aqueous solution (pH 3-8), $[Mn(TMPyP)(OH_2)_2]^{5+}$.

At all pH values greater than 2, the ratio of i_{pc}/i_{pa} values were around 1 for the Mn(III)/(II) couple, however the peak-to peak separation (ΔE) was consistent with a quasi-reversible redox event with ΔE > 60 mV (**Tables SI 4.2 – SI 4.15 and Figures SI 4.1 – SI 4.15**).[15] We note that the large observed ΔE can be attributed in part to the anticipated structural reorganization of the Mn center undergoing reduction from d^4 to d^5: previous

reports with Mn porphyrin complexes have established that the coordination environment of the parent species undergoes a transformation from six-coordinate to five-coordinate upon reduction.[12-14] At pH 2 and below, the Mn(III)/(II) redox feature becomes irreversible, restricting the analysis of the pH-dependent standard potentials, $E_{1/2}$, under Ar saturation from pH 3–14 (**Figure SI 4.14**). Notably, the quasi-reversible shape of Mn(III/II) redox couple from pH 3–13 (**Figure SI 4.14**) is characteristic of waveforms which fall under the *KO* regime of the *CE* (*C* – chemical process; *E* – electron transfer) kinetic zone diagram.[15-16] We attribute this to pre-equilibrium processes involving multiple metal–ligand (buffer components, Cl^- and H_2O) exchange reactions that are dependent on the underlying Mn aquo acid–base equilibria. The increased asymmetry of ΔE and decreasing i_{pc}/i_{pa} values of the Mn(III)/(II) reduction at higher scan rates are consistent with the interception of a K_{eq} process for a *CE* reaction (**Tables SI 4.2- SI 4.14; Figures SI 4.1- SI 4.13**).[14-16]

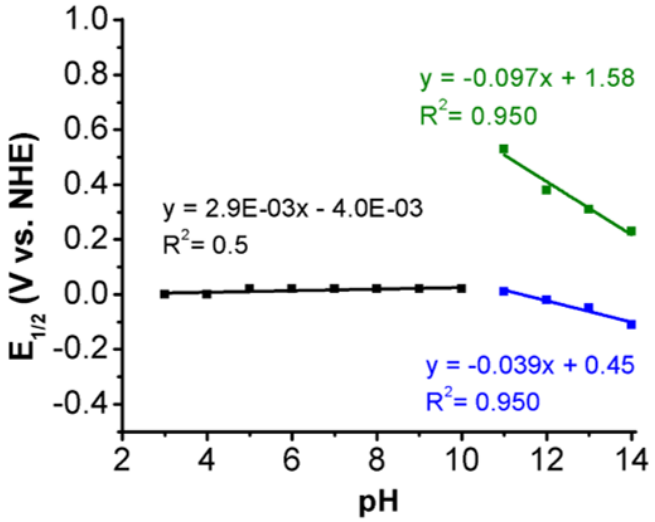

Figure 4.2. Potential-pH plot constructed from CV data obtained on the Mn(III)/(II) (black and blue) and Mn(IV)/(III) (green) reduction features of $[Mn(TMPyP)Cl]^{4+}$ in Britton-Robinson buffer conditions under Ar saturation.

4.3.2 Description of Speciation in Solution

The potential-pH plot shown in **Figure 4.2**, revealed two distinct regimes for the Mn(III)/(II) reduction. The first regime (**Figure 4.2, black**) was located from pH 3–10 where the $E_{1/2}$ was independent of pH, which is consistent with previous results.[3, 14, 17-18] In this region, the reduction of Mn(III)/(II) is not dependent on proton transfer and can be described by eqn (1) for 3 ≤ pH < 8.0 and eqn (2) for 8.0 < pH < 10.6

$$[Mn(III)L(OH_2)_2]^{5+} + e^- \rightleftharpoons [Mn(II)L(OH_2)]^{4+} + H_2O \quad (1)$$

$$[Mn(III)L(OH)(OH_2)]^{4+} + e^- \rightleftharpoons [Mn(II)L(OH)]^{3+} + H_2O \quad (2)$$

where L refers to the porphyrin ligand TMPyP. The second regime extends between pH 11 and 14, where the $E_{1/2}$ of Mn(III/II) shifts towards more reducing potentials with a slope of 39 mV per pH unit (**Figure 4.2, blue**). The Nernstian dependence deviates slightly from 59 mV per pH for Mn(III)/(II) across this pH range, which suggests a $1H^+$ /$1e^-$ reaction with slow proton transfer kinetic parameters at basic pH values or a competing equilibrium process. The proposed electrochemical reaction is described by eqn (3) for 10.6 < pH < 14.[12] Another contributing factor in this region may be an additional acid–base equilibrium of the product Mn(II) species formed at more basic conditions, $[Mn(II)(TMPyP)(OH)]^{3+}$; the pK_{a1} of this species has previously been characterized as 12.4.[12]

$$[Mn(III)L(OH)_2]^{3+} + H^+/e^- \rightleftharpoons [Mn(II)L(OH)]^{3+} + H_2O \quad (3)$$

CVs obtained from pH 10–14 also revealed a second feature at more positive potentials, which previous reports assign to a Mn(IV)/(III) reduction (**Figure SI 4.15**).[17, 19-20] This redox wave shifts from quasi-reversible at pH 10, where the two species ($[Mn(III)(TMPyP)(OH_2)(OH)]^{4+}$ and $[Mn(III)(TMPyP)(OH)_2]^{3+}$) should exist, to reversible from pH 11–14 (**Table SI 4.15**).[12, 14] The known pK_a values of the Mn(IV) porphyrin should establish two regions for potential-pH dependence involving Mn(IV)/(III) (7.5 < pH < 10.7

and 10.7 < pH ≤ 14), which have good overlap with those of the Mn(III) species. The Mn(IV)/(III) reduction feature also shifts towards negative potentials at higher pH values from pH 11 to 14, with a slope of 97 mV per pH suggesting a $2H^+/e^-$ process as described by eqn (4) and (5) (**Figure 4.2, green**). Limited electrochemical reversibility restricts our analysis to the second region only, however.[21-23] The Nernstian dependence of $E_{1/2}$ on pH in this region appears to describe a $2H^+/1e^-$ reaction more than a $1H^+/1e^-$ reaction, for which both eqn (4) and (5) have been proposed previously,[14] but again deviation from the expected 118 mV per pH unit occurs. It should be noted that based on known pK_a values, the putative product in eqn (4) should not be stable, the dihydroxo species $[Mn(III)(TMPyP)(OH)_2]^{3+}$ is expected under these conditions. Conversely, eqn (5) proposes a Mn(IV) dioxo species where only one double bond is possible based on d electron count.[24] One possible explanation for the observed deviation from 118 mV per pH is a dimerization reaction involving the Mn(IV) porphyrin to generate $[[Mn(IV)(TMPyP)]_2(\mu_2\text{-}O)]^{10+}$, evidence of which is observed spectroscopically in the broadening of the Soret band, vide infra (**Figure 4.3B**).[14, 25-26] Clearly, the competing acid–base and dimerization equilibria correspond to a complex reaction environment where it is difficult to assign speciation unequivocally. The general consensus in published reports[12-14, 21, 23, 25, 27-29] is to formulate the monomeric Mn(IV) species at pH > 11 as $[Mn(IV)(TMPyP)(O)(OH)]^{3+}$, which suggests that the potential pH slope for the Mn(IV)/(III) reduction from pH 11 to 14 should describe a $1H^+/1e^-$ reaction, eqn (6); the observed deviation from 59 mV per pH is then likely to be a consequence of the competing dimerization equilibrium and diminished proton transfer kinetic parameters under basic conditions eqn (7).

$$[Mn(IV)L(O)(OH)]^{3+} + 2H^+/e^- \rightleftharpoons [Mn(III)L(OH)(OH_2)]^{3+} \qquad (4)$$

$$[Mn(IV)(O)_2]^{2+} + 2H^+/e^- \rightleftharpoons [Mn(III)L(OH)_2]^{3+} \quad (5)$$

$$[Mn(IV)L(O)(OH)]^{3+} + H^+/e^- \rightleftharpoons [Mn(III)(OH)_2]^{3+} \quad (6)$$

$$2[Mn(IV)L(O)(OH)]^{3+} \rightleftharpoons [[Mn(IV)L]_2(\mu_2 O)]^{10+} + 2OH^- \quad (7)$$

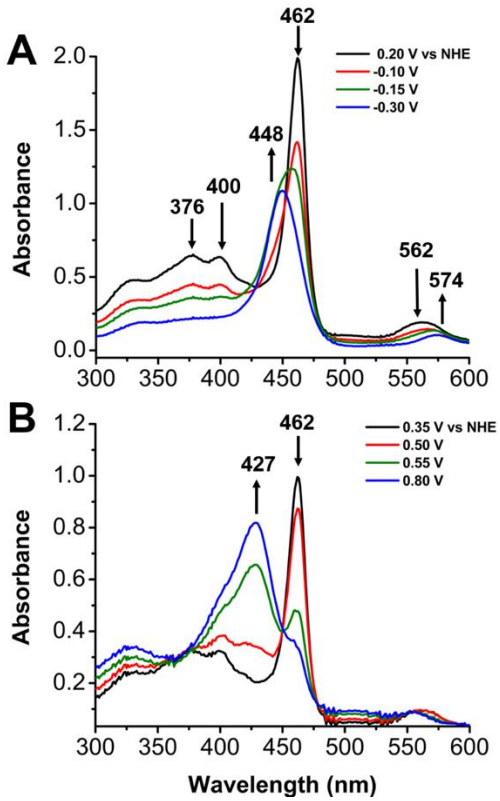

Figure 4.3. UV-vis SEC of 0.1 mM [Mn(III)(TMPyP)Cl]$^{4+}$ in a pH 10 Britton-Robinson Buffer solution **(A)** under reducing conditions and **(B)** under oxidizing conditions. Conditions: Honeycomb platinum electrode and a Ag/AgCl sat'd KCl aqueous reference electrode corrected to NHE.

UV-vis spectroscopic studies were subsequently used to evaluate the stability of [Mn(TMPyP)Cl]$^{4+\cdot}$ UV-vis absorbance data were collected with equimolar amounts of the free-base porphyrin and [Mn(TMPyP)Cl]$^{4+}$ at pH 1 and pH 14, using 1 M HCl/0.1 M NaCl and 1 M KOH/0.1 M NaCl, respectively: no demetallation was observed under these conditions (**Figure SI 4.16**). Analysis of [Mn(TMPyP)Cl]$^{4+}$ from pH 1 to 14 by UV-vis also revealed a decrease in the absorbance intensity of the Soret band (462 nm), with the concomitant appearance of a band at 453 nm at pH values greater than 10.6, consistent with

the diaquo species undergoing two pK_a transitions to form $[Mn(III)TMPyP(OH)_2]^{3+}$ (**Figure SI 4.17 and SI 4.18**).[12, 17, 19] With this information in hand, UV-vis spectroelectrochemical (SEC) studies were conducted under an Ar atmosphere to assess the speciation in solution as a function of potential and pH. At pH 1, as the potential is moved to more reducing potentials from +0.40 to +0.10 V vs. NHE to examine the Mn(III)/(II) reduction, a decrease in the intensity of the Soret band at 462 nm with a corresponding blue shift from 462 to 440 nm occurs along with a blue shift in the Q band from 560 nm to 502 nm (**Figure SI 4.19**). Upon returning the potential to 0.40 V vs. NHE, UV-vis spectra consistent with free base TMPyP are observed (**Figure SI 4.16A and SI 4.19**). These results indicate that upon reduction at +0.10 V vs. NHE, $[Mn(II)(TMPyP)(OH_2)]^{4+}$ is unstable and de-metalation occurs. This is consistent with previous reports that suggest the decomposition of analogous Mn porphyrins at a pH of 2 and below.[27-28] We note that with the Universal Buffer, the same Mn(III)/(II) reduction at a pH of 3 shows some degradation: moving from +0.20 V to −0.10 V vs. NHE caused a shift in the Soret band from 463 nm to 450 nm that was only partially reversible after 4 minutes at reducing potentials (**Figure SI 4.20A**). Returning the cell potential to +0.20 V vs. NHE resulted in the appearance of a new band at 422 nm and restored only 70% of the original absorbance intensity at 463 nm, consistent with partial demetallation (**Figure SI 4.20A**). For comparison, when the Soret band is monitored during the same Mn(III)/(II) reduction at pH 7, a blue shift is still observed as reducing potentials are applied stepwise from +0.20 to −0.10 V vs. NHE (**Figure SI 4.20B**). Under these pH conditions, however, this process is reversible: returning the potential to +0.20 V vs. NHE restores the features of the original absorbance spectrum and no new bands are observed. Following spectral

changes in the absorbance of the Soret band during the Mn(III)/(II) reduction at pH 10 revealed a new band at 448 nm with the disappearance of the parent species at 462 nm, suggesting the quantitative formation of [Mn(II) (TMPyP)(OH)]$^{3+}$ (**Figure 4.3A;** eqn (2)).[12] Conversely, as the potential is moved stepwise to more oxidizing potentials from +0.35 to +0.80 V vs. NHE to probe the changes corresponding to the Mn(IV/III) reduction, a blue shift of the Soret band is observed with the appearance of a new band at 427 nm (**Figure 4.3B**), which is indicative of the formation of [Mn(IV)(TMPyP)(O)(OH)]$^{3+}$, eqn (4)–(6). It is worth noting here that Mn(IV) porphyrins are known to form μ_2-oxo-dimers [(Mn(IV)(TMPyP) (OH))$_2$(μ_2-O)]$^{8+}$ in alkaline solutions eqn (7). [25-26] The large half-width observed for the Soret band at 427 nm (**Figure 4.3B**) in this experiment is characteristic of this type of Mn-μ_2-oxo-dimer and is observed at pH values to or greater than 10 with the formation of a Mn(IV) oxidation state.[25-26]

At pH 14 as the potential is moved stepwise from +0.10 V to −0.20 V vs. NHE to probe Mn(III)/(II) reduction, a shoulder appears on the Soret band at 416 nm along with a concomitant red shift in the Q band, which suggests the generation of [Mn(II)TMPyP(OH)]$^{3+}$ (eqn (3); **Figure SI 4.21A**).[12] Nota bene the pK_{a2} of the parent Mn(III) diaquo is 10.6.[12] As the potential is moved stepwise to more oxidizing potentials from +0.15 to +0.50 V vs. NHE to observe changes corresponding to the Mn(IV/III) reduction, a shoulder at 425 nm appears, representative of [Mn(IV)(TMPyP)(O)(OH)]$^{3+}$ eqn (5) and the corresponding formation of the [(Mn(IV)(TMPyP)(OH))$_2$(μ_2-O)]$^{8+}$ dimer based on the broadening of this feature (**Figure SI 4.21B**).[12] These speciation results are generally consistent with prior reports, suggesting that the use of the universal buffer

system does not have significant consequences on the electrochemical behavior of the parent $[Mn(TMPyP)Cl]^{4+}$ species.[12-14]

4.3.3 Catalytic Activity

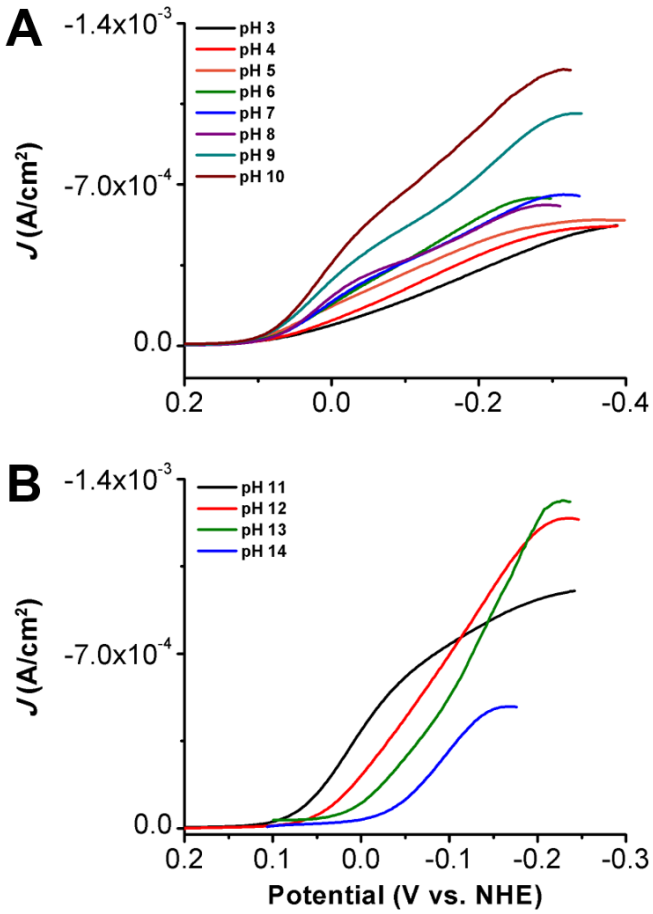

Figure 4.4. Linear-sweep voltammetry of $[Mn(TMPyP)Cl]^{4+}$ (partial plots of CV data), demonstrating reactivity under O_2 saturation conditions with corresponding shifts **(A)** from pH 3-10 and **(B)** from pH 11-14. Conditions: Glassy carbon working electrode, glassy carbon counter electrode, 3.0 M NaCl Ag/AgCl reference electrode; Scan rate 100 mV/s.

Based on the observed speciation of $[Mn(TMPyP)Cl]^{4+}$, we were interested in determining if the distinct potential-pH regimes would have a significant effect on its product selectivity, efficiency or activity for the electrocatalytic ORR. $[Mn(TMPyP)Cl]^{4+}$ was initially examined via CV studies under variable O_2 saturation conditions (max $[O_2]$ =

1.3 mM [2, 30]) across all pH values (**Figures SI 4.22 – SI 4.35**). At pH 1, minimal increases in catalytic current were observed with changes in [O_2] (**Figure SI 4.22**). Between pH 2–14, however, current increased proportionally to the concentration of O_2, indicative of a catalytic response (**Figures SI 4.23–SI 4.35**). A series of control CVs obtained at all pH values demonstrated that a heterogenous reduction response from the electrode occurred at more negative potentials than the molecular regime in all cases (**Figures SI 4.36–SI 4.49**). A plot of the catalytic response for ORR at each pH showed two regimes based on pH. From pH 3 to pH 10, the catalytic response shifted to positive potentials with increasing pH (**Figure 4.4A**). However, from pH 11 to 14, a shift back towards negative potentials occurred with increasing pH values (**Figure 4.4B**). Interestingly, the appearance of two distinct waves was also observed in the catalytic feature for pH 7–11 (**Figure 4.4B**). These pH-dependent differences in the shape of the CV wave may be suggestive of a different mechanism occurring at more basic potentials in comparison to acidic conditions (**Figure 4.5**); it is also noteworthy that this pH regime spans the pK_{a1} and pK_{a2} values of 8.0 and 10.6 for $[Mn(III)(TMPyP)(OH_2)_2]^{5+}$. [12-13] It is possible that at more basic pH values concerted reduction and protonation steps involving superoxide/peroxide-type intermediates could require more reducing potentials than acidic conditions.

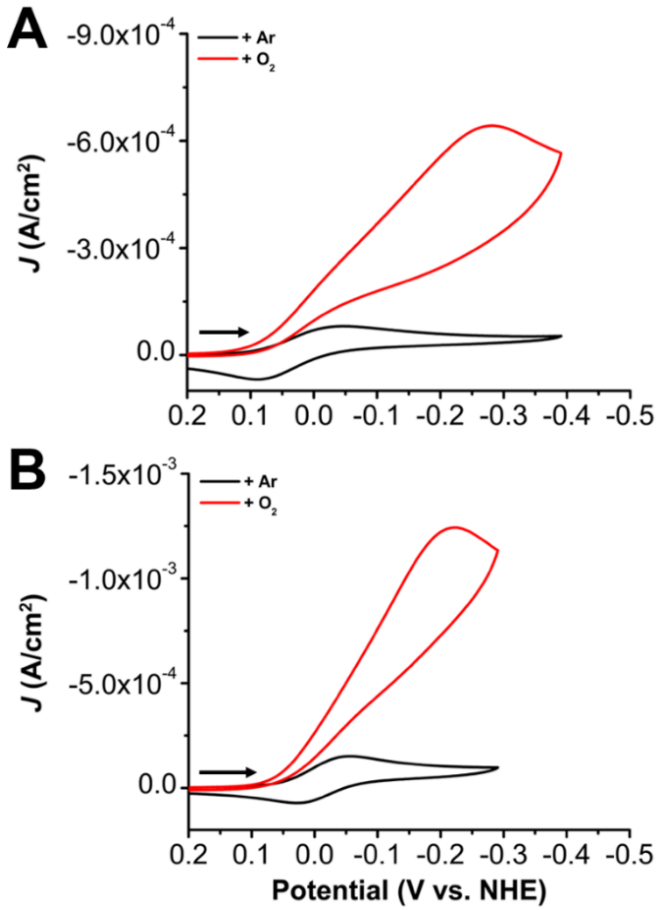

Figure 4.5. CVs of $[Mn(TMPyP)Cl]^{4+}$ under Ar and O_2 saturation conditions in **(A)** pH 6 buffer **(B)** pH 12 buffer solution. Conditions: glassy carbon working electrode, glassy carbon counter electrode, 3.0 M NaCl Ag/AgCl reference electrode; scan rate 100 mV/s.

Previous studies on the $[Fe(TMPyP)]^{5+}$ system in acidic conditions found that a heterogenous pathway arising from adsorption on the electrode contributed significantly to the observed activity.[10] Likewise, non-specific adsorption was also reported in a prior study of $[Mn(TMPyP)Cl]^{4+}$.[3] To ensure a similar mechanism was not occurring for $[Mn(TMPyP)Cl]^{4+}$, a rinse test was performed at pH values 1, 3, 6, 7, and 12 (**Figures SI 4.50–SI 4.54**). No adsorption was observed at any of the tested pH values, suggesting a purely homogenous response. Catalytic efficiency was subsequently determined using RRDE experiments (**See Section 4.5**). These results suggested $[Mn(TMPyP)Cl]^{4+}$ was primarily selective for the four-electron pathway to H_2O (82 to 93%) from pH 3 to 6

(**Figures SI 4.55–SI 4.70, Table 4.1**). Reliable product analysis could not be performed at pH values outside of this range because the background disk and ring current were larger than the observed catalytic current (**Figure SI 4.71**). The quasi-reversibility of the Mn(III)/(II) reduction under non-catalytic conditions as a result of the competing chemical equilibria described previously precludes accurate use of foot-of-the-wave analysis (FOWA)[31] and variable scan-rate studies did not establish a scan rate-independent catalytic response because of the background electrode response at higher scan rates. In order to estimate an upper limit for the TOF_{max} value of this system, we used the i_{cat}/i_p ratio method as described in the Experimental methods.[32-33] For completeness, overpotential (η) values calculated using the $E_{1/2}$ of Mn(III)/(II) under Ar saturation conditions are included in **Table 4.1** for reference.

Table 4.1. Catalytic efficiencies, overpotentials and TOF_{max} determined for $[Mn(TMPyP)Cl]^{4+}$ from pH 3 to 6.

pH	Current Efficiency for H_2O	electrons transferred (n)[a]	Overpotential (η)	TOF_{max} (s^{-1})[b]
3	82 (±4) %	3.64	1.05 V	4.3
4	89 (±2) %	3.77	0.99 V	2.1
5	93 (±1) %	3.86	0.91 V	2.2
6	85 (±5) %	3.69	0.85 V	3.9

[a] – determined from current efficiencies based on RRDE data; [b] – determined from i_{cat}/i_p ratios at $0.1 Vs^{-1}$.

To investigate the possibility of a 2 + 2 pathway, where H_2O_2 is generated and subsequently reduced to H_2O, CVs a pH 3 and 6 were obtained in the presence of 1 mM and 4 mM H_2O_2. Prior reports indicate that catalase-type reactivity is expected at pH 7 and

higher, with the fastest rates at the highest pH values; this background reactivity precludes accurate CV measurements for the 2 + 2 pathway at pH values >7.[34-35] Minimal electrocatalytic activity is observed for H_2O_2 reduction at pH 3, a region where significant catalase-type reactivity is not expected **(Figure SI 4.72)**.[35] Only slight activity for H_2O_2 reduction occurs at 1 mM concentrations at pH 6, suggesting that the contribution of the 2 + 2 pathway is minimal (**Figure SI 4.73**). A stability test of $[Mn(TMPyP)Cl]^{4+}$ in the presence of H_2O_2 was also conducted at pH 3 and 6, which showed that the rate of reaction, as monitored by the Soret band, was much slower than the timescale of our electrochemical experiments, with no observed decrease in absorbance over 30 minutes (**Figure SI 4.74 and SI 4.75**).

At the pH values between 3 and 6, where electrocatalytic activity could be measured, the resting species should be primarily $[Mn(III)(TMPyP)(OH_2)_2]^{5+}$, according to our potential-pH and UV-vis absorbance data (**Figures 4.2 and 4.3**). Upon a single-electron reduction, the resultant $[Mn(II)(TMPyP)(OH_2)]^{4+}$ species can bind O_2 to generate a superoxide species, $[Mn(III)(O_2^{\bullet-})(TMPyP)]^{4+}$. We presume the subsequent reduction of the superoxide to a Mn bound hydroperoxo species is facile at the same potential under these conditions. Although a sufficient pH to protonate the hydroperoxide anion is present (<11.6[7]), the faradaic efficiencies obtained from RRDE experiments suggest that at the operating potential, reduction and cleavage of the O–O bond to complete the overall $4e^-$ pathway and ultimately generate two equivalents of H_2O is the dominant pathway. The less than-quantitative efficiencies suggest that the O–O bond cleavage step could be rate-limiting. As noted above, contributions from catalase-type reactivity are expected to be minimal at these pH values.[34-35]

4.4 Conclusion

In summary, we have electrochemically characterized $[Mn(III)(TMPyP)Cl]^{4+}$ and assessed its electrocatalytic behavior with respect to O_2 reduction through the entire pH domain. Mechanistic studies have established that the use of the universal buffer system does not appear to have any consequences on the observed electrochemical behavior, suggesting a comparison between this and previous studies is reasonable. Speciation studies conducted by UV-vis absorbance and SEC methods suggest that at pH values greater than 10, dimer formation is possible upon oxidation. These methods also demonstrated that decomposition occurred at pH 1 after the application of reducing potentials, which had not been previously reported with a different buffer system at this pH.[4] Where catalytic efficiency could be assessed from pH 3 to 6, efficiencies for H_2O ranged from 82 to 93% (the pH range for quantitative electrocatalytic efficiency assessment was limited by the heterogeneous electrode response). Further studies assessing whether the O–O bond cleavage step is rate-determining and the kinetic parameters of the overall mechanism are the subject of future study. The notable difference in efficiency with prior publications is attributed to the method of reaction efficiency analysis: here direct RRDE methods were used, whereas in previous studies reaction efficiency was assessed via indirect RDE methods.[3-4]

4.5 Experimental Methods

4.5.1 Materials and Methods

General. All chemicals and solvents (ACS or HPLC grade) were commercially available and used as received unless otherwise indicated. Mn(III) meso-tetra(N-methylpyridinium-4-yl)porphyrin pentachloride was obtained from Frontier Scientific. Gas cylinders were

obtained from Praxair (Ar as 5.0; O_2 as 4.0). Gas mixing for variable concentration experiments was accomplished using a gas proportioning rotameter from Omega Engineering (O_2 saturation in aqueous solutions is 1.3 mM [2, 30]). UV-vis absorbance spectra were recorded on a Cary 60 from Agilent. A Mettler Toledo (LE438) pH probe using a glass electrode calibrated with standard buffers (pH 4.00, 7.01 and 10.01) was used to determine the aqueous pH of solutions in all experiments in this study.

4.5.2 Aqueous Buffer Solutions[9-10]

The buffer solution utilized to conduct the majority of the electrochemical studies from pH 2–13 was the "universal" Britton–Robinson buffer.[10] The Britton–Robinson buffer was prepared on a 1 L scale and was checked with a pH probe prior to use to ensure a pH of 2 was maintained. The buffer solution contained 2.47 g of H_3BO_3 (0.04 M), 1.55 mL H_3PO_4 (0.04 M), and 2.29 mL CH_3COOH (0.04 M) and 1 L of DI water. Experimental solutions at other pH values were prepared by titrating 0.2 M NaOH into Britton–Robinson stock buffer solution (described above) to reach the desired pH. Experiments at pH 1 used a buffer of 1.0 M HCl with 0.1 M NaCl and at pH 14 a buffer of 1.0 M KOH and 0.1 M NaCl was used.

4.5.3 Electrochemistry

All electroanalytical experiments were performed using a Metrohm Autolab PGSTAT302N potentiostat. All CV experiments used a glassy carbon working electrode (∅ = 3 mm, CH Instruments), glassy carbon rod counter electrode (Type 2, ∅ = 3 mm, Alfa Aesar), and 3.0 M NaCl aqueous silver/silver chloride reference electrode (BASi MF-2052). Experiments were performed in a modified scintillation vial (20 mL volume) as a single-chamber cell with a cap modified with ports for all electrodes and a sparging needle.

All data referenced to 3.0 M NaCl aqueous Ag/AgCl which were then converted to NHE (+209 mV).[36] Manual iR compensation was performed to minimize ohmic drop using systematic testing to determine the optimal resistance correction for each experiment. Rotating ring-disk electrode (RRDE) experiments were conducted using a Metrohm rotator with a Metrohm electrode consisting of a glassy carbon disk (∅ = 5 mm) and a Pt ring. The collection efficiency of the RRDE electrode was experimentally determined to be 26.6%.[37] The counter electrode in the RRDE experiments was a glassy carbon rod in a gas diffusion tube (Type 2, ∅ = 3 mm; Alfa Aesar) and the aqueous reference was a Ag/AgCl/3 M KCl electrode (+210 mV vs. NHE[38]) inserted in a 50 mM KCl/pure buffer salt bridge system (Metrohm).

4.5.4 RRDE Experiments [37, 39]

RRDE experiments were performed under both Ar and O_2 saturation conditions, using 50 mL of the appropriate Britton– Robinson buffer solution (adjusted to the appropriate pH using a 0.2 M NaOH solution), glassy carbon disk electrode (∅ = 5 mm), Pt ring electrode, glassy carbon counter electrode, Ag/AgCl 3 M KCl reference electrode; scan rate 0.02 V s^{-1} . The working solution was sparged with argon until saturation was achieved and confirmed by CV. The analyte $[Mn(TMPyP)\ Cl]^{4+}$ (0.25 mM) was then dissolved in solution. A standard CV was taken of the solution to confirm the potential window to be used for the experiment (+0.15 to −0.75 V vs. Ag/AgCl). At the beginning of the experiment, the platinum ring was set to +1.2 V vs. Ag/AgCl and the glassy carbon disk was set to 0 V vs. Ag/AgCl. LSVs were obtained for rotation rates between 400 and 1000 rpm under the described conditions. Between each LSV, the electrode was sonicated in ethanol. The cleaning procedure for the electrode was standardized by taking repeated

LSVs at the same rotation rates to confirm repeated scans at the same rotation rate were exact overlays of one another. This same procedure was repeated for O_2 saturation conditions, which were achieved by sparging the solution with O_2 for approximately 15 minutes. Between experiments with different pH values, the RRDE electrode was polished on alumina and electrochemically pretreated in a 0.5 M sulfuric acid solution where the ring was held at +1.6 V vs. Ag/AgCl for three minutes and then −0.3 V vs. Ag/AgCl for three minutes. This was then repeated, and the ring was then held at +0.2 V vs. Ag/AgCl for 2 minutes prior to use. For all RRDE data analysis, the background current generated at the experimental pH under argon and O_2 were obtained and subtracted from the data obtained with the analyte solution at the corresponding rotation rate under otherwise identical conditions. The RRDE data plotted in the SI reflect this background current-corrected data. The difference between the corrected values for the amount of current produced at the disk under O_2 saturation conditions and the amount of current produced at the disk under argon saturation conditions was taken as the corrected disk current for O_2 saturation conditions ($i_{disk\ corrected}$) for each rotation rate.

To calculate the percent of H_2O_2 generated catalytically, the $i_{\text{disk corrected}}$ was multiplied by the corresponding $N_{empirical}$ value for the specific rotation rate to determine the maximum amount of ring current for H_2O_2 production ($i_{ring\ max}$). The ratio of $i_{ring\ corrected}$ to $i_{ring\ max}$ was multiplied by a factor of 100 to determine the H_2O_2% generated at the ring across all measured rotation rates.

$$\%H_2O_2 = (100)\frac{i_{ring\ corrected}}{i_{disk\ corrected}(\text{collection efficency})} \qquad (8)$$

Levich and Koutecky–Levich theory was applied to these experiments to calculate the diffusion coefficients for each of the conditions under which the experiment was run (argon

and O_2 saturation). The slope of the Levich plot was obtained by plotting the square root of the angular rotation rate versus the limiting current for both argon and O_2. The slope of these Levich plots were then used to calculate the diffusion coefficients under each of the experimental conditions, argon and O_2 saturation, using the following eqn:

$$D = \sqrt{\left(\frac{slope}{0.620nFA\nu^{-1/6}C_0^*}\right)^3} \qquad (9)$$

where D is the diffusion coefficient, slope is the slope from the Levich plot, n is the number of electrons, F is Faraday's constant, A is the area of the electrode, ν is the kinematic viscosity of the solvent (0.010038 $cm^2 \cdot s^{-1}$ for H_2O[40]) and C_0* is the concentration of the catalyst under Ar saturation (0.25 mM) or the O_2 substrate at saturation under catalytic conditions (1.3 mM [2, 30]).

4.5.5 Description of Number of Electrons Transferred (n_{cat}) and Overpotential (η) Calculations

The production of H_2O_2 is a 2-electron process and the production of O_2 is a 4-electron process. To determine the total number of electrons transferred, the faradaic efficiency for H_2O_2 determined from RRDE is multiplied by two then added to the product of the remaining current efficiency multiplied by four (which represents the water selectivity). The sum of those two numbers represent the total number of electrons transferred in the RRDE experiment. An adjustment for the standard reduction potential, 1.229 V vs. NHE[41] of dioxygen reduction to water, was made for each pH where the number of electrons was determined following:

$$E_{ORR}^0 = E_{O_2/H_2O} - (0.0592pH) \qquad (10)$$

This allowed for the overpotential to be determined from the eqn below using the $E_{1/2}$ of the Mn(III)/(II) reduction for $[Mn(TMPyP)Cl]^{4+}$ at each pH.

$$\eta = \left|E_{1/2(cat)} - E^0_{ORR}\right| \quad (11)$$

4.5.6 TOF_{max} Calculation from CV data[32-33]

Utilizing the number of electrons calculated for the conversion of O_2 to H_2O by $[Mn(TMPyP)Cl]^{4+}$ from RRDE, the maximum turnover frequency (TOF_{max}) was calculated. Under the assumption that this system follows pseudo-first order kinetics for the catalytic process, the observed catalytic current plateau under O_2 results in the following description, if H_2O is assumed to be the proton donor

$$i_{cat} = n_{cat}FAC^0_{cat}\sqrt{Dk_{cat}[O_2]^y[H_2O]^y} \quad (12)$$

$$TOF_{max} = k_{cat}[O_2]^y[H_2O]^y \quad (13)$$

where n_{cat} is the number of electrons determined by RRDE, F is Faraday's constant, A is the surface area of the working electrode, C^0_{cat} is the catalyst concentration in the bulk solution, D is the diffusion coefficient for the electrocatalyst, k_{cat} is the rate constant for the overall process, $[O_2]$ is the substrate concentration and y is the reaction order of each substrate. Normalization of this catalytic current observed under O_2 by the non-catalytic process leads to a relationship between the TOF_{max} and the ratio i_{cat}/i_p described as

$$i_p = 0.4463 n_p^{3/2} FAC^0_{cat}\sqrt{\frac{F}{RT}Dv} \quad (14)$$

$$\frac{i_{cat}}{i_p} = \frac{n_{cat}}{n_p^{3/2}}\frac{1}{0.4463}\sqrt{\frac{RT}{Fv}TOF_{max}} \quad (15)$$

$$TOF_{max} = 0.1992\frac{n_p^3}{n_{cat}^2}\frac{Fv}{RT}\left(\frac{i_{cat}}{i_p}\right)^2 \quad (16)$$

where n_p is the number of electrons transferred in the non-catalytic process (n_p=1), R is the universal gas constant, T is the temperature, and v is the scan rate. Each TOF_{max} value was determined at 0.1 $V \cdot s^{-1}$ and as reported in **Table 4.1**; the calculation of these values under the non-ideal conditions presented here places an upper limit on the likely TOF_{max} for this catalyst.

4.5.7 UV-vis Spectroelectrochemistry

UV-vis SEC experiments were performed utilizing a platinum Honeycomb Spectroelectrochemical Cell Kit from Pine Research Instrumentation coupled with an Agilent Cary 60 UV-vis, Metrohm PGSTAT302N, and a 4.0 M KCl gel Ag/AgCl low profile reference electrode from Pine Research Instrumentation. Data was referenced to NHE by adding 0.199 V to the potential at which it was collected.[42] The desired experimental pH was obtained by utilizing the Britton-Robinson buffer described above with pH adjustments by 0.2 M NaOH (pH = 7 and 10), or utilizing the solutions described below for pH 1 and 14. A background spectrum of the pH adjusted solutions was obtained prior to adding analyte, and this spectrum was utilized to reduce background noise through subtraction. A stock solution of $[Mn(TMPyP)Cl]^{4+}$ was generated by dissolving 9.4 mg of $[Mn(TMPyP)Cl]^{4+}$ in DI water. An aliquot of this stock solution (1 mL) was then diluted with 9 mL of pH adjusted buffer to generate ~0.1 mM solution of $[Mn(TMPyP)Cl]^{4+}$. The solution was then loaded in the UV-vis SEC cell, with special care taken to prevent air bubbles within the honeycomb electrode. The cell and solution were degassed with Ar sparging for 10 minutes prior to measurement. The resting potential was set in a potential region where only a single species should be present (according to the reduction waves of interest seen in CV experiments) and was held for 30 s prior to collection of a spectrum.

The potential was then stepped in 50 mV increments with a subsequent 30 s electrolysis prior to collection of a UV-vis spectrum. The potential was not changed until two consecutive spectra were obtained as overlays under these conditions. The honeycomb electrode was cleaned after electrolysis by first rinsing with DI water, and then taking 20 CVs with a start potential of –0.3 V vs Ag/AgCl, upper vertex, in 0.5 M H_2SO_4 as described in the Honeycomb Spectroelectrochemical Cell Kit Manual.

4.5.8 Rinse Test Procedure

A stock solution of the Britton–Robinson buffer was made for pH values of 3, 6, 7 and 12. At each pH, a CV was taken of the blank buffer solution under Ar saturation. After this initial CV, 1 mM of $[Mn(TMPyP)(Cl)]^{4+}$ was added to the solution and sonicated to ensure dissolution. The electrode was then poised at the potential of the Mn(III/II) reduction under an Ar atmosphere. The working electrode was then removed and gently dried with a Kimwipe® before being placed into a blank electrolyte solution saturated with Ar. A CV was taken through the same potential window as the solution containing the 1 mM of catalyst to confirm that no adsorption had taken place (**Figure SI 4.50–4.54**).

4.6 Supporting Information

Table SI 4.1. Solutions utilized in this study.

pH Range	Solution
1	1 M HCl and 0.1 M NaCl
2-13	0.04 M Britton-Robinson Buffer[9]
14	1 M KOH and 0.1 M NaCl

Table SI 4.2. Electrochemical characterization of the Mn(III)/(II) reduction in a pH 1 solution (1 M HCl /0.1 M NaCl) under Ar saturation conditions as the scan rate is increased.

Scan Rate (V s^{-1})	$E_{1/2}$ vs. NHE (V)	ΔE vs. NHE (mV)	i_{pc}/i_{pa}
0.1	0.09	299	1.60
0.2	0.08	326	1.50
0.3	0.07	342	1.60
0.5	0.06	371	1.80
1.0	0.04	453	1.80

Table SI 4.3. Electrochemical characterization of the Mn(III)/(II) reduction in pH 3 Britton-Robinson Buffer solution under Ar saturation conditions as the scan rate is increased.

Scan Rate (V s^{-1})	$E_{1/2}$ vs. NHE (V)	ΔE vs. NHE (mV)	i_{pc}/i_{pa}
0.1	0.00	226	1.10
0.2	0.01	292	1.20
0.3	0.00	318	1.20
0.5	0.00	368	1.20
1.0	0.00	412	1.20

Table SI 4.4. Electrochemical characterization of the Mn(III)/(II) reduction in pH 4 Britton-Robinson Buffer solution under Ar saturation conditions as the scan rate is increased.

Scan Rate (V s^{-1})	$E_{1/2}$ vs. NHE (V)	ΔE vs. NHE (mV)	i_{pc}/i_{pa}
0.1	0.00	238	0.99
0.2	0.00	280	1.03
0.3	-0.01	324	1.10
0.5	-0.02	352	1.12
1.0	-0.03	415	1.26

Table SI 4.5. Electrochemical characterization of the Mn(III)/(II) reduction in pH 5 Britton-Robinson Buffer solution under Ar saturation conditions as the scan rate is increased.

Scan Rate (V s^{-1})	$E_{1/2}$ vs. NHE (V)	ΔE vs. NHE (mV)	i_{pc}/i_{pa}
0.1	0.02	167	0.92
0.2	0.02	193	0.95
0.3	0.02	215	0.95
0.5	0.01	246	1.00
1.0	0.01	290	1.05

Table SI 4.6. Electrochemical characterization of the Mn(III)/(II) reduction in pH 6 Britton-Robinson Buffer solution under Ar saturation conditions as the scan rate is increased.

Scan Rate (V s^{-1})	$E_{1/2}$ vs. NHE (V)	ΔE vs. NHE (mV)	i_{pc}/i_{pa}
0.1	0.02	132	1.10
0.2	0.02	156	1.05
0.3	0.02	165	1.05
0.5	0.02	189	1.05
1.0	0.01	237	1.05

Table SI 4.7. Electrochemical characterization of the Mn(III)/(II) reduction in pH 7 Britton-Robinson Buffer solution under Ar saturation conditions as the scan rate is increased.

Scan Rate (V s^{-1})	$E_{1/2}$ vs. NHE (V)	ΔE vs. NHE (mV)	i_{pc}/i_{pa}
0.1	0.02	114	0.92
0.2	0.02	120	0.92
0.3	0.02	134	0.88
0.5	0.02	146	0.89
1.0	0.01	170	0.92

Table SI 4.8. Electrochemical characterization of the Mn(III)/(II) reduction in pH 8 Britton-Robinson Buffer solution under Ar saturation conditions as the scan rate is increased.

Scan Rate (V s^{-1})	$E_{1/2}$ vs. NHE (V)	ΔE vs. NHE (mV)	i_{pc}/i_{pa}
0.1	0.02	86	1.01
0.2	0.02	94	1.01
0.3	0.02	95	0.98
0.5	0.02	103	1.00
1.0	0.02	119	1.03

Table SI 4.9. Electrochemical characterization of the Mn(III)/(II) reduction in pH 9 Britton-Robinson Buffer solution under Ar saturation conditions as the scan rate is increased.

Scan Rate (V s^{-1})	$E_{1/2}$ vs. NHE (V)	ΔE vs. NHE (mV)	i_{pc}/i_{pa}
0.1	0.02	110	0.99
0.2	0.02	126	0.98
0.3	0.02	139	0.99
0.5	0.02	155	1.00
1.0	0.01	186	1.03

Table SI 4.10. Electrochemical characterization of the Mn(III)/(II) reduction in pH 10 Britton-Robinson Buffer solution under Ar saturation conditions as the scan rate is increased.

Scan Rate (V s^{-1})	$E_{1/2}$ vs. NHE (V)	ΔE vs. NHE (mV)	i_{pc}/i_{pa}
0.1	0.02	84	0.95
0.2	0.02	94	0.97
0.3	0.02	97	0.96
0.5	0.02	105	0.96
1.0	0.02	112	0.99

Table SI 4.11. Electrochemical characterization of the Mn(III)/(II) reduction in pH 11 Britton-Robinson Buffer solution under Ar saturation conditions as the scan rate is increased.

Scan Rate (V s^{-1})	$E_{1/2}$ vs. NHE (V)	ΔE vs. NHE (mV)	i_{pc}/i_{pa}
0.1	0.01	75	1.10
0.2	0.01	82	0.99
0.3	0.01	88	1.00
0.5	0.01	97	0.97
1.0	0.01	107	0.94

Table SI 4.12. Electrochemical characterization of the Mn(III)/(II) reduction in pH 12 Britton-Robinson Buffer solution under Ar saturation conditions as the scan rate is increased.

Scan Rate (V s^{-1})	$E_{1/2}$ vs. NHE (V)	ΔE vs. NHE (mV)	i_{pc}/i_{pa}
0.1	-0.02	77	1.30
0.2	-0.03	86	1.31
0.3	-0.03	91	1.22
0.5	-0.03	100	1.17
1.0	-0.02	107	1.09

Table SI 4.13. Electrochemical characterization of the Mn(III)/(II) reduction in pH 13 Britton-Robinson Buffer solution under Ar saturation conditions as the scan rate is increased.

Scan Rate (V s^{-1})	$E_{1/2}$ vs. NHE (V)	ΔE vs. NHE (mV)	i_{pc}/i_{pa}
0.1	-0.05	125	1.08
0.2	-0.07	126	1.06
0.3	-0.08	128	1.02
0.5	-0.08	129	1.06
1.0	-0.08	130	1.04

Table SI 4.14. Electrochemical characterization of the Mn(III)/(II) reduction in pH 14 Britton-Robinson Buffer solution under Ar saturation conditions as the scan rate is increased.

Scan Rate (V s^{-1})	$E_{1/2}$ vs. NHE (V)	ΔE vs. NHE (mV)	i_{pc}/i_{pa}
0.1	-0.11	223	1.14
0.2	-0.12	235	1.15
0.3	-0.12	244	1.19
0.5	-0.12	254	1.25
1.0	-0.12	249	1.40

Table SI 4.15. Electrochemical characterization of Mn(IV)/(III) feature from pH 10-14, CVs taken at a scan rate of 100 mV/s under Ar saturation conditions.

pH	$E_{1/2}$ vs. NHE (V)	ΔE vs. NHE (mV)	i_{pc}/i_{pa}
10	0.65	250	0.81
11	0.53	110	1.08
12	0.39	70	1.05
13	0.32	70	1.00
14	0.24	120	1.15

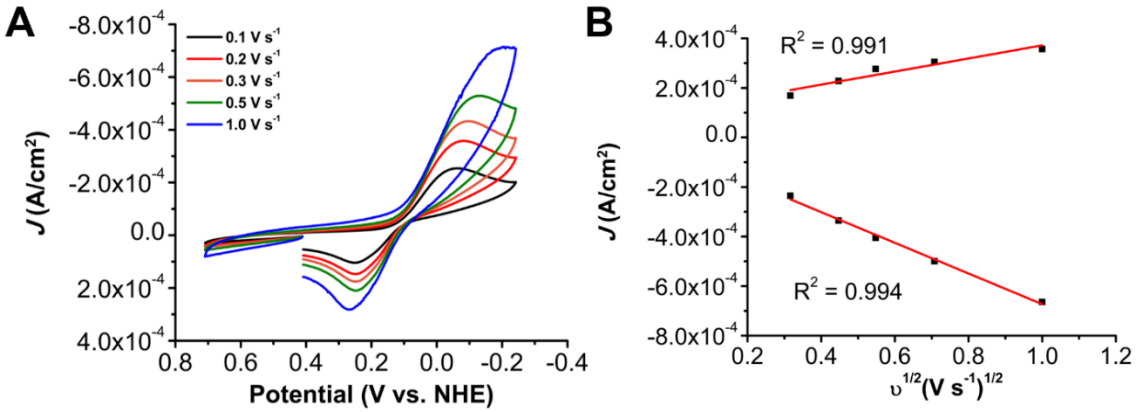

Figure SI 4.1. (A) Variable scan rate CVs **(B)** Linear fit demonstrating a homogenous response of the $[Mn(TMPyP)Cl]^{4+}$. Conditions: 1 mM $[Mn(TMPyP)Cl]^{4+}$ in a pH 1 (1 M HCl /0.1 M NaCl) solution under Ar saturation conditions, glassy carbon working electrode, glassy carbon counter electrode, 3.0 M NaCl Ag/AgCl reference electrode; varied scan rate.

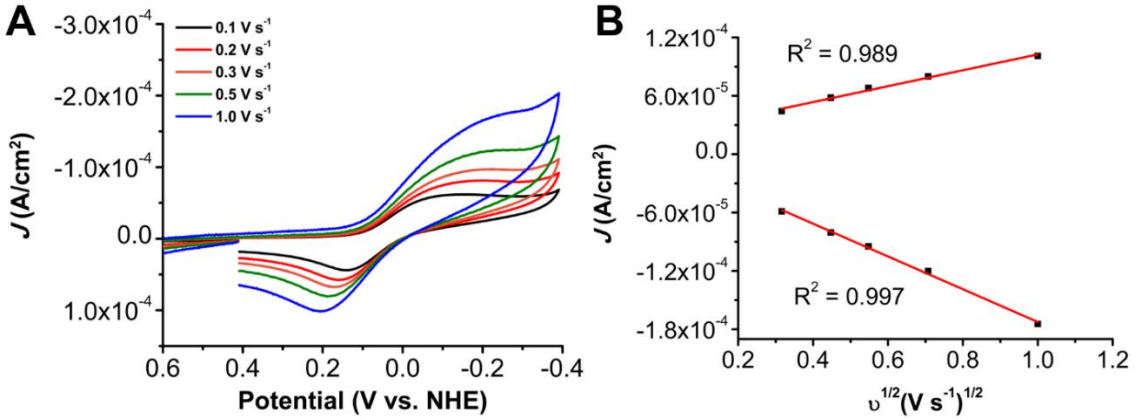

Figure SI 4.2. (A) Variable scan rate CVs **(B)** Linear fit demonstrating a homogenous response of the $[Mn(TMPyP)Cl]^{4+}$. Conditions: 1 mM $[Mn(TMPyP)Cl]^{4+}$ in a pH 3 Britton-Robinson Buffer solution under Ar saturation conditions, glassy carbon working electrode, glassy carbon counter electrode, 3.0 M NaCl Ag/AgCl reference electrode; varied scan rate.

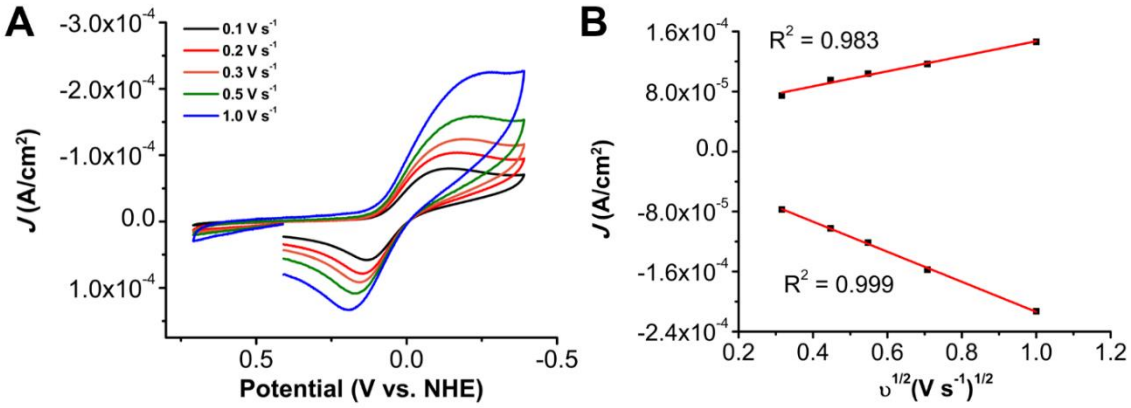

Figure SI 4.3. (A) Variable scan rate CVs **(B)** Linear fit demonstrating a homogenous response of the $[Mn(TMPyP)Cl]^{4+}$. Conditions: 1 mM $[Mn(TMPyP)Cl]^{4+}$ in a pH 4 Britton-Robinson Buffer solution under Ar saturation conditions, glassy carbon working electrode, glassy carbon counter electrode, 3.0 M NaCl Ag/AgCl; varied scan rate.

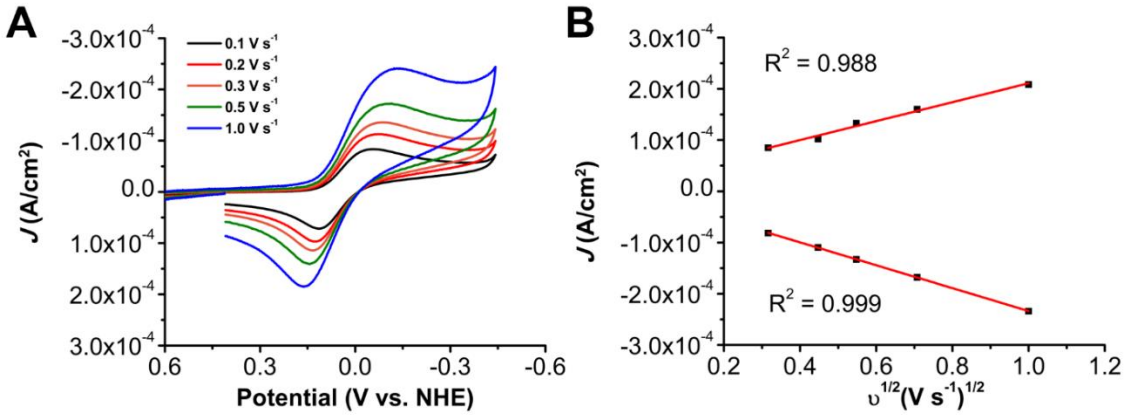

Figure SI 4.4. (A) Variable scan rate CVs **(B)** Linear fit demonstrating a homogenous response of the $[Mn(TMPyP)Cl]^{4+}$. Conditions: 1 mM $[Mn(TMPyP)Cl]^{4+}$in a pH 5 Britton-Robinson Buffer solution under Ar saturation conditions, glassy carbon working electrode, glassy carbon counter electrode, 3.0 M NaCl Ag/AgCl reference electrode; varied scan rate.

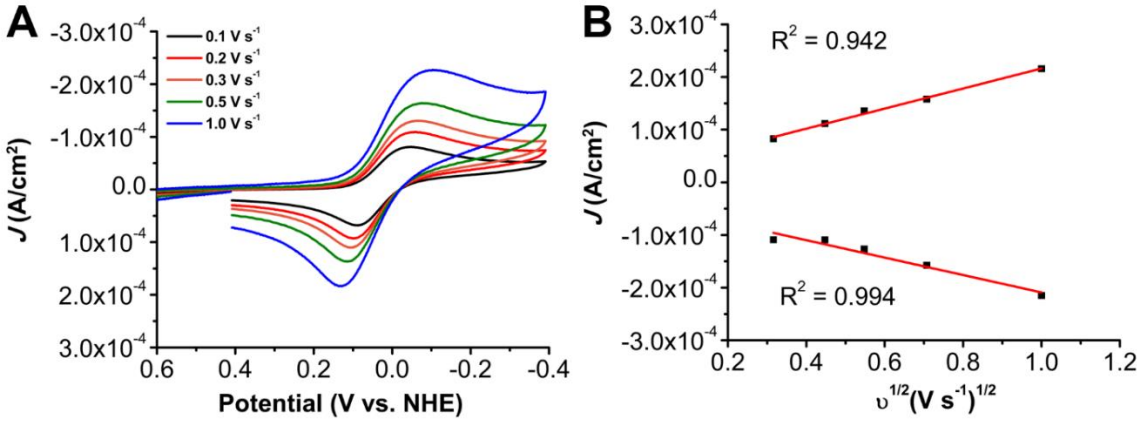

Figure SI 4.5. (A) Variable scan rate CVs **(B)** Linear fit demonstrating a homogenous response of the $[Mn(TMPyP)Cl]^{4+}$. Conditions: 1 mM $[Mn(TMPyP)Cl]^{4+}$ in a pH 6 Britton-Robinson Buffer solution under Ar saturation conditions, glassy carbon working electrode, glassy carbon counter electrode, 3.0 M NaCl Ag/AgCl reference electrode; varied scan rate.

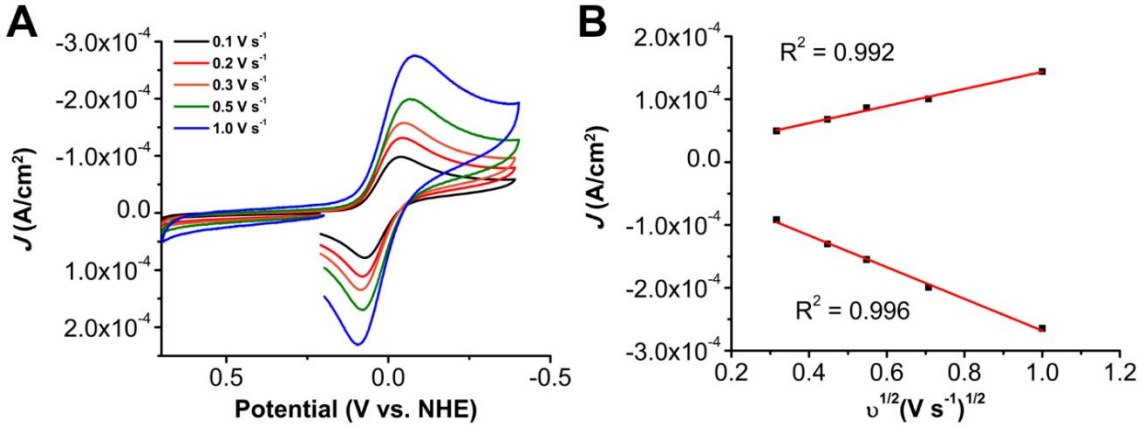

Figure SI 4.6. (A) Variable scan rate CVs **(B)** Linear fit demonstrating a homogenous response of the $[Mn(TMPyP)Cl]^{+}$. Conditions: 1 mM $[Mn(TMPyP)Cl]^{4+}$ in a pH 7 Britton-Robinson Buffer solution under Ar saturation conditions, glassy carbon working electrode, glassy carbon counter electrode, 3.0 M NaCl Ag/Ag4Cl reference electrode; varied scan rate.

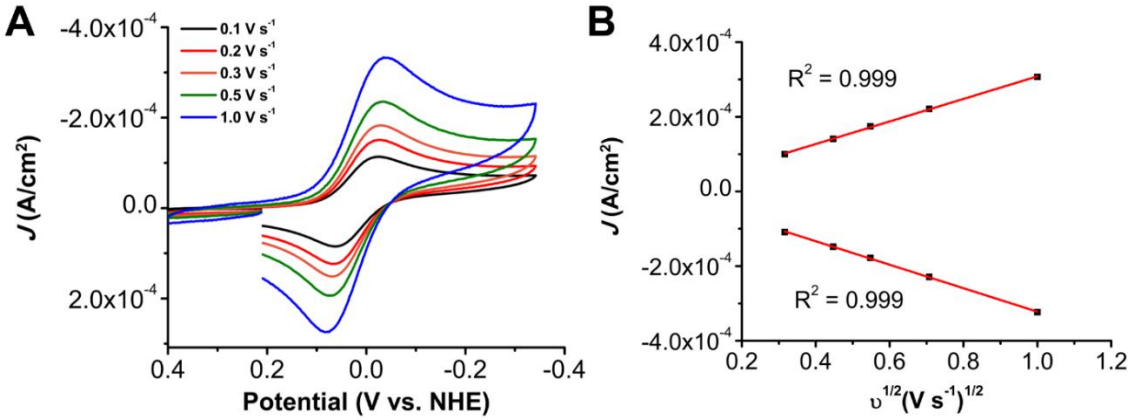

Figure SI 4.7. (A) Variable scan rate CVs **(B)** Linear fit demonstrating a homogenous response of the $[Mn(TMPyP)Cl]^{4+}$. Conditions: 1 mM $[Mn(TMPyP)Cl]^{4+}$ in a pH 8 Britton-Robinson Buffer solution under Ar saturation conditions, glassy carbon working electrode, glassy carbon counter electrode, 3.0 M NaCl Ag/AgCl reference electrode; varied scan rate.

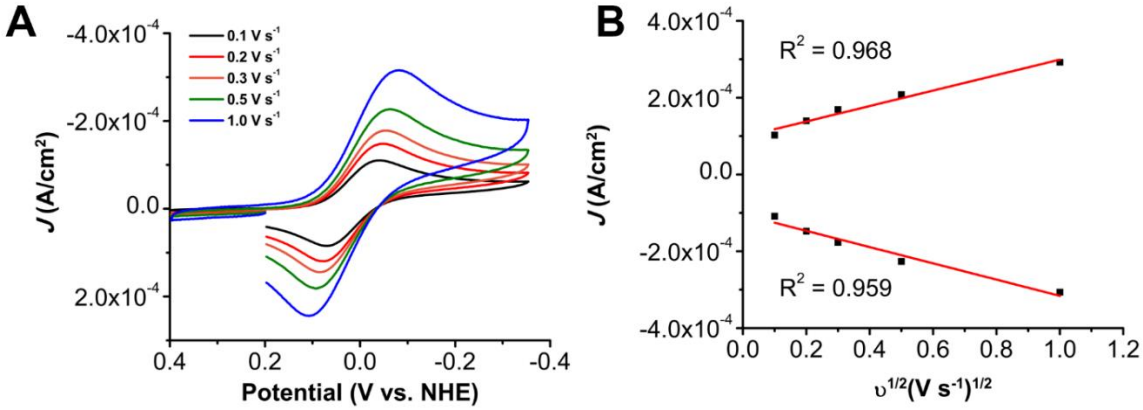

Figure SI 4.8. (A) Variable scan rate CVs **(B)** Linear fit demonstrating a homogenous response of the $[Mn(TMPyP)Cl]^{4+}$. Conditions: 1 mM $[Mn(TMPyP)Cl]^{4+}$ in a pH 9 Britton-Robinson Buffer solution under Ar saturation conditions, glassy carbon working electrode, glassy carbon counter electrode, 3.0 M NaCl Ag/AgCl reference electrode; varied scan rate.

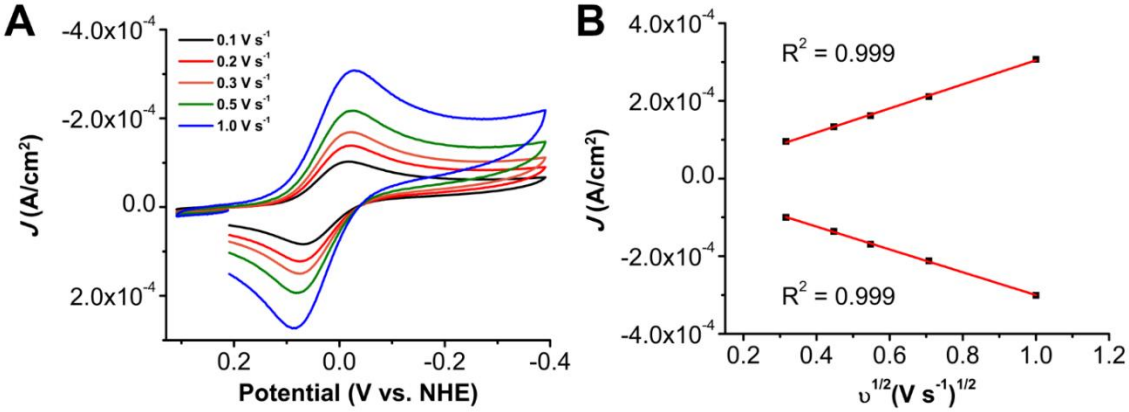

Figure SI 4.9. (A) Variable scan rate CVs **(B)** Linear fit demonstrating a homogenous response of the $[Mn(TMPyP)Cl]^{4+}$. Conditions: 1 mM $[Mn(TMPyP)Cl]^{4+}$ in a pH 10 Britton-Robinson Buffer solution under Ar saturation conditions, glassy carbon working electrode, glassy carbon counter electrode, 3.0 M NaCl Ag/AgCl reference electrode; varied scan rate.

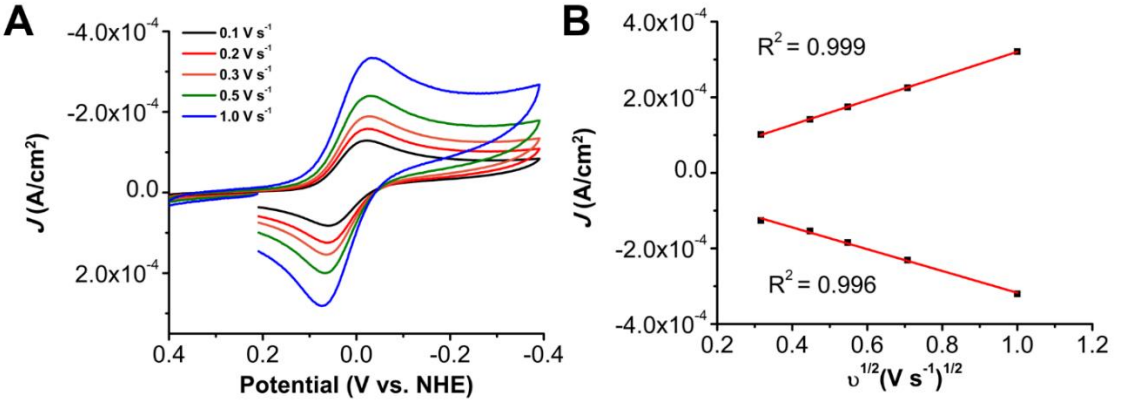

Figure SI 4.10. (A) Variable scan rate CVs **(B)** Linear fit demonstrating a homogenous response of the $[Mn(TMPyP)Cl]^{4+}$. Conditions: 1 mM $[Mn(TMPyP)Cl]^{4+}$ in a pH 11 Britton-Robinson Buffer solution under Ar saturation conditions, glassy carbon working electrode, glassy carbon counter electrode, 3.0 M NaCl Ag/AgCl reference electrode; varied scan rate.

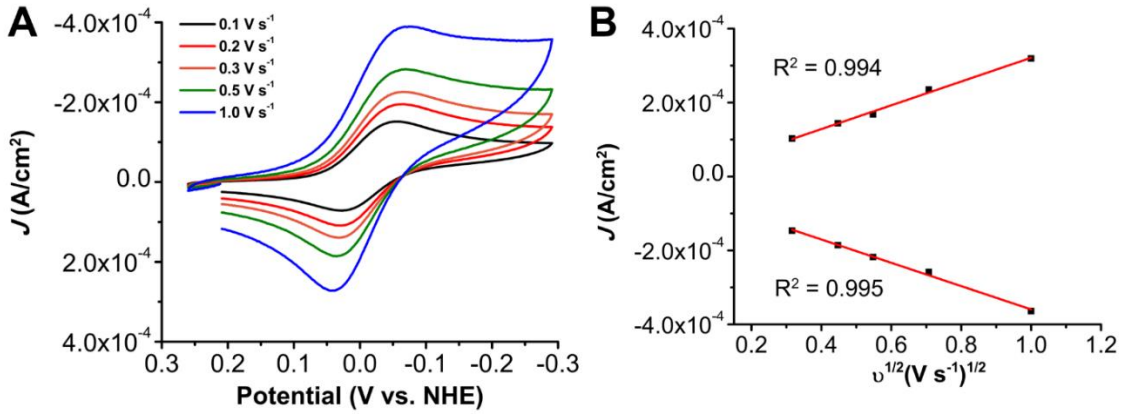

Figure SI 4.11. (A) Variable scan rate CVs **(B)** Linear fit demonstrating a homogenous response of the $[Mn(TMPyP)Cl]^{4+}$. Conditions: 1 mM $[Mn(TMPyP)Cl]^{4+}$ in a pH 12 Britton-Robinson Buffer solution under Ar saturation conditions, glassy carbon working electrode, glassy carbon counter electrode, 3.0 M NaCl Ag/AgCl reference electrode; varied scan rate.

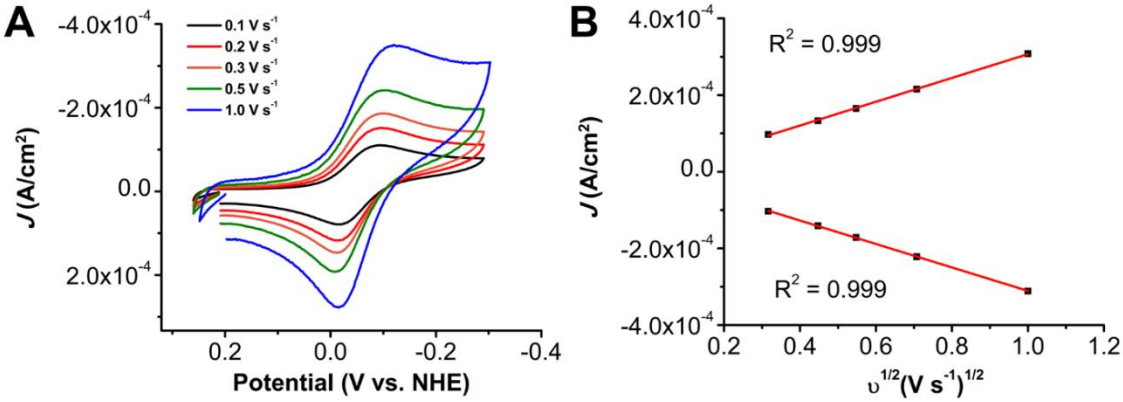

Figure SI 4.12. (A) Variable scan rate CVs **(B)** Linear fit demonstrating a homogenous response of the $[Mn(TMPyP)Cl]^{4+}$. Conditions: 1 mM $[Mn(TMPyP)Cl]^{4+}$ in a pH 13 Britton-Robinson Buffer solution under Ar saturation conditions, glassy carbon working electrode, glassy carbon counter electrode, 3.0 M NaCl Ag/AgCl reference electrode; varied scan rate.

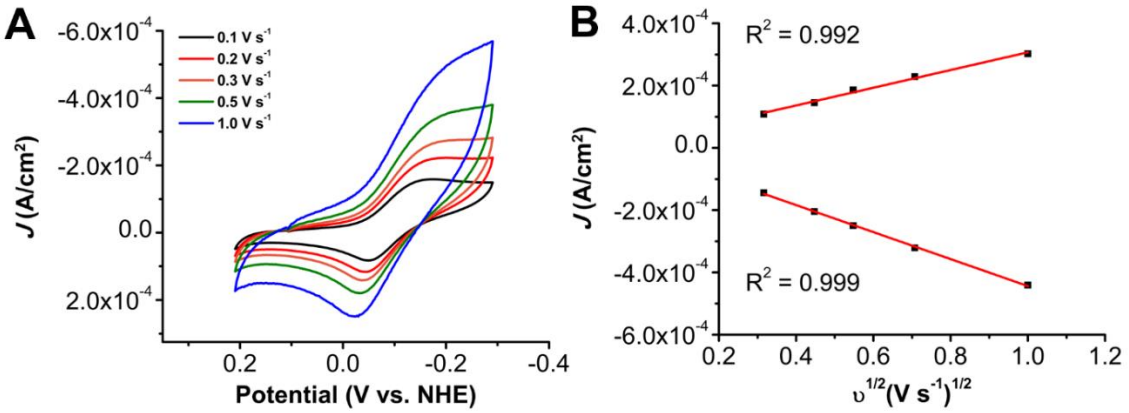

Figure SI 4.13. **(A)** Variable scan rate CVs **(B)** Linear fit demonstrating a homogenous response of the $[Mn(TMPyP)Cl]^{4+}$. Conditions: 1 mM $[Mn(TMPyP)Cl]^{+}$ in a pH 14 Britton-Robinson Buffer solution under Ar saturation conditions, glassy carbon working electrode, glassy carbon counter electrode, 3.0 M NaCl Ag/AgCl reference electrode; varied scan rate.

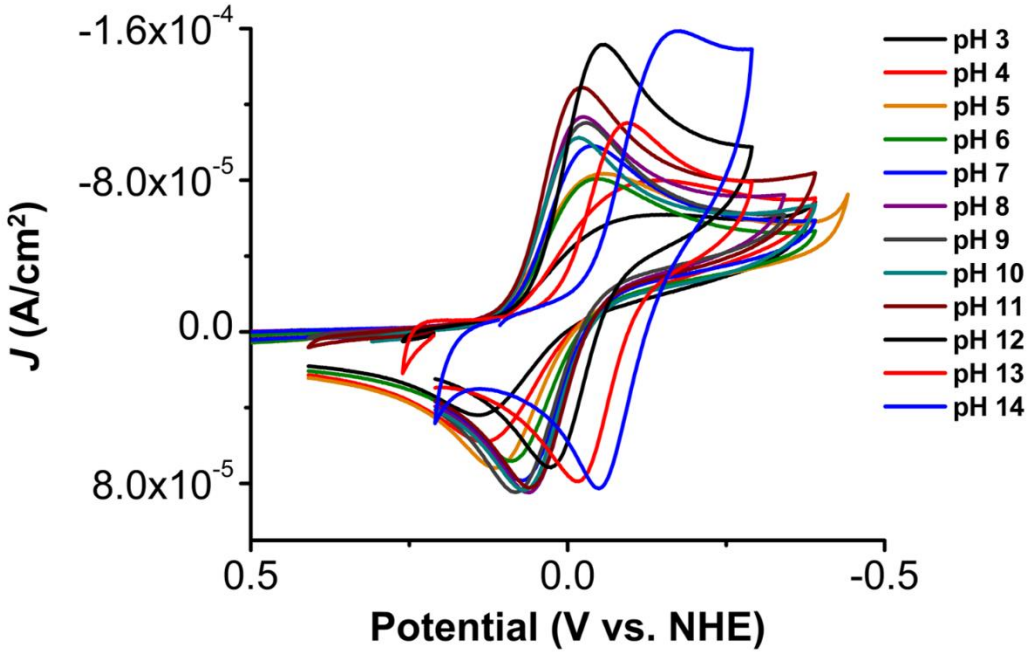

Figure SI 4.14. CVs of 1 mM $[Mn(TMPyP)Cl]^{4+}$ demonstrating the shift in $E_{1/2}$ throughout the entire pH domain studied. Ar saturation conditions, glassy carbon working electrode, glassy carbon counter electrode, 3.0 M NaCl Ag/AgCl reference electrode; Scan rate 100 mV/s.

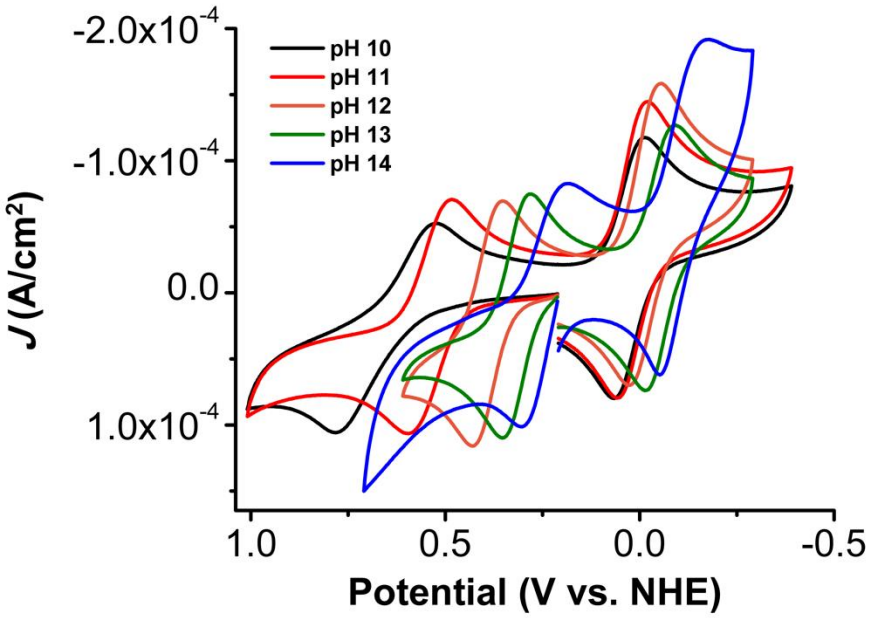

Figure SI 4.15. CV of 1 mM $[Mn(TMPyP)Cl]^{4+}$ establishing the appearance of a second feature and the pH dependence of the $E_{1/2}$'s under basic conditions in a Britton-Robinson buffer. Ar saturation conditions, glassy carbon working electrode, glassy carbon counter electrode, 3.0 M NaCl Ag/AgCl reference electrode; Scan rate 100 mV/s.

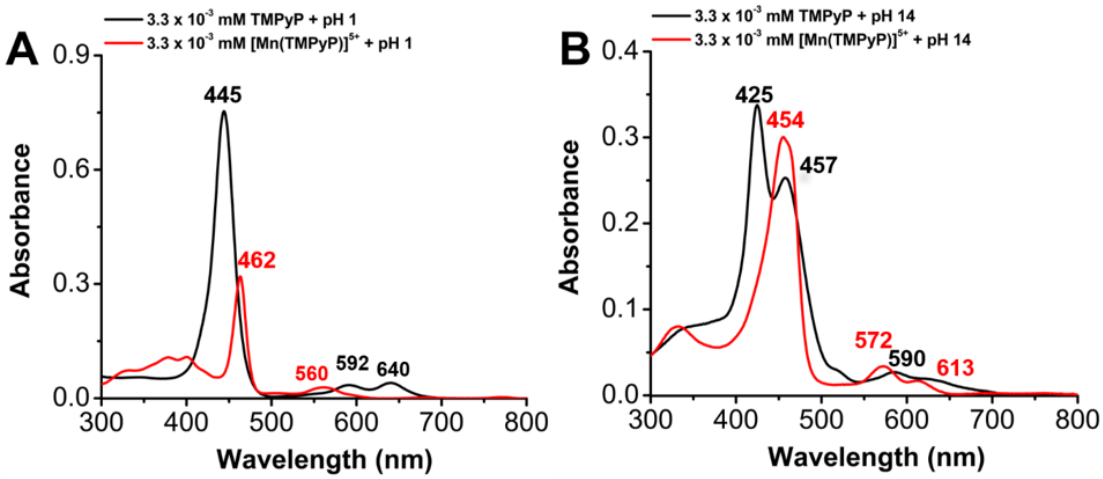

Figure SI 4.16. (A) UV-Vis spectrum of $[Mn(TMPyP)Cl]^{4+}$ and free base TMPyP showing that de-metalation does not occur in solution by monitoring the Soret band **(B)** and Q band shifts under pH 1 or 14 conditions.

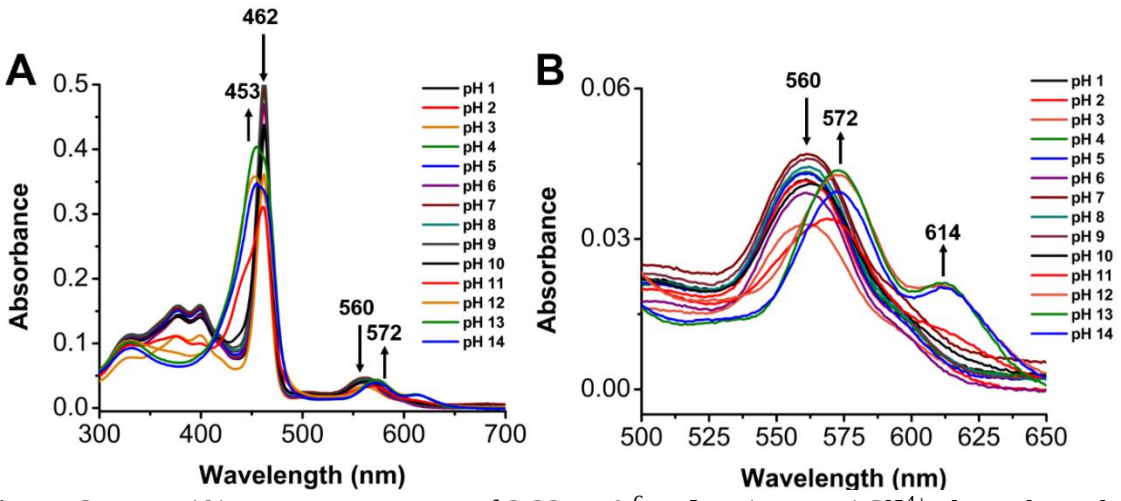

Figure SI 4.17. (A) UV-Vis spectrum of 3.33 x 10^{-6} M $[Mn(TMPyP)Cl]^{4+}$ throughout the pH domain with a decrease in absorbance at the characteristic Soret band occurring at 462 nm and the growth of a new band at 453 nm at higher pH **(B)** The characteristic Q band shifting from 560 to 572 towards high pH.

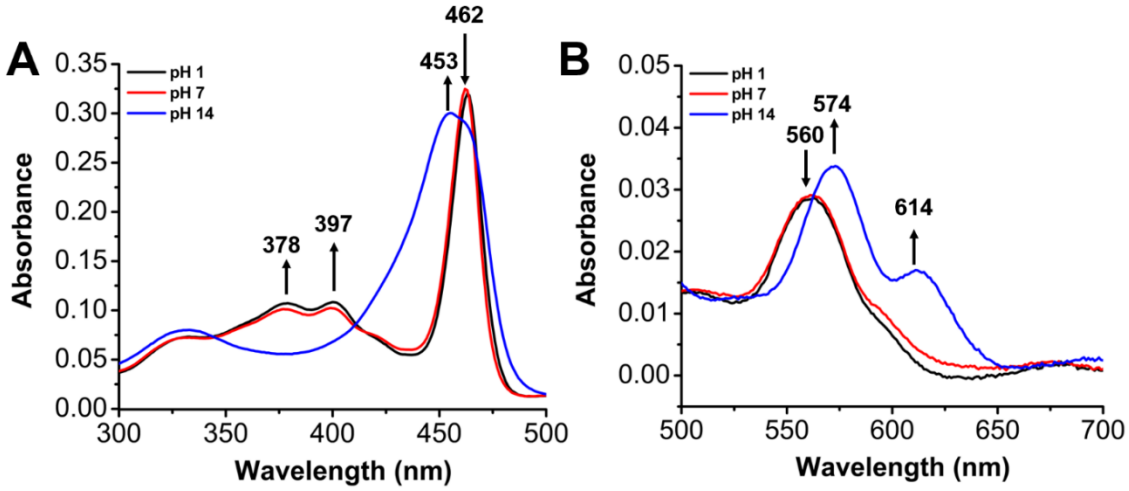

Figure SI 4.18. UV-Vis spectrum of 3.33 x 10^{-6} M $[Mn(TMPyP)Cl]^{4+}$ **(A)** Moving to higher pH demonstrates a decrease in absorbance at the Soret band (462 nm) with the appearance of a new band at 453 nm **(B)** While the Q band shifts from 560 to 572 nm.

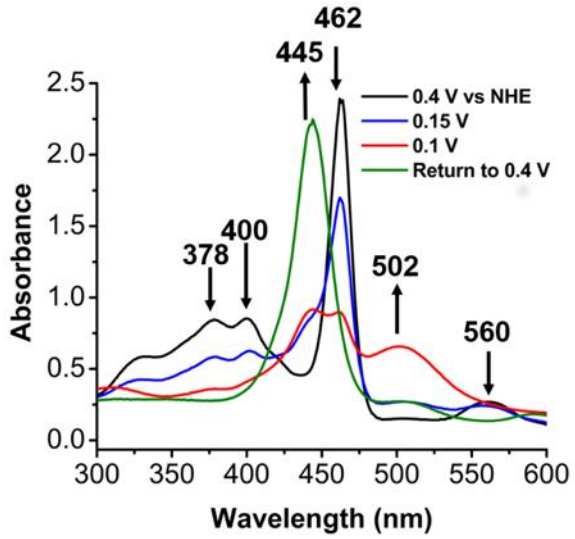

Figure SI 4.19. UV-Vis SEC spectrum of 0.1 mM $[Mn(TMPyP)Cl]^{4+}$ in pH 1 showing a decrease in the Soret band at 462 nm with the appearance of a new band at 440 nm (red trace) as the potential is decreased from 0.40 V to 0.10 V vs NHE. The Q band is blue shifted from 560 to 502 nm upon reduction. Conditions: Honeycomb platinum electrode and a Ag/AgCl sat'd KCl aqueous reference electrode.

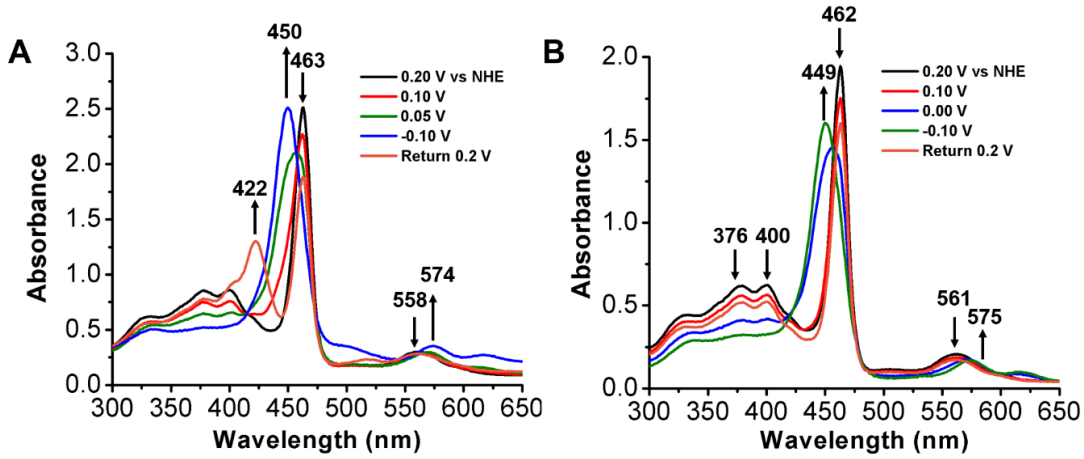

Figure SI 20. UV-Vis SEC spectra of 0.1 mM $[Mn(TMPyP)Cl]^{4+}$ in **(A)** pH 3 Britton-Robinson buffer solution showing a decrease in the Soret band at 463 nm with the appearance of a new band at 450 nm as the potential is decreased from +0.20 V to –0.10 V vs NHE. The Q band is red shifted from 558 to 574 nm upon reduction. **(B)** pH 7 Britton-Robinson buffer solution showing a decrease in the Soret band at 462 nm with the appearance of a new band at 449 nm as the potential is decreased from +0.20 V to –0.10 V vs NHE. The Q band is red shifted from 561 to 575 nm upon reduction. Conditions: Honeycomb platinum electrode and Ag/AgCl sat'd KCl aqueous reference electrode.

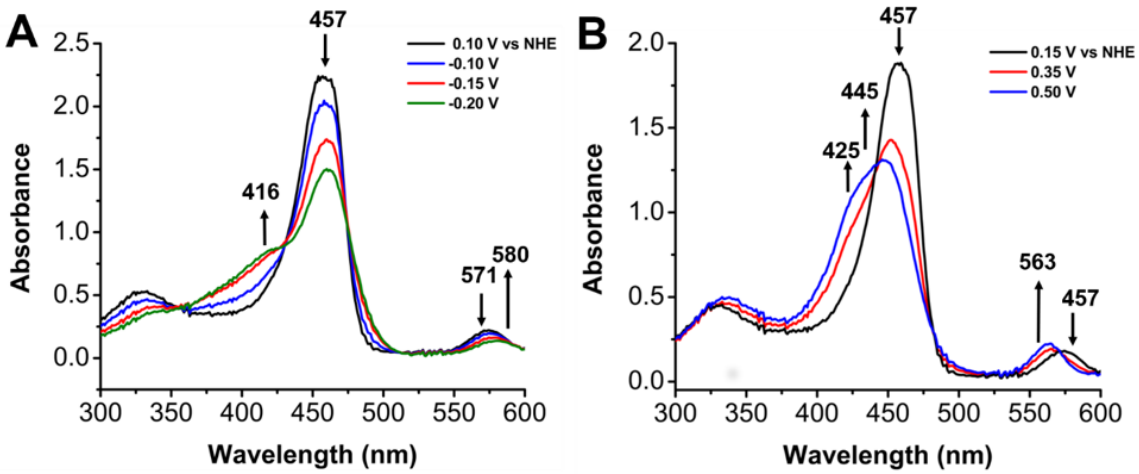

Figure SI 4.21. UV-Vis SEC spectrum of 0.1 mM $[Mn(TMPyP)Cl]^{4+}$ in pH 14 Britton-Robinson buffer **(A)** as the potential is decreased from 0.10 V to -0.20 V vs NHE a decrease in the Soret band at 457 nm occurs with the appearance of a new band at 416 nm **(B)** as the potential is increased from 0.15 to 0.50 V vs. NHE the formation of $[Mn(IV)(O)(TMPyP)(OH)]^{3+}$ occurs as apparent from the new band at 425 nm with the loss of the Soret band observed. Conditions: Honeycomb platinum electrode and a Ag/AgCl sat'd KCl aqueous reference electrode.

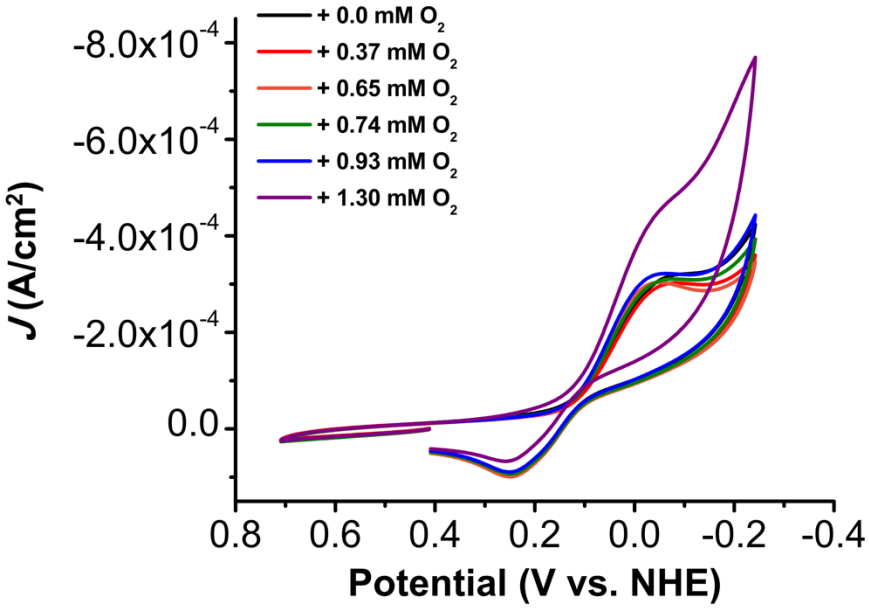

Figure SI 4.22. CV of 1 mM $[Mn(TMPyP)Cl]^{4+}$ with O_2 titration showing low activity at pH 1. Conditions: 1 mM $[Mn(TMPyP)Cl]^{4+}$ in a pH 1 (1 M HCl /0.1 M NaCl) solution; glassy carbon working electrode, glassy carbon counter electrode, 3.0 M NaCl Ag/AgCl; Scan rate 100 mV/s.

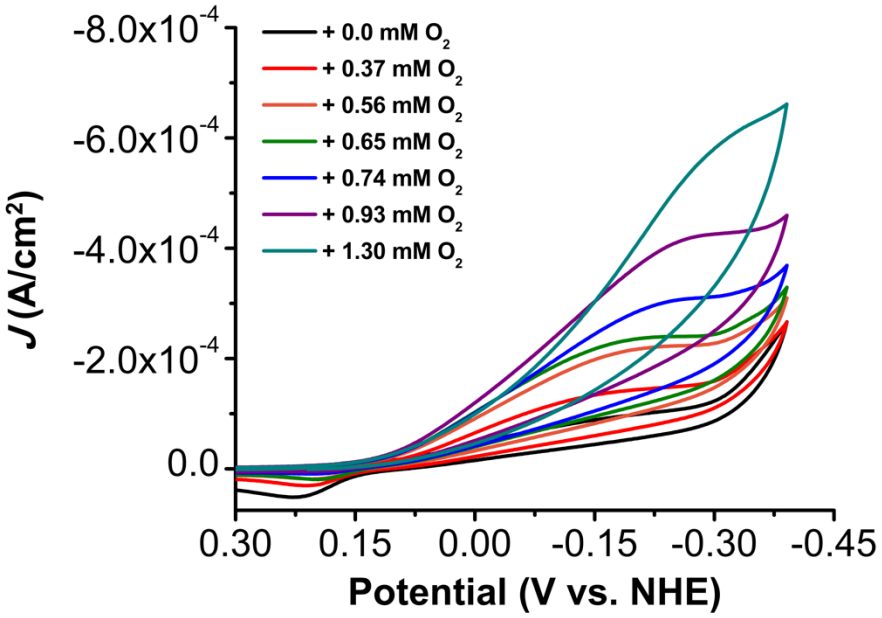

Figure SI 4.23. CVs under variable [O_2] showing an irreversible feature under pH 2 Britton-Robinson buffer conditions. Conditions: 1 mM $[Mn(TMPyP)Cl]^{4+}$ in a pH 2 Britton-Robinson buffer conditions under Ar saturation conditions, glassy carbon working electrode, glassy carbon counter electrode, 3.0 M NaCl Ag/AgCl reference electrode; Scan rate 100 mV/s.

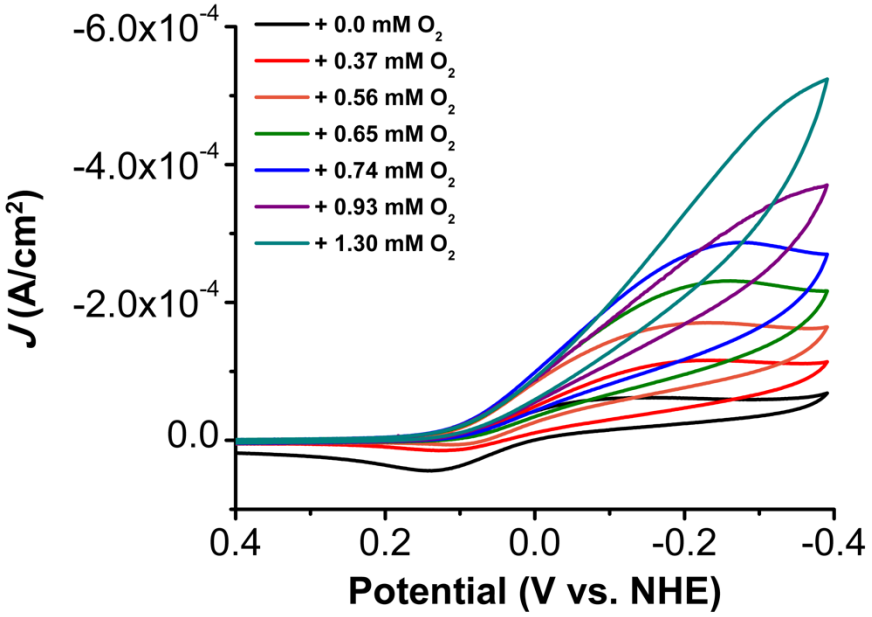

Figure SI 4.24. CVs of 1 mM $[Mn(TMPyP)Cl]^{4+}$ with O_2 titration demonstrating catalytic activity. Conditions: 1 mM $[Mn(TMPyP)Cl]^{4+}$ in a pH 3 Britton-Robinson Buffer solution; glassy carbon working electrode, glassy carbon counter electrode, 3.0 M NaCl Ag/AgCl reference electrode; Scan rate 100 mV/s.

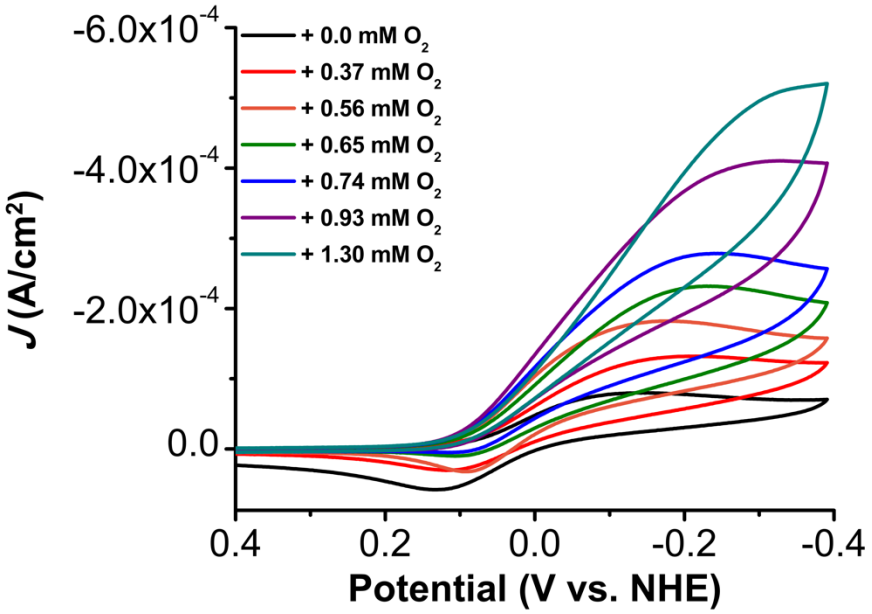

Figure SI 4.25. CVs of 1 mM $[Mn(TMPyP)Cl]^{4+}$ with O_2 titration demonstrating catalytic activity. Conditions: 1 mM $[Mn(TMPyP)Cl]^{4+}$ in a pH 4 Britton-Robinson Buffer solution; glassy carbon working electrode, glassy carbon counter electrode, 3.0 M NaCl Ag/AgCl reference; Scan rate 100 mV/s.

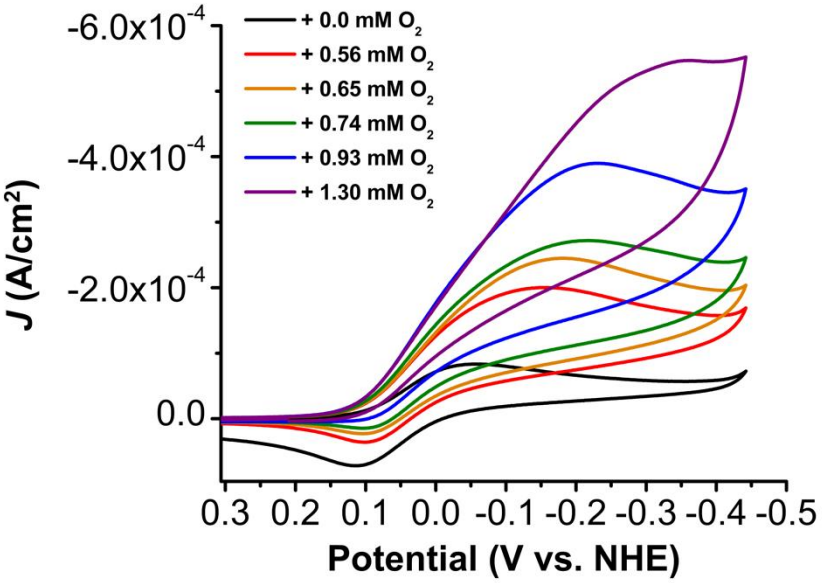

Figure SI 4.26. CVs of 1 mM $[Mn(TMPyP)Cl]^{4+}$ with O_2 titration demonstrating catalytic activity. Conditions: 1 mM $[Mn(TMPyP)Cl]^{4+}$ in a pH 5 Britton-Robinson Buffer solution; glassy carbon working electrode, glassy carbon counter electrode, 3.0 M NaCl Ag/AgCl reference; Scan rate 100 mV/s.

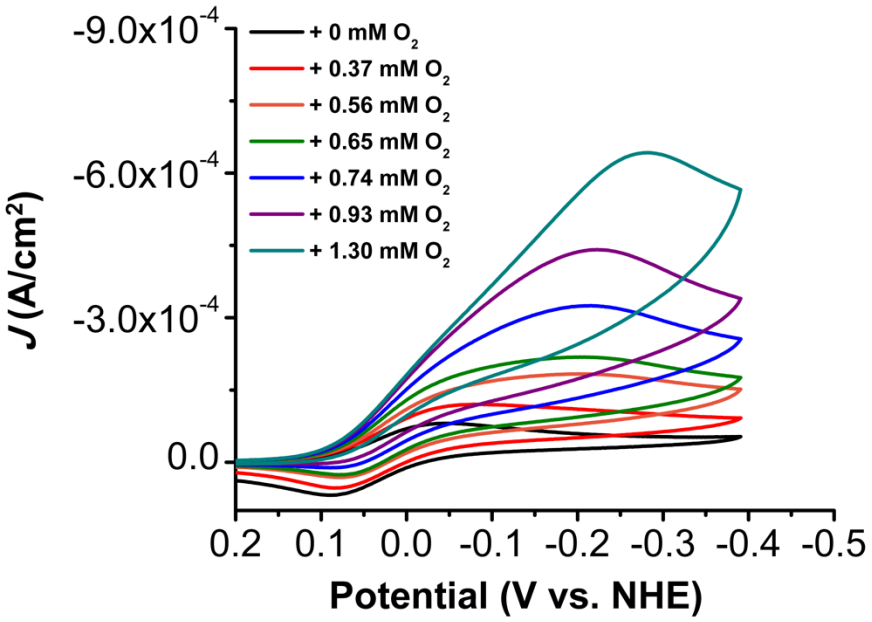

Figure SI 4.27. CVs of 1 mM $[Mn(TMPyP)Cl]^{4+}$ with O_2 titration demonstrating catalytic activity. Conditions: 1 mM $[Mn(TMPyP)Cl]^{4+}$ in a pH 6 Britton-Robinson Buffer solution; glassy carbon working electrode, glassy carbon counter electrode, 3.0 M NaCl Ag/AgCl reference; Scan rate 100 mV/s.

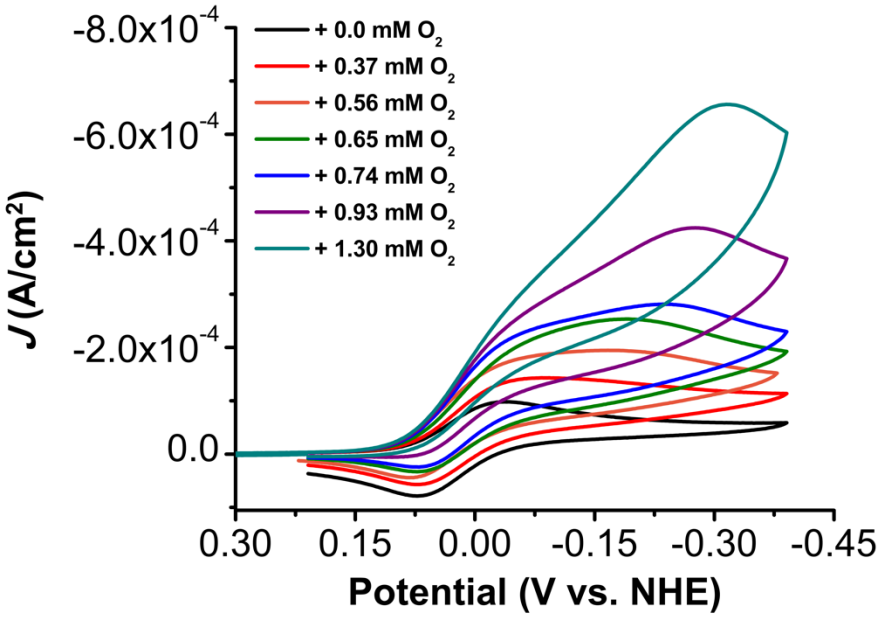

Figure SI 4.28. CVs of 1 mM $[Mn(TMPyP)Cl]^{4+}$ with O_2 titration. Conditions: 1 mM $[Mn(TMPyP)Cl]^{4+}$ in a pH 7 Britton-Robinson Buffer solution; glassy carbon working electrode, glassy carbon counter electrode, 3.0 M NaCl Ag/AgCl reference; Scan rate 100 mV/s.

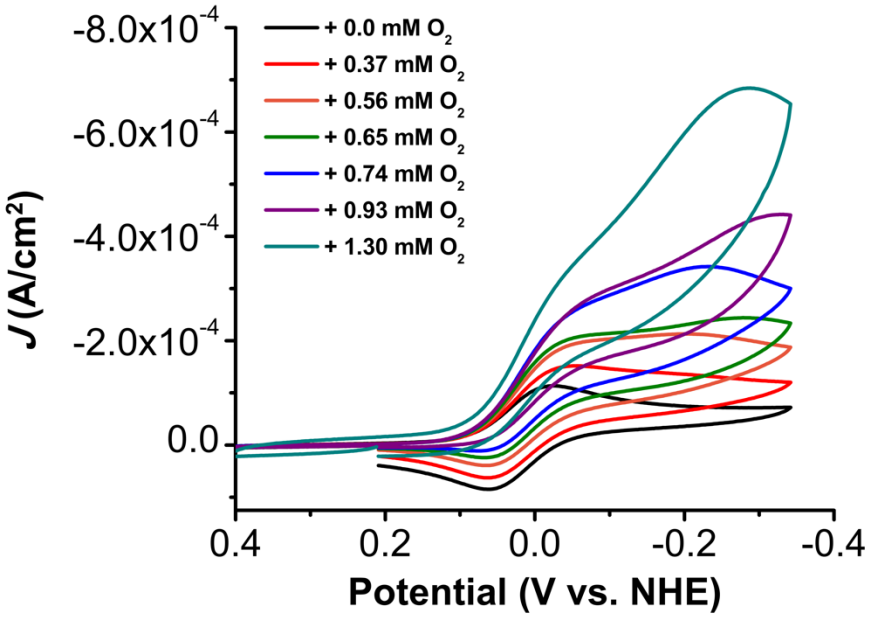

Figure SI 4.29. CVs of 1 mM $[Mn(TMPyP)Cl]^{4+}$ with O_2 titration. Conditions: 1 mM $[Mn(TMPyP)Cl]^{4+}$ in a pH 8 Britton-Robinson Buffer solution; glassy carbon working electrode, glassy carbon counter electrode, 3.0 M NaCl Ag/AgCl; Scan rate 100 mV/s.

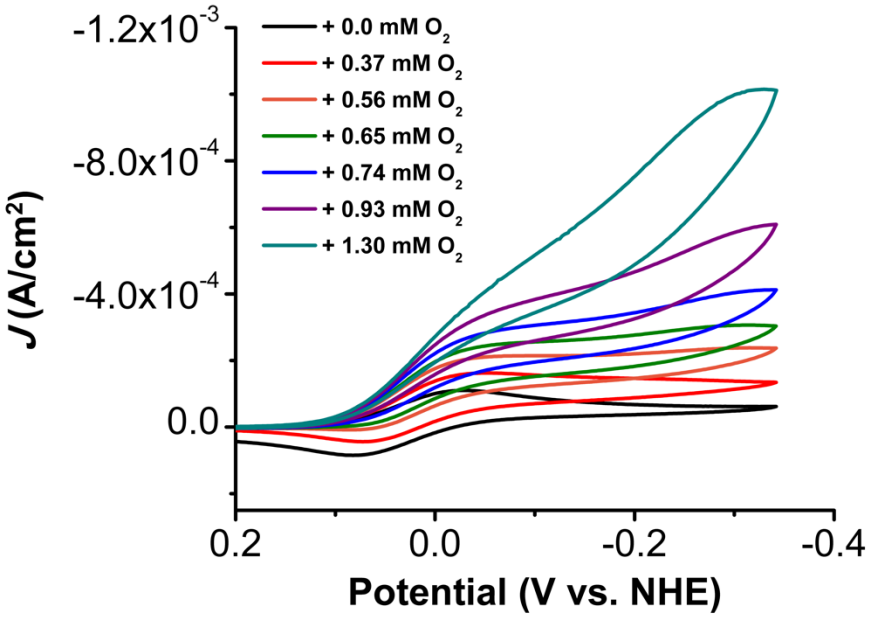

Figure SI 4.30. CVs of 1 mM $[Mn(TMPyP)Cl]^{4+}$ with O_2 titration. Conditions: 1 mM $[Mn(TMPyP)Cl]^{4+}$ in a pH 9 Britton-Robinson Buffer solution; glassy carbon working electrode, glassy carbon counter electrode, 3.0 M NaCl Ag/AgCl reference; Scan rate 100 mV/s.

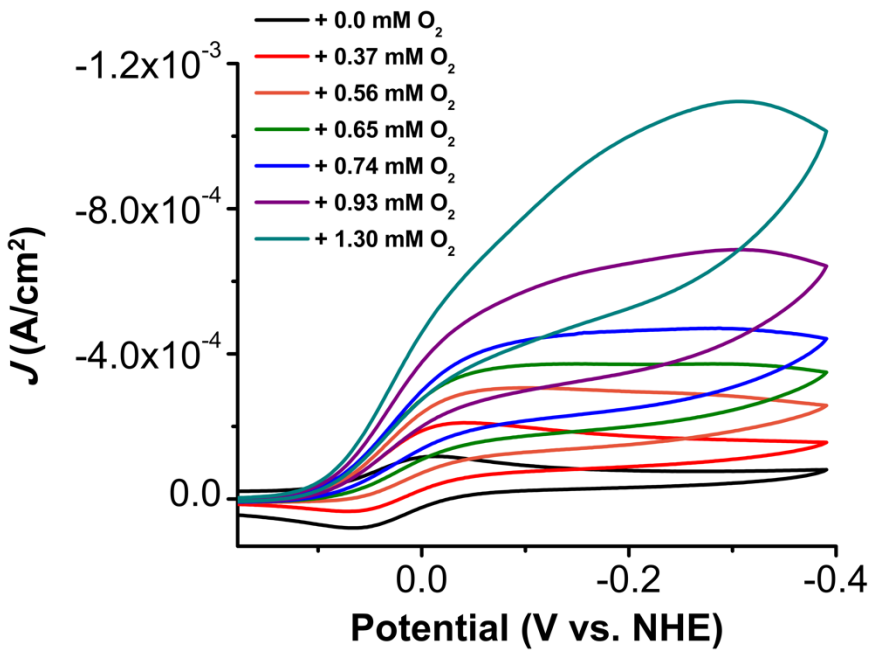

Figure SI 4.31. CVs of 1 mM $[Mn(TMPyP)Cl]^{4+}$ with O_2 titration. Conditions: 1 mM $[Mn(TMPyP)Cl]^{4+}$ in a pH 10 Britton-Robinson Buffer solution; glassy carbon working electrode, glassy carbon counter electrode, 3.0 M NaCl Ag/AgCl reference; Scan rate 100 mV/s.

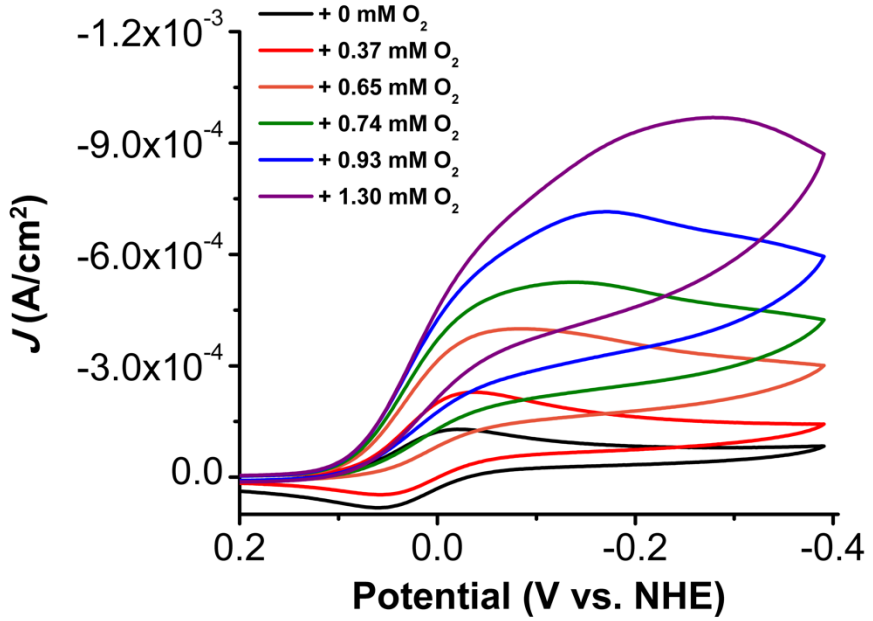

Figure SI 4.32. CVs of 1 mM $[Mn(TMPyP)Cl]^{4+}$ with O_2 titration. Conditions: 1 mM $[Mn(TMPyP)Cl]^{4+}$ in a pH 11 Britton-Robinson Buffer solution; glassy carbon working electrode, glassy carbon counter electrode, 3.0 M NaCl Ag/AgCl reference; Scan rate 100 mV/s.

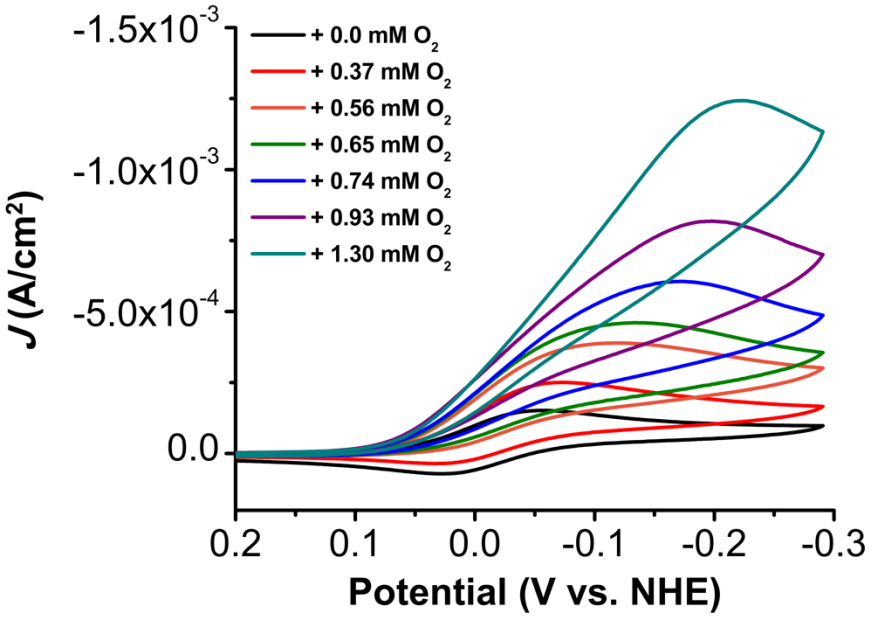

Figure SI 4.33. CVs of 1 mM $[Mn(TMPyP)Cl]^{4+}$ with O_2 titration. Conditions: 1 mM $[Mn(TMPyP)Cl]^{4+}$ in a pH 12 Britton-Robinson Buffer solution; glassy carbon working electrode, glassy carbon counter electrode, 3.0 M NaCl Ag/AgCl reference; Scan rate 100 mV/s.

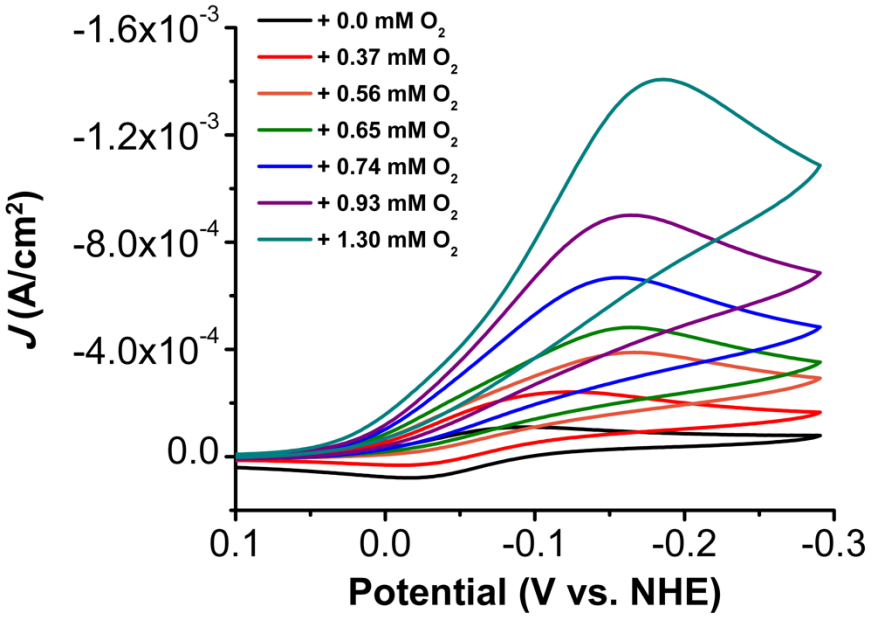

Figure SI 4.34. CVs of 1 mM $[Mn(TMPyP)Cl]^{4+}$ with O_2 titration. Conditions: 1 mM $[Mn(TMPyP)Cl]^{4+}$ in a pH 13 Britton-Robinson Buffer solution; glassy carbon working electrode, glassy carbon counter electrode, 3.0 M NaCl Ag/AgCl reference; Scan rate 100 mV/s.

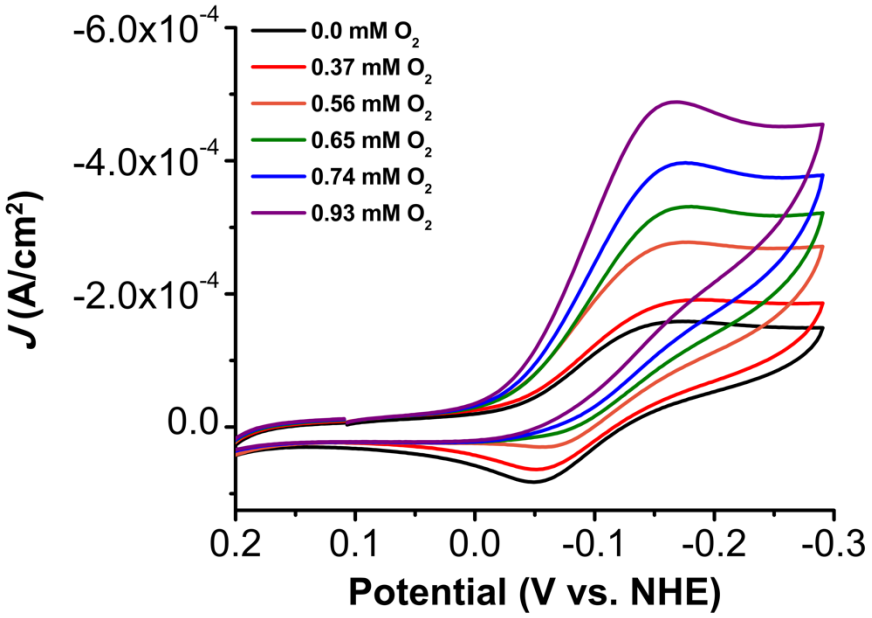

Figure SI 4.35. CVs of 1 mM $[Mn(TMPyP)Cl]^{4+}$ with O_2 titration. Conditions: 1 mM $[Mn(TMPyP)Cl]^{4+}$ in a pH 14 Britton-Robinson Buffer solution; glassy carbon working electrode, glassy carbon counter electrode, 3.0 M NaCl Ag/AgCl reference; Scan rate 100 mV/s.

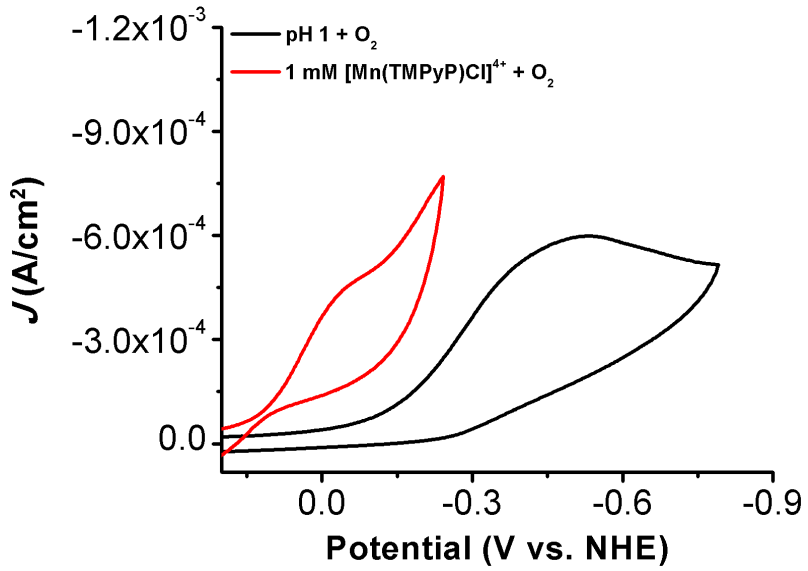

Figure SI 4.36. Control CV of a blank pH 1 (1 M HCl / 0.1 M NaCl) solution under O_2 saturation conditions in comparison to a 1 mM $[Mn(TMPyP)Cl]^{4+}$ solution under O_2 showing the molecular regime for the catalyst. Conditions: Glassy carbon working electrode, glassy carbon counter electrode, 3.0 M NaCl Ag/AgCl reference electrode; Scan rate 100 mV/s.

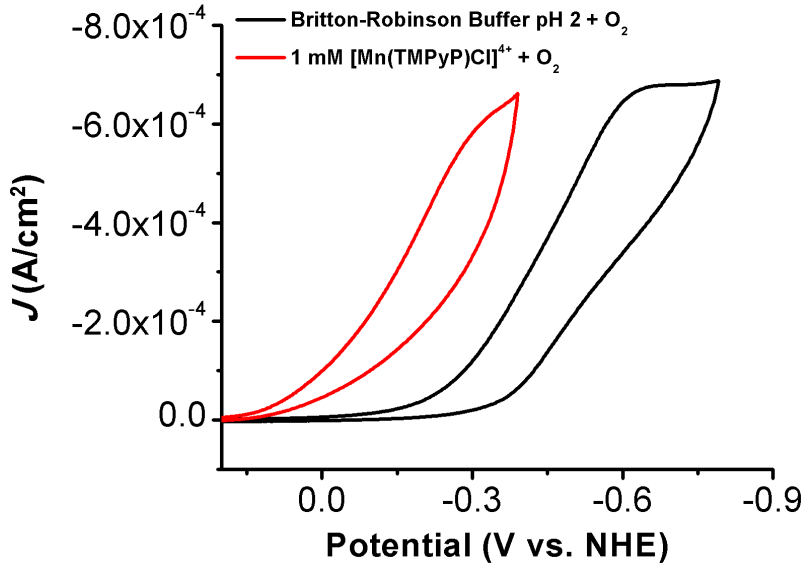

Figure SI 4.37. Control CV of a blank pH 2 Britton-Robinson Buffer solution under O_2 saturation conditions in comparison to a 1 mM $[Mn(TMPyP)Cl]^{4+}$ solution under O_2 showing the molecular regime for the catalyst. Conditions: Glassy carbon working electrode, glassy carbon counter electrode, 3.0 M NaCl Ag/AgCl reference electrode; Scan rate 100 mV/s.

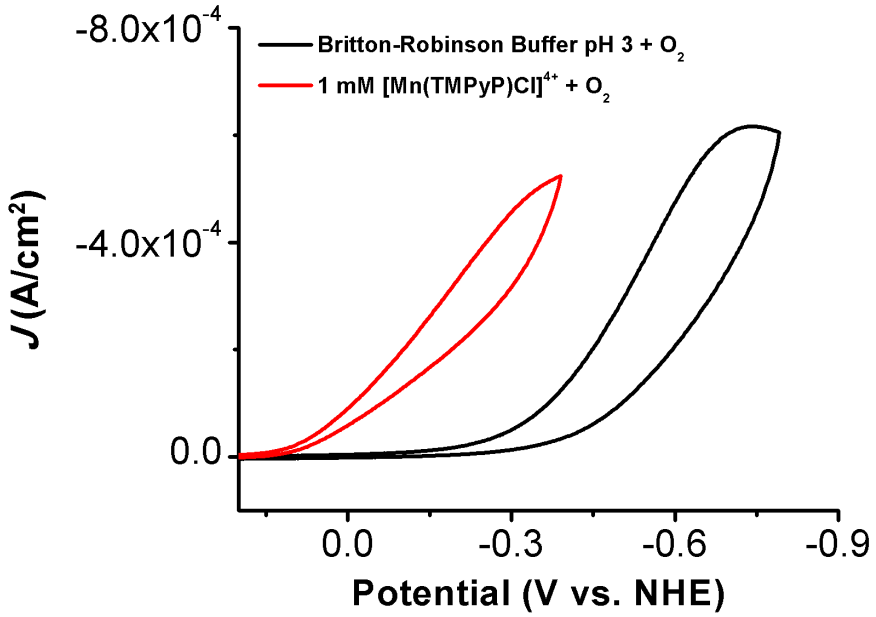

Figure SI 4.38. Control CV of a blank pH 3 Britton-Robinson Buffer solution under O_2 saturation conditions in comparison to a 1 mM $[Mn(TMPyP)Cl]^{4+}$ solution under O_2 showing the molecular regime for the catalyst. Conditions: Glassy carbon working electrode, glassy carbon counter electrode, 3.0 M NaCl Ag/AgCl reference electrode; Scan rate 100 mV/s.

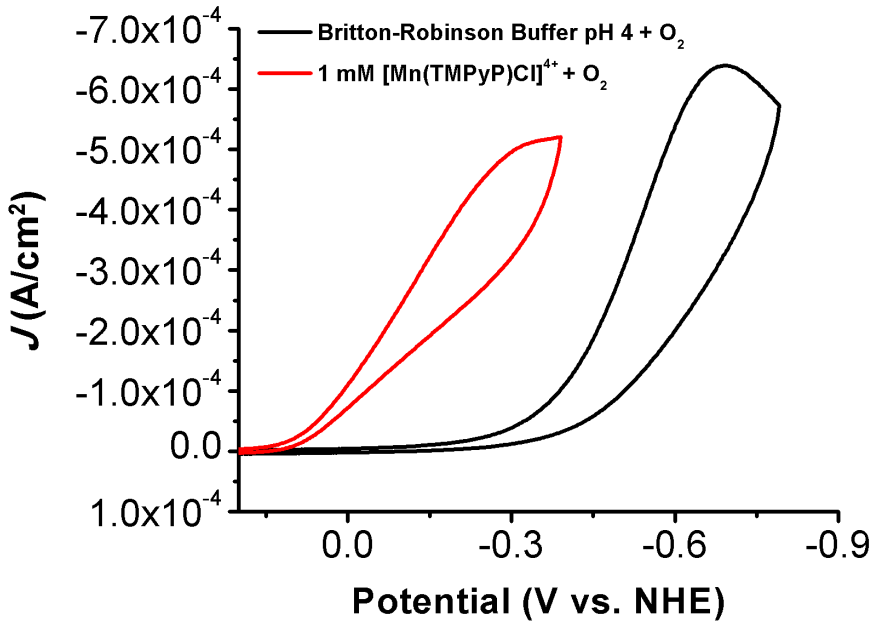

Figure SI 4.39. Control CV of a blank pH 4 Britton-Robinson Buffer solution under O_2 saturation conditions in comparison to a 1 mM $[Mn(TMPyP)Cl]^{4+}$ solution under O_2 showing the molecular regime for the catalyst. Conditions: Glassy carbon working electrode, glassy carbon counter electrode, 3.0 M NaCl Ag/AgCl reference electrode; Scan rate 100 mV/s.

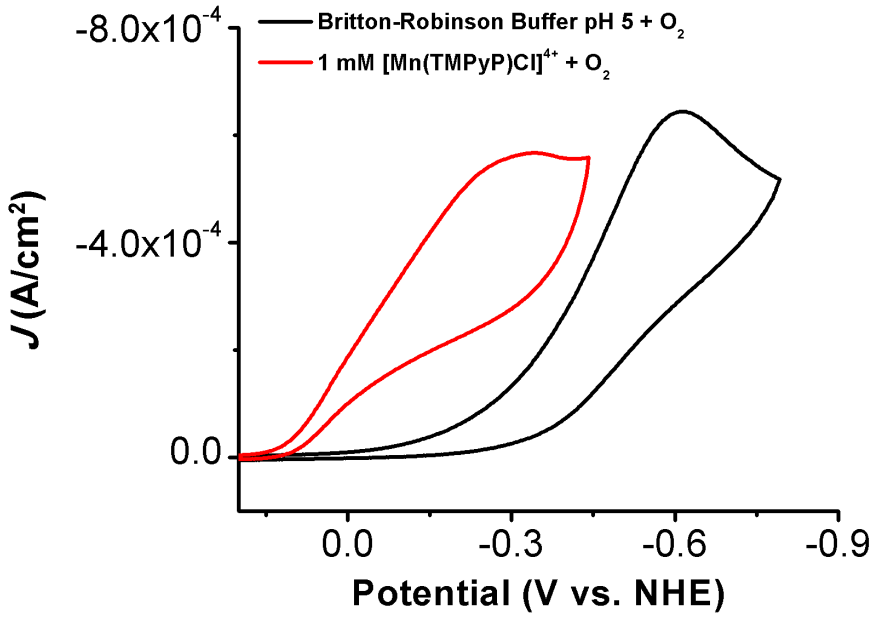

Figure SI 4.40. Control CV of a blank pH 5 Britton-Robinson Buffer solution under O_2 saturation conditions in comparison to a 1 mM $[Mn(TMPyP)Cl]^{4+}$ solution under O_2 showing the molecular regime for the catalyst. Conditions: Glassy carbon working electrode, glassy carbon counter electrode, 3.0 M NaCl Ag/AgCl reference electrode; Scan rate 100 mV/s.

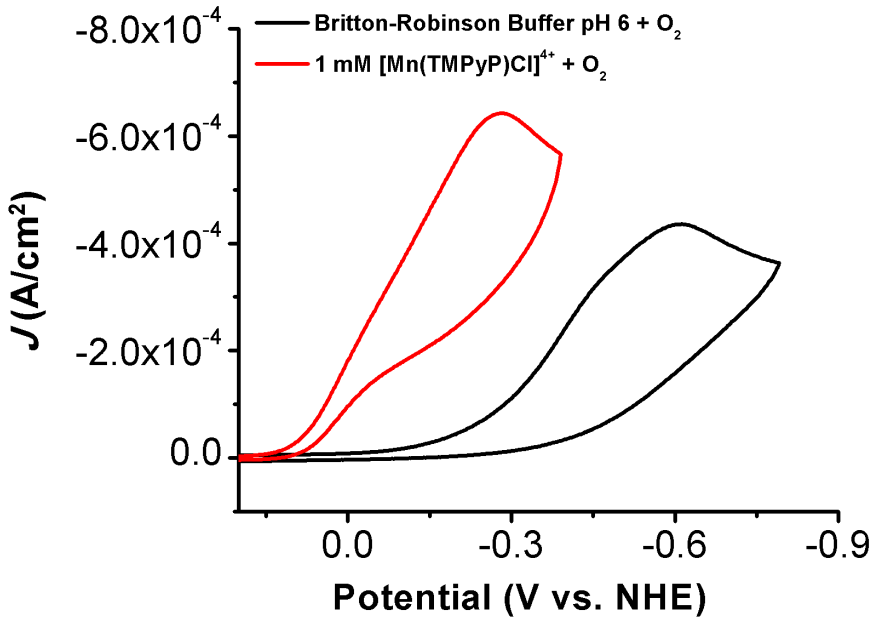

Figure SI 4.41. Control CV of a blank pH 6 Britton-Robinson Buffer solution under O_2 saturation conditions in comparison to a 1 mM $[Mn(TMPyPCl)]^{4+}$ solution under O_2 showing the molecular regime for the catalyst. Conditions: Glassy carbon working electrode, glassy carbon counter electrode, 3.0 M NaCl Ag/AgCl reference electrode; Scan rate 100 mV/s.

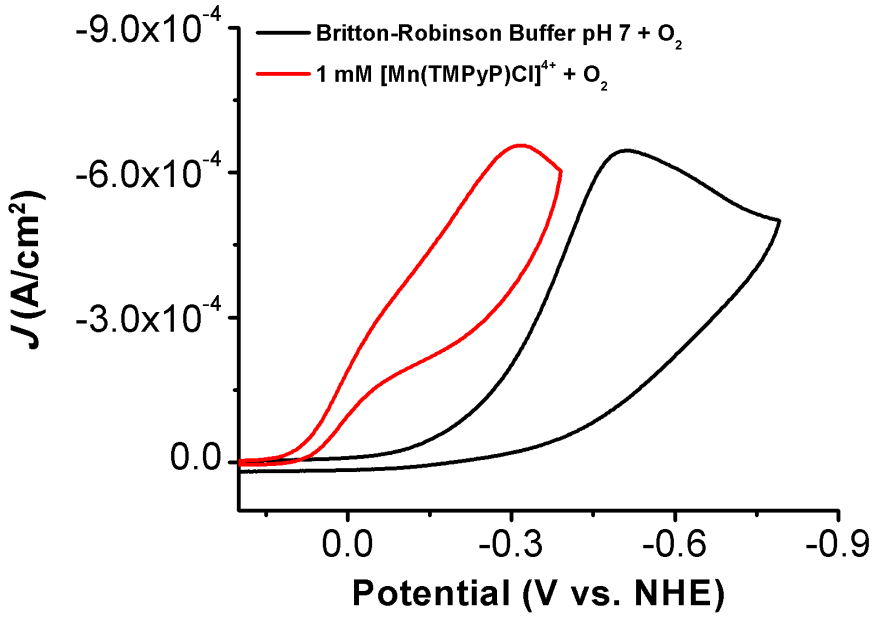

Figure SI 4.42. Control CV of a blank pH 7 Britton-Robinson Buffer solution under O_2 saturation conditions in comparison to a 1 mM $[Mn(TMPyP)Cl]^{4+}$ solution under O_2 showing the molecular regime for the catalyst. Conditions: Glassy carbon working electrode, glassy carbon counter electrode, 3.0 M NaCl Ag/AgCl reference electrode; Scan rate 100 mV/s.

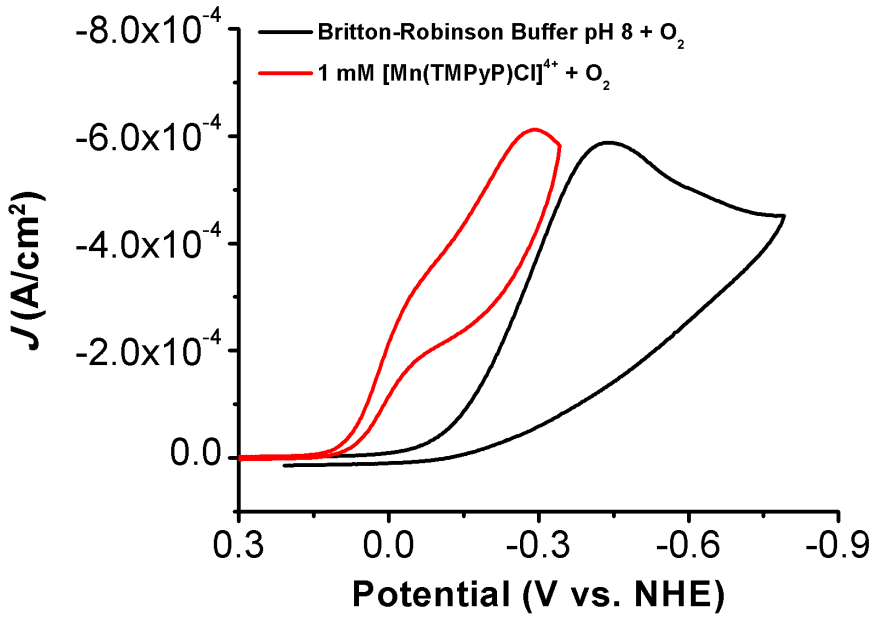

Figure SI 4.43. Control CV of a blank pH 8 Britton-Robinson Buffer solution under O_2 saturation conditions in comparison to a 1 mM $[Mn(TMPyP)Cl]^{4+}$ solution under O_2 showing the molecular regime for the catalyst. Conditions: Glassy carbon working electrode, glassy carbon counter electrode, 3.0 M NaCl Ag/AgCl reference; Scan rate 100 mV/s.

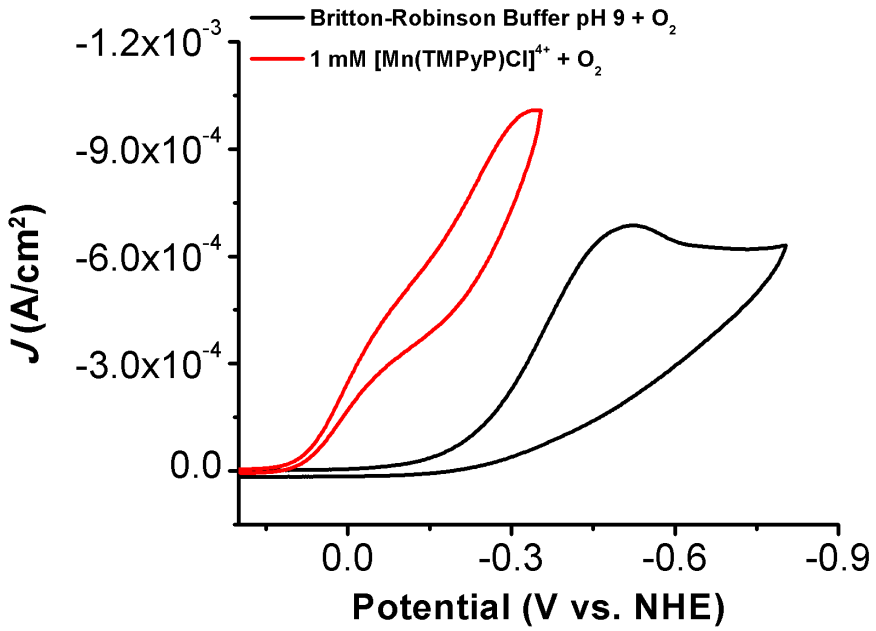

Figure SI 4.44. Control CV of a blank pH 9 Britton-Robinson Buffer solution under O_2 saturation conditions in comparison to a 1 mM $[Mn(TMPyP)Cl]^{4+}$ solution under O_2 showing the molecular regime for the catalyst. Conditions: Glassy carbon working electrode, glassy carbon counter electrode, 3.0 M NaCl Ag/AgCl reference electrode; Scan rate 100 mV/s.

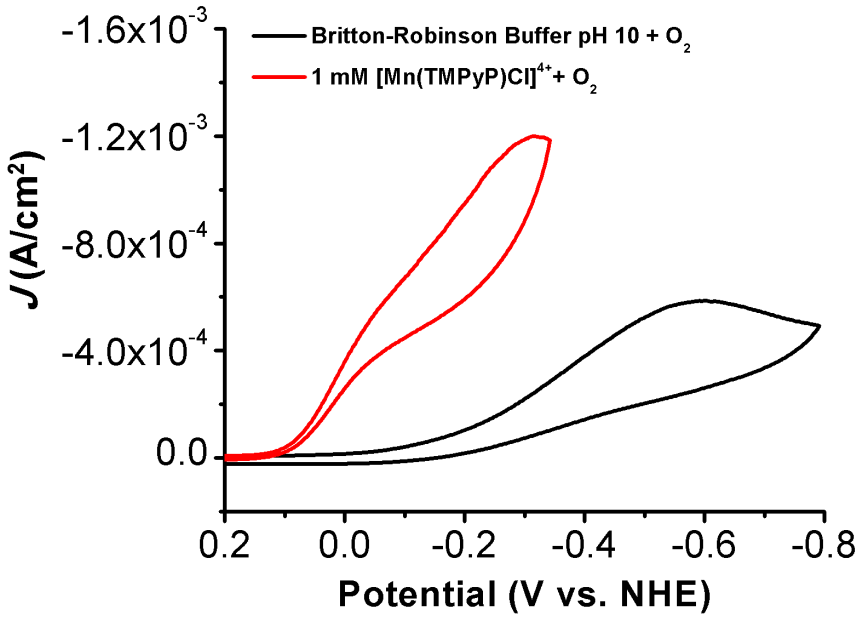

Figure SI 4.45. Control CV of a blank pH 10 Britton-Robinson Buffer solution under O_2 saturation conditions in comparison to a 1 mM $[Mn(TMPyP)Cl]^{4+}$ solution under O_2 showing the molecular regime for the catalyst. Conditions: Glassy carbon working electrode, glassy carbon counter electrode, 3.0 M NaCl Ag/AgCl reference electrode; Scan rate 100 mV/s.

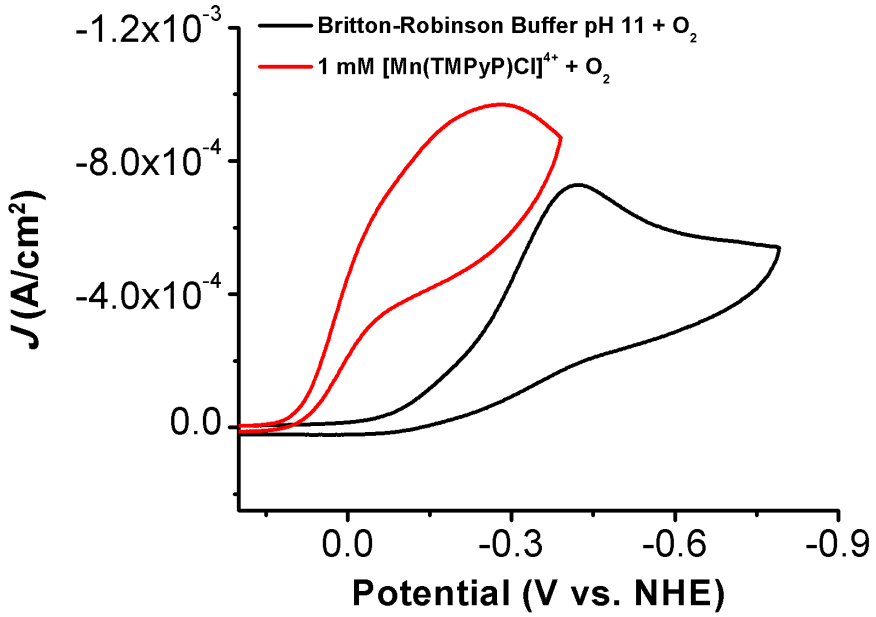

Figure SI 4.46. Control CV of a blank pH 11 Britton-Robinson Buffer solution under O_2 saturation conditions in comparison to a 1 mM $[Mn(TMPyP)Cl]^{4+}$ solution under O_2 showing the molecular regime for the catalyst. Conditions: Glassy carbon working electrode, glassy carbon counter electrode, 3.0 M NaCl Ag/AgCl reference electrode; Scan rate 100 mV/s.

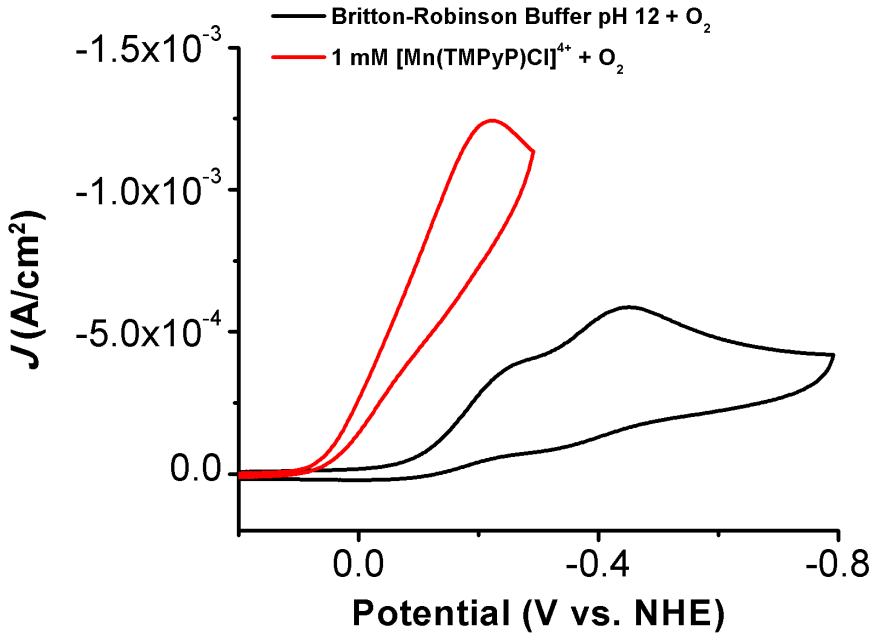

Figure SI 4.47. Control CV of a blank pH 12 Britton-Robinson Buffer solution under O_2 saturation conditions in comparison to a 1 mM $[Mn(TMPyP)Cl]^{4+}$ solution under O_2 showing the molecular regime for the catalyst. Conditions: Glassy carbon working electrode, glassy carbon counter electrode, 3.0 M NaCl Ag/AgCl reference electrode; Scan rate 100 mV/s.

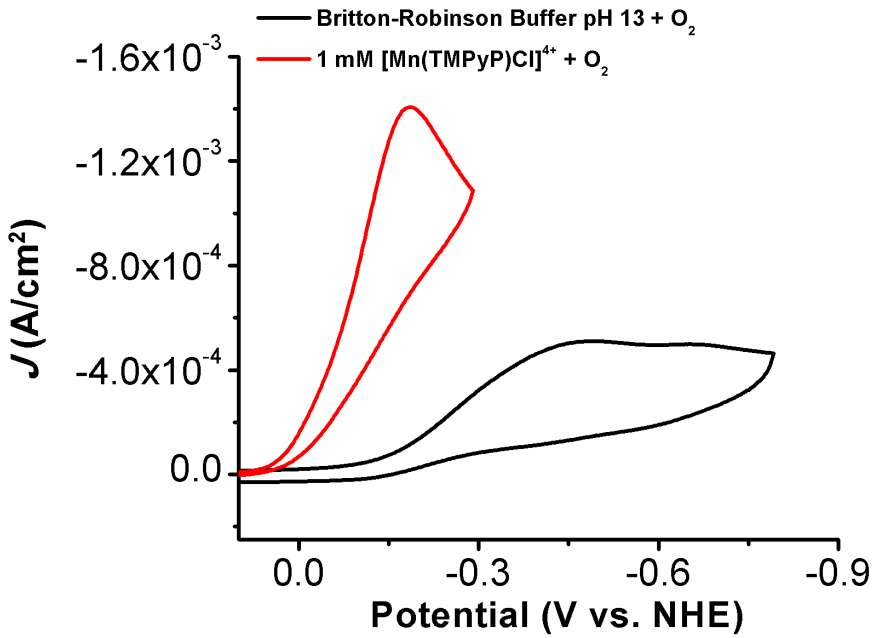

Figure SI 4.48. Control CV of a blank pH 13 Britton-Robinson Buffer solution under O_2 saturation conditions in comparison to a 1 mM $[Mn(TMPyP)Cl]^{4+}$ solution under O_2 showing the molecular regime for the catalyst. Conditions: Glassy carbon working electrode, glassy carbon counter electrode, 3.0 M NaCl Ag/AgCl reference electrode; Scan rate 100 mV/s.

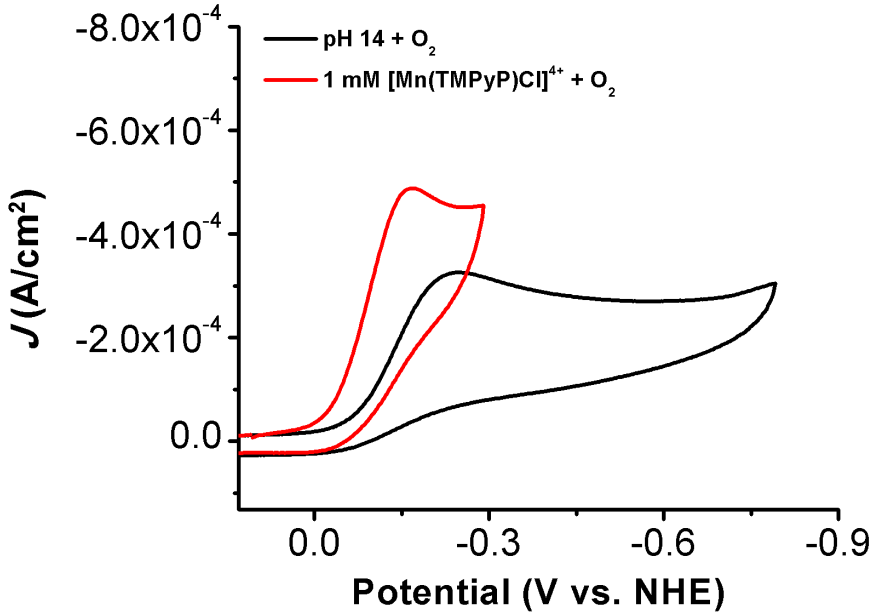

Figure SI 4.49. Control CV of a blank pH 14 (1 M KOH / 0.1 M NaCl) solution under O_2 saturation conditions in comparison to a 1 mM $[Mn(TMPyP)Cl]^{4+}$ solution under O_2 showing the molecular regime for the catalyst. Conditions: Glassy carbon working electrode, glassy carbon counter electrode, 3.0 M NaCl Ag/AgCl reference electrode; Scan rate 100 mV/s.

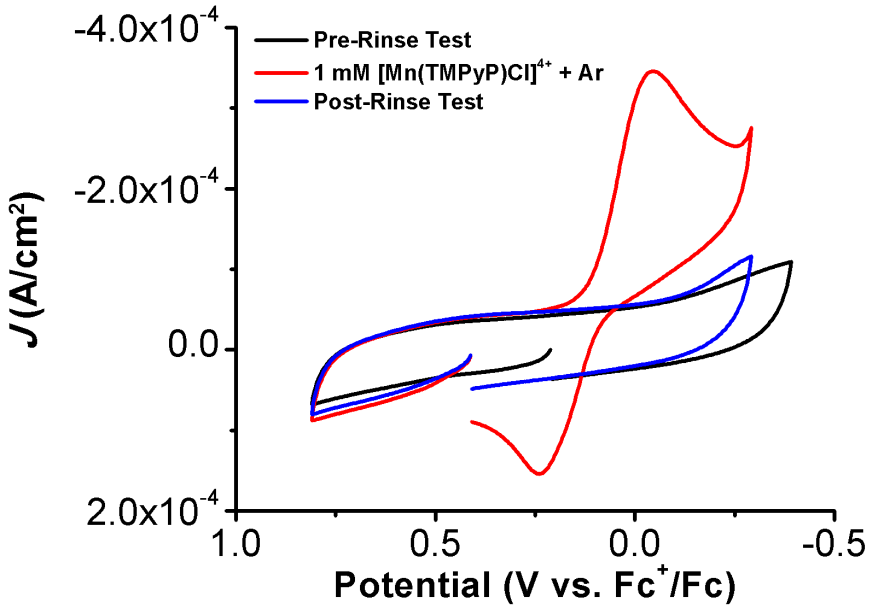

Figure SI 4.50. Adsorption test at pH 1 (1 M HCl / 0.1 M NaCl) solution under Ar. Conditions: Glassy carbon working electrode, glassy carbon counter electrode, 3.0 M NaCl Ag/AgCl reference electrode; Scan rate 100 mV/s.

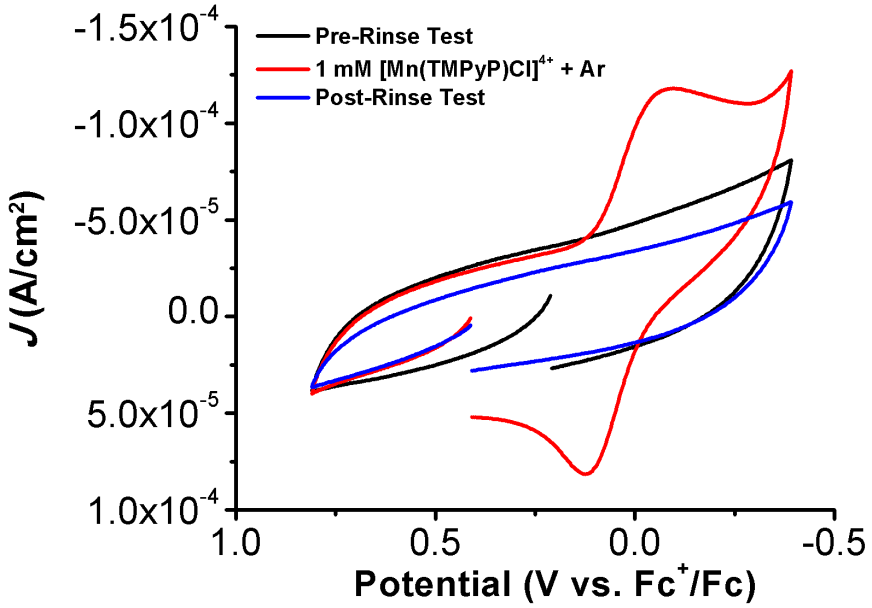

Figure SI 4.51. Adsorption test at pH 3 Britton-Robinson Buffer solution under Ar. Conditions: Glassy carbon working electrode, glassy carbon counter electrode, 3.0 M NaCl Ag/AgCl reference electrode; Scan rate 100 mV/s.

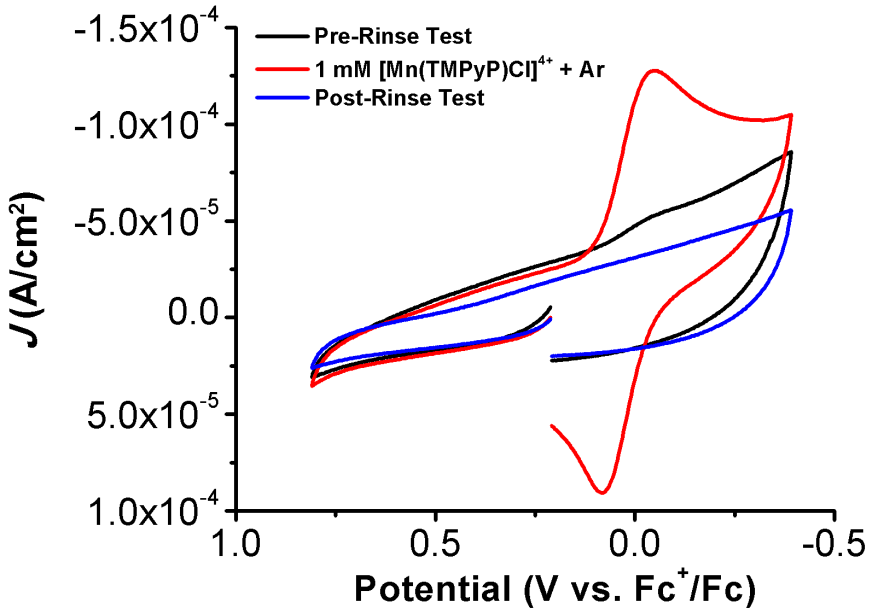

Figure SI 4.52. Adsorption test at pH 6 Britton-Robinson Buffer solution under Ar. Conditions: Glassy carbon working electrode, glassy carbon counter electrode, 3.0 M NaCl Ag/AgCl reference electrode; Scan rate 100 mV/s.

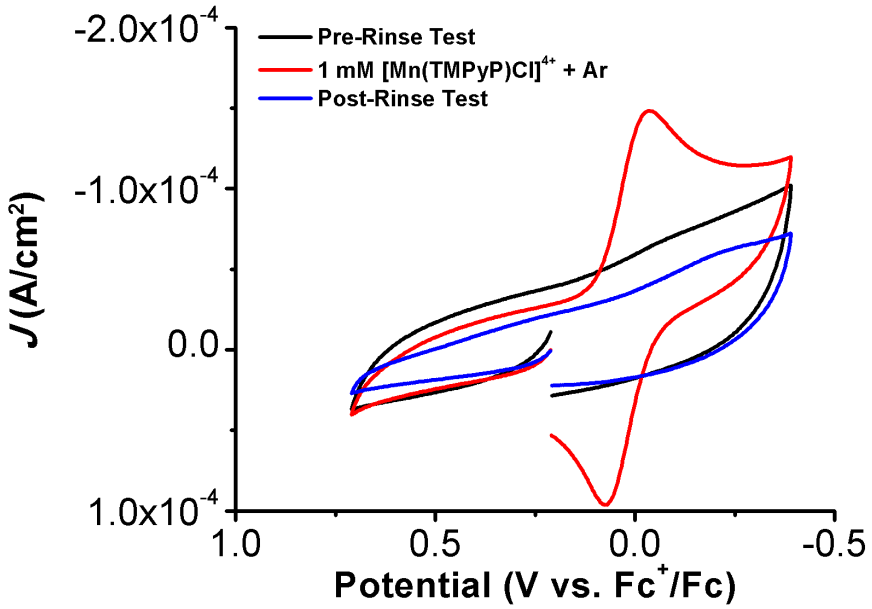

Figure SI 4.53. Adsorption test at pH 7 Britton-Robinson Buffer solution under Ar. Conditions: Glassy carbon working electrode, glassy carbon counter electrode, 3.0 M NaCl Ag/AgCl reference electrode; Scan rate 100 mV/s.

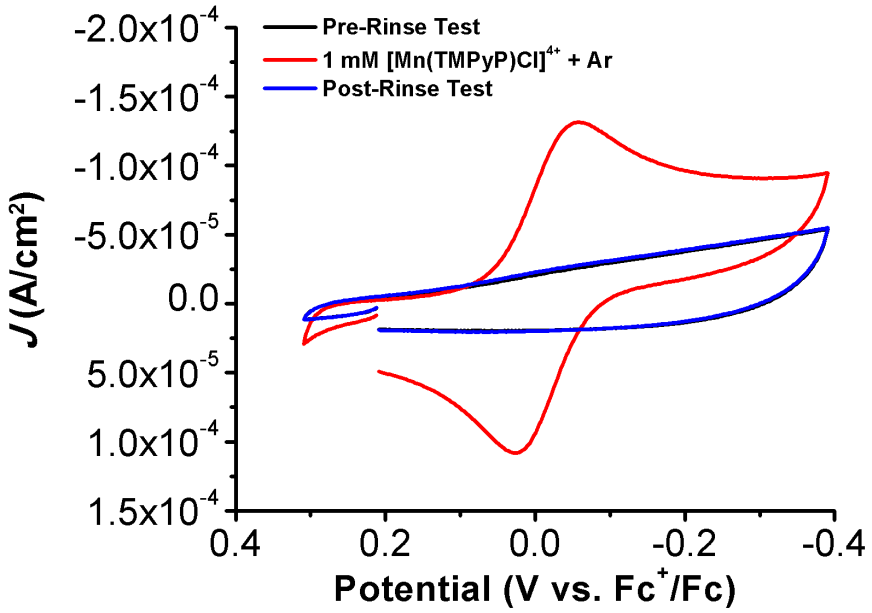

Figure SI 4.54. Adsorption test at pH 12 Britton-Robinson Buffer solution under Ar. Conditions: Glassy carbon working electrode, glassy carbon counter electrode, 3.0 M NaCl Ag/AgCl reference electrode; Scan rate 100 mV/s.

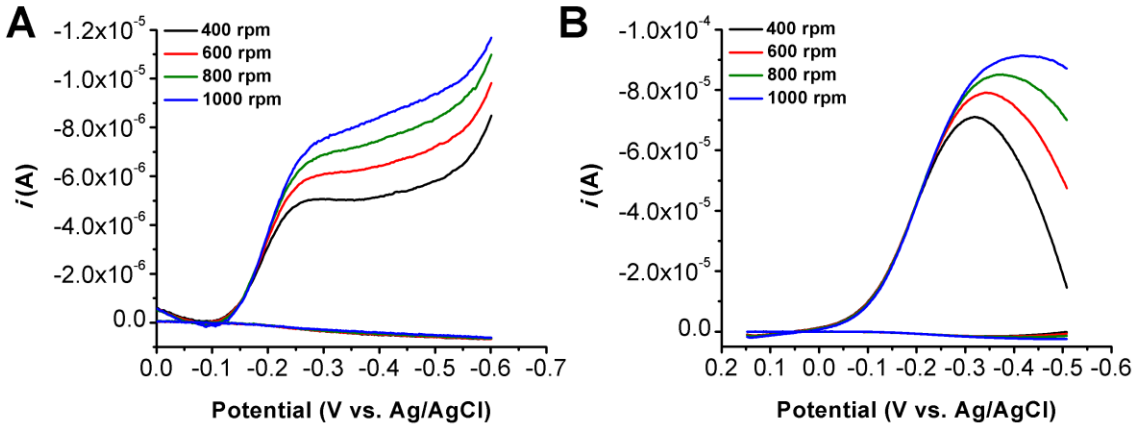

Figure SI 4.55. Linear Sweep Voltammograms of RRDE experiments with $[Mn(TMPyP)Cl]^{4+}$ (0.25 mM) at various rotation rates under argon **(A)** and O_2 **(B)** saturation conditions in a pH 5 buffer solution; ring potential = 1.2 V vs Ag/AgCl. Conditions: 0.25 mM analyte; glassy carbon working electrode/Pt ring working electrode, glassy carbon counter electrode, Ag/AgCl/3 M KCI reference electrode; scan rate 0.02 V/s.

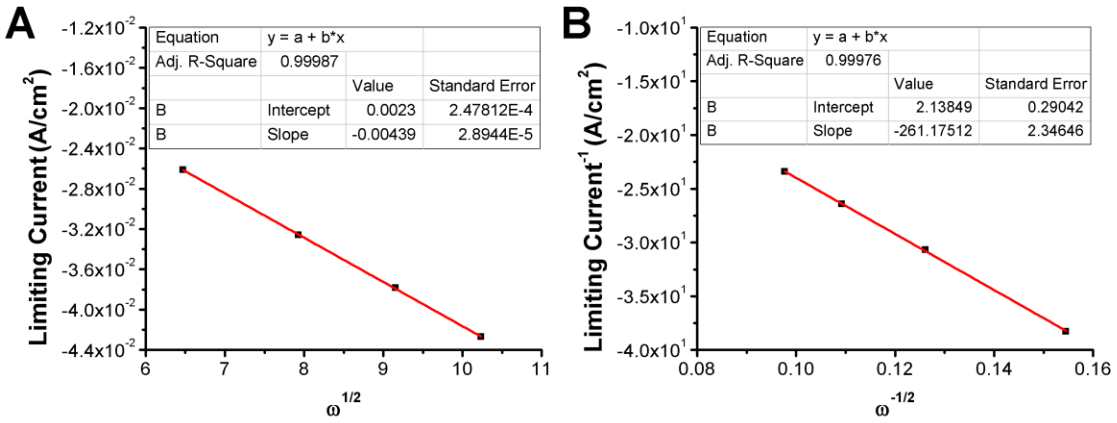

Figure SI 4.56. Levich **(A)** and Koutecky-Levich **(B)** plots from data obtained from Linear Sweep Voltammograms of $[Mn(TMPyP)Cl]^{4+}$ (0.25 mM) by RRDE under argon saturation conditions at various rotation rates in a pH 5 buffer solution.

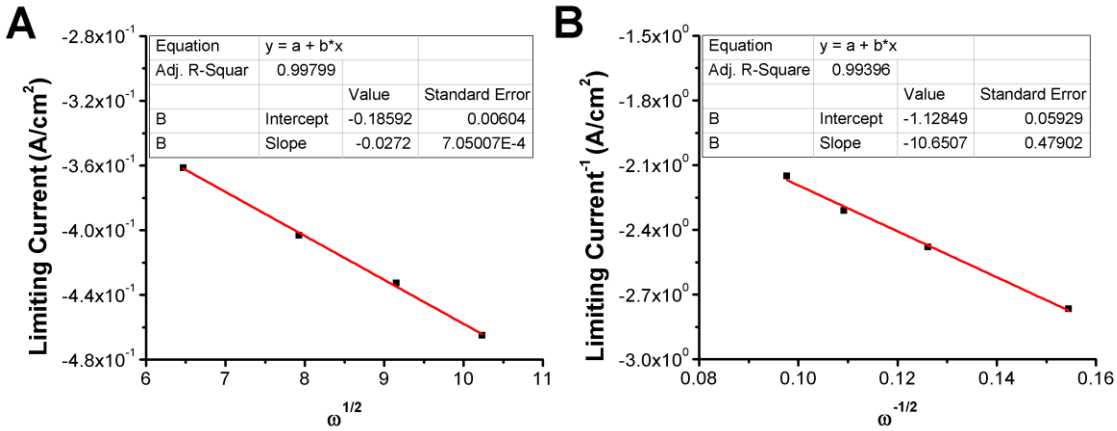

Figure SI 4.57. Levich **(A)** and Koutecky-Levich **(B)** plots from data obtained from Linear Sweep Voltammograms of $[Mn(TMPyP)Cl]^{4+}$ (0.25 mM) by RRDE under O_2 saturation conditions at various rotation rates in a pH 5 buffer solution.

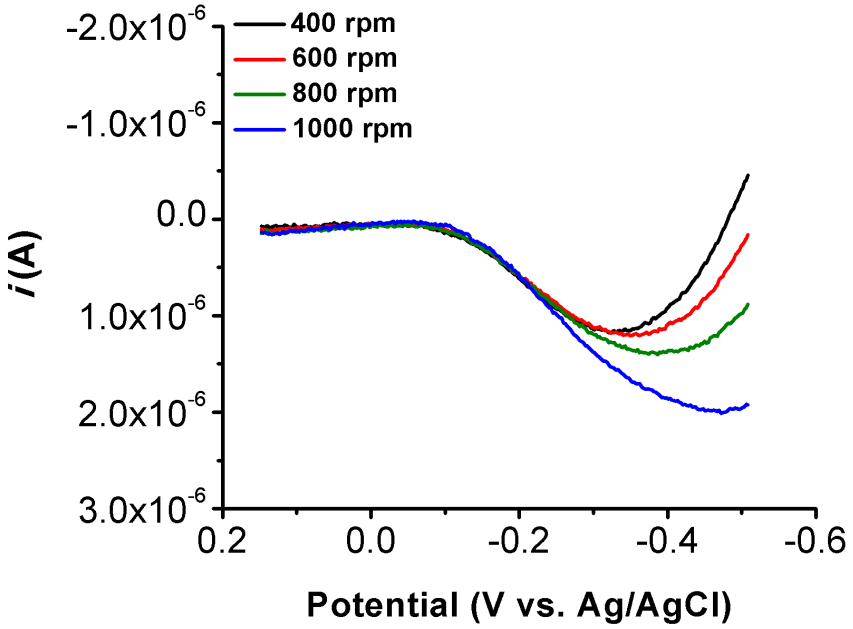

Figure SI 4.58. Linear Sweep Voltammograms of the generated ring current during RRDE experiments with $[Mn(TMPyP)Cl]^{4+}$ (0.25 mM) at various rotation rates with the argon ring current subtracted from the ring current produced under O_2 saturation conditions in a pH 5 buffer solution; ring potential = 1.2 V vs Ag/AgCl. Conditions: 0.25 mM analyte; glassy carbon working electrode/Pt ring working electrode, glassy carbon counter electrode, Ag/AgCl/3 M KCI reference electrode; scan rate 0.02 V/s.

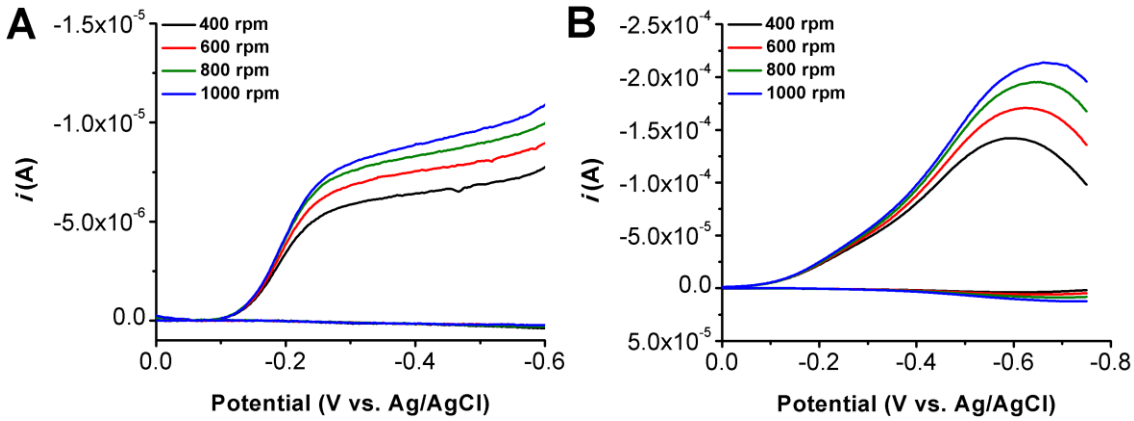

Figure SI 4.59. Linear Sweep Voltammograms of RRDE experiments with $[Mn(TMPyP)Cl]^{4+}$ (0.25 mM) at various rotation rates under argon **(A)** and O_2 **(B)** saturation conditions in a pH 6 buffer solution; ring potential = 1.2 V vs Ag/AgCl. Conditions: 0.25 mM analyte; glassy carbon working electrode/Pt ring working electrode, glassy carbon counter electrode, Ag/AgCl/3 M KCI reference electrode; scan rate 0.02 V/s.

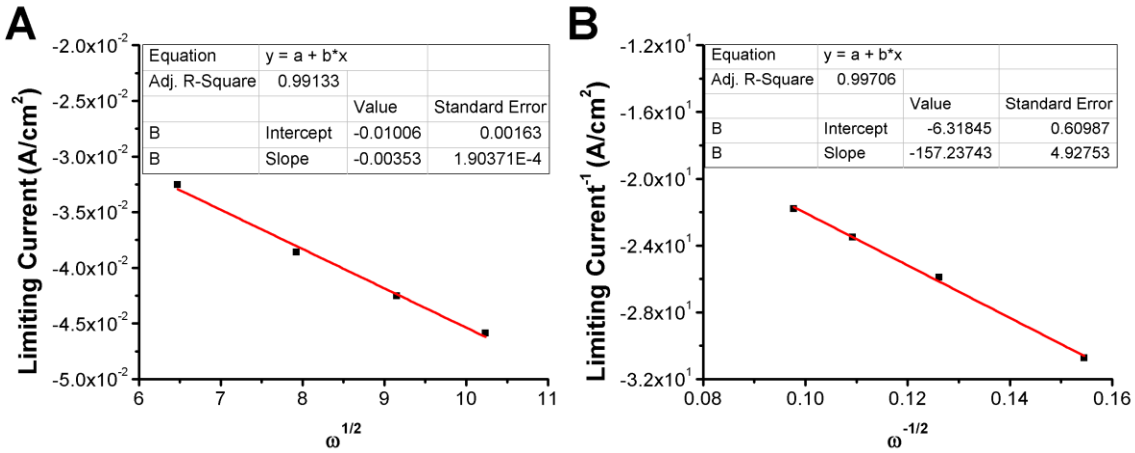

Figure SI 4.60. Levich **(A)** and Koutecky-Levich **(B)** plots from data obtained from Linear Sweep Voltammograms of $[Mn(TMPyP)Cl]^{4+}$ (0.25 mM) by RRDE under argon saturation conditions at various rotation rates in a pH 6 buffer solution.

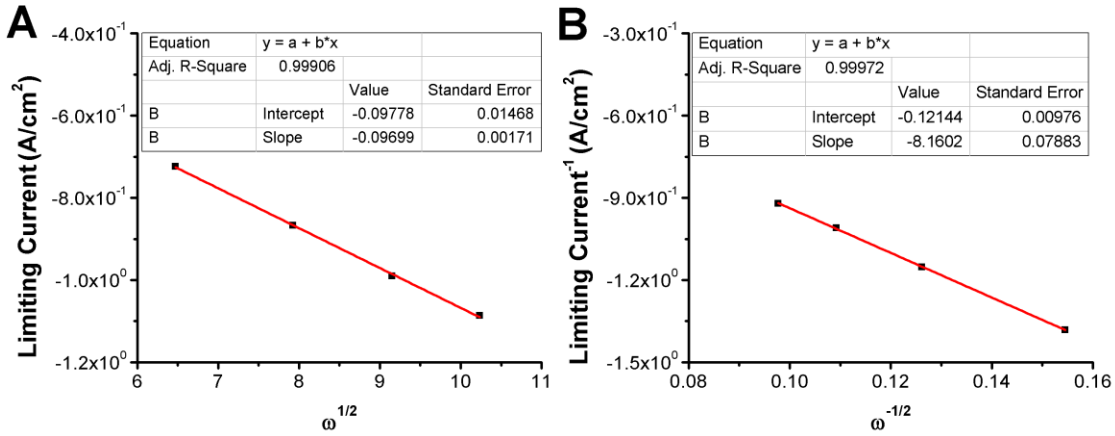

Figure SI 4.61. Levich **(A)** and Koutecky-Levich **(B)** plots from data obtained from Linear Sweep Voltammograms of $[Mn(TMPyP)Cl]^{4+}$ (0.25 mM) by RRDE under O_2 saturation conditions at various rotation rates in a pH 6 buffer solution.

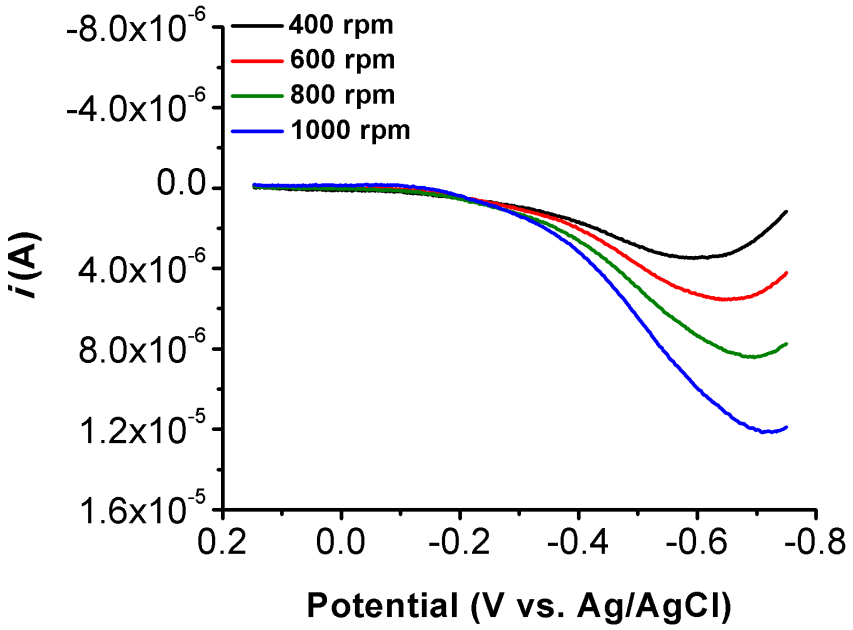

Figure SI 4.62. Linear Sweep Voltammograms of the generated ring current during RRDE experiments with $[Mn(TMPyP)Cl]^{4+}$ (0.25 mM) at various rotation rates with the argon ring current subtracted from the ring current produced under O_2 saturation conditions in a pH 6 buffer solution; ring potential = 1.2 V vs Ag/AgCl. Conditions: 0.25 mM analyte; glassy carbon working electrode/Pt ring working electrode, glassy carbon counter electrode, Ag/AgCl/3 M KCI reference electrode; scan rate 0.02 V/s.

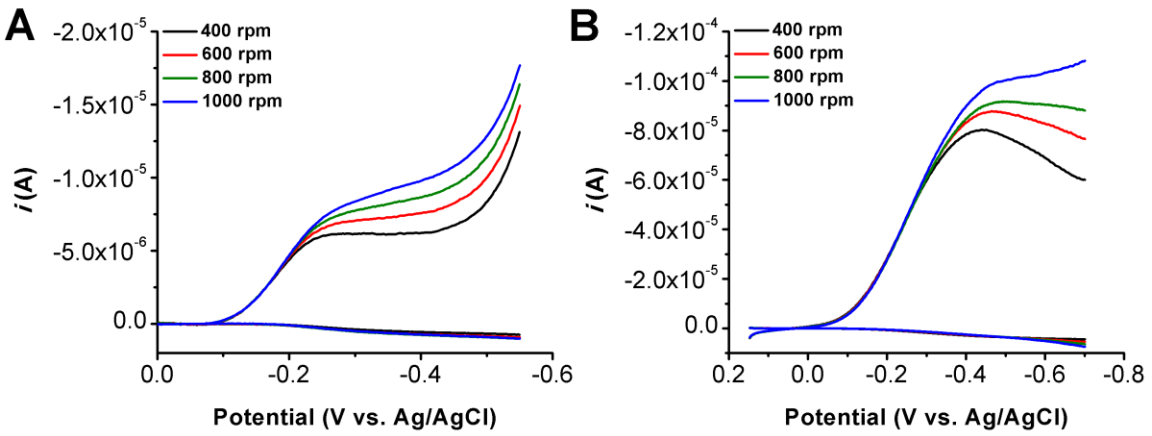

Figure SI 4.63. Linear Sweep Voltammograms of RRDE experiments with $[Mn(TMPyP)Cl]^{4+}$ (0.25 mM) at various rotation rates under argon **(A)** and O_2 **(B)** saturation conditions in a pH 4 buffer solution; ring potential = 1.2 V vs Ag/AgCl. Conditions: 0.25 mM analyte; glassy carbon working electrode/Pt ring working electrode, glassy carbon counter electrode, Ag/AgCl/3 M KCI reference electrode; scan rate 0.02 V/s.

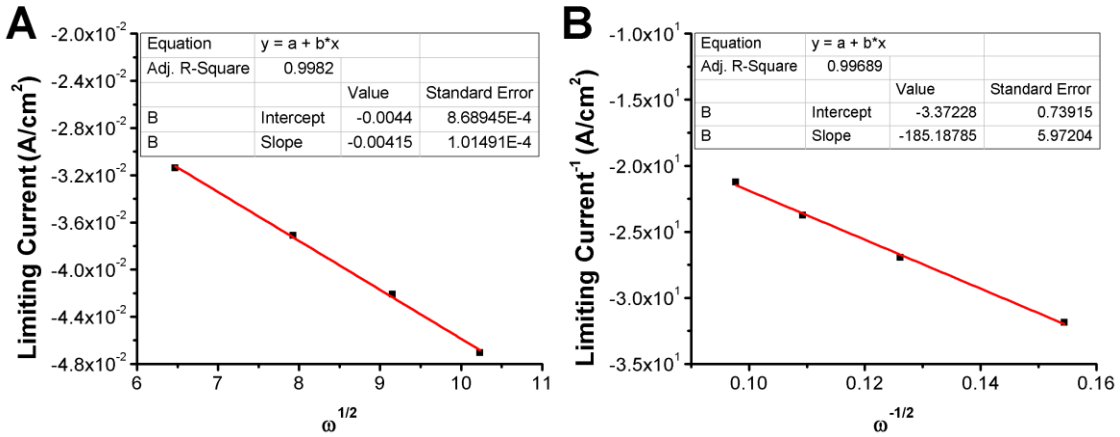

Figure SI 4.64. Levich **(A)** and Koutecky-Levich **(B)** plots from data obtained from Linear Sweep Voltammograms of $[Mn(TMPyP)Cl]^{4+}$ (0.25 mM) by RRDE under argon saturation conditions at various rotation rates in a pH 4 buffer solution.

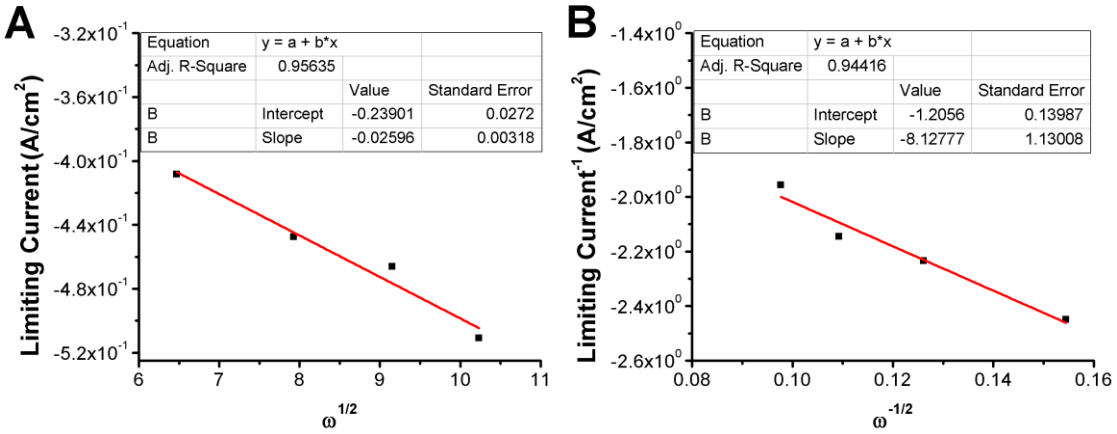

Figure SI 4.65. Levich **(A)** and Koutecky-Levich **(B)** plots from data obtained from Linear Sweep Voltammograms of $[Mn(TMPyP)Cl]^{4+}$ (0.25 mM) by RRDE under O_2 saturation conditions at various rotation rates in a pH 4 buffer solution.

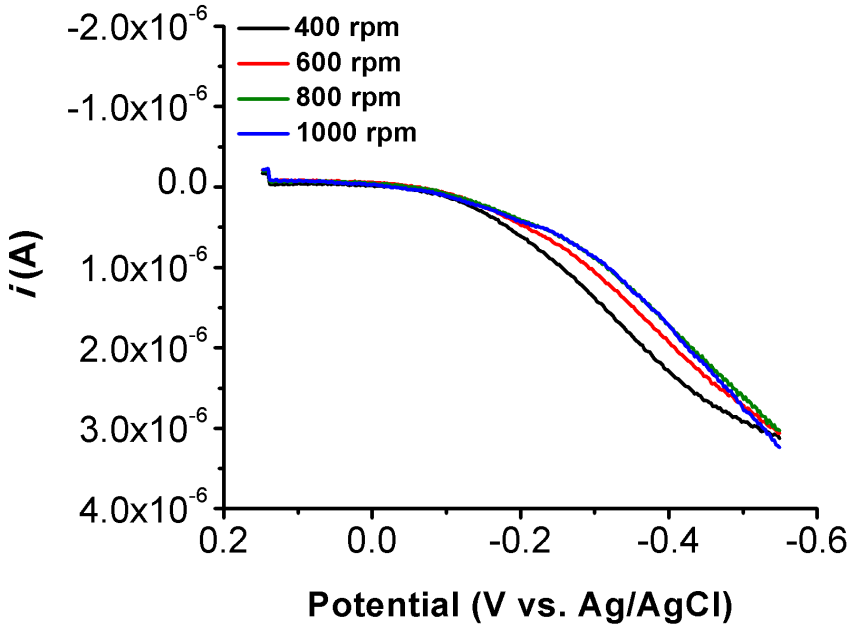

Figure SI 4.66. Linear Sweep Voltammograms of the generated ring current during RRDE experiments with $[Mn(TMPyP)Cl]^{4+}$ (0.25 mM) at various rotation rates with the argon ring current subtracted from the ring current produced under O_2 saturation conditions in a pH 4 buffer solution; ring potential = 1.2 V vs Ag/AgCl. Conditions: 0.25 mM analyte; glassy carbon working electrode/Pt ring working electrode, glassy carbon counter electrode, Ag/AgCl/3 M KCI reference electrode; scan rate 0.02 V/s.

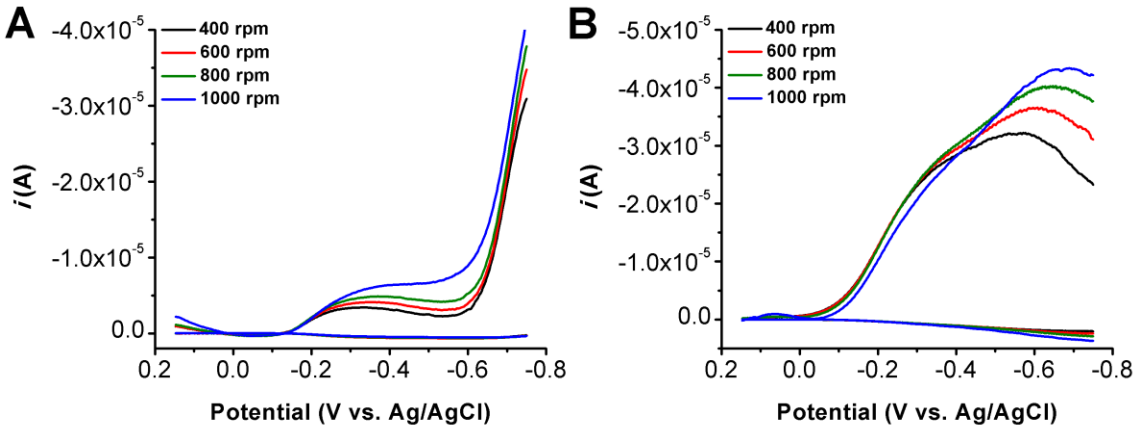

Figure SI 4.67. Linear Sweep Voltammograms of RRDE experiments with $[Mn(TMPyP)Cl]^{4+}$ (0.25 mM) at various rotation rates under argon **(A)** and O_2 **(B)** saturation conditions in a pH 3 buffer solution; ring potential = 1.2 V vs Ag/AgCl. Conditions: 0.25 mM analyte; glassy carbon working electrode/Pt ring working electrode, glassy carbon counter electrode, Ag/AgCl/3 M KCI reference electrode; scan rate 0.02 V/s.

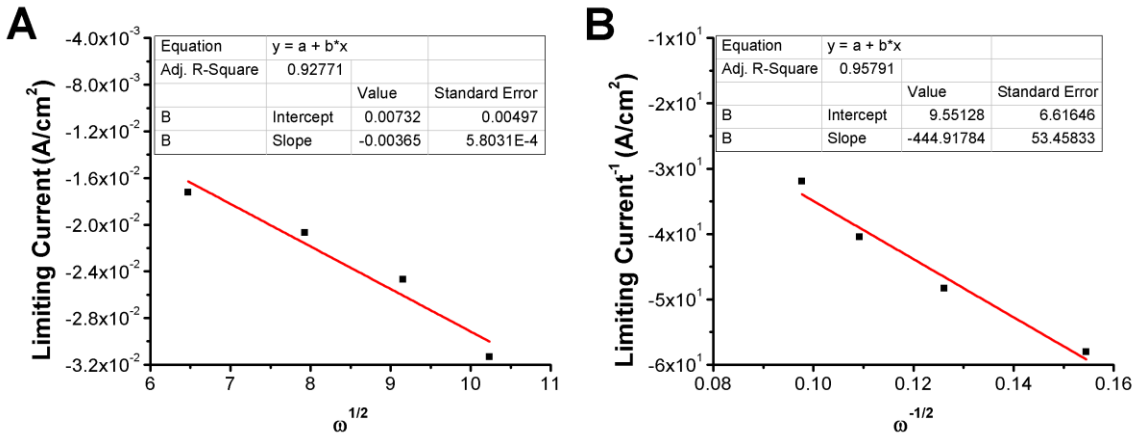

Figure SI 4.68. Levich **(A)** and Koutecky-Levich **(B)** plots from data obtained from Linear Sweep Voltammograms of $[Mn(TMPyP)Cl]^{4+}$ (0.25 mM) by RRDE under argon saturation conditions at various rotation rates in a pH 3 buffer solution.

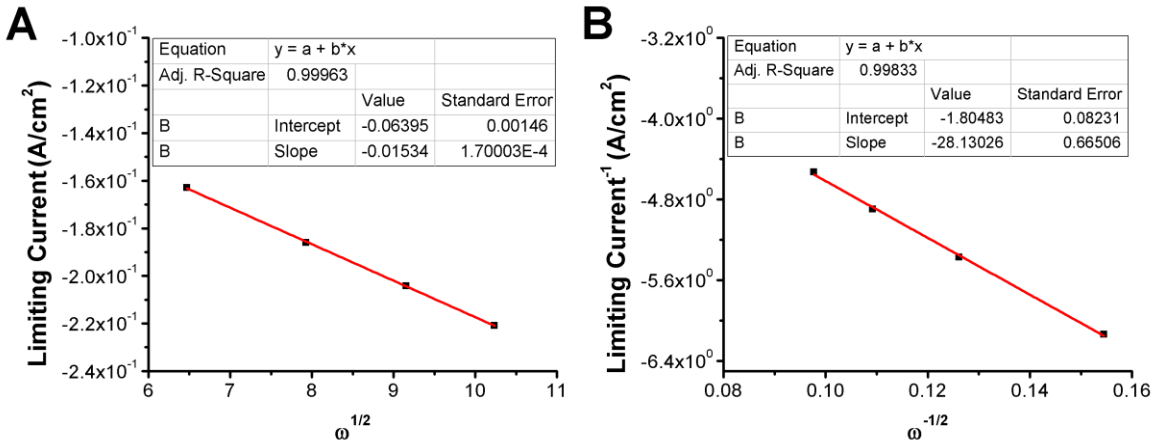

Figure SI 4.69. Levich **(A)** and K4outecky-Levich **(B)** plots from data obtained from Linear Sweep Voltammograms of $[Mn(TMPyP)Cl]^{4+}$ (0.25 mM) by RRDE under O_2 saturation conditions at various rotation rates in a pH 3 buffer solution.

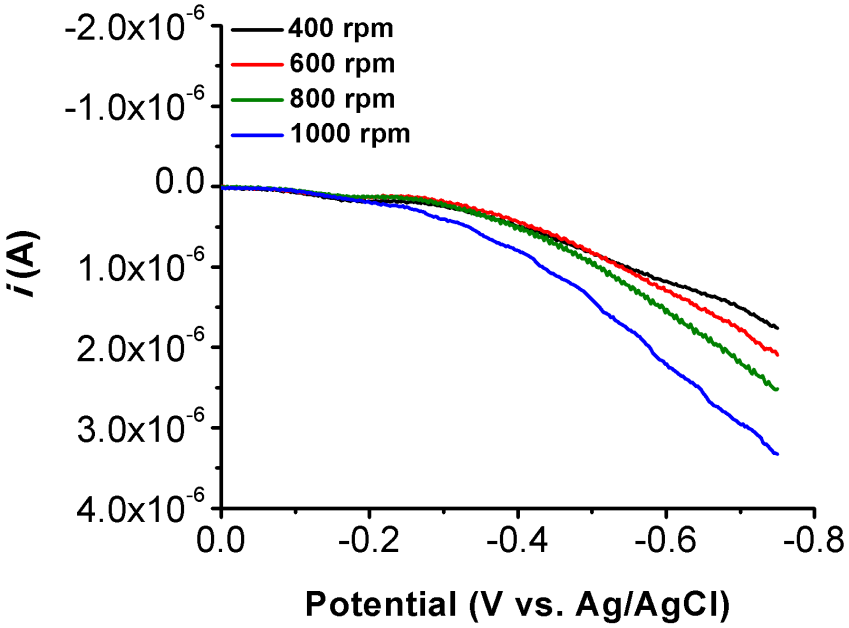

Figure SI 4.70. Linear Sweep Voltammograms of the generated ring current during RRDE experiments with $[Mn(TMPyP)Cl]^{4+}$ (0.25 mM) at various rotation rates with the argon ring current subtracted from the ring current produced under O_2 saturation conditions in a pH 3 buffer solution; ring potential = 1.2 V vs Ag/AgCl. Conditions: 0.25 mM analyte; glassy carbon working electrode/Pt ring working electrode, glassy carbon counter electrode, Ag/AgCl/3 M KCI reference electrode; scan rate 0.02 V/s.

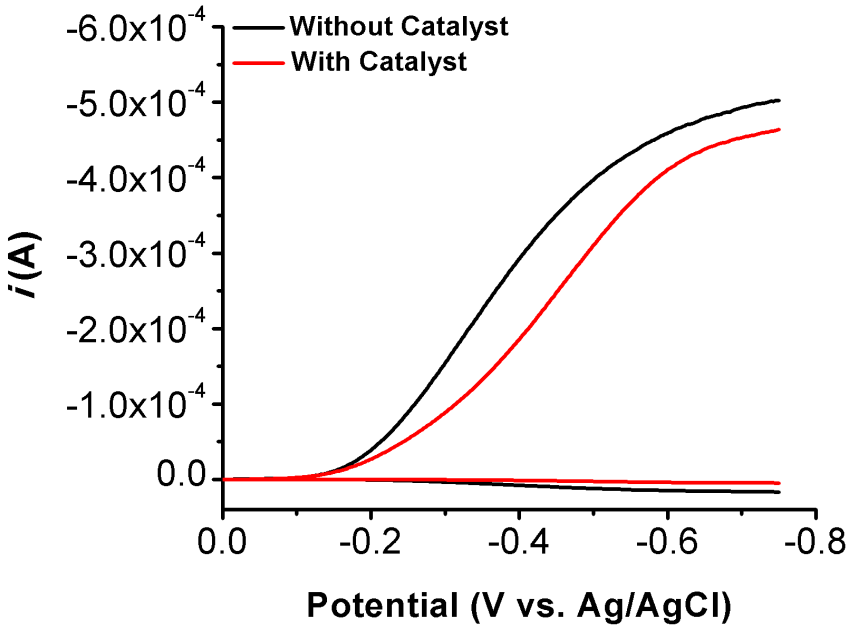

Figure SI 4.71. Linear Sweep Voltammograms of RRDE experiments with $[Mn(TMPyP)Cl]^{4+}$ (0.25 mM) at 1000 rpm under O_2 saturation conditions in a pH 7 buffer solution illustrating the inability to perform RRDE analysis above pH 6 due to the greater background disk and ring current observed at pH 7; ring potential = 1.2 V vs Ag/AgCl. Conditions: 0.25 mM analyte; glassy carbon working electrode/Pt ring working electrode, glassy carbon counter electrode, Ag/AgCl/3 M KCI reference electrode; scan rate 0.02 V/s.

Table SI 4.16. $\%H_2O_2$ calculated from RRDE experiments at various pH values.

pH	**Rotation Rate (rpm)**	**$\%H_2O_2$**	**Average $\%H_2O_2$**
3	400	16.2	
	600	15.4	
	800	17.4	
	1000	23.7	18 (±4)
4	400	14.0	
	600	11.4	
	800	10.4	
	1000	9.45	11 (±2)
5	400	6.71	
	600	6.14	
	800	6.77	
	1000	8.96	7 (±1)
6	400	9.64	
	600	12.8	
	800	16.9	
	1000	22.3	15 (±5)

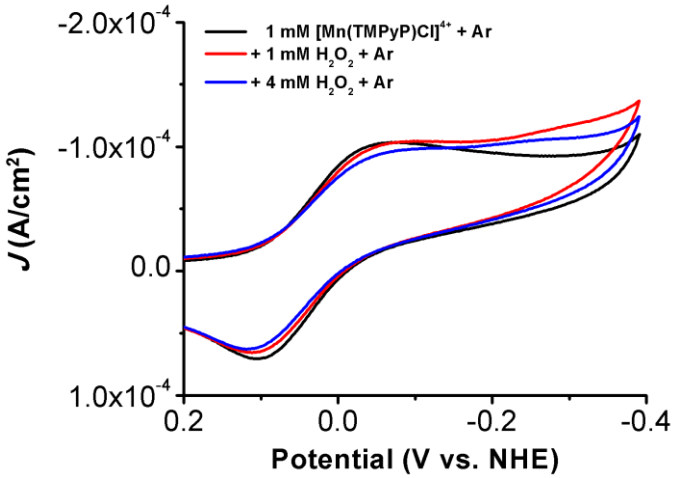

Figure SI 4.72. Control CV of 1 mM $[Mn(TMPyP)Cl]^{4+}$ with 1 mM H_2O_2 (red trace) and 4 mM H_2O_2 (blue trace) to show catalytic response for the dismutase of H_2O_2 in a pH 3 Britton-Robinson Buffer. Conditions: Glassy carbon working electrode, glassy carbon counter electrode, 3.0 M NaCl Ag/AgCl reference electrode; scan rate 100 mV/s.

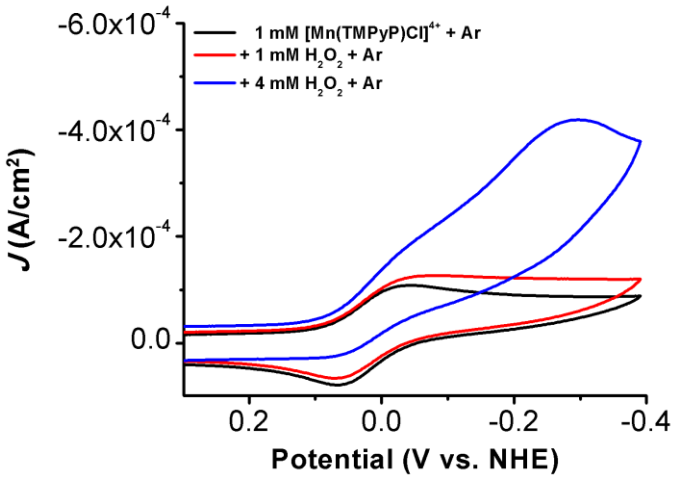

Figure SI 4.73. Control CV of 1 mM $[Mn(TMPyP)Cl]^{4+}$ with 1 mM H_2O_2 (red trace) and 4 mM H_2O_2 (blue trace) to show catalytic response for the dismutase of H_2O_2 in a pH 6 Britton-Robinson Buffer. Conditions: Glassy carbon working electrode, glassy carbon counter electrode, 3.0 M NaCl Ag/AgCl reference electrode; scan rate 100 mV/s.

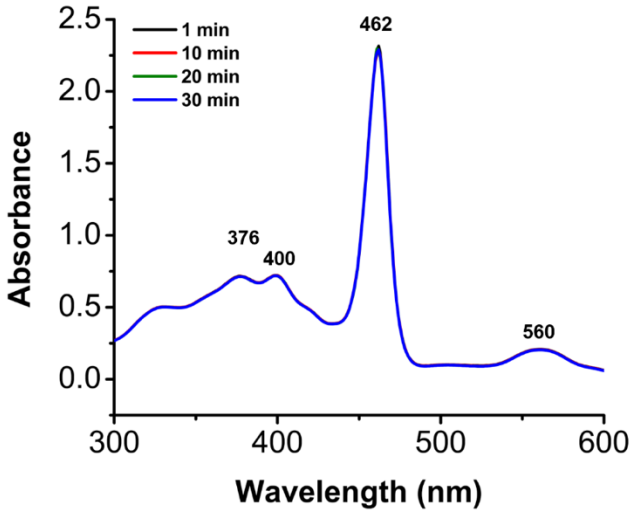

Figure SI 4.74. Control UV-Vis of 1.5 x 10^{-5} M $[Mn(TMPyP)Cl]^{4+}$ and 5.0 x 10^{-5} M H_2O_2 in pH 3 Britton-Robinson buffer.

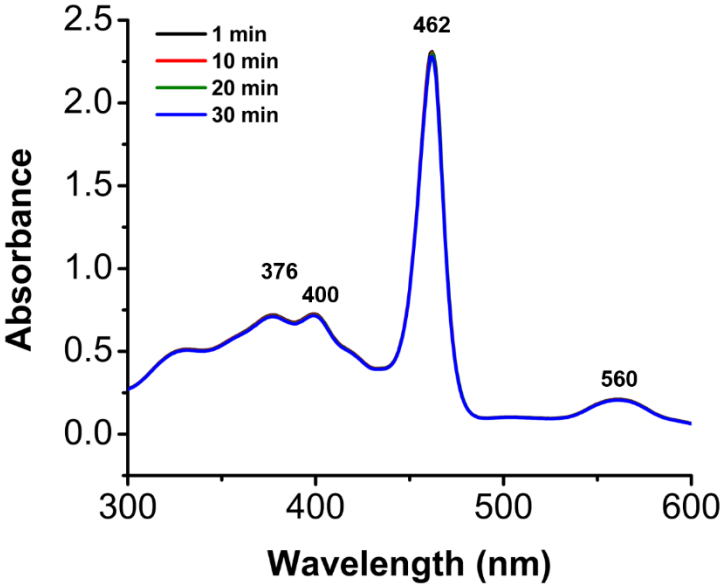

Figure SI 4.75. Control UV-Vis of 1.5 x 10^{-5} M $[Mn(TMPyP)Cl]^{4+}$ and 5.0 x 10^{-5} M H_2O_2 in pH 6 Britton-Robinson buffer.

4.7 Author Contributions

Lauren E. Lieske (first author) performed all of the cyclic voltammetry experiments and UV-Vis experiments; Shelby L. Hooe (second author) performed all RRDE experiments; Asa W. Nichols (third author) performed all UV-Vis spectroelectrochemical experiments; Dr. Charles W. Machan (corresponding author) conceived and supervised the experiments; and Lauren E. Lieske and Charles W. Machan wrote the manuscript.

4.8 References

1. Zhang, W.; Lai, W.; Cao, R., *Chem. Rev.* **2017,** *117*, 3717.
2. Pegis, M. L.; Wise, C. F.; Martin, D. J.; Mayer, J. M., *Chem. Rev.* **2018,** *118*, 2340.
3. Kobayashi, N.; Hiroshi, S.; Tetsuo, O., *Chem. Lett.* **1985,** *14*, 1917.
4. Q. He; T. Mugadza; G. Hwang, T. N., *Int. J. Electrochem. Sci.* **2012,** *7*, 7045.
5. Forshey, P. A.; Kuwana, T., *Inorg. Chem.* **1983,** *22*, 699.
6. Bettelheim, A.; Chan, R. J. H.; Kuwana, T., *J. Electroanal. Chem. Interfacial Electrochem.* **1980,** *110*, 93.
7. Shi, C.; Anson, F. C., *Inorg. Chem.* **1990,** *29*, 4298.
8. Passard, G.; Dogutan, D. K.; Qiu, M.; Costentin, C.; Nocera, D. G., *ACS Catal.* **2018,** *8*, 8671.
9. Britton, H. T. S.; Robinson, R. A., *J. Am. Chem. Soc.* **1931**, 1456.
10. Costentin, C.; Dridi, H.; Savéant, J.-M., *J. Am. Chem. Soc.* **2015,** *137*, 13535.
11. Kang, C.; Anson, F. C., *Inorg. Chem.* **1995,** *34*, 2771.
12. Harriman, A.; Porter, G., *J. Chem. Soc., Faraday Trans. 2* **1979,** *75*, 1532.
13. Harriman, A.; Porter, G., *J. Chem. Soc., Faraday Trans. 2* **1979,** *75*, 1543.
14. Harriman, A., *J. Chem. Soc., Dalton Trans.* **1984**, 141.

15. Zanello, P., *Inorganic Electrochemistry: Theory, Practice and Application* Royal Society of Chemistry 2003.

16. Savéant, J. M., *Elements of Molecular and Biomolecular Electrochemistry*. 2006; p 108.

17. Ruhlmann, L.; Nakamura, A.; Vos, J. G.; Fuhrhop, J.-H., *Inorg. Chem.* **1998,** *37*, 6052.

18. Balahura, R. J.; Kirby, R. A., *Inorg. Chem.***1994,** *33*, 1021.

19. Czernuszewicz, R. S.; Su, Y. O.; Stern, M. K.; Macor, K. A.; Kim, D.; Groves, J. T.; Spiro, T. G., *J. Am. Chem. Soc.* **1988,** *110*, 4158.

20. Chen, S.-M., *Electrochim. Acta* **1997,** *42*, 1663.

21. Spreer, L. O.; Leone, A.; Maliyackel, A. C.; Otvos, J. W.; Calvin, M., *Inorg. Chem.* **1988,** *27*, 2401.

22. Cheng, B.; Cukiernik, F.; Fries, P. H.; Marchon, J.-C.; Scheidt, W. R., *Inorg. Chem.* **1995,** *34*, 4627.

23. Harriman, A.; Christensen, P. A.; Porter, G.; Morehouse, K.; Neta, P.; Richoux, M.-C., *J. Chem. Soc., Faraday Trans. 1* **1986,** *82*, 3215.

24. Cho, K.-B.; Nam, W., *Chem. Comm.* **2016,** *52*, 904.

25. Carnieri, N.; Harriman, A.; Porter, G., *J. Chem. Soc., Dalton Trans.* **1982**, 931.

26. Fleischer, E. B.; Palmer, J. M.; Srivastava, T. S.; Chatterjee, A., *J. Am. Chem. Soc.* **1971,** *93*, 3162.

27. Weitner, T.; Budimir, A.; Kos, I.; Batinić-Haberle, I.; Biruš, M., *Dalton Trans.* **2010,** *39*, 11568.

28. Weitner, T.; Kos, I.; Mandić, Z.; Batinić-Haberle, I.; Biruš, M., *Dalton Trans.* **2013,** *42*, 14757.

29. Boucher, L. J., *Coord. Chem. Rev.* **1972,** *7*, 289.

30. Sanders, R., Henry's Law Constants. In *NIST Chemistry WebBook, NIST Standard Reference Database Number 69*, Mallard, P. J. L. a. W. G., Ed. National Institute of Standards and Technology Gaithersburg, MD, 20899.

31. Costentin, C.; Drouet, S.; Robert, M.; Savéant, J.-M., *J. Am. Chem. Soc.* **2012,** *134*, 11235.

32. Savéant, J. M.; Vianello, E., *Electrochim. Acta* **1963,** *8*, 905.

33. Faulkner, A. J. B. a. L. R., *Electrochemical Methods: Fundamentals and Applications*. 2nd ed.; John Wiley & Sons, Inc.: New York, 2000.

34. Naruta, Y.; Sasayama, M.-A., *J. Chem. Soc., Chem. Comm.* **1994**, 2667.

35. Balasubramanian, P. N.; Schmidt, E. S.; Bruice, T. C., *J. Am. Chem. Soc.* **1987,** *109*, 7865.

36. BASi http://www.bioanalytical.com/products/ec/faqele#Ref_Type (accessed Febuary 14, 2019).

37. Hooe, S. L.; Rheingold, A. L.; Machan, C. W., *J. Am. Chem. Soc.* **2018,** *140*, 3232.

38. Friis, E. P.; Andersen, J. E. T.; Madsen, L. L.; Bonander, N.; Møller, P.; Ulstrup, J., *Electrochim. Acta* **1998,** *43*, 1114.

39. Pegis, M. L.; McKeown, B. A.; Kumar, N.; Lang, K.; Wasylenko, D. J.; Zhang, X. P.; Raugei, S.; Mayer, J. M., *ACS Cent.Sci.* **2016,** *2*, 850.

40. Appendix C: Physical Properties of Water. In *MWH's Water Treatment: Principles and Design, Third Edition*, pp 1861.

41. Bard, A. J.; Parsons, R.; Jordan, J.; International Union of, P.; Applied, C., *Standard potentials in aqueous solution*. M. Dekker: New York, 1985.

42. Instrumentation, P. R., Reference Electrode *Product Guide*. 2017.

CHAPTER FIVE

Conclusions and Future Direction

5.1 Introduction

This thesis discussed various projects that involved the investigation of small molecule activation utilizing electrochemical techniques. The development of catalytic systems capable of reducing the stable small molecules of O_2 and CO_2 is a necessary requirement for future energy applications. Elucidating the mechanism and efficiency of different electrocatalytic systems is imperative for the development of the next generation of catalysts.

5.2 Conclusions

Chapter 2 of this thesis discussed the electrochemical reduction of CO_2 by the molecular species, $[Ni(TPEN)][PF_6]_2$. IR-SEC, CPE and CV experiments found that under protic conditions catalytic decomposition occurred via CO binding to form $Ni(CO)_4$. Attempts to circumvent this decomposition pathway by the addition of a CO scavenger, $[Ni(TMC)]^{2+}$, resulted in the stoichiometric capture of CO. These results suggest that although $[Ni(TPEN)]^{2+}$ is competent at mediating the two electron reduction of CO_2 to CO, the ligand framework needs to be modified to improve stability. Investigation of the deactivation pathway of Ni(cyclam) to $Ni(CO)_4$ suggests that ligand loss occurs at negative potentials generating a highly unstable reduced Ni(0) species which has high affinity for CO.[1-2] With this in mind, strategies to prevent the formation of a stable carbonyl species might include using a different metal center or modifying the ligand backbone with electron withdrawing groups to shift the Ni(II/I) reduction towards more positive potentials.[3] However issues with this may arise if the electron withdrawing groups shift the redox potential too far positive, preventing CO_2 activation by the catalyst.

Building on our investigation for CO_2RR, in Chapter 3 the organic species cyclic alkylamino carbene (^{cy}CAAC) was investigated as a mediator. Our study revealed that this species was competent for mediating the stoichiometric $2e^-$ reduction of CO_2 to carbonate and carbon monoxide. Catalysis for this system was prevented by the formation of degradation products revealed from IR-SEC, CPE, and computational studies (DFT). Possible routes for future work in making this system catalytic is the addition of a co-catalyst or additives that may stabilize the ketene species. One strategy could involve the use of a group 2 metal (Mg^{2+}) such as a Lewis acid to weaken the bound CO_2 adduct. This has been used successfully for inorganic-based catalysts in previous reports.[4-5]

Chapter 4 is devoted to understanding the ORR with a $[Mn(TMPyP)Cl]^{4+}$ catalyst under different pH conditions. After spectrochemical characterization of the catalyst through the entire pH domain, results showed that it was competent towards the reduction of O_2 to H_2O under acidic conditions. Future work on this system might involve a more thorough investigation of the ORR mechanism under acidic conditions in organic solvents or to further increase the selectivity towards H_2O to 100 %. It would be interesting to study the "push" effect on this catalyst to determine if it lowers the overpotential required to drive this reaction towards H_2O. Previous studies on the cytochrome P450 enzyme have shown that the incorporation of an axial *trans* ligand to the bound oxo species creates a "push" effect.[6-7] This ultimately causes a protonation event that promotes O–O bond cleavage and thus selectivity for H_2O production. This has been proven an effective strategy by Dey and co-workers[8] whom found that by using imidazole as the *trans* ligand, the pK_a of the distally bound O atom increases and thus favors the $4e^-$ pathway for an iron porphyrin immobilized onto a gold electrode. This could be tested for the

$[Mn(TMPyP)Cl]^{4+}$ catalyst via CV experiments by simply titrating 1-methylimidazole into solution to fill the vacant site on the manganese porphyrin site and determine if it promotes the stabilization of the O–O adduct.

5.3 Outlook for Future Applications of Molecular Catalysts

5.3.1 Electron-Proton-Transfer Mediators (EPTM)

One alternative approach to current inorganic systems is to turn to organic mediators for assistance.[9-11] Taking notes from nature, biological processes such as mitochondrial respiration utilize small molecule mediators to shuttle electrons and protons during redox reactions.[12] One example of this is ubiquinol which, assists cytochrome *c* oxidase in carrying out its reduction of O_2 to H_2O.[12] Within molecular catalytic systems, these organic mediators can be used with an inorganic catalyst or with another organic species to work cooperatively. Introduction to mediators for facilitating electron transfers in catalytic systems occurred as early as 1990, when Baeckvall[13] and co-workers successfully used hydroquinone as an electron transfer agent in a triple catalytic system. This triple catalytic system was used for aerobic oxidation of olefins and conjugated dienes.[13] The idea behind using a mediator is to lower the energetic demands associated with an electron transfer from metal catalyst to substrate.[9] A well-known mediator, 2,2,6,6-tetramethyl-1-piperidine N-oxyl (TEMPO), for alcohol electrooxidation[10-11] has recently become a promising candidate for ORR. Gerken and Stahl[14] used TEMPO as an electron-proton-transfer mediator (EPTM) within a co-catalytic system with nitrogen oxide mediators (NO_x) for the efficient reduction of O_2 to H_2O. EPTMs offer the unique benefit of shuttling both electrons and protons from the active catalyst to the substrate of interest. The advantage of the TEMPO/NO_x system in applications towards fuel cell technology is

that instead of forming H_2O_2 as a side reaction, nitrogen dioxide (NO_2) is generated instead. Operating independent of each other the co-catalyst shows negligible or no activity at all. However, when both co-catalysts are present together this co-catalytic system operates at a low overpotential of 300 mV in acetonitrile with trifluoracetic acid present. In a different study, Anson and Stahl used para-hydroquinone (H_2Q) as an EPTM as a cocatalyst together with the molecular catalyst, cobalt(salophen).[15] This co-catalytic system was able to selectively reduce O_2 to H_2O in dimethylformamide in the presence of acetic acid without generating H_2O_2. These results are noteworthy because Co(salophens) are typically selective towards H_2O_2.[16-17] Furthermore, the authors modified their EPTM to include a chlorine substituent (2-chlorobenzoquinone) and found an increase in catalytic current. These results suggest that modifications of either the catalyst or mediator can result in enhanced performance of the overall system. With few reports utilizing EPTMs towards ORR and none for CO_2RR, this may be the next big area of discovery for these two critical energy relevant reactions.

5.3.2 Flow Cell Technology for CO_2RR

Although molecular catalysts can be fine-tuned to optimize a reaction, a challenge remains in upscaling the energy technology towards industrial applications. One approach is utilizing flow cell technology to achieve higher current densities required for commercial applications. Technology commonly used in the laboratory settings for product analysis of both heterogenous and molecular CO_2RR catalyzed reactions, are two compartment cells or H-cells. H-Cells separate the cathode and anode reactions via a proton exchange[18] membrane or a glass frit.[19] The major disadvantage to this set up is its mass transport limitation.[20] A flow cell reactor or “flow cell” overcomes this providing a continuous flow

of solution, resulting in a transport of reactants towards the electrode while products are being pushed away mitigating the mass transport effect.[20] The mechanism by which CO_2 can be introduced to the system can also dictate increased current flow. Membrane based flow cells that allow for the introduction of CO_2 as a gas are known as "gas-phase flow cells" and they result in higher concentrations of the substrate in comparison to when CO_2 is dissolved into the solution.[20] These membrane-based flow cells consists of a membrane electrode assembly (MEA) which is situated between the anode and cathode gas diffusion electrodes (GDEs). These GDEs are on either side of a polymer electrolyte membrane (PEM).

Due to these advantages mentioned above, researchers are turning towards immobilizing well-known electrocatalyst for CO_2RR onto the cathodes of these reactors. For example, Berlinguette and co-workers modified the cathode of their zero-gap membrane flow reactor by spray coating it with a "catalyst ink" that consisted of carbon powder supported cobalt phthalocyanine and Nafion.[21] They reported selectivity's greater than 95 % at 150 mA/cm^2 for the reduction of CO_2 to CO. The authors reported that increased flow rates of CO_2 resulted in higher observed selectivity and incorporation of phenol into the catalyst ink resulted in even higher reported current densities. There are numerous systems emerging that are combining the selective power of a molecular catalyst with gas phase flow cells.[20] These systems can be fine-tuned based on physical parameters such as the MEA or PEM as well as tuning the type of molecular catalyst to observe higher current densities over longer periods of time.

5.4 References

1. Froehlich, J. D.; Kubiak, C. P., *J. Am. Chem. Soc.* **2015,** *137*, 3565.

2. Balazs, G. B.; Anson, F. C., *J. Electroanal. Chem.* **1993,** *361*, 149.

3. Costentin, C.; Robert, M.; Savéant, J.-M., *Acc. Chem. Res.* **2015,** *48*, 2996.

4. Sampson, M. D.; Kubiak, C. P., *J. Am. Chem. Soc.* **2016,** *138*, 1386.

5. Bhugun, I.; Lexa, D.; Savéant, J.-M., *J. Phys. Chem.* **1996,** *100*, 19981.

6. Shaik, S.; Kumar, D.; de Visser, S. P.; Altun, A.; Thiel, W., *Chem. Rev.* **2005,** *105*, 2279.

7. Meunier, B.; de Visser, S. P.; Shaik, S., *Chem. Rev.* **2004,** *104*, 3947.

8. Mukherjee, S.; Bandyopadhyay, S.; Chatterjee, S.; Dey, A., *Chem. Comm.* **2014,** *50*, 12304.

9. Piera, J.; Bäckvall, J.-E., *Angew. Chem.Int. Ed.* **2008,** *47*, 3506.

10. Francke, R.; Little, R. D., *Chem. Soc. Rev.* **2014,** *43*, 2492.

11. Badalyan, A.; Stahl, S. S., *Nature* **2016,** *535*, 406.

12. Babcock, G. T.; Wikström, M., *Nature* **1992,** *356*, 301.

13. Baeckvall, J.-E.; Hopkins, R. B.; Grennberg, H.; Mader, M.; Awasthi, A. K., *J. Am. Chem. Soc.***1990,** *112*, 5160.

14. Gerken, J. B.; Stahl, S. S., *ACS Cent. Sci.* **2015,** *1*, 234.

15. Anson, C. W.; Stahl, S. S., *J. Am. Chem. Soc.* **2017,** *139*, 18472.

16. Wang, Y.-H.; Pegis, M. L.; Mayer, J. M.; Stahl, S. S., *J. Am. Chem. Soc.* **2017,** *139*, 16458.

17. Zhang, W.; Lai, W.; Cao, R., *Chem. Rev.* **2017,** *117*, 3717.

18. Tatin, A.; Comminges, C.; Kokoh, B.; Costentin, C.; Robert, M.; Savéant, J.-M., *PNAS* **2016,** *113*, 5526.

19. Morlanés, N.; Takanabe, K.; Rodionov, V., *ACS Catal.* **2016,** *6*, 3092.

20. Weekes, D. M.; Salvatore, D. A.; Reyes, A.; Huang, A.; Berlinguette, C. P., *Acc. Chem. Res.* **2018,** *51*, 910.

21. Wang, M.; Torbensen, K.; Salvatore, D.; Ren, S.; Joulié, D.; Dumoulin, F.; Mendoza, D.; Lassalle-Kaiser, B.; Işci, U.; Berlinguette, C. P.; Robert, M., *Nature Comm.* **2019,** *10*, 3602.